Spring 2020

Nonlinearity Index Aircraft Spin Motion Analysis With Dynamic Inversion Spin Recovery Controller Design

Jeffry Walker
Old Dominion University, jeffry.walker89@gmail.com

NONLINEARITY INDEX AIRCRAFT SPIN MOTION ANALYSIS WITH DYNAMIC INVERSION SPIN RECOVERY CONTROLLER DESIGN

by

Jeffry Walker
B.S., December 2012, Old Dominion University

A Thesis Submitted to the Faculty of
Old Dominion University in Partial Fulfillment of the
Requirements for the Degree of

MASTER OF SCIENCE

AEROSPACE ENGINEERING

OLD DOMINION UNIVERSITY
May 2020

Approved by:

Brett Newman (Director)

Prof. Thomas Alberts (Member)

Prof. Sebastian Bawab (Member)

ABSTRACT

NONLINEARITY INDEX AIRCRAFT SPIN MOTION ANALYSIS WITH
DYNAMIC INVERSION SPIN RECOVERY CONTROLLER DESIGN

Jeffry Walker
Old Dominion University, 2020
Director: Dr. Brett Newman

The aim of this thesis research is to extend the previous work of Tapolcai utilizing nonlinearity index theory to quantitatively analyze nonlinearities in an aircraft model and to augment these undesirable nonlinear characteristics with feedback control. In his work Tapolcai utilized a simplified rotational three degree of freedom model to analyze spin conditions of the F-18 High Angle-of-Attack Research Vehicle model. Through the application of nonlinearity index theory, regions of severe nonlinearity were uncovered exhibiting chaotic non-periodic behavior, periodic limit cycling, and instability. If these conditions were encountered during flight, the aircraft would exhibit undesirable response characteristics thereby requiring augmented control to safely operate. In this research the F-18 model is first implemented with a complete translational and rotational six degree of freedom framework. The trim solution for a steady state spin condition is then determined subject to realizable constraints. The trim equations are then leveraged to create nonlinearity index plots to identify the regions of high nonlinearity that need to be augmented. Nonlinear Dynamic Inversion theory is then employed to design a controller for spin recovery. The effectiveness of the developed controller is confirmed with nonlinear simulations in different spin conditions that were identified from the nonlinearity index analysis.

NOMENCLATURE

Acronyms

1797B	MIL-STD-1797B	
8785C	MIL-F-8785C	
AMS	attainable moment subset	
AOA	angle-of-attack	
CLAW	control law	
CV	control variable	
CZT	chirp-z transform	
DFT	discrete Fourier transform	
DOF	degree of freedom	
EOM	equations of motion	
FCC	flight control computer	
FCS	flight control system	
FFT	fast Fourier transform	
GM	gain margin	db
HARV	high alpha research vehicle	
IRL	inner rate loop	
LC	linear controller	
MAL	middle attitude loop	
MUAD	maximum unnoticeable added dynamics	
NDI	nonlinear dynamic inversion	
NED	North East Down reference frame	
NI	nonlinearity index	
NIT	nonlinearity index theory	
OOP	object oriented programming	

OPL	outer path loop	
PI	proportional integral	
PLA	power lever angle	
PM	phase margin	deg
RLIM	rate limit	
SVD	singular value decomposition	
VVR	velocity vector roll	

Variables

α	angle-of-attack	rad
β	angle-of-sideslip	rad
χ	wind axis z rotation	rad
γ	wind axis y rotation (flight path angle)	rad
λ	eigenvalue	
λ_{MRE}	maximum real component of eigenvalue	
$\mathcal{L}$, $\mathcal{M}$, $\mathcal{N}$	roll, pitch, yaw moments along body axes	$\text{ft} - \text{lbf}$
μ	wind axis x rotation	rad
ν	auxiliary input	
ω	frequency	rad/s
ω_n	natural frequency	rad/s
$\overline{q}$	dynamic pressure $\frac{\rho}{V^2 2}$	lbf/ft^2
ψ	heading angle	rad
τ	time constant	
θ	body pitch attitude	rad
φ	body roll attitude	rad
$\vec{\Omega}_b$	body axis angular rates p, q, r	rad/s
$\vec{m}$	commanded moment	
$\vec{u}$	control vector	

$\vec{V_b}$	body axis velocities u, v, w	ft/s
ζ	damping ratio	
A	state dynamics matrix	
B	input distribution matrix	
b	wing span	ft
C	output distribution matrix	
c	wing chord	ft
D	input-output distribution matrix	
D, Y, L	aircraft drag, side, lift forces in stability axes	lbf
F_x, F_y, F_z	forces along body x, y, z axes	lbf
I_{xx}, I_{yy}, I_{zz}	principal moments of inertia	slug $-$ ft^2
I_{xz}	cross product moment of inertia	slug $-$ ft^2
K_i	integral gain	
K_p	proportional gain	
m	aircraft mass	slug
P	generalized matrix inverse	
p, q, r	body roll, pitch, yaw rate	rad/s
p_s, q_s, r_s	stability axis angular rates	rad/s
p_w, q_w, r_w	wind axis angular rates	rad/s
S	wing area	ft^2
s	complex frequency	rad/s
T	aircraft gross thrust	lbf
t	time	s
V	aircraft total velocity	ft/s

Spin Parameters

Ω	angular velocity about spin axis	rad/s
σ	heading angle relative to the spin axis	rad

$\vec{V}_{E_s}$, $\vec{\Omega}_{E_s}$	earth axis velocity and angular rate	ft/s, rad/s
R	spin radius	ft
V_d	descent velocity	ft/s

Subscripts

A	aerodynamic axes (stability) reference frame
b, B	body axes reference frame
c	command
d	desired
E	Earth-fixed North-East-Down reference frame
I	imaginary number component
R	real number component
s	stability axes reference frame
sp	short period (mode)
w	wind axes reference frame
x, y, z	axes along which variable is applied
E_s	Earth-orientated spin axis

Variable Modifiers

$\angle$	angle, pertaining to complex numbers
Δ	change in primary variable
$\dot{}$	derivative with respect to time
$\frac{\partial <\text{a}>}{\partial <\text{b}>}$	partial derivative of <a> with respect to <b>
$\in$	left-hand-side is in the set of right-hand-side
$\int$	integral
$\mathbb{R}$	real value domain
Re	real component of variable
∇	gradient operator
$<\text{matrix}>^{-1}$	matrix inverse

$\vec{}$	vector notation of primary variable
$C_{<\text{var}>}$	coefficient of <var>
$L_f^r h$	Lie derivative of f with respect to h of the $r^t h$ degree
$R_{<\text{f2}>,<\text{f1}>}$	rotation transformation matrix from frame <f1> to <f2>
$R_{<\text{var}>}$	rotation transformation matrix through <var>

Physical Constants

ρ	atmosphere density, taken at 1000 ft	$0.0023\,\text{slug/ft}^3$
g	gravity	$32.174\,\text{ft/s}^2$

TABLE OF CONTENTS

LIST OF TABLES

LIST OF FIGURES

Figure Page

Figure Page

Figure Page

Figure Page

Figure Page

CHAPTER 1
INTRODUCTION

1.1 Problem Discussion

The flight control system is an essential component in modern fighter aircraft that delivers the capability to satisfy mission goals, provide superior handling qualities, stabilize relaxed stability airframes, suppress flutter and structural vibrations, and operate through intentional and/or unintentional nonlinear conditions.[1] Examples of these nonlinear conditions may include large flight condition envelopes, rapid large angle maneuvering, stall-spin motions, controlled post-stall super-maneuverability, and unexpected departure from controlled flight leading to complex transient behavior such as the falling leaf characteristic.[2,3] Aircraft employing such control systems include the aging F-15 Eagle, F-16 Falcon,[4–6] F-18 Hornet,[7,8] and the present day F-22 Raptor[9] and F-35 Lightning.[10–12] Some of these open-loop airframes incorporate relaxed static stability for increased maneuverability and to increase range-payload performance and fuel economy. The level of stability is incompatible with pure manual control. Digital fly-by-wire flight control systems (FCS) are utilized to augment basic dynamic modes to a degree where the closed-loop airframe exhibits superior handling qualities. The control system typically changes fundamental airframe response behaviors to task tailored response types appropriate for various flight functions such as gross acquisition, fine tracking, guidance, and operation through or recovery from nonlinear conditions.

In academia it is not uncommon to explore new and complex methods of analysis to aid in control design for aircraft. Some examples include symbolic transfer factoring,[13] bifurcation analysis,[14,15] perturbation expansions,[16] multi-integral convolution,[17,18] nonlinearity index (NI) ,[19,20] and even high fidelity simulation. Bifurcation analysis comprises continuation methods to produce trimmed states from which eigenvalues are extracted facilitating the detection of a change in system stability which can provide a high level view of the overall system behavior. Nonlinearity index theory (NIT) uses local subregions to measure the deviation of linear models from the subregions nominal model providing indications of where nonlinear system behavior can be expected. Further, many nonlinear control design methods such as back-stepping,[21] feedback linearization,[22] dynamic inversion,[23] and adaptive[24] have been considered by academia. Dynamic inversion provides a systematic approach to control

design that can be applied to the entire flight envelope without the need for gain scheduling. Comparatively, industry is typically driven by rapid schedules and limited budgets thereby restricting thorough analysis options. Under these constraints, the control design engineer may not be able to conduct a thorough analysis and instead may solely rely on simpler linear methods. Although linear analysis can address many design facets within schedules and budget restrictions, some issues may arise that are not compatible with linear methods or may be inadvertently overlooked by linear methods. Furthermore, development within industry is not always receptive to the adoption of new analysis or control methods as it can be seen as a risk to diverge from previously employed strategies which may have already been proven. The need to bridge the gap between common industrial practice and more powerful analysis and design methods is thus underscored. Hence, it is desirable to further develop nonlinearity index analysis and nonlinear dynamic inversion design as a practical tool for the control design engineer to utilize. This tool would enable the control design engineer to determine whether linear methods will suffice or if further analysis or nonlinear control schemes may be required.

This thesis explores nonlinearity index analysis of six degree of freedom (DOF) aircraft spin motion and spin recovery controller design based on nonlinear dynamic inversion (NDI) . Three primary research objectives are encompassed in this thesis. The first is exploring the feasibility of NIT to detect and describe spin motion characteristics. The second is assessing the feasibility of NDI to recover and/or reduce fully developed spin motion. Lastly, a higher level goal is to facilitate utilization of advanced nonlinear techniques for design and analysis of aircraft systems suitable in the industrial setting. The first objective will be accomplished by extending the previous work done by Tapolcai[25–28] by considering the unconstrained 6DOF spin condition. A systematic framework will be implemented that enables the NI to be determined over the flight envelop thereby identifying regions of concern. The regions of concern are then augmented with NDI controllers designed to recover the aircraft from fully developed spin motion. The systematic framework and NDI implementation will bridge the second and third objectives. Ultimately, the relevance of this thesis is solidified by the comprehensive approach taken from nonlinear analysis to controller implementation which addresses shortcomings in linear methods yielding a better-yet-usable tool for use in industry.

1.2 Literature Review

1.2.1 Spin Analysis

Existing literature on the dynamics of spin primarily focuses on methods to approximate spin modes or utilizes complex computational methods for analysis. Early papers such as References 29, 30 provide an overview of the spin condition utilizing simplifying assumptions. In Reference 31 approximate spin prediction equations are presented using a definition defined by angle-of-attack α, and angle-of-sideslip β. These approximate equations are then used to predict spin modes by solving a balance of the moment equations utilizing a non-dimensional spin parameter ($\Omega b/2V$) with Ω being the angular velocity about the spin axis, b the wing span, and V the aircraft velocity. Furthermore, these equations are extended with rotary balance data to compute post-stall incipient, developed, and recovery spin motions. In Reference 32 the general definition for a spin is presented in body axes with subsequent assumptions applied to develop an approximate closed form solution for a propeller driven plane in a spin. This set of transformations to define the spin are applied in this thesis as it does not introduce unnecessary complexities. References 33, 34 utilize an equilibrium spin technique to graphically determine the spin modes. This method is very much the same as that presented in Reference 31 with the exception of a different rotation sequence to orient the aircraft. The equilibrium spin technique is extended in Reference 35 for the unconstrained spin condition; the results are then compared to the approximate solution method along with further low order approximations. Bifurcation theory is applied to the F-14 model in Reference 14 to determine spin modes by continuation of a single control surface. In Reference 36 bifurcation analysis was applied to the Generic Transport Model (GTM) to determine steady spin modes by varying elevator deflection. Subsequent simulations were used to show that natural damping of the aircraft could recover spins when the control surfaces were returned to neutral.

1.2.2 Nonlinearity Index Theory

Nonlinearity index theory was first introduced by Junkins in Reference 37 as a measure of static and dynamic nonlinearity as it pertains to orbital mechanics. In Reference 38 NIT was presented in greater detail and was used as the analysis method to compare nonlinearities present in different orbital mechanics reference frames and coordinate descriptions. Newman and Omran extended NIT to atmospheric flight mechanics in References

39, 40 and introduced an elliptical subregion approach with four expressions to measure the nonlinearity's strength across the entire flight envelope. In References 25, 27 NIT was applied to the F-18 High Alpha Research Vehicle (HARV) model during high angle-of-attack (AOA) flight regimes. Through application of NIT Tapolcai presented a systematic method to analyze the nonlinearities uncovering periodic-chaotic behavior that would have otherwise been overlooked by simpler linear analysis methods. In Reference 26 NI was applied to the aircraft stall condition providing a measure to discern the accuracy of traditional linear analysis. In Reference 41 NI was used as a novel means to gain schedule a control system.

1.2.3 Nonlinear Dynamic Inversion

In Reference 42 Lockheed Martin and Honeywell provide a practical yet thorough exploration of multivariable control theory including a high level overview of NDI. In Reference 23 the fundamental constructs of NDI are presented as a powerful alternative design method and are specifically applied to the F-18 HARV as an example. Reference 43 presents a model reference NDI control law along with model tracking performance plots which are leveraged in this thesis. In Reference 44, 45 NDI control is implemented using the theory of time-scale separation; this approach is utilized in this thesis. Use of time-scale separation with NDI results in a more traditional control structure than that of Reference 46 which uses a strict interpretation of dynamic inversion theory consisting of a single set of control values yielding higher order derivatives and an overall more complex implementation. The work presented in Reference 47 is closely tied to this thesis research topic as bifurcation analysis was used to determine steady trim states which were subsequently applied as control targets for a NDI controller to transition to and thereby recover the F-18 HARV from a steady spin condition.

1.3 Thesis Outline

In Chapter 2 the governing equations of motion used throughout this thesis are introduced. This chapter also covers the simulation model of the F-18 HARV aircraft that is utilized. Chapter 3 develops the trim process, model linearization, and nonlinearity index framework. These capabilities are then applied to the spin condition. Topics including linear dynamic inversion, nonlinear dynamic inversion, control allocation, and Lie derivatives are introduced in Chapter 4. Linear dynamic inversion is first used as a simple introduction to the theory of dynamic inversion prior to building into NDI which utilizes Lie derivatives for compact notation; control allocation is then discussed as it pertains to the implementation

of NDI. Chapter 5 presents a generalized process with sequential loop strategy applying the concepts introduced in Chapter 4 to the F-18 HARV using MIL-F-8785C requirements as a design reference.[48] Implementation issues specific to this model are discussed and the controller is validated using both frequency response and time-domain methods. The entire control system is evaluated using numerous spin simulations in Chapter 6. Results depicting recovery performance, system engagement profiles, and flight trajectories are presented indicating the ability of the NDI controller to successfully recover the aircraft from a broad range of spin conditions. Chapter 7 concludes this thesis and provides potential future work.

CHAPTER 2
SIMULATION MODEL

This chapter presents material necessary to mechanize a simulation model for engineering analysis. First governing equations for unconstrained aircraft motion are defined in two different reference frames, body and hybrid wind. Elements specific to the aircraft are subsequently introduced including aerodynamics, propulsion, and actuator models. Lastly, the simulation environment used in this research is briefed.

2.1 Modeling Assumptions

Standard aerospace engineering conventions are used throughout and it is assumed the reader has a graduate level understanding of aerospace engineering. A flat Earth, constant gravity, constant atmosphere, and zero wind environment model is utilized. Furthermore, the rigid body aircraft model assumes steady-symmetric aerodynamics, constant mass, inertial symmetry, symmetric thrust, and negligible angular momentum from the engines.

2.2 Equations of Motion

The study of unconstrained aircraft dynamics requires a set of nonlinear equations describing the general 6DOF motion. Two sets of motion equations are in common use and are described here. Differences between the two sets primarily involve the translational position and velocity descriptions. The two equation sets are inherently associated with the body centered axis system and the wind axis system. **??**–3 show these frames along with the inertial Earth-fixed North-East-Down (NED) frame and their relationship. The equation sets are derivable from first principles and can be found in the literature.[49,50]

2.2.1 Body Axis EOM

The body axis equations of motion (EOM) system is described by the twelve nonlinear equations presented in Equation (2.2-1).

$$\dot{u} = rv - qw - g\sin\theta + \frac{F_x}{m} \tag{2.2-1a}$$

$$\dot{v} = pw - ru + g\sin\varphi\cos\theta + \frac{F_y}{m} \tag{2.2-1b}$$

$$\dot{w} = qu - pv + g\cos\varphi\cos\theta + \frac{F_z}{m} \tag{2.2-1c}$$

$$\dot{q} = \frac{1}{I_{yy}}\left[\mathcal{M} + I_{xz}(r^2 - p^2) + (I_{zz} - I_{xx})rp\right] \tag{2.2-1d}$$

$$\begin{bmatrix}\dot{p}\\ \dot{r}\end{bmatrix} = \begin{bmatrix} I_{xx} & -I_{xz}\\ -I_{xz} & I_{zz}\end{bmatrix}^{-1}\begin{bmatrix}\mathcal{L} + I_{xz}pq + (I_{yy} - I_{zz})qr\\ \mathcal{N} - I_{xz}qr + (I_{xx} - I_{yy})pq\end{bmatrix} \tag{2.2-1e}$$

$$\dot{\varphi} = p + q\sin\varphi\tan\theta + r\cos\varphi\tan\theta \tag{2.2-1f}$$

$$\dot{\theta} = q\cos\varphi - r\sin\varphi \tag{2.2-1g}$$

$$\dot{\psi} = \sec\theta(q\sin\varphi + r\cos\varphi) \tag{2.2-1h}$$

$$\begin{bmatrix}\dot{x}\\ \dot{y}\\ \dot{z}\end{bmatrix} = R_{E_{NED},b}\begin{bmatrix}u\\ v\\ w\end{bmatrix} \tag{2.2-1i}$$

In Equation (2.2-1) $(\dot{x}, \dot{y}, \dot{z})$ denote the NED velocities, (u, v, w) denote the body axes velocities, (p, q, r) denote the body axes angular rates, and (ψ, θ, φ) correspond to a 3-2-1 Euler angle set. Equations (2.2-1a)–(2.2-1c) and (2.2-1d)–(2.2-1e) represent the kinetic force and moment equations along the body axis directions. Rotational and translational kinematic equations are listed as (2.2-1f)–(2.2-1h) and (2.2-1i), respectively.

In the kinetic force formulations, g is the gravitational constant and the external aerodynamic and propulsive forces (F_x, F_y, F_z) are defined by Equations (2.2-2) to (2.2-4) under the assumption that thrust only acts along the x-body axis. Aerodynamic parameters, (C_D, C_Y, C_L) represent the unitless drag, sideforce, and lift coefficients respectively. Additional aerodynamic parameters utilized henceforth are S the total wing area, wing span b, wing chord c, angle-of-attack α, angle-of-sideslip β, and dynamic pressure $\overline{q}$. Dynamic pressure is defined as $\overline{q} = \frac{1}{2}\rho V^2$, where ρ is the atmosphere density and is presumed constant in this research. Note sideslip is neglected in body axis aerodynamic force build-up.

$$F_x = T + S\overline{q}(C_L\sin\alpha - C_D\cos\alpha) \tag{2.2-2}$$

$$F_y = S\overline{q}C_Y \tag{2.2-3}$$

$$F_z = -S\overline{q}(C_D\sin\alpha + C_L\cos\alpha) \tag{2.2-4}$$

Aerodynamic moments $(\mathcal{L}, \mathcal{M}, \mathcal{N})$ drive the angular acceleration in Equations (2.2-1d) to (2.2-1e) and Figure 2 depicts the sense and direction they are applied. The inertia terms present in these formulations are the moments of inertia (I_{xx}, I_{yy}, I_{zz}) and the cross product moment of inertia I_{xz}.

In the translational kinematic formulation, $R_{E_{NED},b}$ denotes the transformation matrix from the body-fixed axes to the Earth-fixed NED frame and is defined in Appendix A.1.1. Position and yaw angle, which are governed by Equations (2.2-1h) to (2.2-1i), have no effect on the study of aircraft dynamics under the noted assumptions. Thus there are only eight equations that need to be considered for analysis.

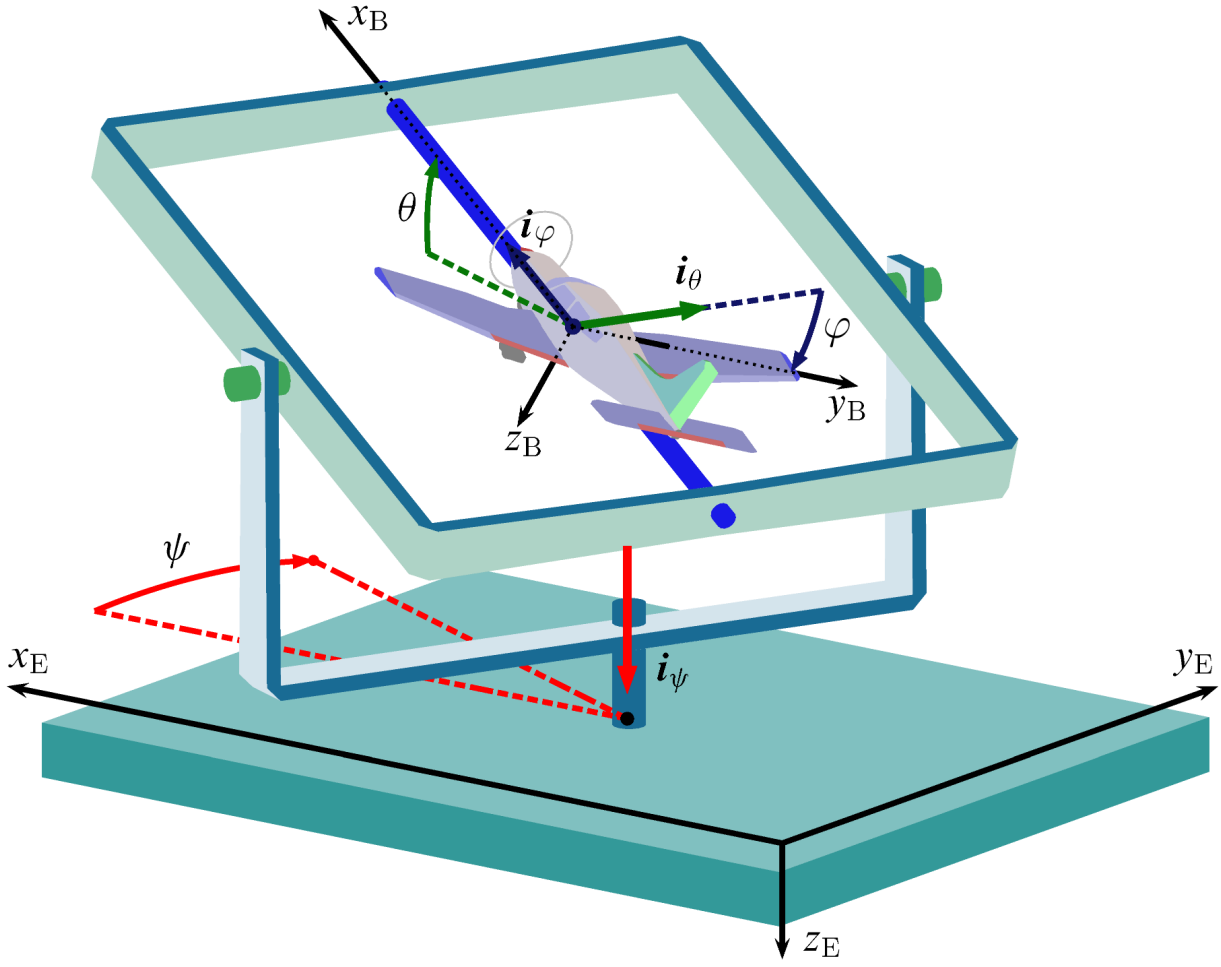

Figure 1 Euler Attitude Angles with respect to Earth-fixed North-East-Down Reference Frame[51]

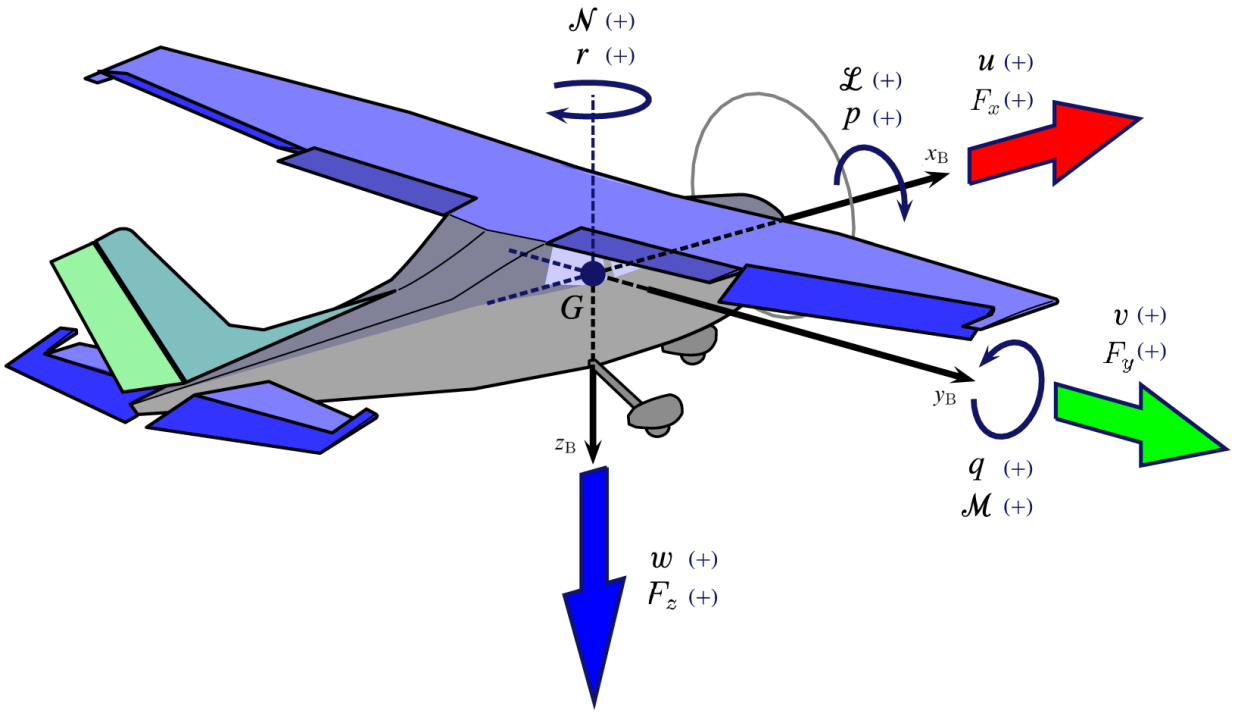

Figure 2 Aircraft Forces, Moments, Velocities, and Angular Rates[51]

2.2.2 Hybrid Wind EOM

While the body axis EOM are convenient for their simplicity, it is sometimes more intuitive to represent the translational equations in terms of spherical variables V, α, β. However, the conventional wind axis angular kinematic equations for velocity roll μ, velocity pitch (commonly referred to as flight path angle) γ, and velocity heading χ are not as intuitive as the body axis kinematic equations for (φ, θ, ψ) and corresponding kinetic equations for rates (p, q, r). Motivated by this observation the body axis angular equations are retained here; thus, Equation (2.2-5) is introduced as the hybrid wind axis EOM system.[50]

$$\dot{V} = \frac{1}{m}\left[T\cos\alpha\cos\beta - D\cos\beta + Y\sin\beta - mg\sin\gamma\right] \tag{2.2-5a}$$

$$\dot{\alpha} = q - q_w\sec\beta - p_s\tan\beta \tag{2.2-5b}$$

$$\dot{\beta} = r_w - r_s \tag{2.2-5c}$$

$$\dot{q} = \frac{1}{I_{yy}}\left[\mathcal{M} + I_{xz}(r^2 - p^2) + (I_{zz} - I_{xx})rp\right] \tag{2.2-5d}$$

$$\begin{bmatrix}\dot{p}\\ \dot{r}\end{bmatrix} = \begin{bmatrix} I_{xx} & -I_{xz}\\ -I_{xz} & I_{zz}\end{bmatrix}^{-1} \begin{bmatrix}\mathcal{L} + I_{xz}pq + (I_{yy} - I_{zz})qr\\ \mathcal{N} - I_{xz}qr + (I_{xx} - I_{yy})pq\end{bmatrix} \tag{2.2-5e}$$

$$\dot{\varphi} = p + q\sin\varphi\tan\theta + r\cos\varphi\tan\theta \tag{2.2-5f}$$

$$\dot{\theta} = q\cos\varphi - r\sin\varphi \tag{2.2-5g}$$

$$\dot{\psi} = \sec\theta(q\sin\varphi + r\cos\varphi) \tag{2.2-5h}$$

$$p_s = p\cos\alpha + r\sin\alpha \tag{2.2-5i}$$

$$r_s = r\cos\alpha - p\sin\alpha \tag{2.2-5j}$$

$$p_w = p_s\cos\beta + (q - \dot{\alpha})\sin\beta \tag{2.2-5k}$$

$$q_w = \frac{1}{mV}\left[T\sin\alpha + L - mg\cos\gamma\cos\mu\right] \tag{2.2-5l}$$

$$r_w = \frac{1}{mV}\left[Y\cos\beta + D\sin\beta - T\cos\alpha\sin\beta + mg\cos\gamma\sin\mu\right] \tag{2.2-5m}$$

$$\dot{x} = V\cos\gamma\cos\chi \tag{2.2-5n}$$

$$\dot{y} = V\cos\gamma\sin\chi \tag{2.2-5o}$$

$$\dot{z} = -V\sin\gamma \tag{2.2-5p}$$

The subscripted angular rates (p_s, r_s) refer to the stability axis roll and yaw rate, and similarly (p_w, q_w, r_w) refer to the wind axis angular rates. The aerodynamic forces, (D, Y, L) present in Equations (2.2-5a), (2.2-5l) and (2.2-5m) are the drag, side, and lift forces; Figure 3 presents the sense and direction (though C as been used instead of Y). Furthermore, Figure 3 depicts the significance of the flight path angle γ and its relationship to the angle-of-attack and sideslip α, β; the angle φ_W is equivalent to μ. In Equation (2.2-5) the wind axis angle terms can be defined in terms of α, β, φ, θ, ψ using the following relationship; the individual rotation matrices are defined in Appendix A.1.1.[52]

$$R_\chi\, R_\gamma\, R_\mu = R_\psi\, R_\theta\, R_\varphi\, R_\alpha^{\mathsf{T}}\, R_{-\beta}^{\mathsf{T}} \tag{2.2-6}$$

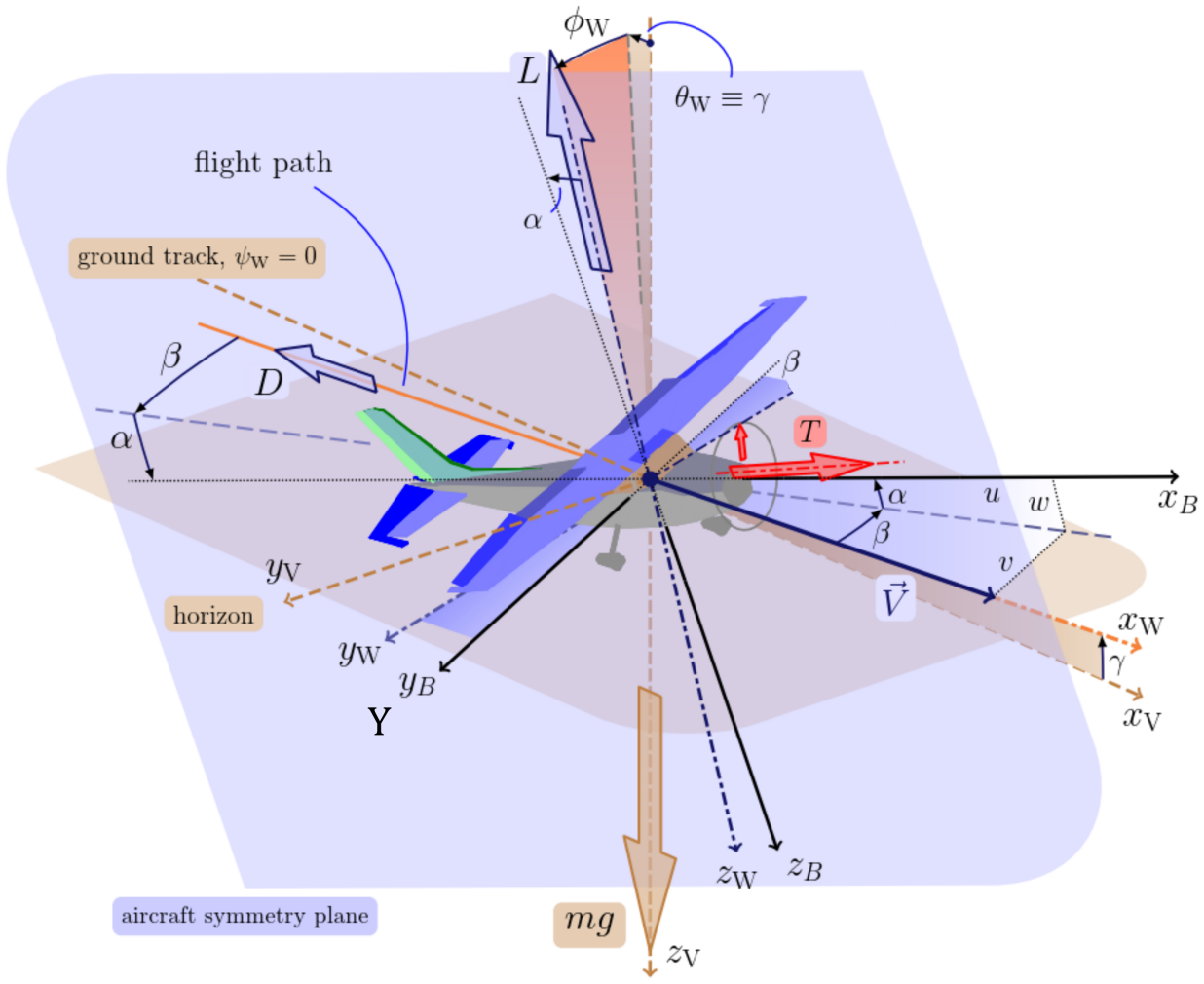

Figure 3 Aircraft Body, Wind, and Local-Vertical Axes Reference Frames[53]

Equation (2.2-7) represents the expanded form of Equation (2.2-6) and is used in the simulation model. Moreover, Equation (2.2-7a) can be used to obtain γ, Equations (2.2-7b) and (2.2-7c) are used to obtain μ, and Equations (2.2-7d) and (2.2-7e) are used to obtain χ.

$$\sin\gamma = \cos\alpha\cos\beta\sin\theta - \sin\beta\sin\varphi\cos\theta - \sin\alpha\cos\beta\cos\varphi\cos\theta \quad (2.2\text{-}7a)$$

$$\cos\gamma\cos\mu = \sin\theta\sin\alpha + \cos\alpha\cos\varphi\cos\theta \quad (2.2\text{-}7b)$$

$$\cos\gamma\sin\mu = \sin\theta\cos\alpha\sin\beta + \sin\varphi\cos\theta\cos\beta - \sin\alpha\sin\beta\cos\varphi\cos\theta \quad (2.2\text{-}7c)$$

$$\cos\gamma\cos\chi = \cos\alpha\cos\psi\cos\theta - \cos\varphi\sin\beta\sin\psi + \cos\beta\sin\alpha\sin\varphi\sin\psi \quad (2.2\text{-}7d)$$

$$
\begin{aligned}
&\quad + \cos\psi \sin\beta \sin\varphi \sin\theta \\
&\quad + \cos\beta \cos\varphi \cos\psi \sin\alpha \sin\theta \\
\cos\gamma \sin\chi \quad &= \cos\varphi \cos\psi \sin\beta \\
&\quad + \cos\alpha \cos\beta \cos\theta \sin\psi \\
&\quad - \cos\beta \cos\psi \sin\alpha \sin\varphi \\
&\quad + \sin\beta \sin\varphi \sin\psi \sin\theta \\
&\quad + \cos\beta \cos\varphi \sin\alpha \sin\psi \sin\theta
\end{aligned}
\tag{2.2-7e}
$$

2.3 F-18 Model

The numeric aircraft model used in this research is the publicly available F-18 High Alpha Research Vehicle (HARV). Numerical data hosted on the NASA website[54] was supplemented with data extracted from NASA technical memorandums such as References 55–57. The components utilized are described in the following sections.

2.3.1 Aerodynamic Model

The aerodynamic model for this aircraft is composed of thirty-three lookup tables, all of which are a function of α.[54] The domain of valid α for this model ranges from $-14°$ to $90°$. No prescribed valid range for β exists with the model; thus, maneuvers inducing large sideslip will be avoided to stay near the $\beta = 0$ datum of the supplied data. Table 1 lists the thirty-three non-dimensional aerodynamic force and moment coefficients and their structure. The available control inputs are the differential aileron deflection δ_a, left-right elevator (stabilator) deflection δ_e, and rudder deflection δ_r.

The total aerodynamic force and moment coefficients are built up as shown in Equations (2.3-1) to (2.3-2).

$$C_D = C_{D,0} + C_{D,\delta_{el}}\,\delta_{e,l} + C_{D,\delta_{er}}\,\delta_{e,r} + C_{D,q}\frac{c\,q}{2\,V} \tag{2.3-1a}$$

$$C_Y = C_{y,\beta}\,\beta + C_{y,\delta_a}\,\delta_a + C_{y,\delta_{el}}\,\delta_{e,l} + C_{y,\delta_{er}}\,\delta_{e,r} + C_{y,\delta_r}\,\delta_r + C_{y,p}\frac{b\,p}{2\,V} + C_{y,r}\frac{b\,r}{2\,V} \tag{2.3-1b}$$

$$C_L = C_{L,0} + C_{L,\delta_{el}}\,\delta_{e,l} + C_{L,\delta_{er}}\,\delta_{e,r} + C_{L,q}\frac{c\,q}{2\,V} \tag{2.3-1c}$$

$$C_l = C_{l,\beta}\,\beta + C_{l,\delta_a}\,\delta_a + C_{l,\delta_{el}}\,\delta_{e,l} + C_{l,\delta_{er}}\,\delta_{e,r} + C_{l,\delta_r}\,\delta_r + C_{l,p}\frac{b\,p}{2\,V} + C_{l,r}\frac{b\,r}{2\,V} \tag{2.3-2a}$$

$$C_m = C_{m,0} + C_{m,\delta_{el}}\,\delta_{e,l} + C_{m,\delta_{er}}\,\delta_{e,r} + C_{m,q}\frac{c\,q}{2\,V} \tag{2.3-2b}$$

$$C_n = C_{n,\beta}\,\beta + C_{n,\delta_a}\,\delta_a + C_{n,\delta_{el}}\,\delta_{e,l} + C_{n,\delta_{er}}\,\delta_{e,r} + C_{n,\delta_r}\,\delta_r + C_{n,p}\frac{b\,p}{2\,V} + C_{n,r}\frac{b\,r}{2\,V} \tag{2.3-2c}$$

The aerodynamic lookup tables are implemented in a MATLAB system object utilizing an optimized lookup routine. This implementation is convenient as it enables the aerodynamics to be queried from either the MATLAB or Simulink environment.

Table 1 F-18 HARV Aerodynamic Tables

Parameter	Drag	Sideforce	Lift	Roll	Pitch	Yaw
α	C_{D_0}		C_{L_0}		C_{m_0}	
β		$C_{y,\beta}$		$C_{l,\beta}$		$C_{n,\beta}$
p		$C_{y,p}$		$C_{l,p}$		$C_{n,p}$
q	$C_{D,q}$		$C_{L,q}$		$C_{m,q}$	
r		$C_{y,r}$		$C_{l,r}$		$C_{n,r}$
δ_a		C_{y,δ_a}		C_{l,δ_a}		C_{n,δ_a}
$\delta_{e,l}, \delta_{e,r}$	$C_{D,\delta_{el}}$ $C_{D,\delta_{er}}$	$C_{y,\delta_{el}}$ $C_{y,\delta_{er}}$	$C_{L,\delta_{el}}$ $C_{L,\delta_{er}}$	$C_{l,\delta_{el}}$ $C_{l,\delta_{er}}$	$C_{m,\delta_{el}}$ $C_{m,\delta_{er}}$	$C_{n,\delta_{el}}$ $C_{n,\delta_{er}}$
δ_r		C_{y,δ_r}		C_{l,δ_r}		C_{n,δ_r}

2.3.2 Propulsion Model

The HARV is powered by two F404-GE-400 engines. For the purpose of nonlinear simulation the engines will be represented with simple first order dynamics.[55] Typically engines are modeled using comprehensive lookup tables relating thrust as a function of altitude, Mach number, and power lever angle (PLA); however, this information is not publicly available so thrust will be a percentage of the maximum available thrust based on the current throttle value. This simplification will not impact the validity of the research as comprehensive testing across the entire flight envelope is not required.

Figure 4 presents the block diagram implementation of the engine dynamics by shaping the throttle command, δ_t. Note these dynamics consist of a first order system with variable time constant τ and rate limiting (RLIM) on the power lever signal. The shaped δ_t output scaled from zero to one simply multiplies by the maximum afterburner thrust, 32e3 lbf. The linear interpolation implementation of the breakpoint blocks are defined in Equation (2.3-3) while the block diagram conventions used hereafter are defined in Appendix A.2. In Figure 4, RLIM refers to the rate limit values to be used in the block diagram implementation defined in Figure 95.

$$\begin{aligned} PLA &= 31 + 99\delta_t \\ \tau &= \begin{cases} (PLA > 87)0.55 \\ (PLA \leq 87)0.625 \end{cases} \\ \delta_t &= \frac{1}{99}(PLA - 31) \end{aligned} \tag{2.3-3}$$

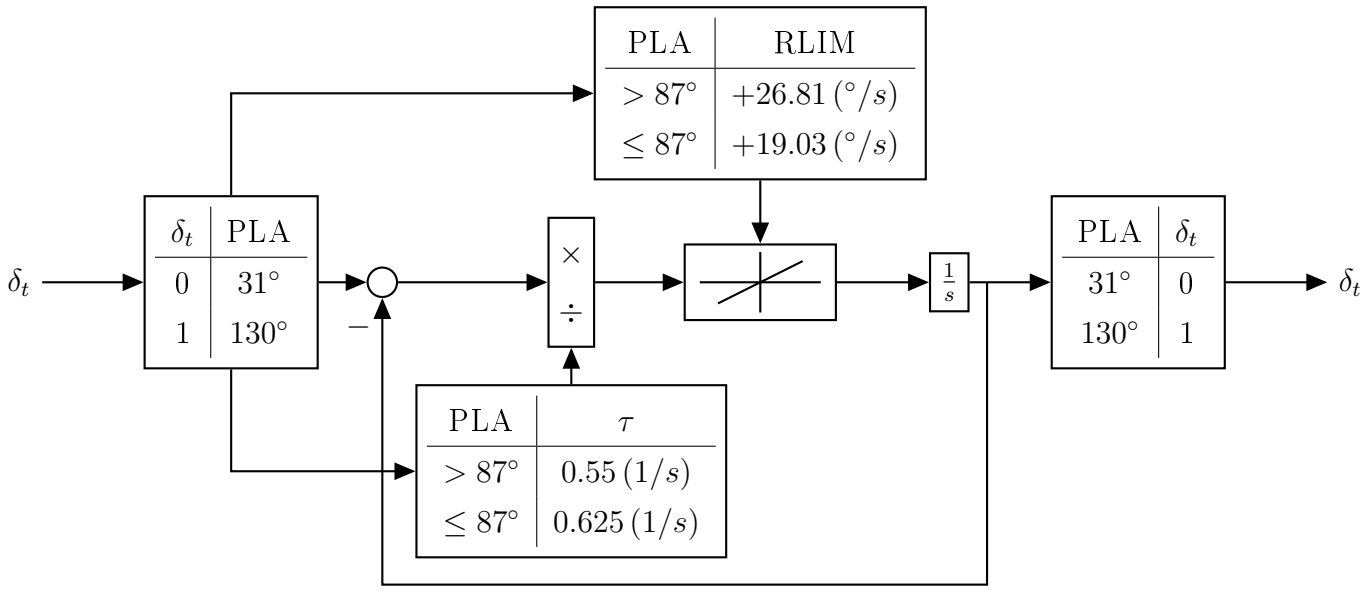

Figure 4 F404-GE-400 Engine Dynamics

2.3.3 Actuator Model

The dynamics of the aerodynamic surface actuators on the HARV are modeled as first and second order linear transfer functions as defined in Reference 56 . Additionally, rate and

position limits will be imposed as these nonlinearities are critical in realistically evaluating controller performance in nonlinear simulations.

The actuator position and rate limits utilized in the simulation are provided in Table 2. Note that the aileron position limits have been modified from Reference 56 . In Reference 56 the aileron position limits are given as $-25°$, $+42°$. However, the aerodynamic database is not implemented with independent left/right surfaces. To simplify this matter, the ailerons have been given equal control authority in both directions corresponding to the maximum travel of $42°$. The linear actuator models are presented in Table 3 where the input/output units are rad/rad and the natural frequencies use rad/s.

Table 2 F-18 HARV Actuator Physical Limits

Actuator	Rate Limit	Position Limit
Aileron	$\pm 100°/s$	$\pm 42°$
Elevator	$\pm 40°/s$	$-24°$, $+10.5°$
Rudder	$\pm 82°/s$	$\pm 30°$

Table 3 F-18 HARV Linear Actuator Models

Actuator	Linear Model
Aileron	$\frac{75^2}{s^2+2(0.59)(75)s+75^2}$
Elevator	$\frac{30.74^2}{s^2+2(0.509)(30.74)s+30.74^2}$
Rudder	$\frac{72.1^2}{s^2+2(0.69)(72.1)s+72.1^2}$

2.4 Simulation Environment

Models presented in the previous section will be implemented utilizing the MATLAB and Simulink environment. Nonlinear simulations conducted in the Simulink environment will utilize a fixed step solver. All MATLAB based systems will be implemented using Object Oriented Programing (OOP), specifically MATLAB Systems. The benefits of OOP and MATLAB Systems include:

- strict control on system interfaces,
- seamless integration into the Simulink environment,
- re-usability of common components.

CHAPTER 3
SPIN ANALYSIS

In this chapter the analysis of the 6DOF spin is conducted utilizing nonlinearity index theory. Two prerequisites to calculating the NI are (1) trimming the aircraft in a steady state spin condition, and (2) linearizing the system. These topics will first be covered in the following sections. The formulation of the nonlinearity index requires many equilibrium points to be determined. To facilitate this requirement the equations of motion must be solved subject to constraints that define a steady state spin. The solutions also should be predictable and be systematically determined by varying a single parameter.

3.1 Spin Analysis Trim

In order to solve the system of nonlinear equations, MATLAB's *lsqnonlin* function will be utilized. This solver method enables constraints to be set on the input variables which is necessary to ensure the solution is realizable.

3.1.1 Spin Parameterization

The aircraft spin motion can readily be defined in an Earth-orientated coordinate system that rotates with the aircraft. Let the subscript $_{E_s}$ denote this reference frame and define the axis system such that the x axis points towards the spin center of rotation, and the z axis points down. Figure 5 depicts the aircraft spin motion and depicts the angle σ defined herein. Using this reference frame results in the following conditions where V_d is the vertical descent velocity, R the spin radius, Ω the angular spin velocity, $\vec{V}_{E_s}$ the inertial velocity vector, and $\vec{\Omega}_{E_s}$ is the inertial angular velocity vector.

$$\vec{V}_{E_s} = \begin{bmatrix} 0 \\ -R\Omega \\ V_d \end{bmatrix}, \quad \vec{\Omega}_{E_s} = \begin{bmatrix} 0 \\ 0 \\ \Omega \end{bmatrix} \tag{3.1-1}$$

Parameters R, Ω, V_d fundamentally describe the spin characteristics and although they could be specified in the trim process, they are typically treated as unknowns along with other remaining state variables and control inputs after specifying a subset of these variables and inputs. Unknowns are computed from the governing motion relations from Chapter 2 and the constraint relations are presented above and below.

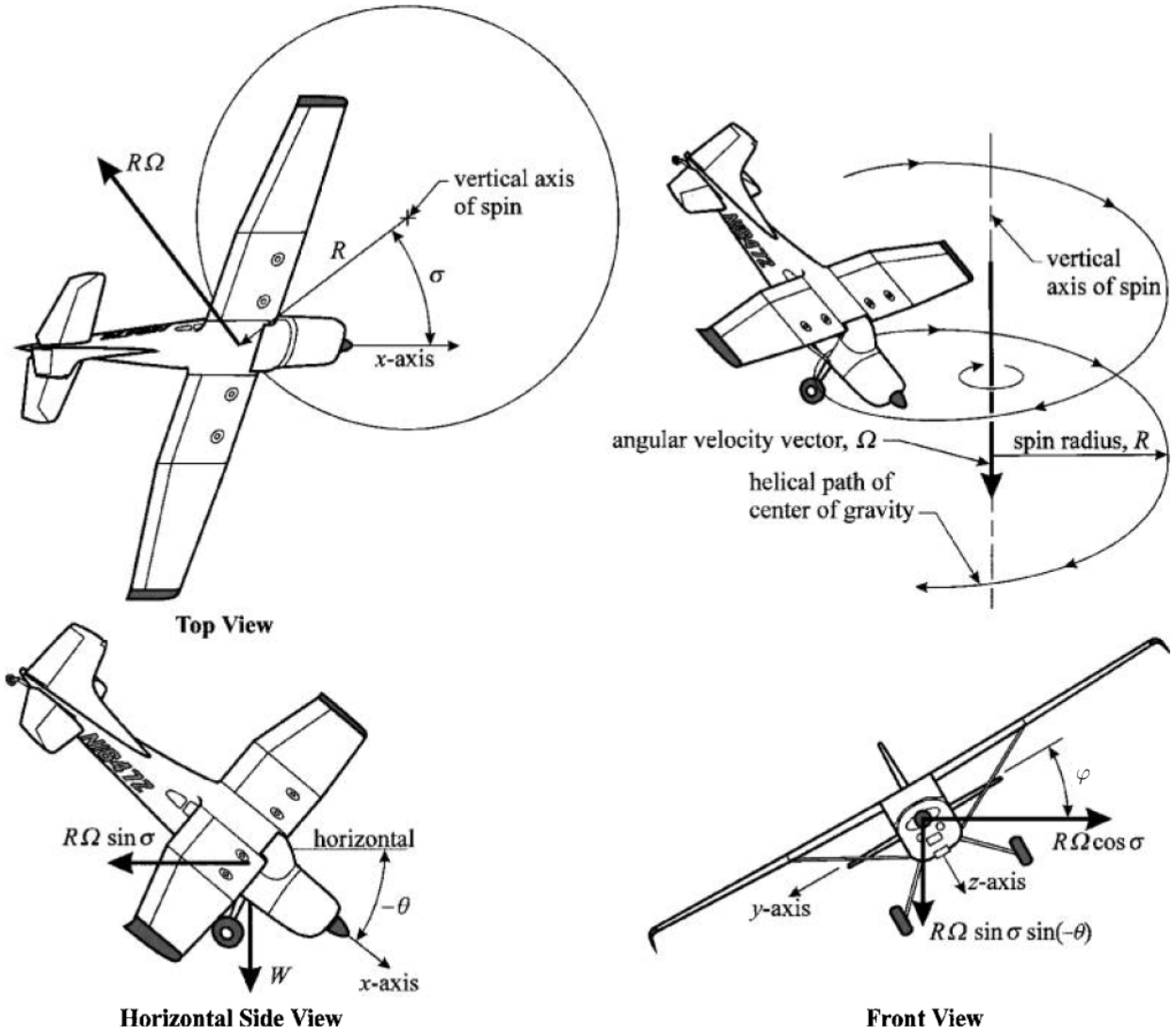

Figure 5 Aircraft Spin Motion[32]

In order to determine the body angular rates (p, q, r) and velocities (u, v, w) or (V, α, β), the method of rotation must be defined. The rotations introduced in Reference 32 are utilized here. This consists of a rotation σ about the vertical axis followed by the conventional pitch and roll angles (θ, φ). In this context σ is the heading angle, but is measured from the radial plane. Equation (3.1-2) defines the necessary transformation matrices to transform a vector

from the E_s frame to the body axes.

$$R_\sigma = \begin{bmatrix} \cos\sigma & \sin\sigma & 0 \\ -\sin\sigma & \cos\sigma & 0 \\ 0 & 0 & 1 \end{bmatrix} \quad R_\theta = \begin{bmatrix} \cos\theta & 0 & -\sin\theta \\ 0 & 1 & 0 \\ \sin\theta & 0 & \cos\theta \end{bmatrix}$$
$$R_{b,E_s} = R_\varphi\, R_\theta\, R_\sigma \qquad R_\varphi = \begin{bmatrix} 1 & 0 & 0 \\ 0 & \cos\varphi & \sin\varphi \\ 0 & -\sin\varphi & \cos\varphi \end{bmatrix} \tag{3.1-2}$$

Utilizing Equation (3.1-2) the body axis angular rates (p, q, r), which are the components of angular velocity vector $\vec{\Omega}_b$, are defined by Equation (3.1-3).

$$\vec{\Omega}_b = R_{b,E_s}\vec{\Omega}_{E_s} = \begin{bmatrix} -\Omega\sin\theta \\ \Omega\cos\theta\sin\varphi \\ \Omega\cos\theta\cos\varphi \end{bmatrix} \tag{3.1-3}$$

Similarly, the body axis translational velocities (u, v, w), the components of velocity vector $\vec{V}_b$, are defined by Equation (3.1-4).

$$\vec{V}_b = R_{b,E_s}\vec{V}_{E_s} = \begin{bmatrix} -V_d\sin\theta - R\Omega\sin\sigma\cos\theta \\ V_d\cos\theta\sin\varphi - R\Omega\left(\cos\sigma\cos\varphi + \sin\sigma\sin\theta\sin\varphi\right) \\ V_d\cos\theta\cos\varphi + R\Omega\left(\cos\sigma\sin\varphi - \sin\sigma\sin\theta\cos\varphi\right) \end{bmatrix} \tag{3.1-4}$$

Equation (3.1-3) is the same definition of body angular rates also presented in Reference 58. The formulation here is also the same as that presented in Reference 59 except for θ being measured from vertical. Similarly, Reference 29 uses the same representation but measures θ positive from the $x - z$ plane.

3.1.2 Trim Solution

To determine the steady state trim solution, the necessary eight equations from Equation (2.2-1) or Equation (2.2-5) must be solved and the six constraints defined by Equations (3.1-3) and (3.1-4) must also be satisfied. This calculation is described overall by fourteen coupled nonlinear algebraic equations with fifteen unknowns, but the equation set contains certain structure that can be exploited in the computations. Note two formulations are possible based on the choice for translational velocities. Table 4 depicts the mapping between six constraint equations and six state variables and the remaining nine free and fixed

variables. For this analysis there are two sensible options: α or δ_e. Specifying α would be beneficial as this choice could ensure the full range of the aerodynamic database is covered, whereas specifying δ_e is pertinent as it is related to inducing stall/spin conditions under normal flight operations (i.e., level flight transitioning to steep climb). However, position of the elevator control surface is in general arbitrary; thus, the angle-of-attack is used as the parameter to be specified.

Table 4 Solution Map ($\boldsymbol{\sigma - \theta - \varphi}$)

State	Value	Inputs	Value	Spin Parameter	Value
u, (V)	Equation (3.1-4)	δ_a	free	R	free
v, (α)	Equation (3.1-4)	δ_e	free	Ω	free
w, (β)	Equation (3.1-4)	δ_r	free	σ	free
p	Equation (3.1-3)			V_d	free
q	Equation (3.1-3)				
r	Equation (3.1-3)				
φ	free				
θ	free				

In Table 4 it is clear that α enters as a function of the components in Equation (3.1-4). In order to facilitate an α constraint the relationship $\tan\alpha = \frac{w}{u}$ can be introduced. Substituting in the component values from Equation (3.1-4) yields the following relationship.

$$\tan\alpha = -\frac{V_d\cos\varphi\cos\theta + R\Omega\left(\cos\sigma\sin\varphi - \cos\varphi\sin\sigma\sin\theta\right)}{V_d\sin\theta + R\Omega\cos\theta\sin\sigma} \tag{3.1-5}$$

Equation (3.1-5) can subsequently be solved for one of three options V_d, R, Ω resulting in the following α dependent parameters.

$$V_d = -\frac{R\Omega\left(\cos\sigma\sin\varphi - \cos\varphi\sin\sigma\sin\theta + \tan\alpha\cos\theta\sin\sigma\right)}{\cos\varphi\cos\theta + \tan\alpha\sin\theta} \tag{3.1-6a}$$

$$R = -\frac{V_d\left(\cos\varphi\cos\theta + \tan\alpha\sin\theta\right)}{\Omega\left(\cos\sigma\sin\varphi - \cos\varphi\sin\sigma\sin\theta + \tan\alpha\cos\theta\sin\sigma\right)} \tag{3.1-6b}$$

$$\Omega = -\frac{V_d\left(\cos\varphi\cos\theta + \tan\alpha\sin\theta\right)}{R\left(\cos\sigma\sin\varphi - \cos\varphi\sin\sigma\sin\theta + \tan\alpha\cos\theta\sin\sigma\right)} \tag{3.1-6c}$$

Thus in order to specify the angle-of-attack, one must decide which parameter is dependent and let the solver determine the remaining two parameters. For this analysis Ω was chosen as the dependent parameter as it retains physical significance irrespective of sign thereby

avoiding potential numerical issues such as a solution with a negative spin radius. During the course of building the database V_d and R were temporarily used in an exploratory effort to increase trim accuracy in particular regions as well as an attempt to make the spin direction uniform across the entire envelope. However, this uncovered that using V_d or R caused the solved α to vary from the specified α and was attributed to the solver specifying negative values of V_d, R which have no physical meaning. Furthermore, forcing Ω to be negative in the regions of $\alpha \approx 72 - 74.5, 76 - 89$ degrees resulted in greater trim errors than those attained with a positive Ω. Details of the numerical accuracy of the trim database are presented in Appendix A.3.

3.2 Model Linearization

The linearized plant must be calculated at every trim point in order to calculate the NI. While there are numerous ways to calculate a linear model, this research will utilize small perturbation theory. Briefly stated, a linearized model can be approximated by a summation of first order partial derivatives with respect to the state and input variables.

$$\begin{aligned}
\Delta f_1 &= \frac{\partial f_1}{\partial x_1}\Delta x_1 + \frac{\partial f_1}{\partial x_2}\Delta x_2 + \frac{\partial f_1}{\partial x_n}\Delta x_n + \cdots + \frac{\partial f_1}{\partial u_1}\Delta u_1 + \frac{\partial f_1}{\partial u_2}\Delta u_2 + \cdots + \frac{\partial f_1}{\partial u_m}\Delta u_m \\
\Delta f_2 &= \frac{\partial f_2}{\partial x_1}\Delta x_1 + \frac{\partial f_2}{\partial x_2}\Delta x_2 + \frac{\partial f_2}{\partial x_n}\Delta x_n + \cdots + \frac{\partial f_2}{\partial u_1}\Delta u_1 + \frac{\partial f_2}{\partial u_2}\Delta u_2 + \cdots + \frac{\partial f_2}{\partial u_m}\Delta u_m \\
&\vdots \\
\Delta f_n &= \frac{\partial f_n}{\partial x_1}\Delta x_1 + \frac{\partial f_n}{\partial x_2}\Delta x_2 + \frac{\partial f_n}{\partial x_n}\Delta x_n + \cdots + \frac{\partial f_n}{\partial u_1}\Delta u_1 + \frac{\partial f_n}{\partial u_2}\Delta u_2 + \cdots + \frac{\partial f_n}{\partial u_m}\Delta u_m
\end{aligned} \tag{3.2-1}$$

There are two common methods to calculate the coefficient values of Equation (3.2-1): carrying out the partial derivatives and numerically perturbing the model. Generally speaking, analytically derived models can provide more insight into the dynamics of the system; however, this process can be tedious and error prone when the equations are complex. Comparatively, numerically calculated models can be attained quickly and commercial software such as Simulink have built in linearization functionality.

In the following sections the analytically linearized models will be presented in state-space form as defined by Equation (3.2-2) where A represents the state dynamics and B the input distribution. Matrix entries that are zero are not presented. For example, if $a_{11} = 0$

the entry for a_{11} will not be presented as zero is the prescribed default value.

$$\Delta\vec{f} = A\Delta\vec{x} + B\Delta\vec{u}$$

where,

$$A = \begin{bmatrix} a_{11} & \cdots & a_{18} \\ \vdots & \ddots & \vdots \\ a_{81} & \cdots & a_{88} \end{bmatrix} \quad B = \begin{bmatrix} b_{11} & \cdots & b_{13} \\ \vdots & \ddots & \vdots \\ b_{81} & \cdots & b_{83} \end{bmatrix} \tag{3.2-2}$$

In the development that follows the delta operator (Δ) is dropped for brevity when appropriate.

3.2.1 Body Axis Linear Equations

This section details the development of the body axis linear equations. The final matrix entries are presented in Appendix A.4. Note in the following development σ with a numeric subscript denotes a temporary variable utilized to more clearly present the equation of interest.

Linearization of $\dot{u}$

Recast Equation (2.2-1a) with the generalized form presented by Equation (3.2-3).

$$\dot{u} = (\sigma_1 + \sigma_2 + \sigma_3)(u^2 + v^2 + w^2) + \sigma_4 \tag{3.2-3a}$$

where,

$$k = \frac{-S\rho}{2m} \tag{3.2-3b}$$

$$\sigma_1 = \frac{kc}{2V}\left(\cos\alpha\, C_{D,q} - \sin\alpha\, C_{L,q}\right) q \tag{3.2-3c}$$

$$\sigma_2 = k\left(\cos\alpha\, C_{D,\delta_e} - \sin\alpha\, C_{L,\delta_e}\right) \delta_e \tag{3.2-3d}$$

$$\sigma_3 = k\left(\cos\alpha\, C_{D,0} - \sin\alpha\, C_{L,0}\right) \tag{3.2-3e}$$

$$\sigma_4 = v\, r - w\, q - g\sin\theta \tag{3.2-3f}$$

The first three partial derivatives with respect to the body axis velocities are summarized by Equation (3.2-4).

$$\text{for } N = u,\, v,\, w,\, p,\, q,\, r,\, \varphi,\, \theta,\, \delta_a,\, \delta_e,\, \delta_r$$

$$\frac{\partial \dot{u}}{\partial N} = 2N\sum_{i=1}^{3}\sigma_i + V^2\sum_{i=1}^{3}\frac{\partial}{\partial N}\sigma_i + \frac{\partial}{\partial N}\sigma_4 \tag{3.2-4}$$

Linearization of $\dot{\mathbf{v}}, \dot{\mathbf{w}}$

The linearization of $\dot{v}$ and $\dot{w}$ follow the same process utilized in the linearization of $\dot{u}$. Thus the development for these variables is not depicted.

Linearization of $\dot{\mathbf{p}}$

To develop the $\dot{p}$ equation for body axes consider recasting Equation (2.2-1e) in the generalized form given by Equation (3.2-5).

$$\dot{p} = \sigma_6 + (\sigma_5 + \sigma_4 + \sigma_3 + \sigma_2 + \sigma_1)(u^2 + v^2 + w^2) \tag{3.2-5a}$$

where,

$$k_I = I_{xz}^2 - I_{xx} I_{zz} \tag{3.2-5b}$$

$$K = \frac{-Sb\rho}{2k_I} \tag{3.2-5c}$$

$$\sigma_1 = \frac{Kb}{2V}\left[\left(I_{xz} C_{n,p} + I_{zz} C_{l,p}\right) p + \left(I_{xz} C_{n,r} + I_{zz} C_{l,r}\right) r\right] \tag{3.2-5d}$$

$$\sigma_2 = K\left(I_{xz} C_{n,\beta} + I_{zz} C_{l,\beta}\right) \beta \tag{3.2-5e}$$

$$\sigma_3 = K\left(I_{xz} C_{n,\delta_r} + I_{zz} C_{l,\delta_r}\right) \delta_r \tag{3.2-5f}$$

$$\sigma_4 = K\left(I_{xz} C_{n,\delta_e} + I_{zz} C_{l,\delta_e}\right) \delta_e \tag{3.2-5g}$$

$$\sigma_5 = K\left(I_{xz} C_{n,\delta_a} + I_{zz} C_{l,\delta_a}\right) \delta_a \tag{3.2-5h}$$

$$\sigma_6 = \frac{1}{k_I}\left[I_{xz}\left(I_{xx} - I_{yy} + I_{zz}\right) pq + \left(I_{xz}^2 + I_{zz}^2 - I_{yy} I_{zz}\right) qr\right] \tag{3.2-5i}$$

$$\text{for } N = u,\ v,\ w,\ p,\ q,\ r,\ \varphi,\ \theta,\ \delta_a,\ \delta_e,\ \delta_r$$

$$\frac{\partial \dot{p}}{\partial N} = 2N \sum_{i=1}^{5} \sigma_i + V^2 \sum_{i=1}^{5} \frac{\partial}{\partial N} \sigma_i \tag{3.2-5j}$$

Linearization of $\dot{\mathbf{q}}$

Similarly for $\dot{q}$, recast Equation (2.2-1d) in the generalized form given by Equation (3.2-6).

$$\dot{q} = (\sigma_1 + \sigma_2 + \sigma_3)(u^2 + v^2 + w^2) + \sigma_4 \tag{3.2-6a}$$

where,

$$K = \frac{Sc\rho}{2I_{yy}} \tag{3.2-6b}$$

$$\sigma_1 = \frac{Kc}{2V} C_{m,q} q \tag{3.2-6c}$$

$$\sigma_2 = KC_{m,\delta_e}\delta_e \tag{3.2-6d}$$

$$\sigma_3 = KC_{m,0} \tag{3.2-6e}$$

$$\sigma_4 = \frac{1}{I_{yy}}\left(I_{xz}(r^2 - p^2) + (I_{zz} - I_{xx})pr\right) \tag{3.2-6f}$$

$$\text{for } N = u,\ v,\ w,\ p,\ q,\ r,\ \varphi,\ \theta,\ \delta_a,\ \delta_e,\ \delta_r$$

$$\frac{\partial \dot{q}}{\partial N} = 2N\sum_{i=1}^{3}\sigma_i + V^2\sum_{i=1}^{3}\frac{\partial}{\partial N}\sigma_i \tag{3.2-6g}$$

Linearization of $\dot{\mathbf{r}}$

Lastly, recasting Equation (2.2-1e) in the generalized form given by Equation (3.2-7).

$$\dot{r} = \sigma_6 + (\sigma_5 + \sigma_4 + \sigma_3 + \sigma_2 + \sigma_1)(u^2 + v^2 + w^2) \tag{3.2-7a}$$

where,

$$k_I = I_{xz}^2 - I_{xx}I_{zz} \tag{3.2-7b}$$

$$K = \frac{-Sb\rho}{2k_I} \tag{3.2-7c}$$

$$\sigma_1 = \frac{Kb}{2V}\left[\left(I_{xz}C_{l,p} + I_{xx}C_{n,p}\right)p + \left(I_{xz}C_{l,r} + I_{xx}C_{n,r}\right)r\right] \tag{3.2-7d}$$

$$\sigma_2 = K\left(I_{xz}C_{l,\beta} + I_{xx}C_{n,\beta}\right)\beta \tag{3.2-7e}$$

$$\sigma_3 = K\left(I_{xz}C_{l,\delta_r} + I_{xx}C_{n,\delta_r}\right)\delta_r \tag{3.2-7f}$$

$$\sigma_4 = K\left(I_{xz}C_{l,\delta_e} + I_{xx}C_{n,\delta_e}\right)\delta_e \tag{3.2-7g}$$

$$\sigma_5 = K\left(I_{xz}C_{l,\delta_a} + I_{xx}C_{n,\delta_a}\right)\delta_a \tag{3.2-7h}$$

$$\sigma_6 = \frac{1}{k_I}\left[\left(I_{yy}I_{xx} - I_{xx}^2 - I_{xz}^2\right)pq + I_{xz}\left(I_{xx} - I_{yy} + I_{zz}\right)qr\right] \tag{3.2-7i}$$

$$\text{for } N = u,\ v,\ w,\ p,\ q,\ r,\ \varphi,\ \theta,\ \delta_a,\ \delta_e,\ \delta_r$$

$$\frac{\partial \dot{r}}{\partial N} = 2N\sum_{i=1}^{5}\sigma_i + V^2\sum_{i=1}^{5}\frac{\partial}{\partial N}\sigma_i \tag{3.2-7j}$$

Linearization of $\dot{\varphi}, \dot{\theta}$

The roll and pitch angles (φ, θ) follow the same process taking the partial derivatives. The development is left to the reader.

3.2.2 Hybrid Wind Axis Linear Equations

Similarly the wind axis linearized equations can be defined where $a_{4-8,4-8}, b_{4-8,1-3}$ are

the same as in the body axis equations. In Equation (A.5-1) the $C'_{x,y}$ and θ'_x parameters denote the derivative of the lookup tables with respect to α evaluated at the trim α. The $C'_{x,y}$ and θ'_x parameters must be calculated numerically by differencing the lookup table and is done with a step size of $1e{-}5 + 1e{-}8|\alpha|$.

3.2.3 Numerical Perturbation

As a cross-reference check to catch errors in the analytical build-up, a numerical routine was used to calculate the Jacobian. The algorithm for this calculation was adapted from *linmodv5.m.*[60] The pseudocode for this operation is presented in Figure 6.

```
x0; % operating point states
u0; % operating point inputs
ptb = 1e-5;
dx  = ptb + (1e-3)*ptb*abs(x0);
du  = ptb + (1e-3)*ptb*abs(u0);
% A matrix forumlation
A   = zeros(numel(x0));
xdot0 = stepSystem(x0, u0); % initial state derivative
for j=1:numel(x0)
    x      = x0;
    x(j)   = x + dx(j);
    A(:,j) = (stepSystem(x, u0) - xdot0) / dx(j);
end
% B matrix formulation
B = zeros(size(A,1), numel(u0));
for j=1:numel(u0)
    u      = u0;
    u(j)   = u + du(j);
    B(:,j) = (stepSystem(x0, u) - xdot0) / du(j);
end
```

Figure 6 Numerical Jacobian Pseudocode

3.2.4 Linear Model Validation

The linear models were validated by running nonlinear simulations with perturbations independently applied to all states and inputs. The condition of $\alpha = 60°$ was arbitrarily chosen as the evaluation case. The linear models were taken to be correct as the analytical and numerical models both behaved the same. Furthermore the linear models closely matched the nonlinear model for most state perturbations; however, the control input perturbations were more sensitive. Results of the nonlinear and linear simulation comparisons are presented in Appendices A.6 and A.7 for the linear wind and body equations, respectively where the plots depict the deviations (Δ) from the nominal trim value.

3.3 Nonlinearity Index Analysis

Nonlinearity index theory is used to identify the severely nonlinear regimes of the aircraft model that should be the focus for control augmentation facilitating spin recovery. Further, the NI highlights potential regions of the flight envelope where linear controllers should be rigorously tested and/or nonlinear controllers may be required. Nonlinearity index is a quantitative measure of how much the state dynamics and state input distribution matrix vary from a trim point. A NI of zero indicates that the system is linear whereas large nonzero NI values indicate strong nonlinearities in the system.

Consider the general dynamic system with states x, inputs u, and time t with initial states and time x_0, t_0.

$$\dot{x} = f(t, x, u) \tag{3.3-1}$$

$$y = g(t, x, u) \tag{3.3-2}$$

$$x(t_0) = x_0 \tag{3.3-3}$$

The system described by Equations (3.3-1) to (3.3-3) can be linearized through various methods. Once linearized the system can be represented by a standard state space representation as presented in Equation (3.3-4).

$$\begin{aligned} \delta\dot{x} &= \overline{A}\delta x + \overline{B}\delta u \\ \delta y &= \overline{C}\delta x + \overline{D}\delta u \\ \delta x(t_0) &= \delta x_0 \end{aligned} \tag{3.3-4}$$

In Equation (3.3-4) the overlined matrices $\overline{A}, \overline{B}, \overline{C}, \overline{D}$ represent the state dynamics, input

distribution, output distribution, and input-output matrices respectively evaluated at a nominal trim condition ($\overline{x_0}$). Similarly, the system can be linearized at a deviated condition, $x_0 = \overline{x_0} + \delta x_0$ bounded by δx_{max} such that $0 \leq ||\delta x_0|| \leq \delta x_{max}$. The deviated system is defined by Equation (3.3-5).

$$\begin{aligned} \delta\dot{x} &= A\delta x + B\delta u \\ \delta y &= C\delta x + D\delta u \\ \delta x(t_0) &= \delta x_0 \end{aligned} \tag{3.3-5}$$

Four different static nonlinearity indices can be defined which measure the strength of the nonlinearity of the dynamic system. These indices are defined by Equations (3.3-6) to (3.3-9).

$$\nu_s^A = \sup_{||\delta_{x_0}|| \leq \delta x_{max}} \frac{||A - \overline{A}||}{||\overline{A}||} \tag{3.3-6}$$

$$\nu_s^B = \sup_{||\delta_{x_0}|| \leq \delta x_{max}} \frac{||B - \overline{B}||}{||\overline{B}||} \tag{3.3-7}$$

$$\nu_s^C = \sup_{||\delta_{x_0}|| \leq \delta x_{max}} \frac{||C - \overline{C}||}{||\overline{C}||} \tag{3.3-8}$$

$$\nu_s^D = \sup_{||\delta_{x_0}|| \leq \delta x_{max}} \frac{||D - \overline{D}||}{||\overline{D}||} \tag{3.3-9}$$

Equations (3.3-6) to (3.3-9) capture the maximum deviation of the matrix Jacobian across a local subregion bounded by δx_{max}. The static state and output indices, ν_s^A and ν_s^C capture the initial condition excitation, whereas the input and direct indices, ν_s^B and ν_s^D capture the input excitation. In Equations (3.3-6) to (3.3-9), $||\cdot||$ denotes the Frobenious norm.[37]

Typical in aircraft dynamics, the direct input-output matrix D is zero; thus, the index ν_s^D will not be computed. Additionally, the output matrix C consists of the identity matrix simply mapping the states as outputs; thus, the index ν_s^C will also be neglected.

3.3.1 Numerical Results

Calculation of the Nonlinearity Index over the widest range of the operational envelope as possible is desirable. For the HARV database this would allow for a range of $\alpha = 5$ to $\alpha = 85$ degrees which would ensure the table limits are obeyed. However, due to the inability to trim the aircraft in a sufficiently accurate steady state spin (i.e., state errors, $|e| < 1e{-}4$)

the region had to be truncated resulting in spin conditions with $\alpha > 75°$ being discarded. This decision was made after inspecting the trim database and plotting the distribution of trim errors which is presented in Figure 97 in Appendix A.3. In Figure 97 it can be seen that there are still some trim solutions in the range of consideration that exceed $|e| < 1e{-}4$; however, these are few and further spread out compared to the the higher alpha region. Given the constraint of $\alpha <= 75°$ and the desired subrange of $10\% \times (\alpha_{max} - \alpha_{min})$, the range of $\alpha = 5$ to $\alpha = 71.6$ degrees with a step size of $0.1°$ was considered. Furthermore, the trim database was generated with a $0.02°$ step; thus, the subregion is sampled by 333 equally spaced trim points where the indices defined by Equations (3.3-6) to (3.3-9) are evaluated and stored in a vector. The maximum value of this vector is then kept as the index for the given value of α. Mathematically this process is described by Equations (3.3-12) to (3.3-13).

$$\nu_{A_k} = \frac{||A_k - A_j||}{||A_j||} \tag{3.3-10}$$

$$\nu_{B_k} = \frac{||B_k - B_j||}{||B_j||} \tag{3.3-11}$$

$$\nu_{A_j} = \max_k(\nu_{A_k}) \tag{3.3-12}$$

$$\nu_{B_j} = \max_k(\nu_{B_k}) \tag{3.3-13}$$

$$\begin{aligned}
&\text{where } j = \alpha_{min} : \alpha_{step} : \alpha_{max} \\
&\text{define } \alpha_{rng} = (\alpha_{max} - \alpha_{min}) \\
&\text{define } \alpha_{srmax} = \alpha_j + 5\% * \alpha_{rng} \\
&\text{define } \alpha_{srmin} = \alpha_j - 5\% * \alpha_{rng} \\
&\text{define } \alpha_{srstp} = \frac{\alpha_{srmax} - \alpha_{srmin}}{N_{subregion}} \\
&\text{where } k = \alpha_{srmin} : \alpha_{srstp} : \alpha_{srmax}
\end{aligned} \tag{3.3-14}$$

To efficiently calculate the NI a trim database was first built over the range of $\alpha = 1 : 0.02 : 89$ degrees thereby ensuring the trim solution for any given α is only calculated once. The initial condition for the trim solver was seeded with the previous result ($x_{0,i} = x_{0,i-1}$) in an effort to speed up the trim algorithm and to find a continuous solution. Details of the accuracy and validity of the trim database are presented in Appendix A.3. At this point let a "quality trim" be defined by Equation (3.3-15).

$$\max(|\dot{x}_0|) < 1e{-}6 \tag{3.3-15}$$

In order to utilize a predefined trim database with step size δ_α, Equation (3.3-14) must

be modified as follows such that the subregion endpoints fall on a pre-calculated α.

$$k = \alpha_{srmin} - \text{mod}(\alpha_{srmin},\, \delta_\alpha) : \alpha_{srstp} : \alpha_{srmax} + \text{mod}(\alpha_{srmax},\, \delta_\alpha) \tag{3.3-16}$$

The NI was calculated using both the analytical and numerical linear models for both the hybrid wind and body axes. The results for this analysis are presented in Figure 7. From Figure 7 it is clear the body axis representation exhibits less nonlinearities in the states whereas both the wind and body axes exhibit similar trends with respect to the inputs. Given the higher NI for the wind axis, further investigation was conducted. The minimum NI for the A matrix (based on numerical linearization) occurred at $\alpha = 37.9°$ for the wind axis while the maximum occurred at $\alpha = 71.6°$. Similar minimum values also existed for $\alpha = 53.9°, 65.4°$. The minimum NI for the B matrix occurred at $\alpha = 62.7°$ whereas the maximum occurred at $\alpha = 9.3°$. These minimum and maximum values are marked on the wind axis NI plot presented in Figure 8.

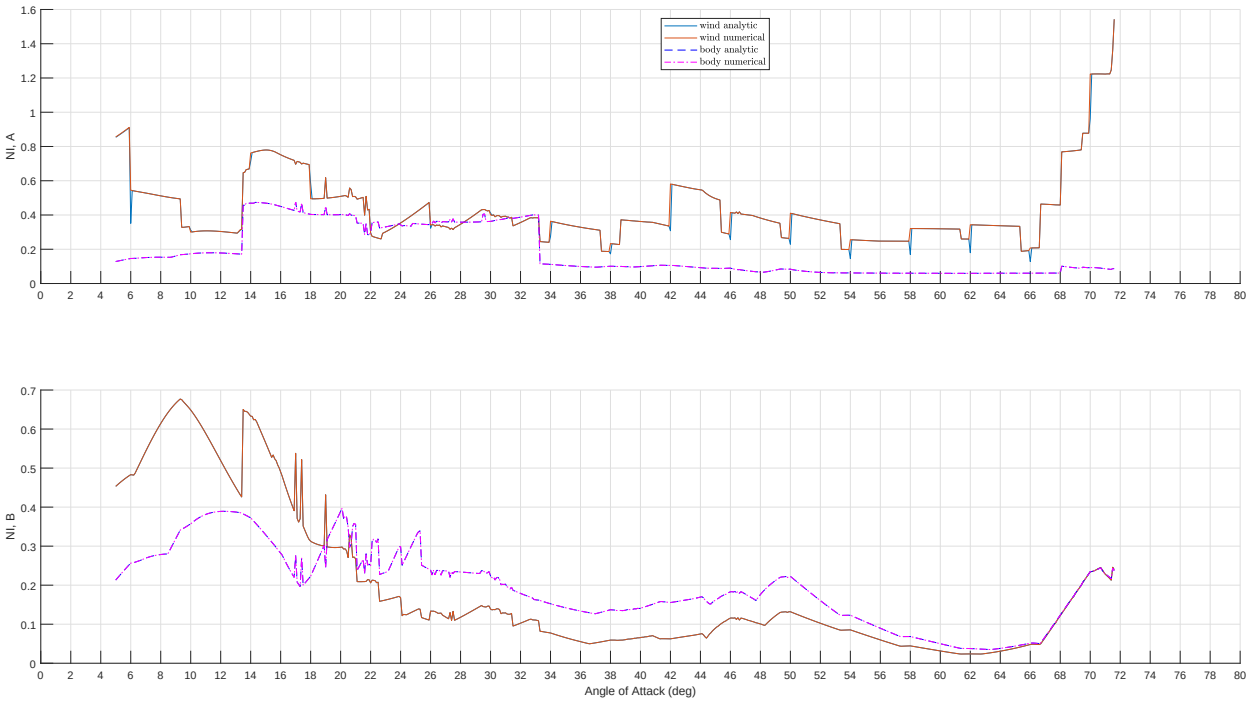

Figure 7 Nonlinearity Index (Analytic/Numerical)

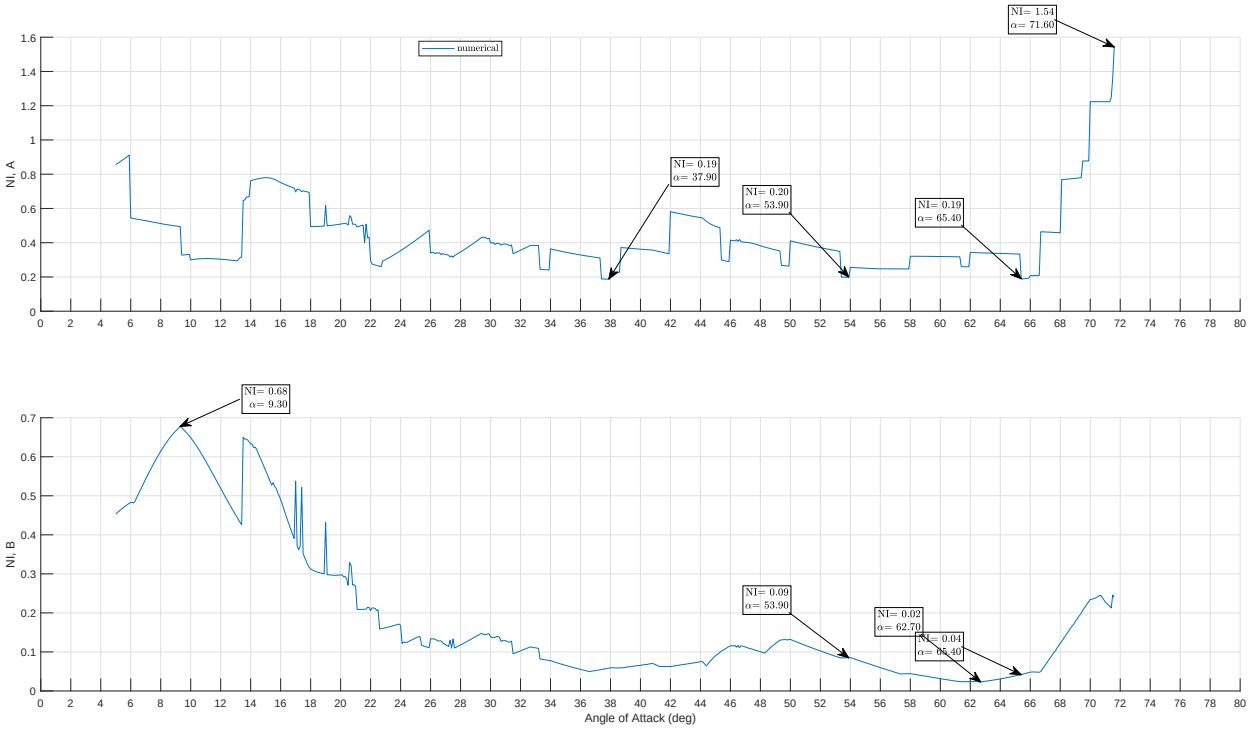

Figure 8 Wind Axis NI Marked

From Equations (3.3-12) and (3.3-13), the NI for any one α is the single max value over the subregion. Thus any one linear model has the potential to dominate multiple test points. With this in mind the α where the maximum value occurred (α_ν) is of interest. In Figure 9 α_ν is plotted against α which reveals regions over α where the maximum NI corresponded to the same α_ν. The maximum NI occurring at the same α_ν across multiple subregions (such as near $\alpha = 14°$ to $20°$ for NI, A) indicates a dominant model. The existence of a single dominant model which is the product of a numerical process raises concerns regarding the validity of that particular model.

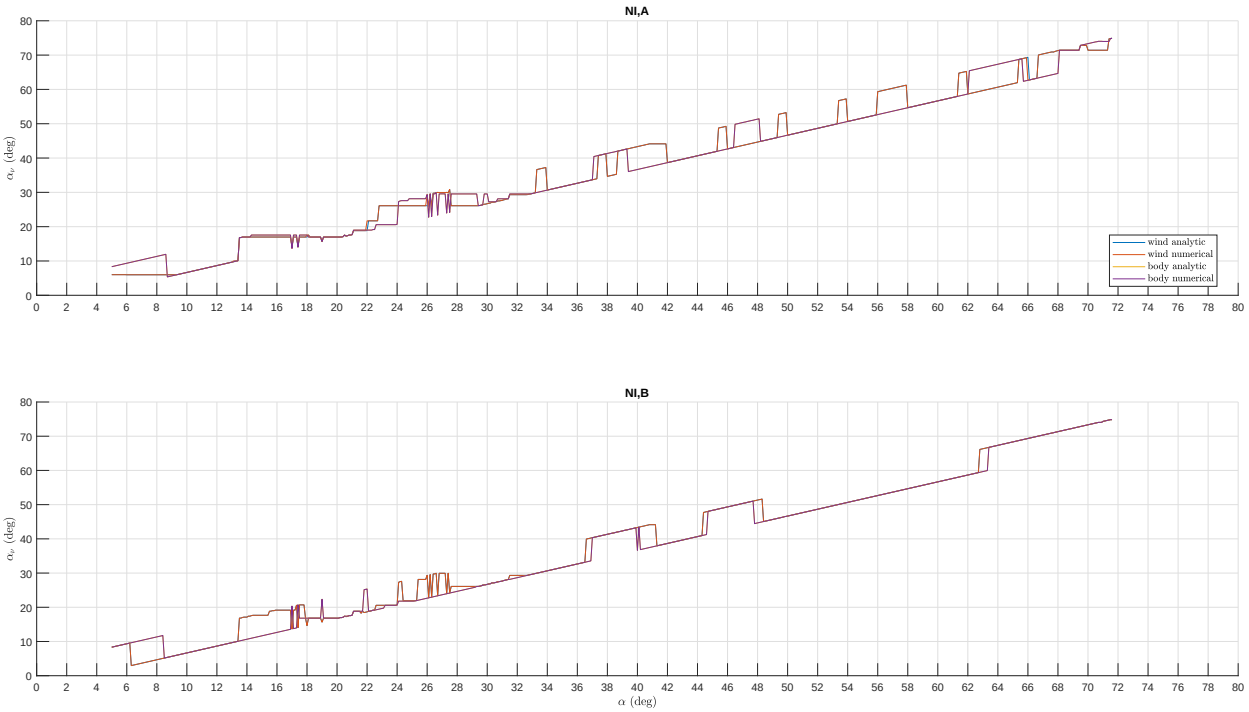

Figure 9 α where Maximum NI Value Occurred

In the presence of isolated dominant models, further investigation was conducted in order to either rule out the existence of a potential numerical error or to determine a rational explanation for this behavior. Subsequently, the NI was plotted with the stability and trim accuracy indicated in Figure 10. Stable trim points are plotted with the color green while trim points with solutions that have errors exceeding 1e−4 are plotted in black. This investigation indicates that the majority of all trim points are unstable while few trim solutions have errors above acceptable limits. Thus it is concluded that the trim solution does not negatively impact this analysis. The color breakpoints used in Figure 10 were determined by inspection of Figure 105 in Appendix A.3 in order to reflect the relationship between instability and time to diverge from steady state. A decisive conclusion regarding the dominant models could not be made as no single attribute (such as trim error or instability) was shared solely among the dominant models alone. Note in Figure 10, λ_{MRE} denotes the maximum real part of the linear system eigenvalues, $\lambda_{MRE} = \max \mathrm{Re}(\lambda)$.

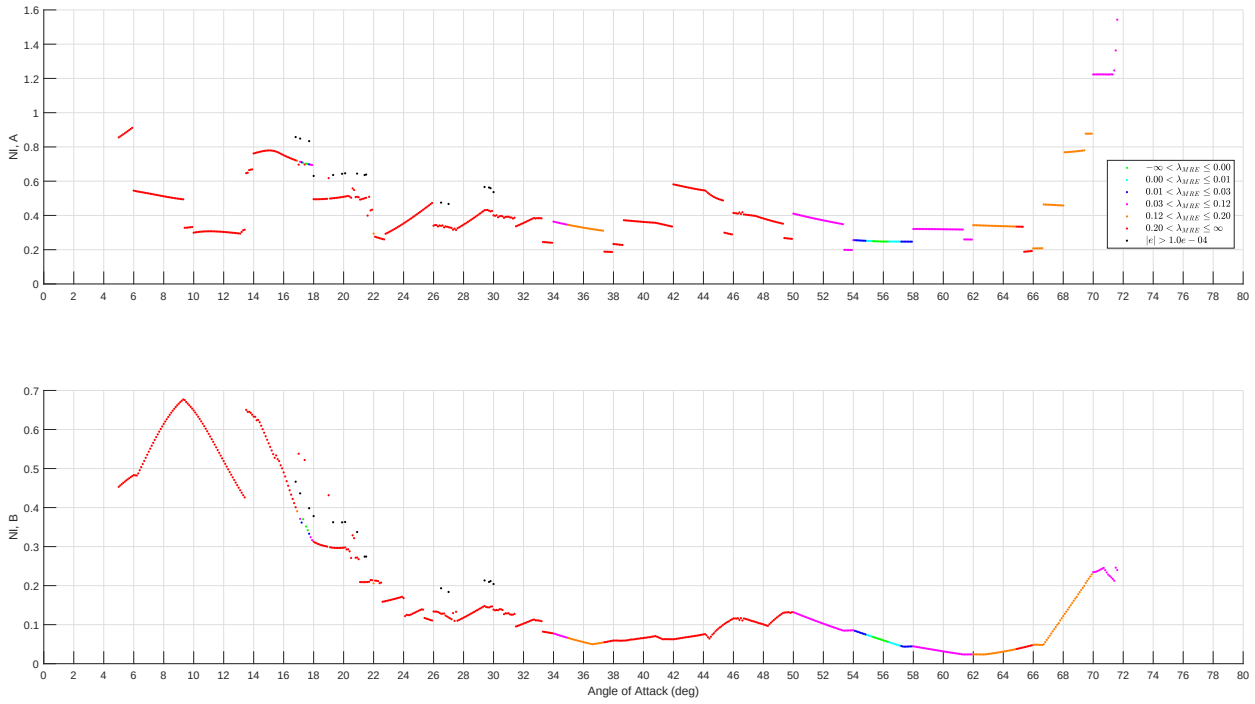

Figure 10 Nonlinearity Index with Stability and Trim Resolution Indicated

3.3.2 Nonlinear Simulation: Time Responses

In the following discussion NI refers to the A matrix NI unless otherwise specified. The validity of the NI can be confirmed by running simulations with perturbations and comparing the time histories of the linear and nonlinear models. In order to ensure the comparison is only due to the applied disturbance the model is first simulated without perturbations to ensure steady state is maintained. The model is then simulated with a perturbation of 0.05 (rad/s) on the roll rate channel, p. This process was conducted for three high NI solutions, $\alpha = 70.0$, 71.0, 71.6 degrees and four minimum value NI solutions, $\alpha = 56.0$, 58.76, 59.06, 59.24 degrees. The first minimum NI at alpha of 56.0° was added as a stable model test point; all remaining test points are unstable with the high/low NI test points chosen such that they share a similar magnitude instability as determined by the maximum positive eigenvalue (λ_{MRE}).

The linear model fit to the nonlinear model was then calculated for all scenarios using a normalized mean square error. A fit criteria of 95% on all states was chosen to provide a quantitative comparison. The minimum time for any state to have a fit below the 95% threshold was then used as the measure of comparison. The pseudocode for this calculation is presented in Figure 11 where the algorithm iteratively determines the maximum time

where all state errors comply with the 95% fit criteria. Table 5 summarizes the findings and indicates the linear models in the simulations with a lower NI have a longer duration of 95% fit. This finding supports the underlying theory of the nonlinearity index.

```
% states: [V alpha beta p q r phi theta]
t;  % time vector of length N
xr; % nonlinear simulation states [ N x 8]
x;  % linear model states, [N x 8]
a = find( t > 1, 1); % index of time greater than one
b = numel(t);        % number of data samples.
errorTolerance = 0.1;
fitTolerance   = 0.95;
while n ≤ maxIteration
  c = round( (a + b) / 2);
  REF = xr(1:c, :); % reference data
  TST = x(1:c, :);  % test data
  % normalized mean square error of all states
  for i = 1:8
    fit(i) = 1 - 2-Norm( REF(:,i) - TST(:,i) )^2 / ...
                 2-Norm( REF(:,i) - mean(REF(:,i)))^2;
  end
  if any( fit < fitTolerance )
    b = c;
  else
    a = c;
  end
  err = abs( fit - fitTolerance);
  if all( err < errorTolerance )
    break
  end
  n=n+1;
end
Time 95 Percent Fit = t(c);
```

Figure 11 95% Fit Calculation

Figure 12 depicts the entire 500 second simulation (linear and nonlinear) with the perturbation applied. Figures depicting the entire simulation range for the remaining test

cases have been excluded as the linear models are unstable and go without bound. Figures 13 to 19 depict the linear model fit to the nonlinear model with the $\Delta p = 0.05\,(\text{rad/s})$ perturbation over a short time horizon. Figures 20 and 21 show the nonlinear model response to the perturbation for a low and high NI test point with similar instabilities ($\lambda = 6.873\text{e}{-2}, 6.878\text{e}{-2}\,\text{rad/s}$). Figures 22 and 23 shows the same condition with the linear model included up until the linear model diverges from the nonlinear model. Comparing these two images it is clear that the higher NI test point resulted in a more severe divergence than that of the lower NI.

At this point it is worth noting that these results are as expected given the high/low NI test points have a similar instability. However, one must exercise caution when carrying out this analysis as it is possible for a low NI to have a 95% fit time shorter than that of a higher NI test point if the low NI test point has a larger instability. This is demonstrated in Figure 24 where a low NI of 0.1888 has a significantly shorter time of 95% fit due to the model instabilities.

Table 5 NI vs. Time 95% Fit

NI, A	α (deg)	λ_{MRE} (rad/s)	time 95% fit (sec)
0.1888	65.5	0.2153	10.25
0.2476	56	-4.9e-03	65.19
0.3203	59.24	0.06873	36.61
0.3203	59.06	0.06597	36.61
0.3205	58.76	0.06125	37.24
1.223	71	0.06595	18.78
1.223	70	0.06129	1.03
1.543	71.6	0.06878	19.76

Inspecting the aerodynamic tables in the range of the high state NI it is observed that the coefficient C_{n_p} undergoes a sharp change in slope as depicted in Figure 25. This discovery demonstrates the ability of the nonlinearity index to identify regions of the aerodynamic database which may require special attention of the control engineer.

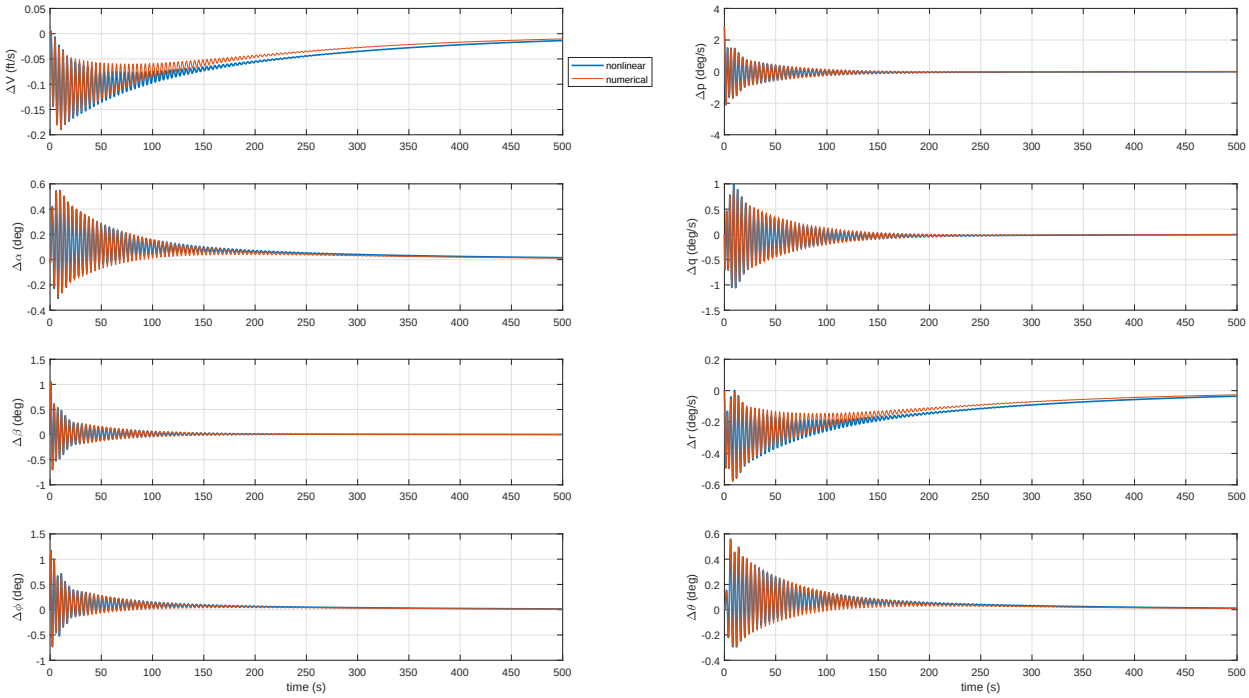

Figure 12 Response for NI = 0.2476, Stable, $\alpha = 56.0°$ (Long Term)

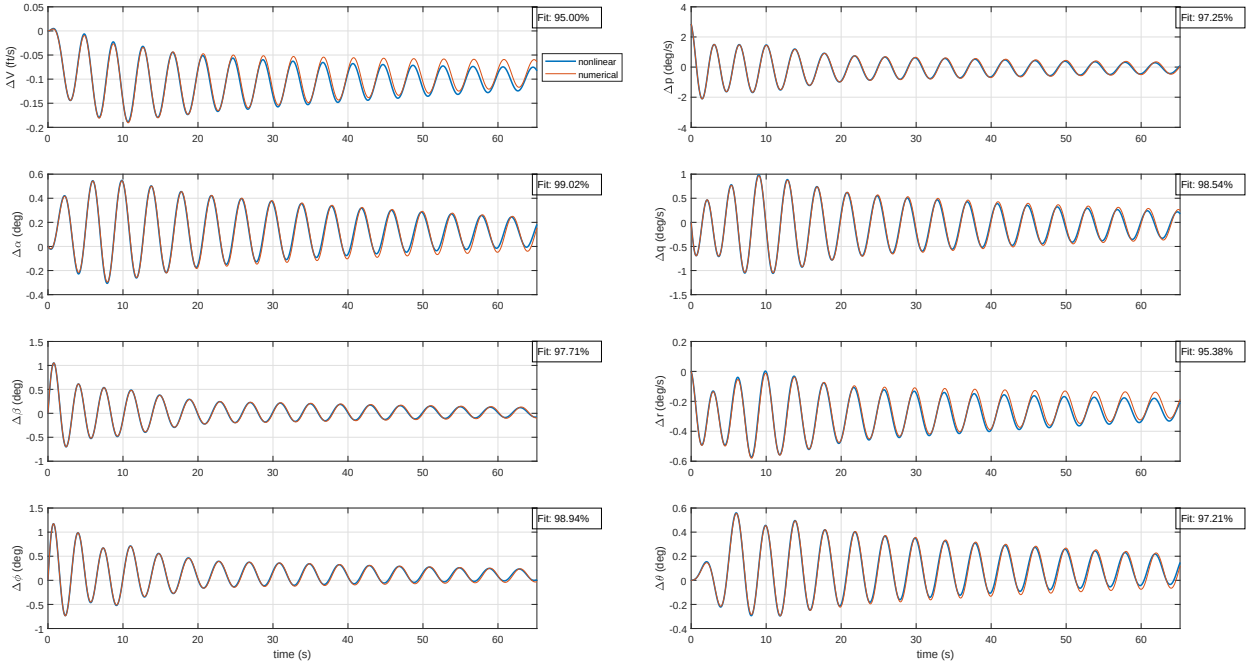

Figure 13 Response for NI = 0.2476, Stable, $\alpha = 56.0°$

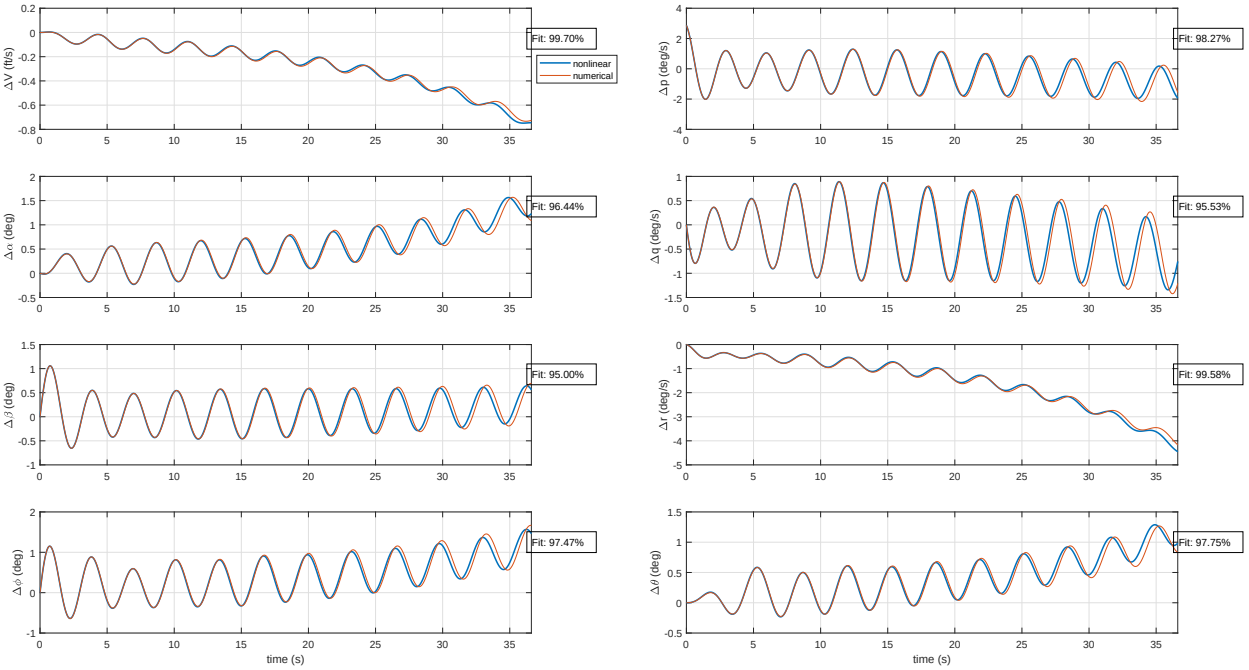

Figure 14 Response for NI = 0.3203, $\lambda_{MRE} = 6.873\text{e}{-2}\,(\text{rad/s})$, $\alpha = 59.24°$

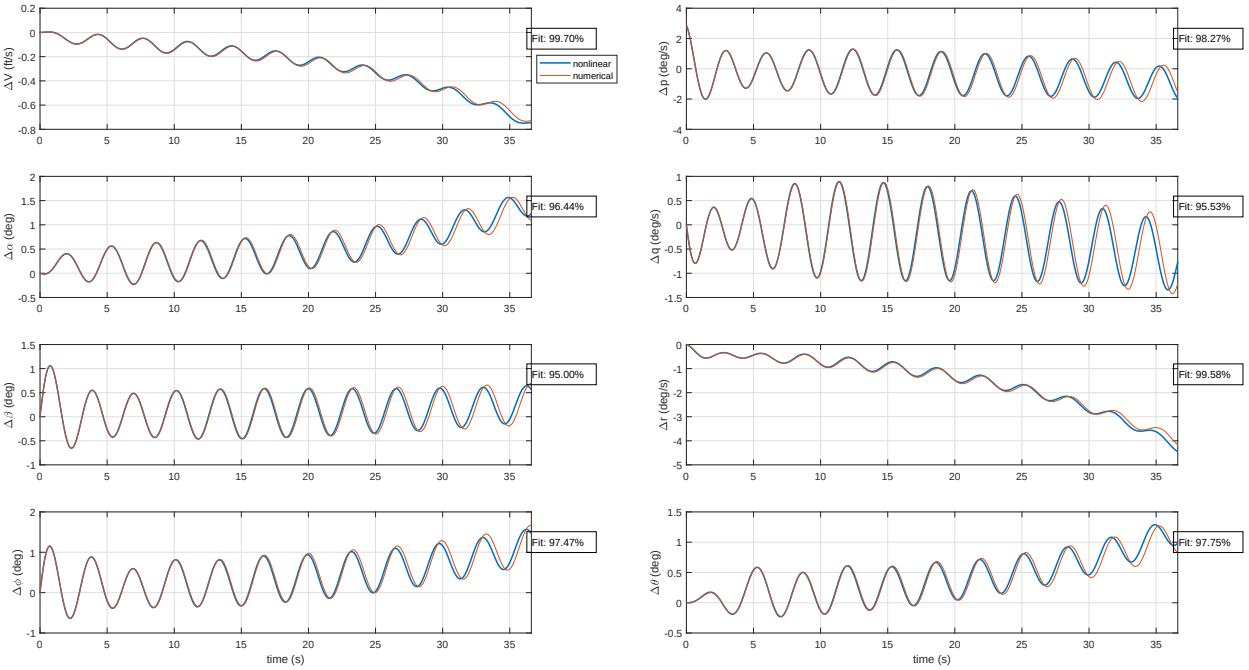

Figure 15 Response for NI = 0.3203, $\lambda_{MRE} = 6.597\text{e}{-2}\,(\text{rad/s})$, $\alpha = 59.06°$

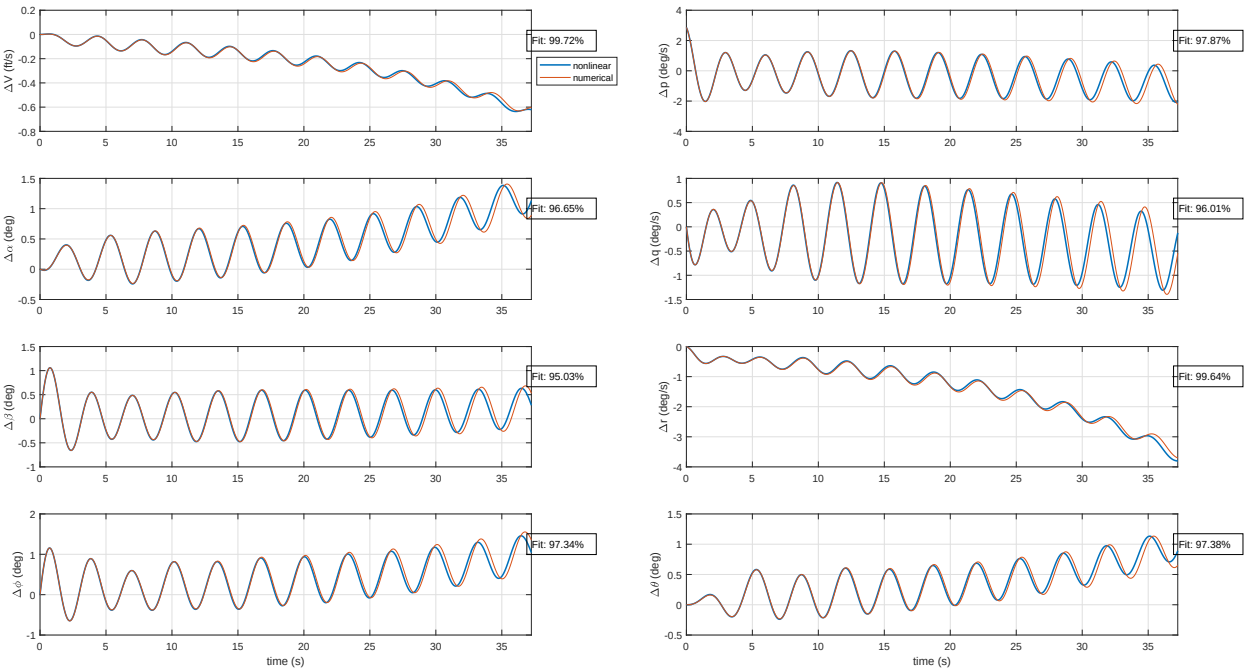

Figure 16 Response for NI = 0.3205, $\lambda_{MRE} = 6.125\text{e}{-2}\,(\text{rad/s})$, $\alpha = 58.76°$

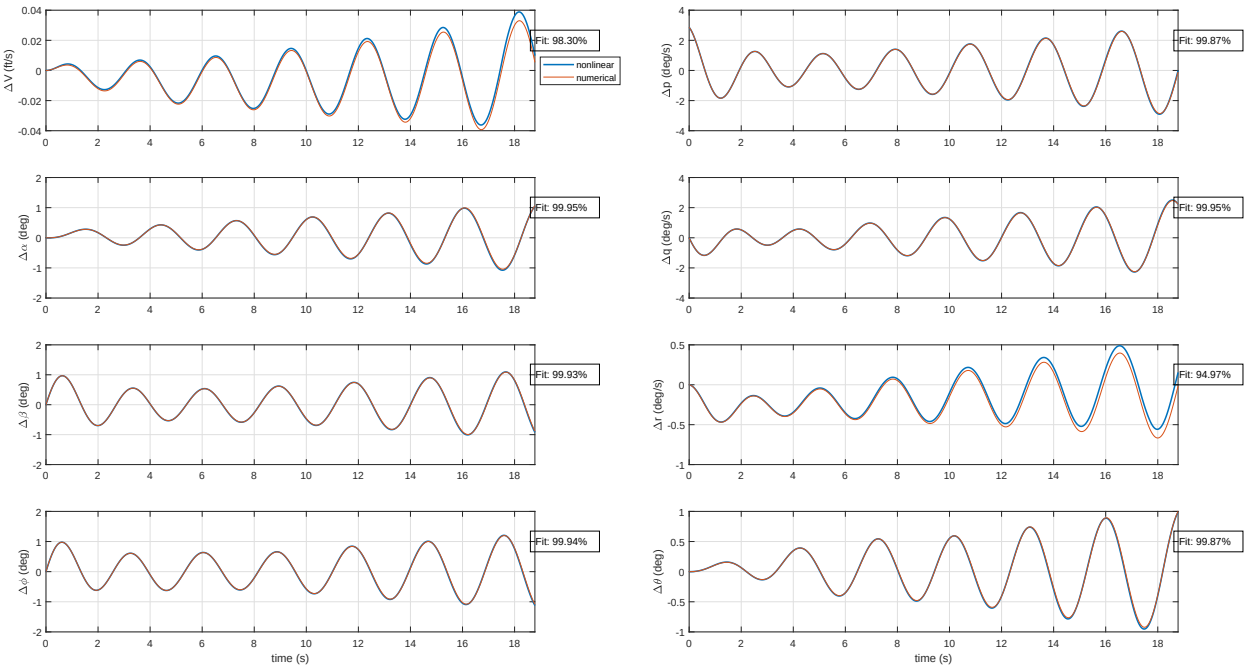

Figure 17 Response for NI = 1.223, $\lambda_{MRE} = 6.595\text{e}{-2}\,(\text{rad/s})$, $\alpha = 71°$

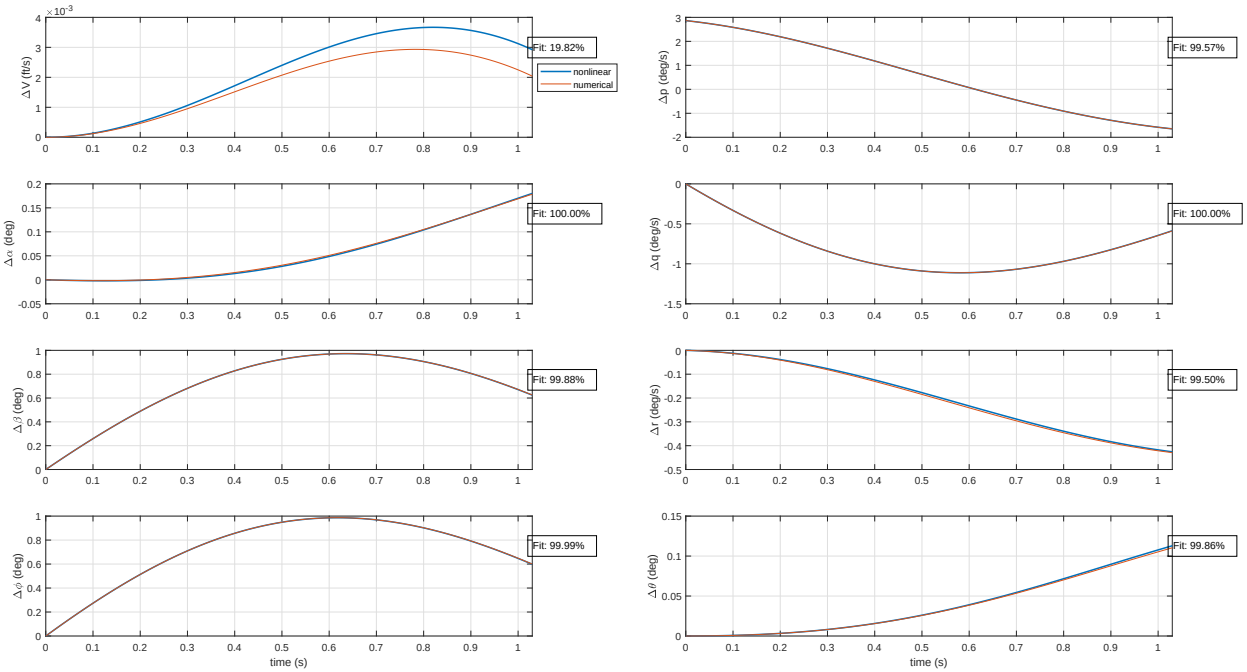

Figure 18 Response for NI = 1.223, λ_{MRE} = 6.129e−2 (rad/s), $\alpha = 70°$

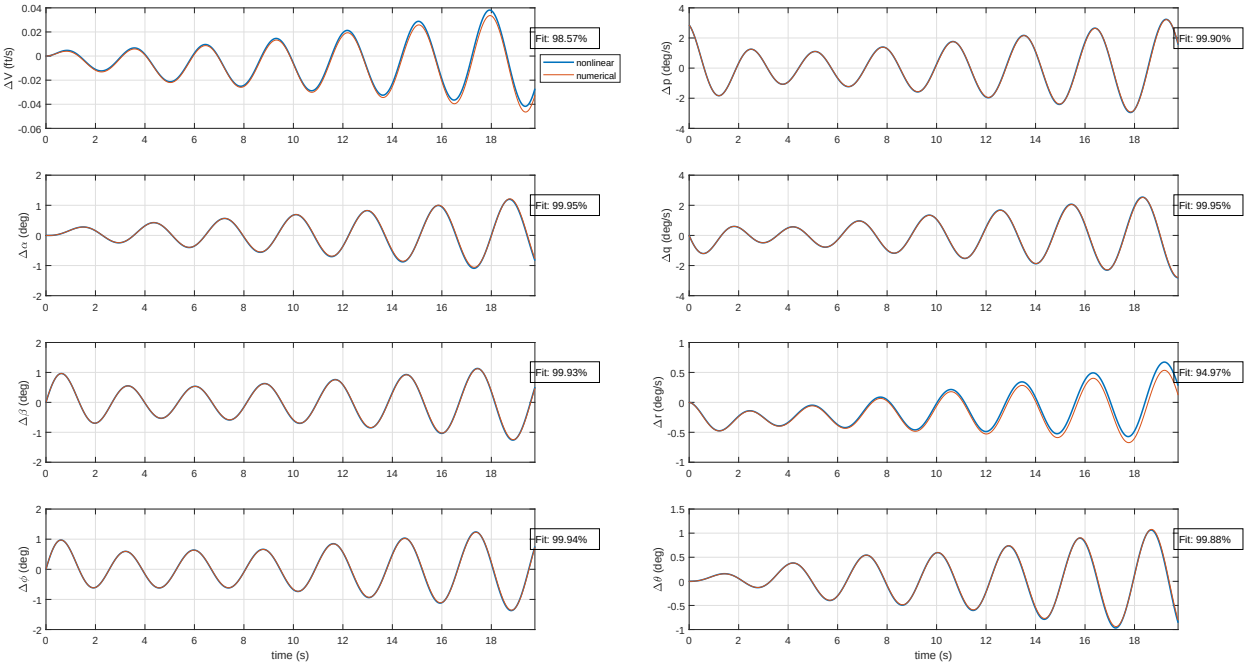

Figure 19 Response for NI = 1.543, λ_{MRE} = 6.878e−2 (rad/s), $\alpha = 71.6°$

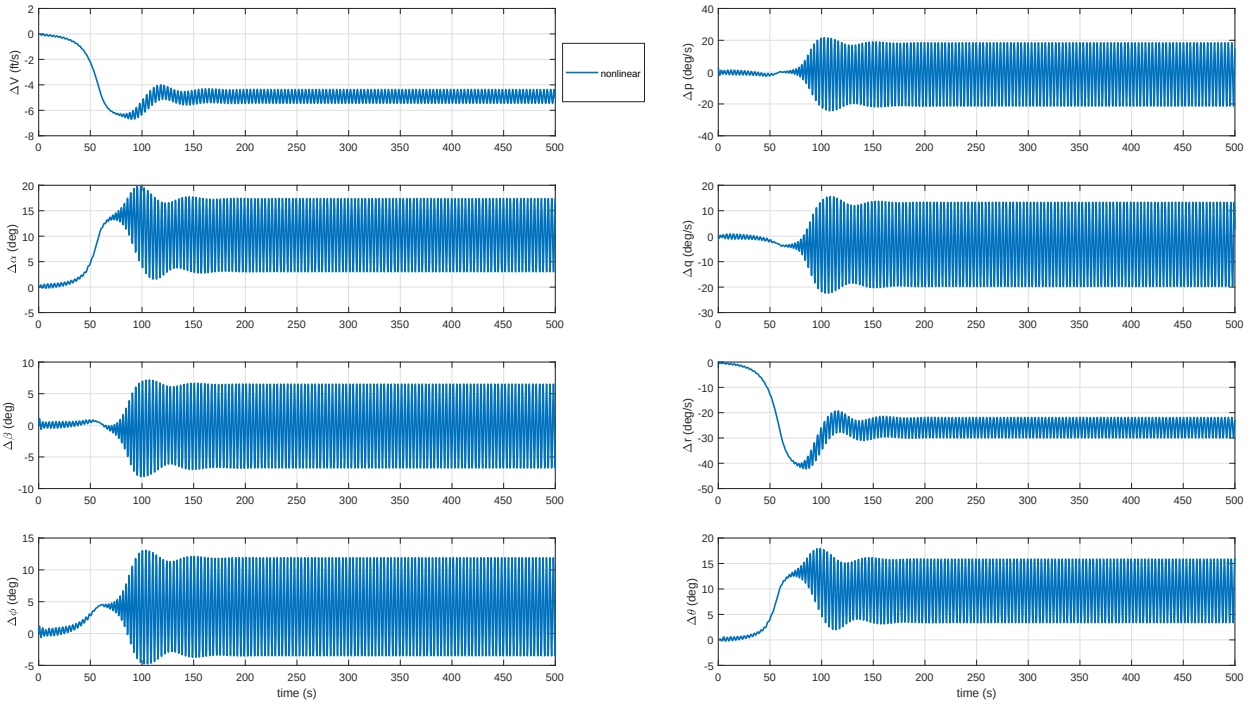

Figure 20 Response for NI = 0.3203, $\alpha = 59.24°$ (Long Term)

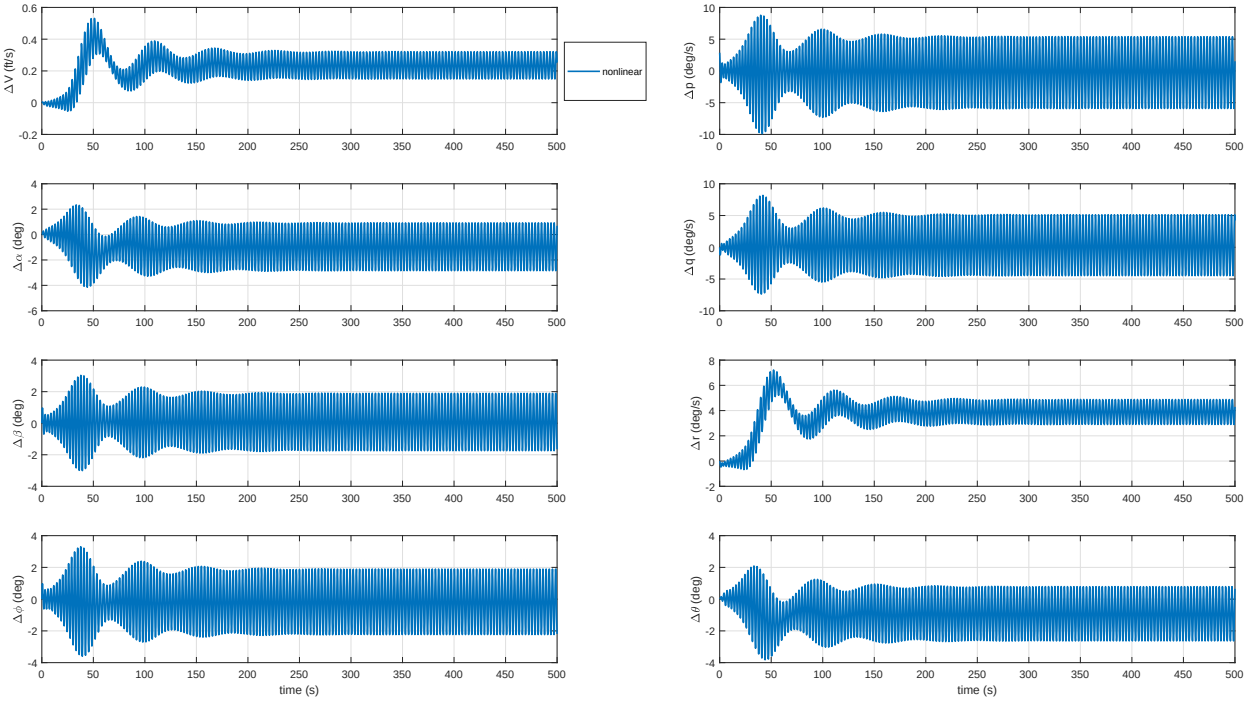

Figure 21 Response for NI = 1.543, $\alpha = 71.6°$ (Long Term)

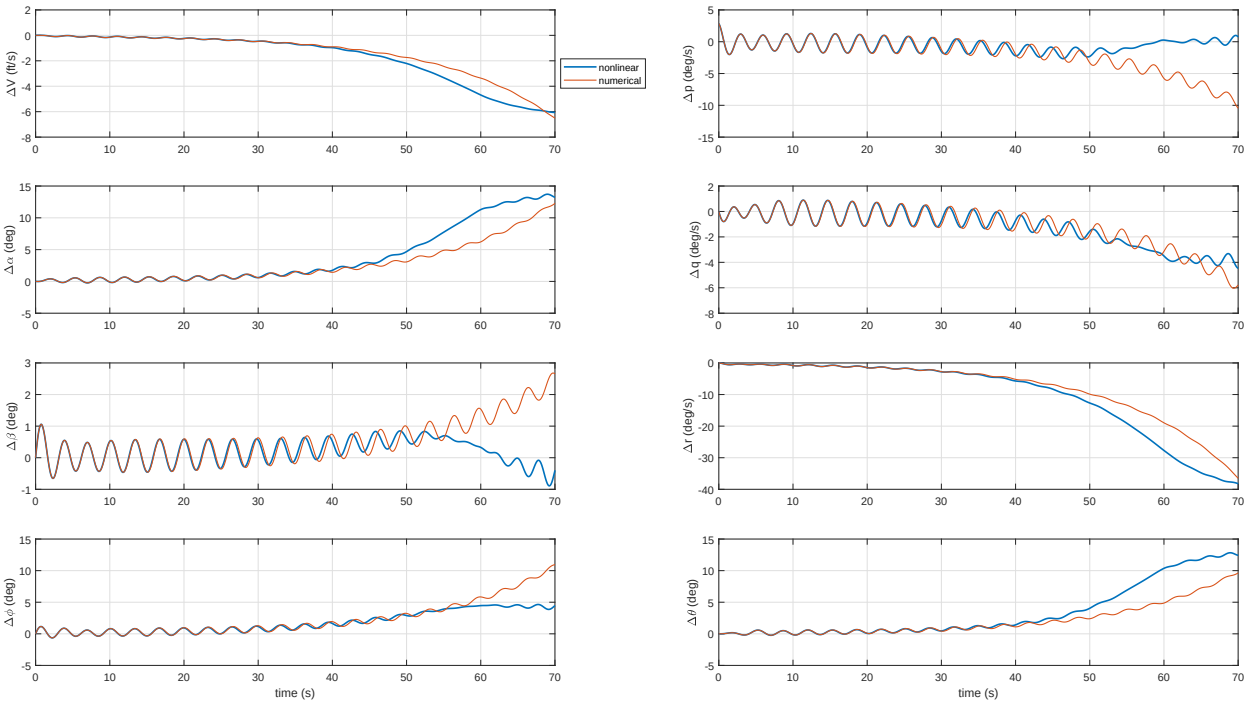

Figure 22 Response for NI = 0.3203, $\alpha = 59.24°$ (Extended Term)

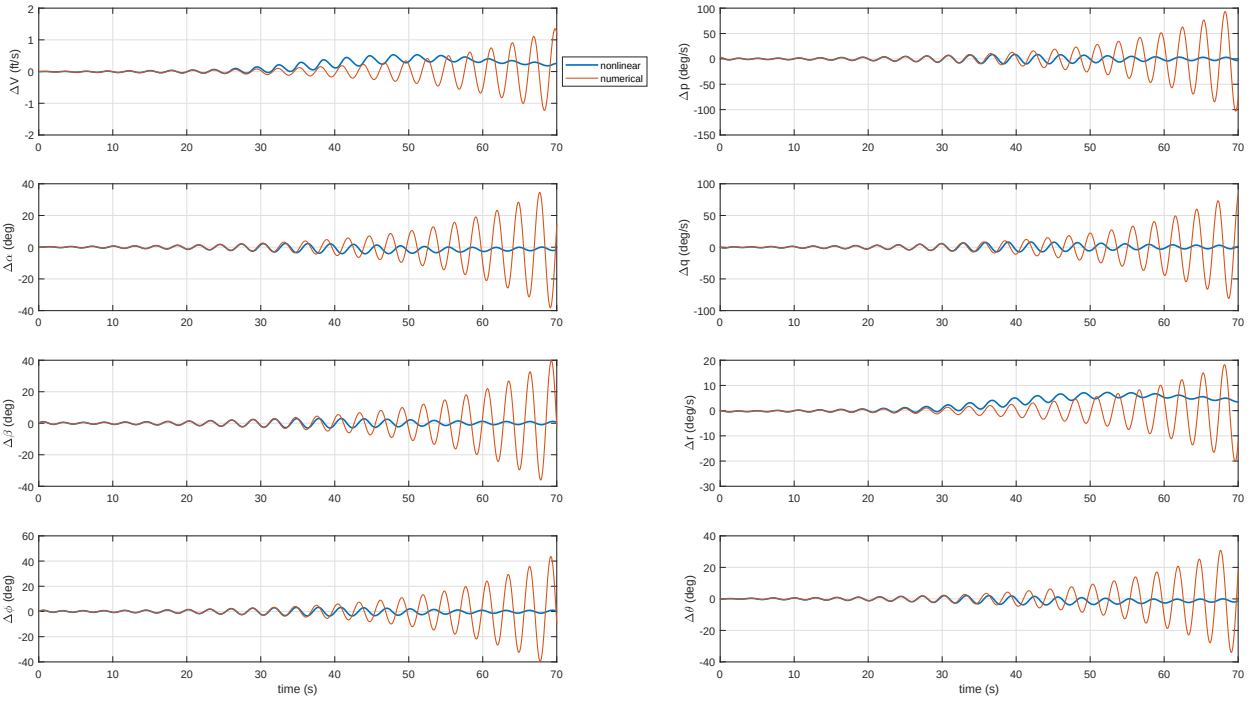

Figure 23 Response for NI = 1.543, $\alpha = 71.6°$ (Extended Term)

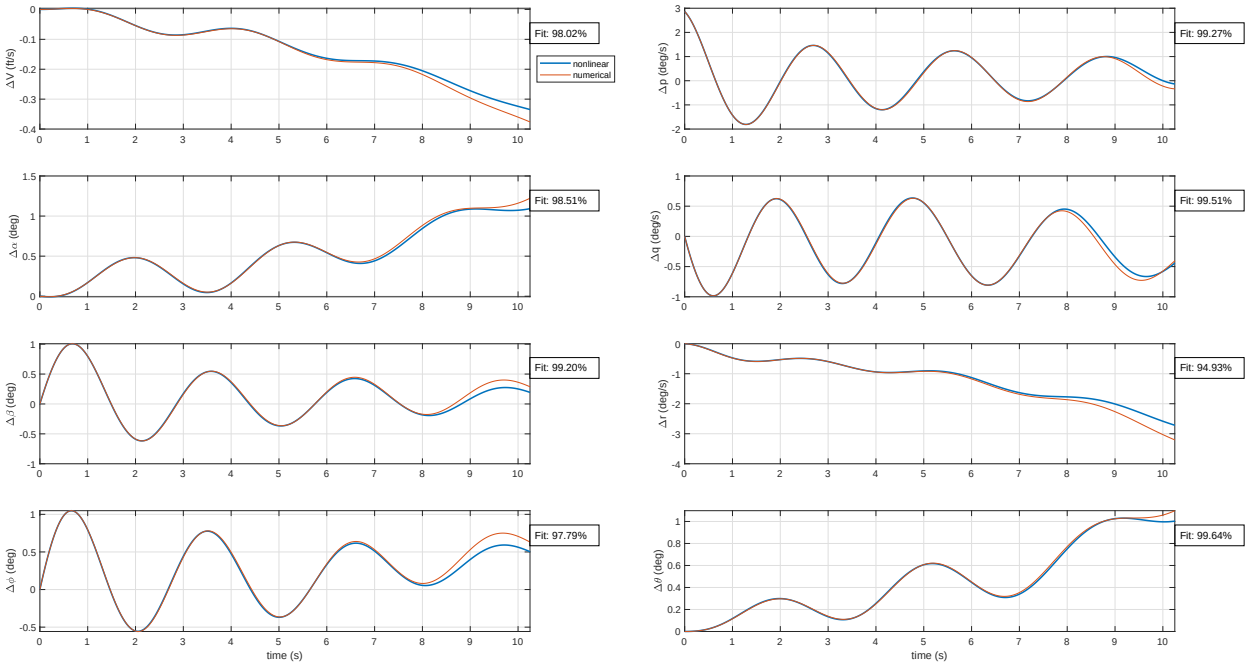

Figure 24 Response for NI $= 0.1888$, $\lambda_{MRE} = 0.2153\,(\text{rad/s})$, $\alpha = 65.5°$

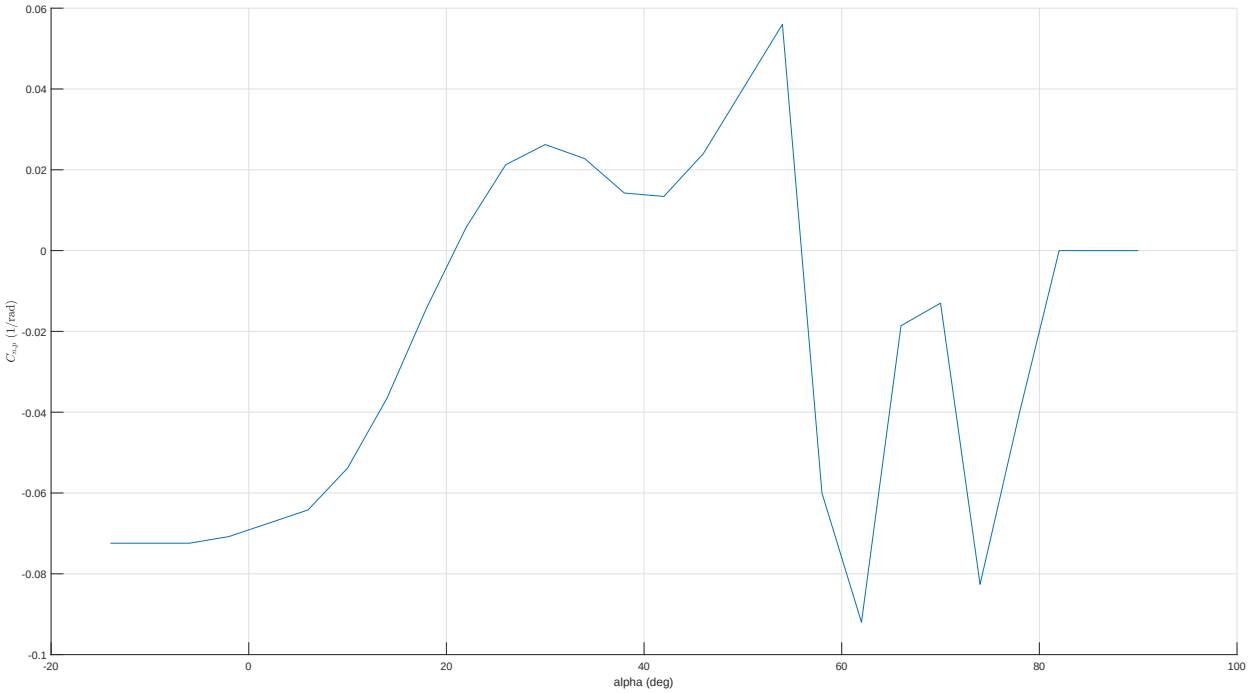

Figure 25 Aero Coefficient C_{n_p}

3.3.3 Nonlinear Simulation: Trajectories

In Figure 26 the trajectories for $\alpha = 56.0, 58.76, 65.40, 71.60$ degrees is shown. These values of α correspond to a stable trim condition, low NI, low NI with relatively high instability, and high NI with instability similar in magnitude to the low NI system. The stable trim solution ($\alpha = 56.0°$) maintains the steady spin motion without deviation throughout the entire 500 second simulation. The remaining trim points all diverge from the initial condition, regardless of NI magnitude, due to the instability of the system at these operating points.

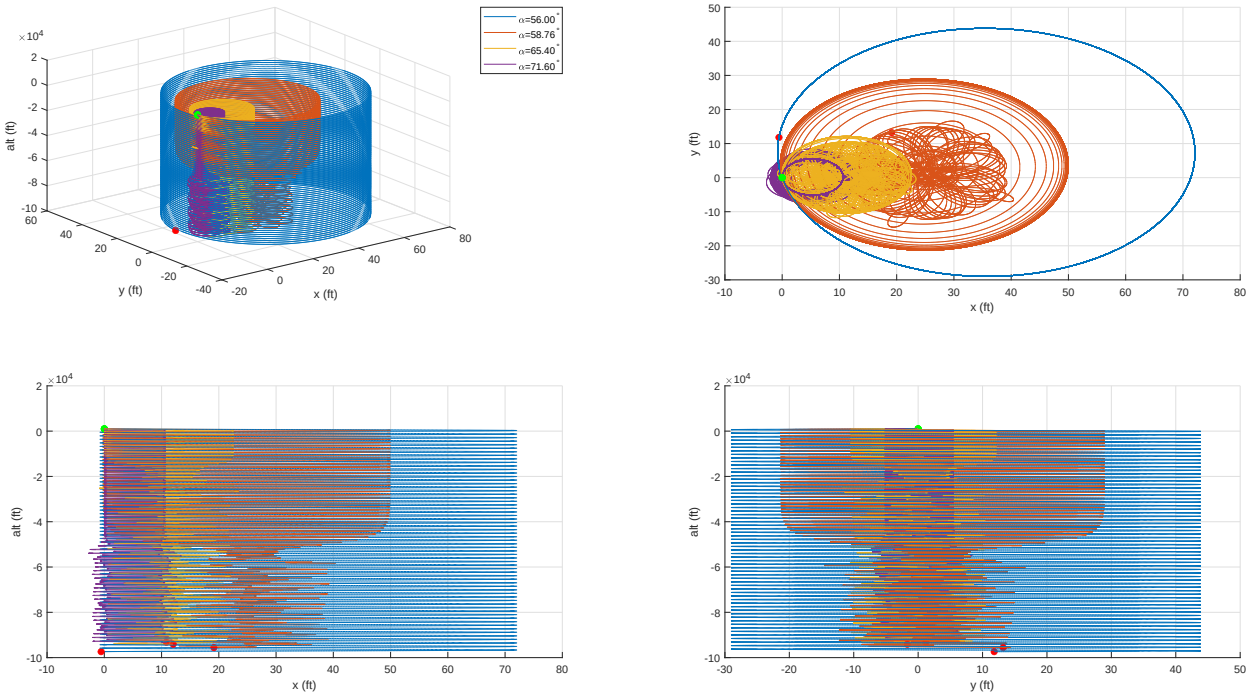

Figure 26 Flight Trajectories of Stable, Low NI, Low NI with High Instability, and High NI

The angular rate phase plots for the low NI at $\alpha = 58.76°$ and the high NI at $\alpha = 71.6°$ is presented in Figures 27 and 28 respectively. The perturbed simulations incorporating $\Delta p = 0.05\,\text{rad/s}$ is also plotted in these figures. In these figures it can be seen that the perturbations shift the response, but the overall trajectory remains mostly the same.

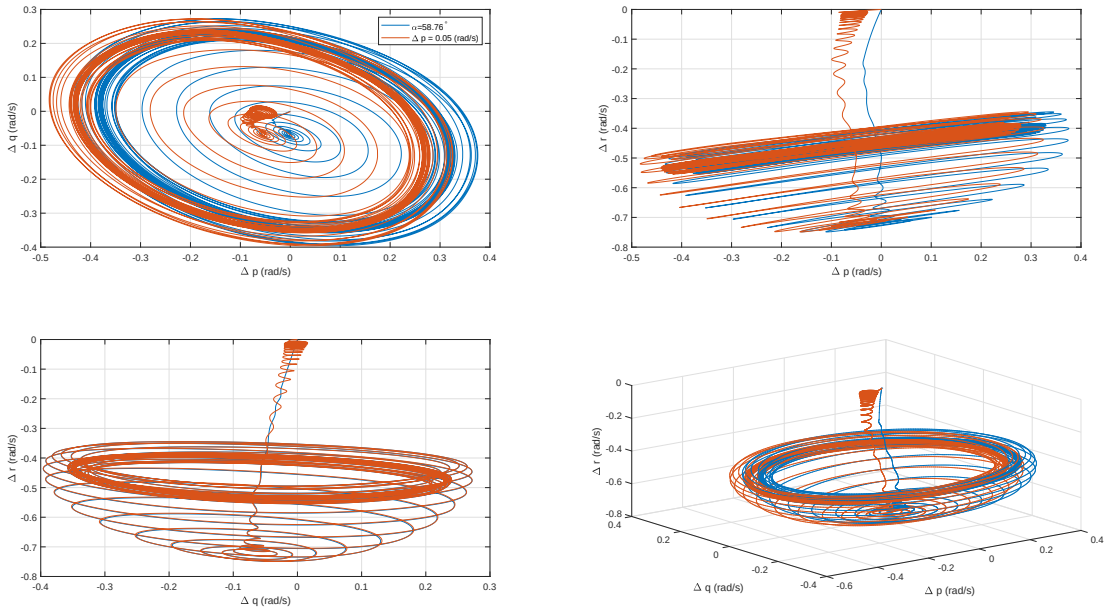

Figure 27 p, q, r Phase Trajectories for Spin Simulation at Low NI, $\alpha = 58.76°$

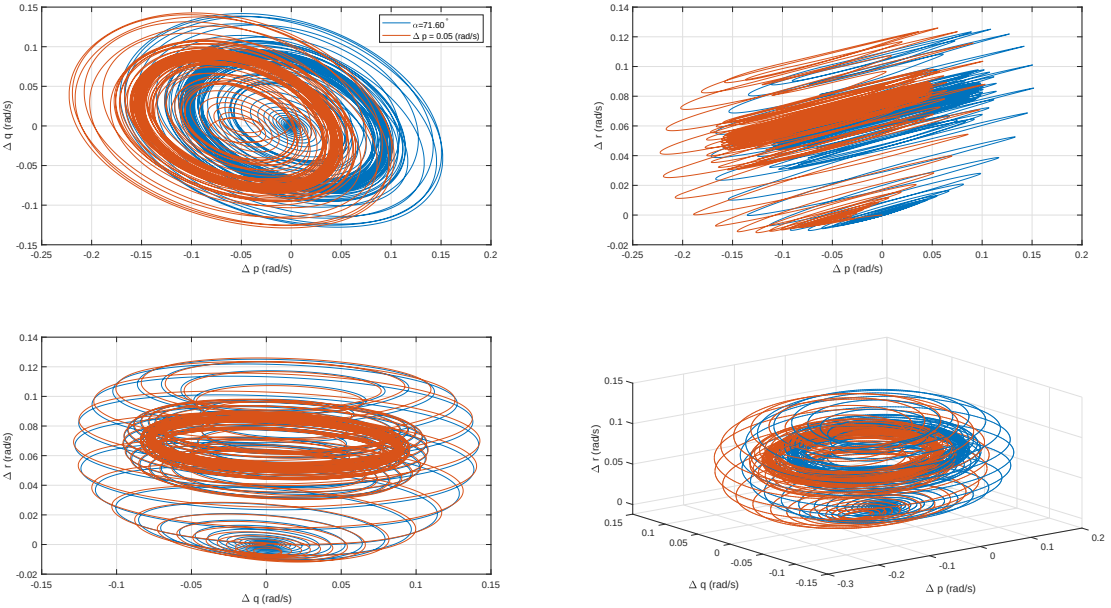

Figure 28 p, q, r Phase Trajectories for Spin Simulation at High NI, $\alpha = 71.60°$

CHAPTER 4
NONLINEAR DYNAMIC INVERSION

Nonlinear dynamic inversion (NDI) is a relatively simple yet powerful method that has gained traction as a popular control method in recent times. As the name implies, NDI explicitly accounts for system nonlinearities by employing the equations of motion in the controller. While this may add some complexity to the overall control structure, inclusion of the nonlinear equations of motion makes the NDI controller applicable over the entire flight envelope without any explicit gain scheduling. Due to this observation, NDI control can be advantageous over conventional controllers as the time consuming and tedious task of gain tuning scheduling is not required.

4.1 NDI: Linear System

In this section NDI is applied to a linear system to build the groundwork for extending it to nonlinear systems. The material presented here closely follows that presented in Reference 49 .

Consider the following square linear state space system with A system dynamics, B input distribution, and C output distribution matrices.

$$\dot{x} = Ax + Bu \tag{4.1-1}$$

$$y = Cx \tag{4.1-2}$$

The state, input, and output are defined as $x \in R^n$, $u \in R^m$, $y \in R^p$, respectively. The objective is to control the output y such that it follows a specified trajectory y_d. In dynamic inversion the process is to differentiate the output until the input appears yielding a direct relationship between the output y and the control input u.

$$\dot{y} = C\dot{x} = CAx + CBu \tag{4.1-3}$$

In Equation (4.1-3) the control input will appear as long as the product CB is not equal to zero. If CB were to equal zero differentiation would be continued until a nonzero result is obtained. Since a square system is assumed CB will also be square. A further requirement is that CB be a nonsingular or invertible matrix. Introduce the auxiliary input ν as given by Equation (4.1-4).

$$\nu = CAx + CBu - \dot{y}_d \tag{4.1-4}$$

Observe that the control input in Equation (4.1-4) can be directly solved for.

$$u = (CB)^{-1}(\nu + \dot{y}_d - CAx) \tag{4.1-5}$$

Substituting Equation (4.1-5) into Equation (4.1-3) gives the relationship shown in Equation (4.1-6).

$$\begin{aligned} \dot{y} &= CAx + CB\left[(CB)^{-1}(\nu + \dot{y}_d - CAx)\right] \\ &= CAx + \nu + \dot{y}_d - CAx \\ &= \nu + \dot{y}_d \end{aligned} \tag{4.1-6}$$

Define the tracking error e as the difference between the desired output and the actual output.

$$e = y_d - y \tag{4.1-7}$$

After utilizing Equations (4.1-6) and (4.1-7) observe that error dynamics are governed by Equation (4.1-8).

$$\dot{e} = -\nu \tag{4.1-8}$$

The choice of auxiliary input has been selected such that the CAx terms do not appear in the error dynamics. This choice results in the error dynamics consisting of p integrators (i.e., p poles at $s = 0$) for which a stabilizing controller can be efficiently designed using various linear control techniques.

The simplest choice for the auxiliary input is a positive definite diagonal gain matrix K that ensures stability and decouples the control inputs. With this selection the control law consists of a proportional outer tracking loop with a full state feedback linearization inner loop as depicted in Figure 29. In Figure 29 the system's control input is defined by Equation (4.1-9).

$$u = (CB)^{-1}(\dot{y}_d + Ke - CAx) \tag{4.1-9}$$

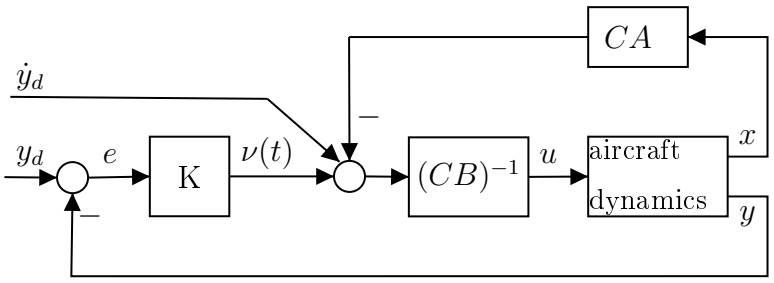

Figure 29 Nonlinear Dynamic Inversion Control Law for Linear System

At this point it is important to discuss the concept of zero dynamics, the dynamics of the system when the input ν is selected to give an output y equal to zero. While the error dynamics are guaranteed stable by ν, there remains $n-p$ poles that are unobservable through y. These poles are defined by the zero dynamics and their behavior should be checked. Internal zeros that are non-minimum phase will result in an unstable closed-loop system.

The zero dynamics can be evaluated by substituting Equation (4.1-9) into Equation (4.1-1) and setting $\nu = -\dot{y}_d$. This value of ν arises from $y = \dot{y} = 0$ being applied to Equation (4.1-8).

$$\dot{x} = Ax + Bu \tag{4.1-10}$$

$$= Ax + B(CB)^{-1}(\dot{y}_d + \nu - CAx) \tag{4.1-11}$$

$$= [I - B(CB)^{-1}C]Ax + B(CB)^{-1}(\dot{y}_d + \nu) \tag{4.1-12}$$

$$= [I - B(CB)^{-1}C]Ax \equiv A_z x \tag{4.1-13}$$

Thus for a given choice of control variables (CV), Equation (4.1-13) can be employed to ensure stable zero dynamics. That is to say, the poles of A_z should all be stable. NDI may not succeed in providing this character and the selection of control variables should be revisited if A_z contains unstable poles. If an unstable pole does exist, the time to double should be considered prior to adjusting the control variable selection as a measure of the instability severity. As an example consider the linear plant presented in Figure 31 extracted from the HARV model for level flight at $M = 0.4, H = 1000$ft with coefficients rounded to four significant digits.

The open-loop system has one unstable pole at $1.779e-3\,$rad/s which has a doubling time $T_2 \approx 389\,$s. With the selected control variables the closed-loop zero dynamics are determined to have the following poles in units of rad/s by Equation (4.1-13).

$$-1.752091635500319e-02$$
$$-1.047404705978418e+00$$
$$-1.370320252152475e-01$$
$$1.523809787396252e-15 + 2.758208778000431e-08i$$
$$1.523809787396252e-15 - 2.758208778000431e-08i$$
$$-5.877961663095412e-19$$
$$0.000000000000000e+00$$

$$0.000000000000000e+00$$

Numerically the control law has produced an unstable pole in the zero dynamics; however, this is in fact the third expected pole at the origin when closely looking at the magnitude of the values. With stable zero dynamics it is safe to proceed with the chosen control variables.

As a simple demonstration the gain matrix K is selected with diagonal elements equal to 10 with units 1/s. This controller is then simulated using the MATLAB function *ode23* with an input pitch pulse and roll doublet. The results for this simulation are presented in Figure 30. Note the control law is forcing the aircraft to closely follow the desired motion commands.

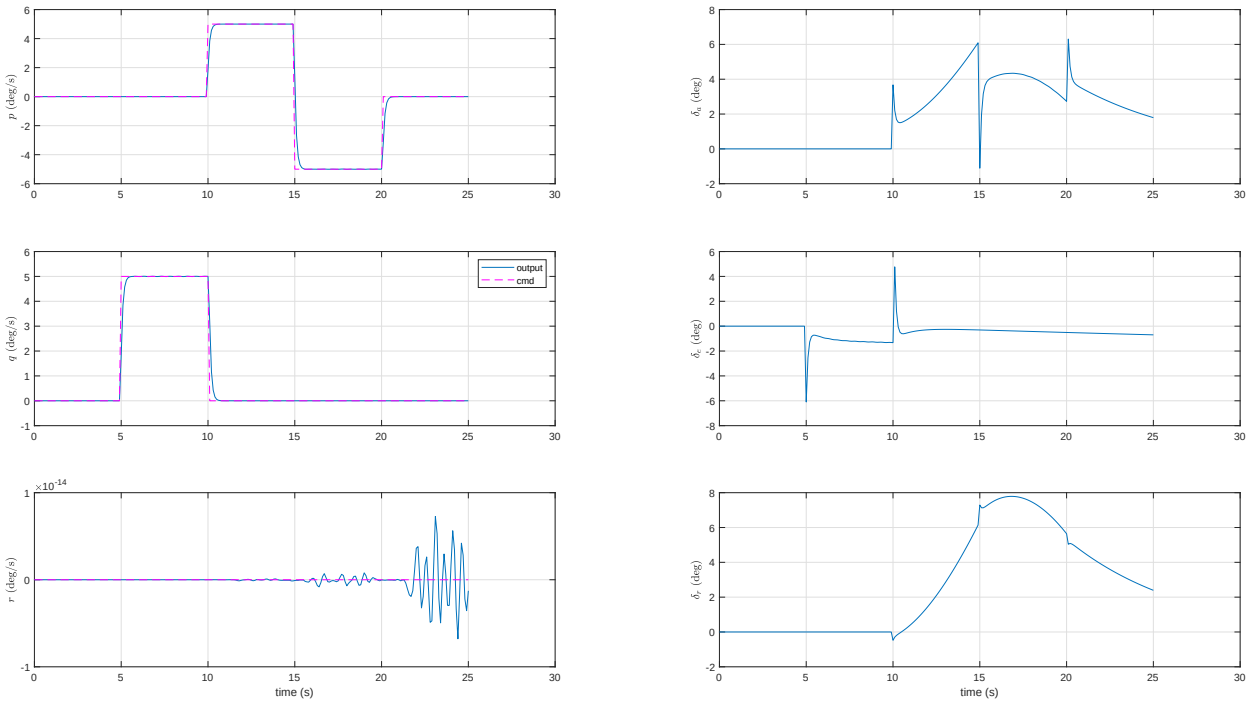

Figure 30 Simulation of Linear NDI Control

```
A = [% V           alpha       beta        p           q           r ...
               phi         theta
-1.7509e-02 -6.9953e+00  3.8080e-12 -6.7100e-16  2.3768e-02 ...
    -1.6447e-14 -7.2005e-13 -3.2174e+01;...
 1.4826e-06 -1.0755e+00  3.5204e-18  2.2380e-14  9.9010e-01  ...
     1.6868e-15 -0.0000e+00  0.0000e+00;...
 9.3924e-18 -3.6571e-16 -1.8625e-01  7.5223e-02  1.1986e-18 ...
     -9.9553e-01  7.2090e-02 -1.6225e-15;...
 1.3272e-15  1.1989e-12 -1.3159e+01 -2.5675e+00 -0.0000e+00  ...
     7.7571e-01  0.0000e+00  0.0000e+00;...
-1.3015e-14 -1.0059e+00  0.0000e+00  0.0000e+00 -3.7121e-01  ...
    0.0000e+00  0.0000e+00  0.0000e+00;...
-1.7360e-16 -6.6401e-15  1.7212e+00 -4.9824e-02 -0.0000e+00 ...
    -1.3577e-01  0.0000e+00  0.0000e+00;...
 0.0000e+00  0.0000e+00  0.0000e+00  1.0000e+00  0.0000e+00  ...
     7.5369e-02  0.0000e+00  0.0000e+00;...
 0.0000e+00  0.0000e+00  0.0000e+00  0.0000e+00  1.0000e+00 ...
     -0.0000e+00 -0.0000e+00  0.0000e+00;...
];
B = [% da          de          dr
 4.5417e-14  6.7773e+00 -3.9190e-13;... V
 0.0000e+00 -1.4841e-01  0.0000e+00;... alpha
-4.5470e-03  3.4178e-16  3.9236e-02;... beta
 1.0156e+01  0.0000e+00  1.9694e+00;... p
 0.0000e+00 -5.3158e+00  0.0000e+00;... q
-3.8666e-02  0.0000e+00 -1.2240e+00;... r
 0.0000e+00  0.0000e+00  0.0000e+00;... phi
 0.0000e+00  0.0000e+00  0.0000e+00;... theta
];
C = [...
% V           alpha       beta        p           q           r ...
               phi         theta
 0.0000e+00  0.0000e+00  0.0000e+00  1.0000e+00  0.0000e+00  ...
     0.0000e+00  0.0000e+00  0.0000e+00;...
 0.0000e+00  0.0000e+00  0.0000e+00  0.0000e+00  1.0000e+00  ...
     0.0000e+00  0.0000e+00  0.0000e+00;...
 0.0000e+00  0.0000e+00  0.0000e+00  0.0000e+00  0.0000e+00  ...
     1.0000e+00  0.0000e+00  0.0000e+00;...
];
```

Figure 31 Linear F-18 Model

4.2 NDI: Nonlinear System

Building on the foundation of the previous section NDI will now be extended to the general case of nonlinear systems. For convenience in notation the Lie derivative will first be introduced. Given a scalar function $h(x)$ and a vector field $f(x)$, the Lie derivative takes the derivative of h with respect to x along direction f and is defined by Equation (4.2-1) where ∇ represents the gradient operator.

$$L_f h = \nabla h f = \frac{\partial h}{\partial x} f \tag{4.2-1}$$

The Lie derivative can be defined recursively using superscript notation to represent the order of differentiation. Equation (4.2-2) presents this recursive notation.

$$\begin{aligned} L_f^0 h &= h \\ L_f^1 h &= \nabla h f \\ L_f^2 h &= L_f(L_f^1 h) = \nabla(L_f^1 h) f \\ &\vdots \\ L_f^n h &= L_f(L_f^{n-1} h) = \nabla(L_f^{n-1} h) f \end{aligned} \tag{4.2-2}$$

Now consider the nonlinear system described by Equation (4.2-3) with vector fields $f(x), g(x)$, scalar function $h(x)$, state vector $x \in R^n$, input vector $u \in R^m$, and output vector $y \in R^p$.

$$\begin{aligned} \dot{x} &= f(x) + g(x)u \\ y &= h(x) \end{aligned} \tag{4.2-3}$$

Applying nonlinear dynamic inversion, differentiate the output function (with $p = 1$) until the input u appears as presented in Equation (4.2-4).

$$\frac{dy}{dt} = \nabla h(x) \left[f(x) + g(x)u \right] = L_f^1 h(x) + L_g h(x) u \tag{4.2-4}$$

If the input doesn't appear after the first differentiation the process is done recursively until it does (for each output function). Equation (4.2-5) defines the general process using superscript notation where j is iterating over all inputs, and subscript i denotes the output function (here $p > 1$).[61] The degree of differentiation for the output is distinguished by r_i, the "relative degree" for the i^{th} output, as in general they may not be the same across all

output functions.

$$y_i^{(r_i)} = L_f^{(r_i)} h_i + \sum_{j=1}^{m} L_{g_{ij}} L_f^{r_i - 1} h_i(x) u_j \tag{4.2-5}$$

In Equation (4.2-5) the relative degree r_i obeys the relationship, $r_i \leq n$ as at most the function will need to be differentiated n times. Grouping similar terms Equation (4.2-5) can be rewritten in the following matrix format.

$$y^r = \hat{A} + \hat{B} u \tag{4.2-6a}$$

$$\hat{A} = \begin{bmatrix} L_f^{r_1} h_1(x) \\ \vdots \\ L_f^{r_p} h_p(x) \end{bmatrix} \tag{4.2-6b}$$

$$\hat{B} = \begin{bmatrix} L_{g_{11}} L_f^{r_1 - 1} h_1(x) & \dots & L_{g_{1m}} L_f^{r_1 - 1} h_1(x) \\ \vdots & \ddots & \vdots \\ L_{g_{p1}} L_f^{r_p - 1} h_p(x) & \dots & L_{g_{pm}} L_f^{r_p - 1} h_p(x) \end{bmatrix} \tag{4.2-6c}$$

Similar to Equation (4.1-4) introduce the auxiliary input ν given by Equation (4.2-7).

$$\nu = \begin{bmatrix} y_1^{r_1} \\ \vdots \\ y_p^{r_p} \end{bmatrix} - \dot{y}_d = y^r - \dot{y}_d \tag{4.2-7}$$

Assuming a square system with $p = m$, the required control input is solved for from Equation (4.2-6a) as

$$u = \hat{B}^{-1} \left[\nu + \dot{y}_d - \hat{A} \right] \tag{4.2-8}$$

where $\dot{y}_d$ has been inserted for the tracking control problem. Similar to the linear development the tracking error is given by Equation (4.2-9).

$$e = y_d - y \tag{4.2-9}$$

Substituting Equation (4.2-8) into Equation (4.2-6a) produces a linear relationship for error dynamics in terms of the auxiliary input ν enabling any linear control design method to be employed.

$$y^r = \hat{A} + \hat{B} \hat{B}^{-1} \left[\nu + \dot{y}_d - \hat{A} \right] \tag{4.2-10}$$

$$\dot{y}_d - y^r = -\nu \tag{4.2-11}$$

$$\dot{e} = -\nu \tag{4.2-12}$$

Similar to the linear implementation, the internal dynamics need to be well behaved and stable. If $r = \sum_i^m r_i = n$, then closed-loop stability can be guaranteed. However, if $r = \sum_i^m r_i < n$, then closed-loop stability can only be guaranteed locally by showing the unobservable internal dynamics are well behaved over the region of interest. The internal dynamics can be checked by utilizing the zero dynamics, that is constraining the output to zero given the input presented in Equation (4.2-13). Similarly, the nonlinear system can be linearized at a given condition and the linearized internal dynamics or zero dynamics can be evaluated.

$$\begin{aligned} y^r = 0 &= \hat{A} + \hat{B}u \\ u &= -\hat{B}^{-1}\hat{A} \end{aligned} \tag{4.2-13}$$

4.3 Control Allocation

A key component in the design of control systems for advanced aircraft is control allocation. This trend is true as many advanced aircraft have multiple surfaces that can control one of the three primary moments. As a comparison consider the controls of a Cessna 172 presented in Figures 32 and 33. Clearly the Cessna only has three primary controls, one for each primary axis of control. Thus for a simple aircraft configuration control allocation isn't of concern. In contrast, modern fighter aircraft have redundant control surfaces. The F-18 HARV control surfaces include ailerons, horizontal stabilators, a rudder, leading and trailing edge flaps, and thrust vectoring (see Figure 34). When an aircraft has redundant controls the question is then how are the control surfaces most effectively employed? The answer to this question is not straight forward nor can it be generalized for all conditions as it depends on the design goals of the system. Since the focus of this thesis is not on solving nor optimizing the control allocation problem, only a brief introduction will be provided.

In order to provide a more illustrative example the model used in the remainder of this section is that of the ADMIRE model presented in Reference 62 and replicated here in Equations (4.3-1) and (4.3-2). The control surface limits presented in Equation (4.3-2) are provided in degrees for readability. However, in subsequent calculations the units are in radians in order to comply with the units of the B matrix presented in Equation (4.3-1). The motivation for using the ADMIRE model is due to the additional aerodynamic control surfaces. The ADMIRE model consists of left/right canard, left/right inboard elevon, left/right outboard elevon, and rudder whereas the aerodynamic control surface data for the F-18 HARV is limited to effective aileron, left/right stabilator, and rudder.

AILERON CONTROL SYSTEM

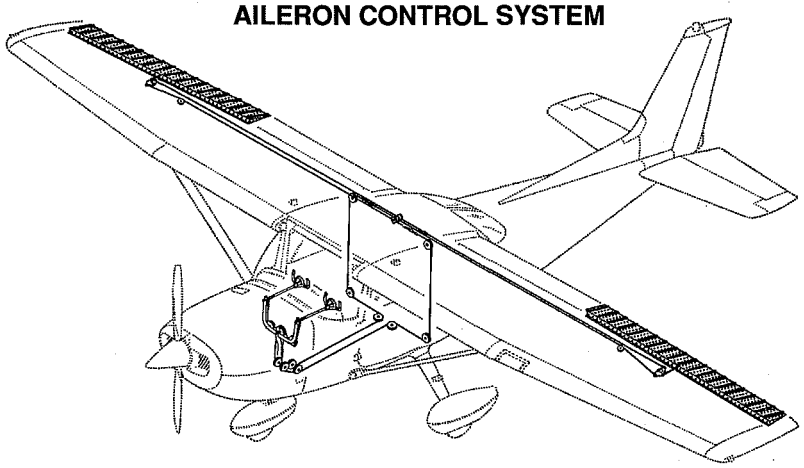

RUDDER CONTROL SYSTEM

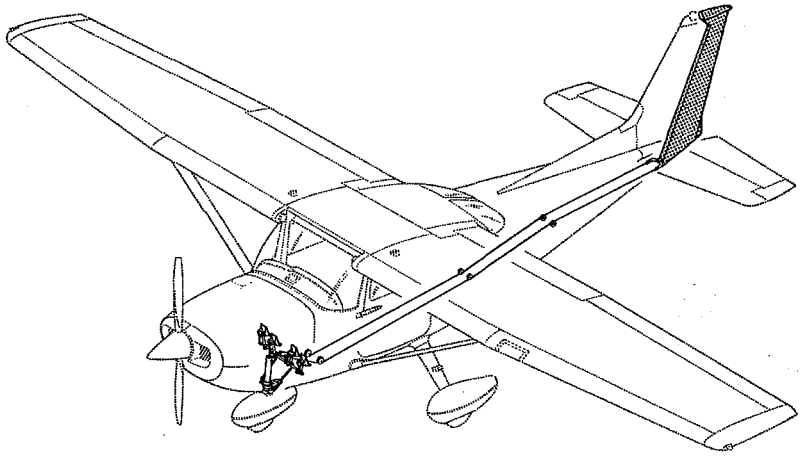

0585X1017

Figure 7-1. Flight Control and Trim Systems (Sheet 1 of 2)

Figure 32 Cessna 172 Lateral-Directional Controls[63]

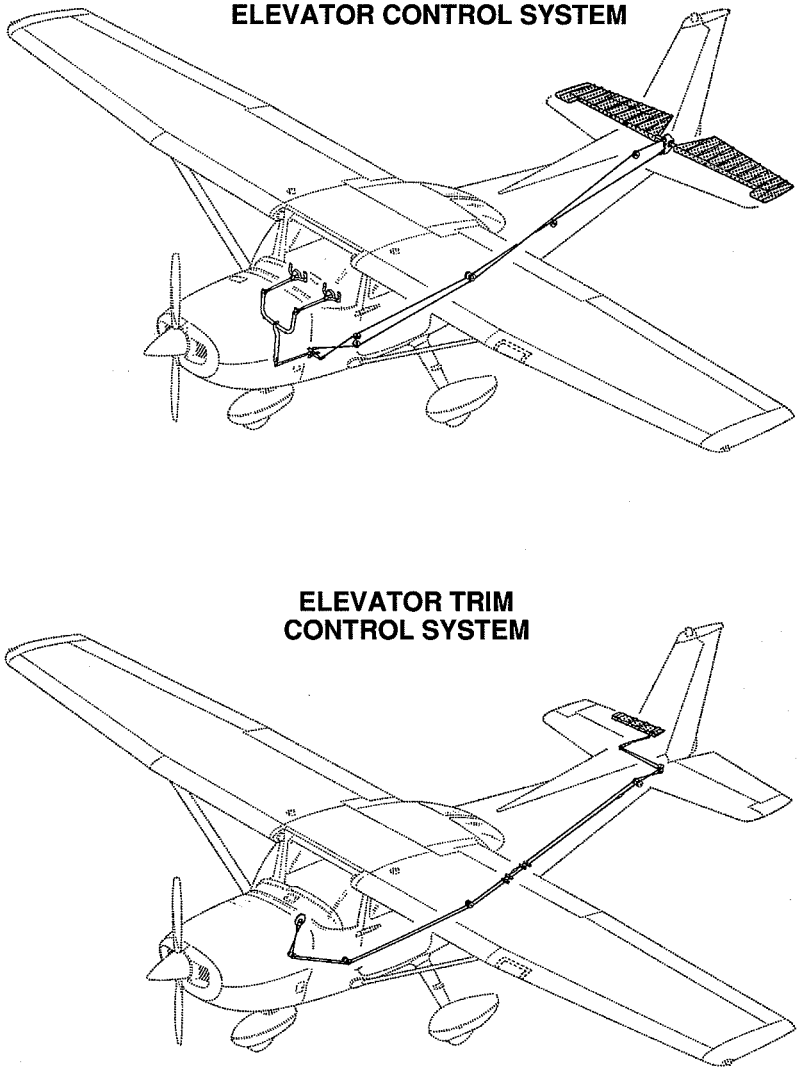

Figure 7-1. Flight Control and Trim Systems (Sheet 2 of 2)

Figure 33 Cessna 172 Longitudinal Controls[63]

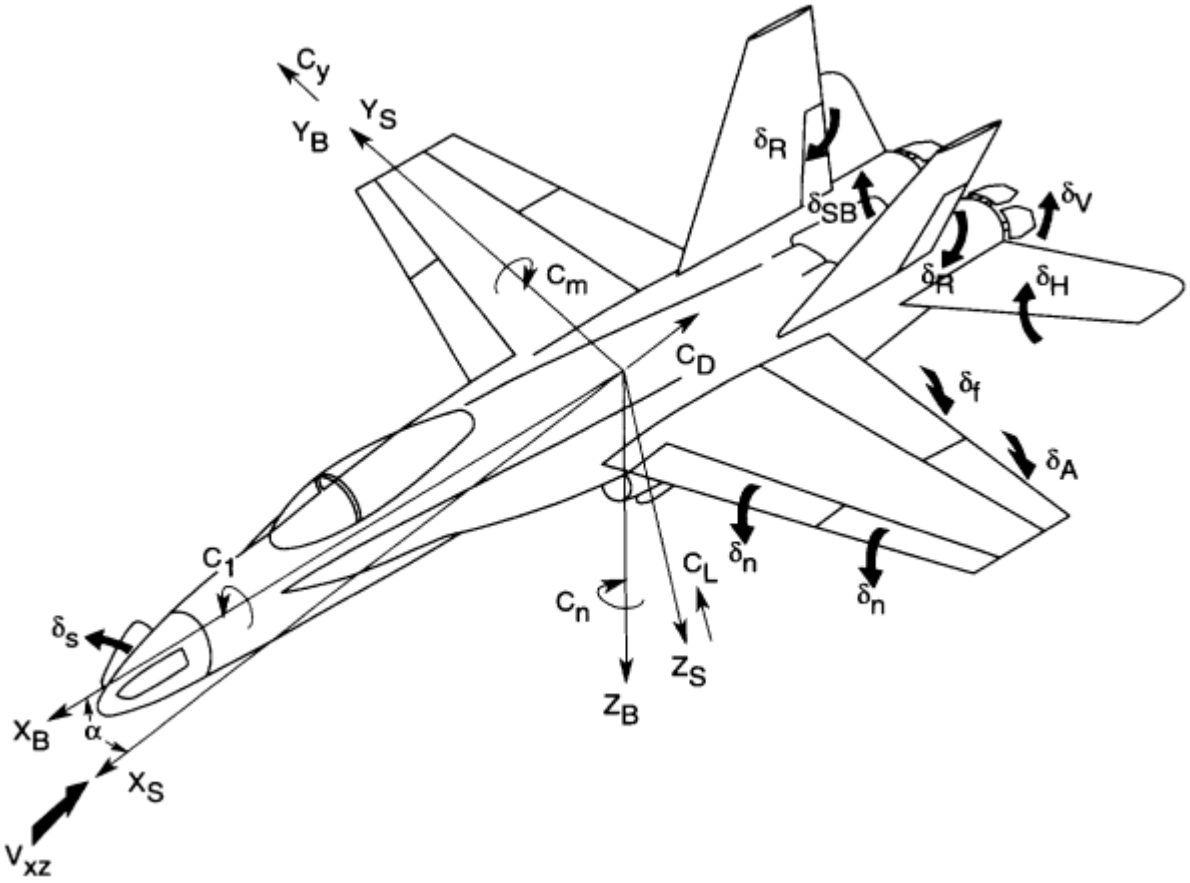

Figure 34 F-18 HARV Control Surfaces[56]

$$B = \begin{bmatrix} 0.7073 & -0.7073 & -3.4956 & -3.0013 & 3.0013 & 3.4956 & 2.1103 \\ 1.1204 & 1.1204 & -0.7919 & -1.2614 & -1.2614 & -0.7919 & 0.0035 \\ -0.3309 & 0.3309 & -0.1507 & -0.3088 & 0.3088 & 0.1507 & -1.2680 \end{bmatrix} \tag{4.3-1}$$

$$u_{min} = \begin{bmatrix} -55 \\ -55 \\ -30 \\ -30 \\ -30 \\ -30 \\ -30 \end{bmatrix} \quad u_{max} = \begin{bmatrix} 25 \\ 25 \\ 30 \\ 30 \\ 30 \\ 30 \\ 30 \end{bmatrix} \quad \text{names} = \begin{bmatrix} \text{R canard} \\ \text{L canard} \\ \text{R OB elevon} \\ \text{L OB elevon} \\ \text{R IB elevon} \\ \text{L IB elevon} \\ \text{rudder} \end{bmatrix} \tag{4.3-2}$$

4.3.1 Attainable Moment Subset

The attainable moment subset (AMS) refers to all moments that can be physically generated at the current flight condition. Mathematically this is the control effectiveness matrix B times every admissible control u. However, of particular interest is the boundary of the AMS. The aircraft three-moment problem will generate a three-dimensional space bounded by two-dimensional facets. The facets are computed by varying two control surfaces at a time while the remaining surfaces are at their limits.

The method to determine the two-dimensional AMS is first presented. Consider the following two-dimensional control effectiveness matrix with control limits ± 0.5 rad.

$$B = \begin{bmatrix} 1 & 0 & -0.5 \\ 0 & 1 & -0.5 \end{bmatrix} \tag{4.3-3}$$

The set of all attainable moments can be determined by varying one control while holding the other two at their limits. Utilizing the same object notation presented in Reference 62, let 1 denote the maximum, 0 the minimum, and 2 a control free to vary. The pseudocode presented in Figure 35 can be used to determine all attainable moments.

```
B  = 2 x 3 control effectiveness
u  = 3 x 1 control input
p = 1 1
    1 0
    0 1
    0 0
for j = 1:3
    for k=1:4
        u(not j) = row j of p
        u(j)     = 1
        vertex1  = B * u
        u(j)     = 0
        vertex2  = B * u
        plot edge connecting vertex1 to vertex2
    end
end
```

Figure 35 Admissible Controls Attainable Moments

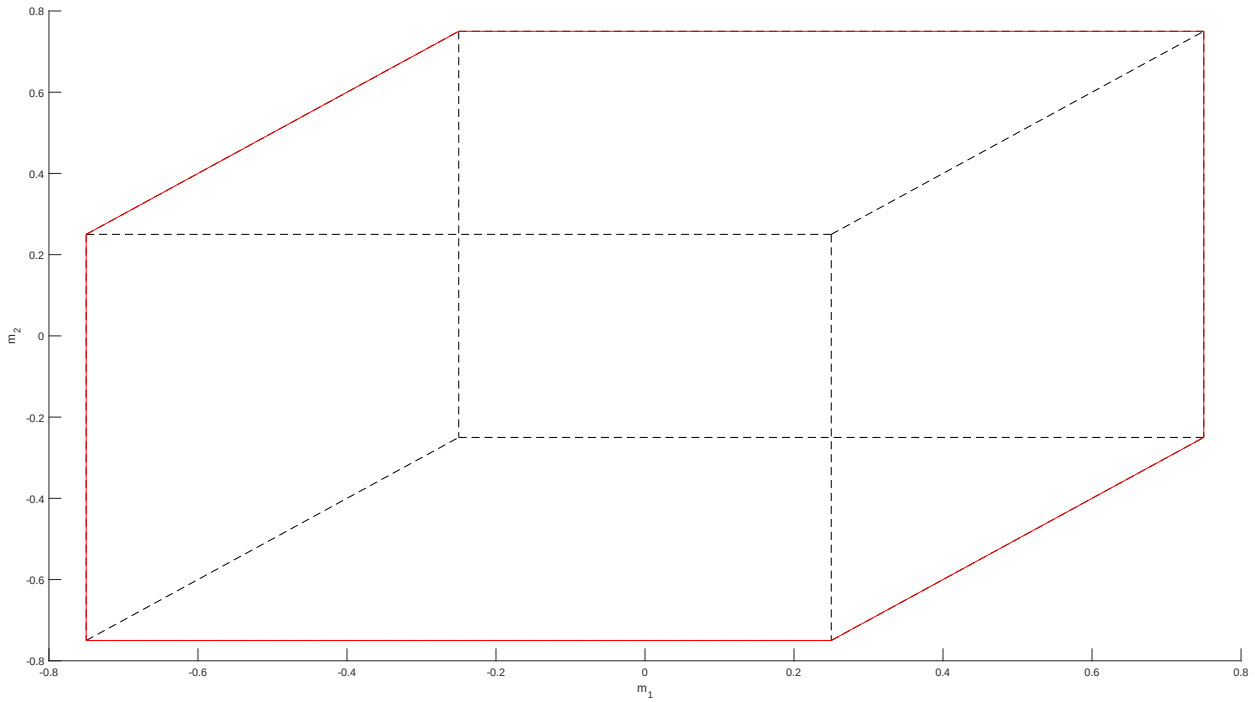

Figure 36 Two-Dimensional AMS

Figure 36 presents the AMS for the B matrix given by Equation (4.3-3). In the figure, concern is only given to determining the boundary of the AMS denoted by the red lines as this represents the maximum attainable moments. Inspecting Figure 36 with consideration to the B matrix, we conclude that the left and right vertical edges map to the second control input as the second column of B points in the vertical m_2 moment direction. Generalizing, a zero in a row of B means there is an edge orthogonal to the AMS axis corresponding to the zero element, and this edge is generated by the control of the corresponding column of B.[62] This statement of course is under the assumption that only one zero appears in any given row. This assumption can be enforced by first setting all zero valued elements to a sufficiently small positive value, μ such that $\mu \ll \min_{ij}(|B_{ij}|)$.

To apply this generalization consider choosing the first row. A transformation t that will rotate B such that there is a zero in position one of the i^{th} column of B (b_{1i}) is sought.

$$\begin{aligned} \vec{t}\,\vec{b_i} &= 0 \\ t_{11}b_{1i} + t_{12}b_{2i} &= 0 \end{aligned} \tag{4.3-4}$$

In Equation (4.3-4) standard (row, column) indexing in the subscript notation is used. Arbitrarily choosing the second element of t as unity,

$$\vec{t} = \begin{bmatrix} -\frac{b_{2i}}{b_{1i}} & 1 \end{bmatrix} \tag{4.3-5}$$

and carrying out the product of t and B results in Equation (4.3-6).

$$\vec{t}B = g_i,\ g_i \in \mathbb{R}^{1\times 3},\ g_{ij} = 0 \text{ for } i = j \tag{4.3-6}$$

The next step is to maximize and minimize the resulting moment. This step can be accomplished by acknowledging the signs of the elements. Utilizing the signum function and assuming logical indexing of arrays, the AMS vertices can be solved by the pseudocode presented in Figure 37.

To extend the solution to the three-dimensional case, take two columns at a time represented by i, j and set the remaining controls at their limits that maximize and minimize the moment. Under the assumption B has already been preconditioned by μ to remove zero elements the rotation transformation can be computed as follows. Solve t such that zeros are placed in the first row of columns i, j. In a similar fashion to the two-dimensional problem, choose one value of t; thus, let $t_{13} = 1$, and carry out the procedure as shown in

Equation (4.3-7).

$$
\begin{aligned}
\vec{t}\begin{bmatrix}\vec{b}_i & \vec{b}_j\end{bmatrix} &= \vec{0} \\
\begin{bmatrix}t_{11} & t_{12} & t_{13}\end{bmatrix}\begin{bmatrix}b_{1i} & b_{1j} \\ b_{2i} & b_{2j} \\ b_{3i} & b_{3j}\end{bmatrix} &= \begin{bmatrix}0 & 0\end{bmatrix} \\
\begin{bmatrix}b_{1i} & b_{2i} \\ b_{1j} & b_{2j}\end{bmatrix}\begin{bmatrix}t_{11} \\ t_{12}\end{bmatrix} &= -\begin{bmatrix}b_{3i} \\ b_{3j}\end{bmatrix} \\
\begin{bmatrix}t_{11} \\ t_{12}\end{bmatrix} &= -\begin{bmatrix}b_{1i} & b_{2i} \\ b_{1j} & b_{2j}\end{bmatrix}^{-1}\begin{bmatrix}b_{3i} \\ b_{3j}\end{bmatrix}
\end{aligned}
\tag{4.3-7}
$$

Once t has been determined the rest of the process is carried out in the same manner as for the two-dimensional case. In order to take two columns at a time for m controls, implement a loop for $i = 1 \ldots m-1, \quad j = i+1 \ldots m$.

Carrying out this process for the ADMIRE control effectiveness matrix with seven control surfaces results in the volume presented in Figure 38. Any point on the surface represents a unique solution of the maximum attainable angular accelerations. Points within the surface are attainable but the solutions are not unique; this situation is where control allocation has the ability to optimize control surface utilization.

Knowledge of this control space is relevant as it can aid in the control surface sizing, actuator selection, and controller evaluation. Required accelerations can be calculated given specific design requirements such as roll performance or more advanced maneuvers. The angular accelerations can subsequently be graphically represented with the AMS providing the engineer with the relevant information to determine whether the maneuver can be achieved. In industry, this process is beneficial as it alleviates the requirement to perform nonlinear simulations on a system that may not yet exist.

```
B = 2 x m control effectiveness
set any B elements that equal zero to mu
umin = m x 1 minimum control positions
umax = m x 1 maximum control positions
for i=1:m
    bi = the ith column of B
    if bi(1) not equal 0
        t  = [-bi(2) / bi(1), 1]`
        tB = t * B
    else
        tB = first row of B
    end
    uo  = logical array size 3 x 4
    uo column one rows (signum tB equal to 1)  = 1
    uo column one rows (signum tB equal to -1) = 0
    uo column 2 = not( uo column 1)
    uo columns one and two, row i = [1 0]
    uo columns 3, 4 = not( uo columns 1, 2)
    for j=1:4
        uc(uo column j)       = umax( uo column j)
        uc(not(uo column j)) = umin(not(uo column j))
        vertex = B * uc
    end
end
```

Figure 37 Pseudocode, Two-Dimensional AMS

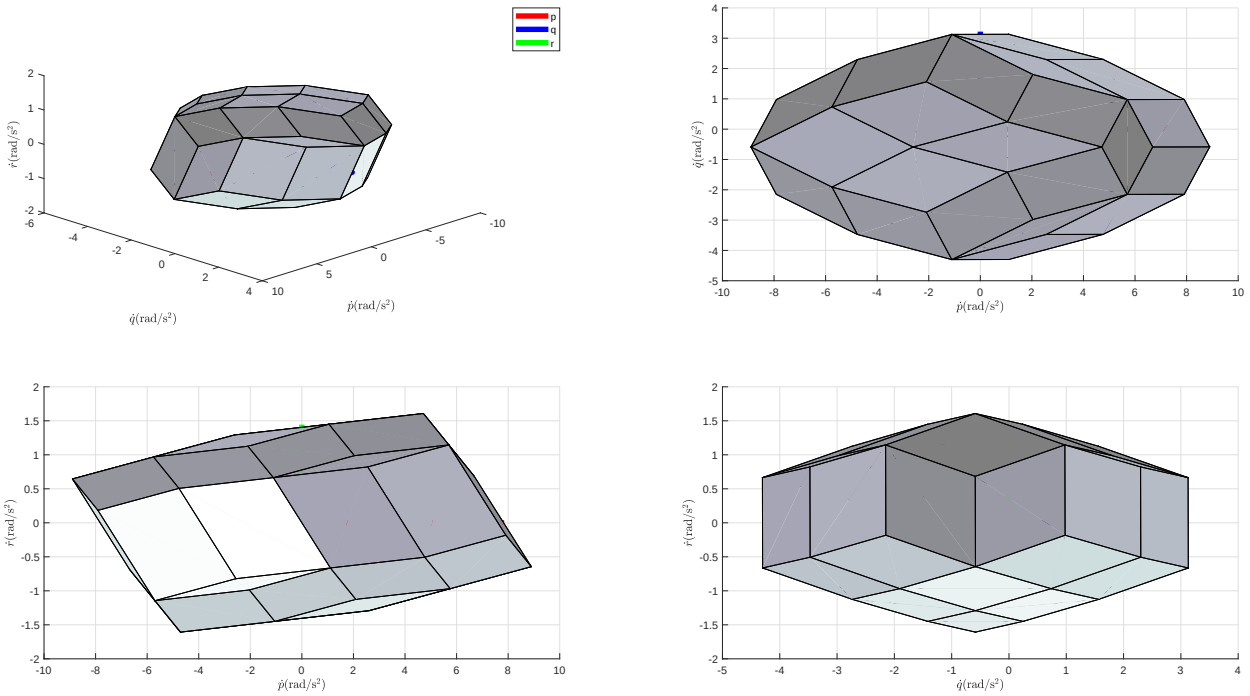

Figure 38 Three-Dimensional AMS

4.3.2 HARV AMS

The AMS for the HARV is presented in Figure 39 to present the benefit of utilizing differential stabilator. The smaller polyhedron colored red represents the attainable moment region using the stabilators as a single effective elevator. The larger gray polyhedron represents the additional control power that is gained by utilizing the stabilators independently. Observe that utilizing the stabilators independently expands the roll authority. In order to quantitatively compare the differences the volumes of the AMS will be used. When the stabilators are used together the volume is $0.4453\,(\mathrm{rad/s^2})^3$ whereas the full potential AMS is $0.6869\,(\mathrm{rad/s^2})^3$. Thus employing the stabilators independently expands the control power by 54%.

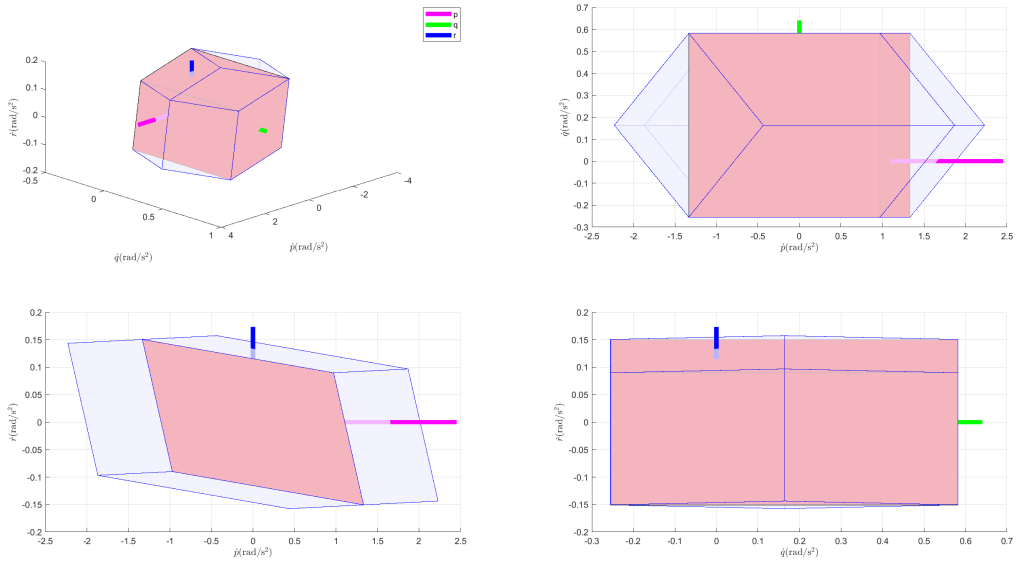

Figure 39 HARV AMS and Effective Elevator AMS

The question now is how to utilize the four controls most effectively? In going from three to four controls the system is now under-determined. The following problem must be solved,

$$\vec{m}_c = B\vec{u} \tag{4.3-8}$$

where $\vec{m}_c$, the commanded moment, and B the control matrix are known and the unknown control vector $\vec{u}$ must be determined. In Equation (4.3-8), $\vec{m}_c$ is of dimension 3×1, B is $3 \times m$, and $\vec{u}$ is $m \times 1$. In the case that $m = n = 3$ the problem can be solved with the matrix inverse.

$$\vec{u} = B^{-1}\vec{m}_c \tag{4.3-9}$$

If $m > n = 3$ the matrix inverse does not exist. To solve the problem the generalized inverse that solves $PB = I$ can be used and is defined by Equation (4.3-10).

$$P = N(BN)^{-1}$$

where

$$\begin{aligned} B &\in \mathbb{R}^{n\times m} \\ N &\in \mathbb{R}^{m\times n} \\ |BN| &\neq 0 \end{aligned} \tag{4.3-10}$$

In Equation (4.3-10) an additional requirement that N and B are real such that the control algorithm is implementable has been imposed. Now the control vector can be solved,

$$\vec{u} = P\vec{m}_c \tag{4.3-11}$$

When going from the square system to an under-determined system an additional constraint must be imposed, that is defining N for the inverse. Consider the B matrix for the HARV aircraft without flaps and thrust vectoring ($m = 4$) defined by the matrix presented in Equation (4.3-12).

$$B = \begin{bmatrix} \frac{\partial \mathcal{L}}{\partial \delta_a} & \frac{\partial \mathcal{L}}{\partial \delta_{el}} & \frac{\partial \mathcal{L}}{\partial \delta_e r} & \frac{\partial \mathcal{L}}{\partial \delta_r} \\ \frac{\partial \mathcal{M}}{\partial \delta_a} & \frac{\partial \mathcal{M}}{\partial \delta_{el}} & \frac{\partial \mathcal{M}}{\partial \delta_e r} & \frac{\partial \mathcal{M}}{\partial \delta_r} \\ \frac{\partial \mathcal{N}}{\partial \delta_a} & \frac{\partial \mathcal{N}}{\partial \delta_{el}} & \frac{\partial \mathcal{N}}{\partial \delta_e r} & \frac{\partial \mathcal{N}}{\partial \delta_r} \end{bmatrix} \tag{4.3-12}$$

The N matrix maps the control inputs and can be defined in such a manner that it produces the same effect as the square system with three controls, that is a single effective elevator. Equation (4.3-13) creates the single effective elevator.

$$N = \begin{bmatrix} 1 & 0 & 0 \\ 0 & 1 & 0 \\ 0 & 1 & 0 \\ 0 & 0 & 1 \end{bmatrix} \tag{4.3-13}$$

Exploring another option, impose a common conventional control method by ganging controls together. An example would be stabilator-rudder interconnect and is obtained if N is defined by Equation (4.3-14). This ganging scheme leverages the ability of differential stabilators to generate a yawing moment. In Figure 40 the stabilator-rudder interconnect configuration AMS is depicted; it has a volume of $0.3096\,(\mathrm{rad/s^2})^3$, significantly lower than the maximum attainable control power. However, the attainable yaw moments are increased with respect to nonzero rolling moments.

$$N = \begin{bmatrix} 1 & 0 & 0 \\ 0 & 1 & -0.5 \\ 0 & 1 & 0.5 \\ 0 & 0 & 1 \end{bmatrix} \tag{4.3-14}$$

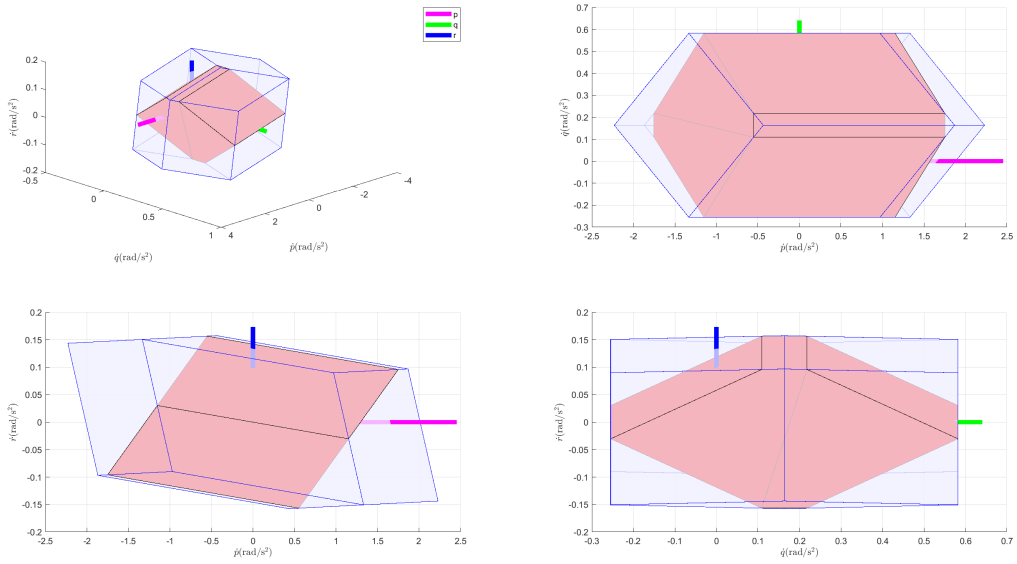

Figure 40 AMS with Ganged Control within Full AMS

There are numerous approaches to optimize the control allocation but for simplicity consideration is only given to the Moore-Penrose pseudo-inverse. This implementation minimizes the 2-norm of the control vector. If the control matrix B has full rank this method simplifies to that of Equation (4.3-15).[62]

$$P = B^{\mathsf{T}}(BB^{\mathsf{T}})^{-1} \tag{4.3-15}$$

If B is rank deficient then singular value decomposition (SVD) can be used where the SVD is defined by Equation (4.3-16). Literature such as Reference 64 presents a more detailed introduction to SVD.

$$B = U\Sigma V^{\mathsf{T}} \tag{4.3-16}$$

Given the diagonal matrix Σ of singular values σ_i which must be invertible, define a suitable minimum value $\epsilon > 0$. If any σ_i in Σ is less than ϵ the corresponding row/column is removed, the resultant matrix is then defined as $\hat{\Sigma}$. The indexed row/column removed from Σ are also removed from the corresponding column in U, V thereby defining $\hat{U}$, $\hat{V}$.

$$\begin{aligned} \hat{\Sigma} &= \Sigma(\sigma_i > \epsilon) \\ \hat{U} &= U(\sigma_i > \epsilon) \\ \hat{V} &= V(\sigma_i > \epsilon) \end{aligned} \tag{4.3-17}$$

where $(\sigma_i > \epsilon)$ refers to logical indexing

Subsequently the pseudo-inverse is formulated as shown by Equation (4.3-18).

$$P = \hat{V}\hat{\Sigma}^{-1}\hat{U}^{\mathsf{T}} \tag{4.3-18}$$

Unless otherwise specified any inverse of a non-square matrix henceforth will utilize the inverse defined by Equation (4.3-18) as this is the method utilized by MATLAB. Figure 41 depicts the AMS with the pseudo-inverse where a volume of $0.2839\,(\mathrm{rad/s^2})^3$ is attained. Though more complex methods could optimize this volume such work is beyond the scope of this thesis.

Figures 42 and 43 compare the ganged and pseudo-inverse allocation methods (blue) against the single effective elevator (red). All three methods have trade-offs and all fall short of the full potential AMS.

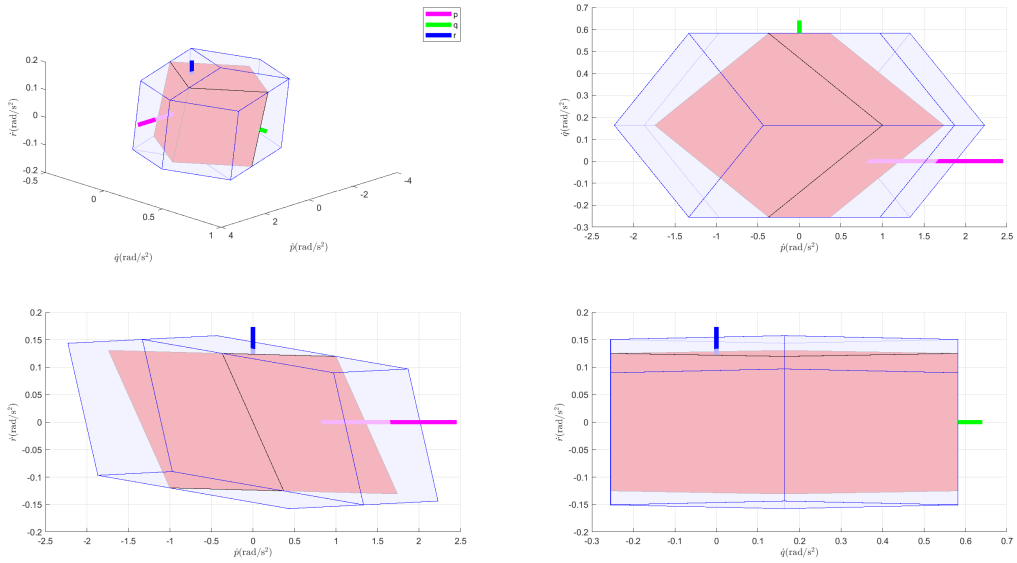

Figure 41 Pseudo-Inverse AMS

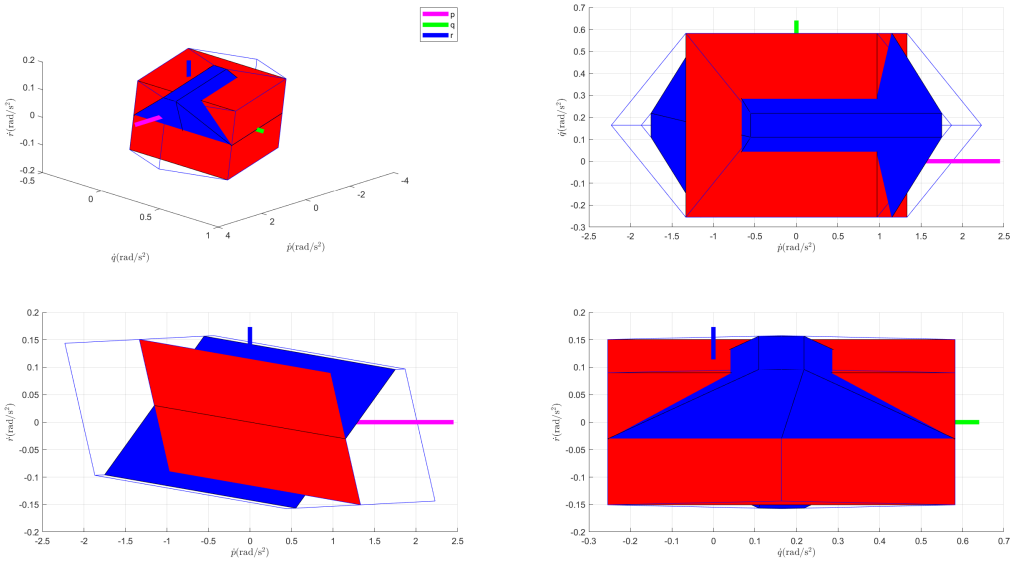

Figure 42 Effective Elevator (red) vs. Ganged (blue) AMS

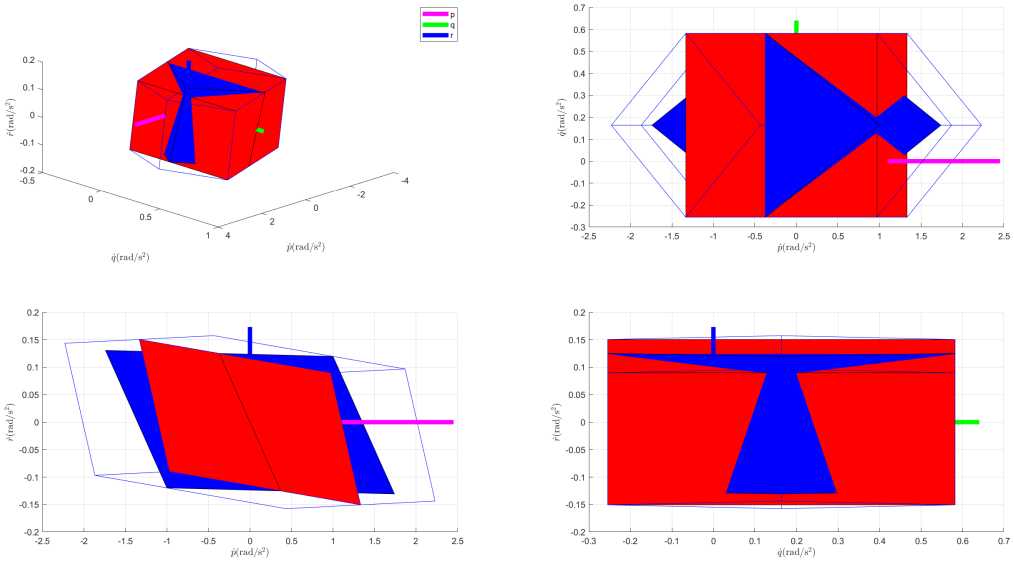

Figure 43 Effective Elevator (red) vs. Pseudo-Inverse (blue) AMS

CHAPTER 5
CONTROL DESIGN

In this section a NDI control law (CLAW) is developed for the purpose of spin recovery. This CLAW should be capable of returning the aircraft to a level flight condition with minimum altitude loss. Given the task at hand one could develop a NDI CLAW directly for control variables (CV) $\begin{bmatrix} V & \gamma & \mu & \beta \end{bmatrix}^T$ given control inputs $\begin{bmatrix} \delta_t & \delta_a & \delta_e & \delta_r \end{bmatrix}^T$. However, the derivation and implementation of such control law would be overly complex and would not find much practical use in piloted aircraft. Instead, a time scale separation method will be employed. This method consists of splitting the system into fast and slow dynamics and has been utilized by various different researchers such as Reference 44, 61.

Utilizing the principle of time scale separation the CLAW will consist of a fast inner rate loop (IRL), slower middle attitude loop (MAL), and still slower outer path loops (OPL). The IRL will control the aircraft rotational rates in stability axes, p_s, q, r_s. These CVs are chosen such that equations can be developed to ensure coordinated flight at the innermost and subsequently fastest loop. This practice is desirable in manned aircraft as it provides a "feet flat on the floor" pilot interaction thereby relieving pilot workload. The MAL will control velocity roll μ and aerodynamic angles α and β. Velocity roll μ is chosen as it eliminates the issue of commanding body axis roll at nonzero AOA. Further, the command channel around β will ensure sideslip is small during large maneuvers. Finally, the OPL will provide control of the flight path angle γ and velocity V.

5.1 Generalized NDI Control Law

This section defines the generalized control law architecture that is employed in the subsequent sections. Any given control loop will be comprised of reference dynamics, linear controller, and dynamic inversion components as depicted in Figure 44 where δ represents any of the available aircraft control inputs.

5.1.1 Reference Dynamics

Reference dynamics define the desired behavior the system should track. In other words this component prescribes the y_d value defined in Chapter 4. In general, the reference dynamics could be arbitrarily prescribed by the designer. However, much experience of manned flight has been amassed such that desirable flying qualities and characteristics are

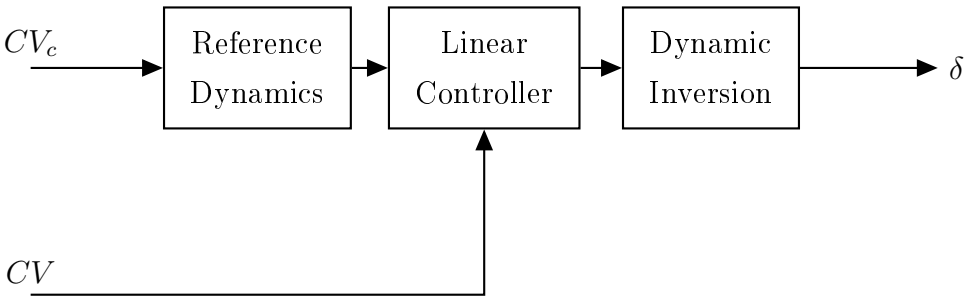

Figure 44 Controller Components

known. These characteristics as they pertain to military manned aircraft are presented in reports such as MIL-F-8785C (8785C) and standards such as MIL-STD-1797B (1797B).[48,65] The reference dynamics used herein will be either first or second order depending on requirements prescribed by 8785C. More details pertaining to specific reference models will be described in subsequent sections.

5.1.2 Linear Controllers

Proportional integral (PI) linear controllers (LC) will be employed as they sufficiently handle uncertainties in the dynamic inversion process. This choice will avoid the added complexities of alternative linear control methods such as H_∞ loop shaping or structured singular value synthesis.[66,67] Further, the reference dynamics can be integrated within the PI network as the prescribed dynamics are restricted to second order implementations. This process simplifies the architecture to be implemented in code and is described in the following subsections for both the first and second order dynamic models.

First Order Implementation

This section derives a PI network which tracks a prescribed first order response. To do this first consider a generic PI controller with proportional gain K_p and integral gain K_i as shown in Figure 45. Manipulating the architecture as depicted in Figure 46 allows the equivalent closed-loop system to be determined. Equating the prescribed first order system to the control second order system gives the relationship shown in Equation (5.1-1).

$$\frac{\omega}{s+\omega} = \frac{AK_p s + BK_i}{s^2 + K_p s + K_i} \tag{5.1-1}$$

In order for Equation (5.1-1) to hold true a pole-zero cancellation must occur as defined by

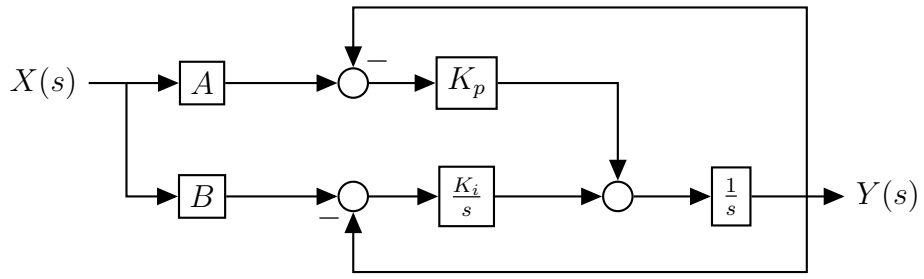

Figure 45 Generic First Order PI Architecture

Equation (5.1-2).

$$\frac{\omega(s+\omega)}{(s+\omega)^2} = \frac{AK_p s + BK_i}{s^2 + K_p s + K_i}$$
$$\therefore A = \frac{1}{2},\ B = 1,\ K_p = 2\omega,\ K_i = \omega^2 \tag{5.1-2}$$

Figure 47 depicts the final architecture.

Second Order Implementation

Similar to the development of the first order controller, a second order controller shown in Figure 48 with $K_p = 2\zeta\omega$ and $K_i = \omega^2$ can be implemented utilizing Equation (5.1-3).

$$\frac{K(s+\omega_n)\omega^2}{s^2 + K_p s + K_i} \tag{5.1-3}$$

The additional terms, K, ω_n are provided as a means to match the 8785C construct. In this application $K = \frac{1}{\omega}$ and $\omega_n = \omega$ ensure unity dc gain. Unless otherwise stated, take the damping ratio as $\zeta = \frac{\sqrt{2}}{2}$.

5.1.3 Dynamic Inversion

The inversion component consists of rigorous application of Section 4.2 for the given control path problem.

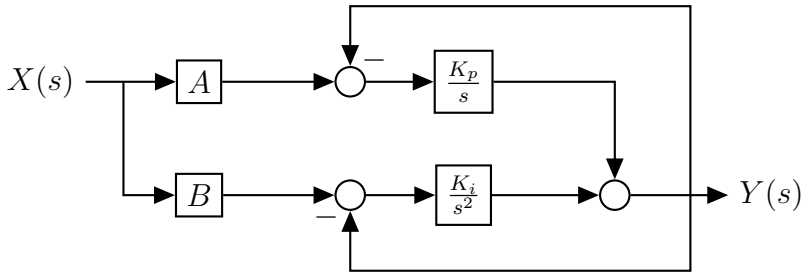

Consolidate Summing Junction

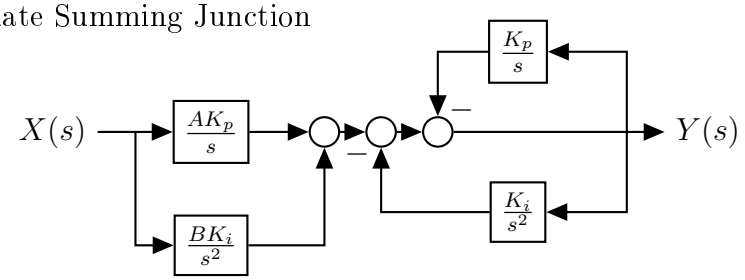

Simplify Parallel Path and Loops

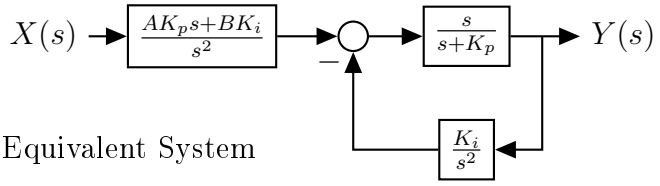

Final Equivalent System

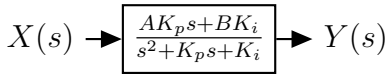

Figure 46 Generic PI Manipulation

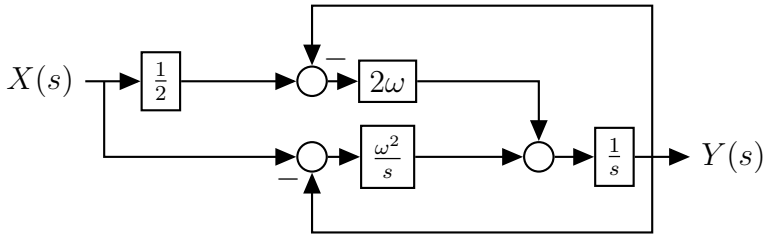

Figure 47 Integrated PI Architecture

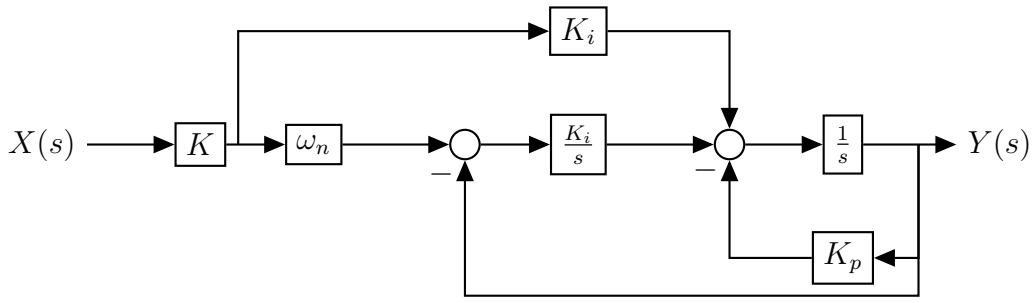

Figure 48 Generic Second Order PI Architecture

5.2 Inner Rate Loop

Though the objective is to control the stability axis angular rates, (p_s, r_s), moments are most conveniently dealt with in the body axis. With this in mind first develop the inversion control law for the body axis angular rates, p, q, r. The first step in the process is to differentiate the output function, $y = h(x) = CV$ until the input appears. Starting with Equations (2.2-5d) and (2.2-5e) it is clear the control inputs appear in the first derivative through the aerodynamic moments. For generality, subscript notation will now be used to denote the output function; superscript notation will be used to denote the degree of differentiation.

The first output function is governed by Equation (5.2-1).

$$\begin{aligned} L_f^{(1)} h_1 &= \nabla p \dot{x} \\ &= \dot{p} \\ &= \frac{I_{xz}}{I_{xx} I_{zz} - I_{xz}^2} \left(\mathcal{N} + (I_{xx} - I_{yy}) pq - I_{xz} qr \right) \\ &+ \frac{I_{zz}}{I_{xx} I_{zz} - {I_{xz}}^2} \left(\mathcal{L} + I_{xz} pq + (I_{yy} - I_{zz}) qr \right) \end{aligned} \tag{5.2-1}$$

Similarly for the second output function is governed by Equation (5.2-2).

$$\begin{aligned} L_f^{(1)} h_2 &= \nabla q \dot{x} \\ &= \dot{q} \\ &= \frac{1}{I_{yy}} \left[\mathcal{M} + I_{xz}(r^2 - p^2) + (I_{zz} - I_{xx}) rp \right] \end{aligned} \tag{5.2-2}$$

Lastly the third output function is governed by Equation (5.2-3).

$$\begin{aligned} L_f^{(1)} h_3 &= \nabla r \dot{x} \\ &= \dot{r} \\ &= \frac{I_{xx}}{I_{xx} I_{zz} - {I_{xz}}^2} \left(\mathcal{N} + \left(I_{xx} - I_{yy} \right) pq - I_{xz} qr \right) \\ &+ \frac{I_{xz}}{I_{xx} I_{zz} - {I_{xz}}^2} \left(\mathcal{L} + I_{xz} pq + \left(I_{yy} - I_{zz} \right) qr \right) \end{aligned} \tag{5.2-3}$$

Equations (5.2-1) to (5.2-3) are subsequently grouped together in order to solve for the control input resulting in the formulation defined by Equation (5.2-4). In this context $c_{1,2,3,4,5}$ provide intermediate inertia variables. State dependent dynamic values are prescribed by $f_{1,2,3}$ and have a dependence on the x subscripted $\mathcal{L}, \mathcal{M}, \mathcal{N}$. The input mapping parameters are denoted by the u subscript on $\mathcal{L}, \mathcal{M}, \mathcal{N}$.

$$\dot{y} = \begin{bmatrix} f_1 \\ f_2 \\ f_3 \end{bmatrix} + S\overline{q} \begin{bmatrix} b & 0 & 0 \\ 0 & c & 0 \\ 0 & 0 & b \end{bmatrix} \begin{bmatrix} c_2 \mathcal{N}_u + c_3 \mathcal{L}_u \\ \frac{1}{I_{yy}} \mathcal{M}_u \\ c_1 \mathcal{N}_u + c_2 \mathcal{L}_u \end{bmatrix} u$$

$$f_1 = c_2 \left(\mathcal{N}_x + c_4 \right) + c_3 \left(\mathcal{L}_x + c_5 \right)$$

$$f_2 = \frac{1}{I_{yy}} \left[\mathcal{M}_x + I_{xz}(r^2 - p^2) + (I_{zz} - I_{xx}) rp \right]$$

$$f_3 = c_1 \left(\mathcal{N}_x + c_4 \right) + c_2 \left(\mathcal{L}_x + c_5 \right)$$

where

$$\begin{aligned} c_1 &= \frac{I_{xx}}{I_{xx} I_{zz} - {I_{xz}}^2} & c_4 &= \left(I_{xx} - I_{yy} \right) pq - I_{xz} qr \\ c_2 &= \frac{I_{xz}}{I_{xx} I_{zz} - {I_{xz}}^2} & c_5 &= I_{xz} pq + \left(I_{yy} - I_{zz} \right) qr \\ c_3 &= \frac{I_{zz}}{I_{xx} I_{zz} - {I_{xz}}^2} \\ \mathcal{L}_x &= S\overline{q} b \left(C_{l,\beta} \beta + \frac{b}{2V} \left(C_{l,p} p + C_{l,r} r \right) \right) & \mathcal{L}_u &= \begin{bmatrix} C_{l,\delta_a} & C_{l,\delta_e,l} & C_{l,\delta_e,r} & C_{l,\delta_r} \end{bmatrix} \\ \mathcal{M}_x &= S\overline{q} c \left(C_{m,0} + \frac{c}{2V} C_{m,q} q \right) & \mathcal{M}_u &= \begin{bmatrix} 0 & C_{m,\delta_e,l} & C_{m,\delta_e,r} & 0 \end{bmatrix} \\ \mathcal{N}_x &= S\overline{q} b \left(C_{n,\beta} \beta + \frac{b}{2V} \left(C_{n,p} p + C_{n,r} r \right) \right) & \mathcal{N}_u &= \begin{bmatrix} C_{n,\delta_a} & C_{n,\delta_e,l} & C_{n,\delta_e,r} & C_{n,\delta_r} \end{bmatrix} \end{aligned} \tag{5.2-4}$$

The inner loop control law can be solved for from Equation (5.2-4) noting that it follows the form of Equation (4.2-6a). The control effectiveness matrix present in Equation (5.2-4) is not square; thus, the pseudo-inverse will be utilized as defined by Equation (4.3-18).

$$\begin{bmatrix}\delta_a\\ \delta_e\\ \delta_r\end{bmatrix} = \frac{1}{S\overline{q}}\left\{\begin{bmatrix}b & 0 & 0\\ 0 & c & 0\\ 0 & 0 & b\end{bmatrix}\begin{bmatrix}c_2\mathcal{N}_u + c_3\mathcal{L}_u\\ \frac{1}{I_{yy}}\mathcal{M}_u\\ c_1\mathcal{N}_u + c_2\mathcal{L}_u\end{bmatrix}\right\}^{-1} \cdot \left\{\begin{bmatrix}\nu_{\dot{p}}\\ \nu_{\dot{q}}\\ \nu_{\dot{r}}\end{bmatrix} + \begin{bmatrix}\dot{p}_d\\ \dot{q}_d\\ \dot{r}_d\end{bmatrix} - \begin{bmatrix}f_1\\ f_2\\ f_3\end{bmatrix}\right\} \tag{5.2-5}$$

In Equation (5.2-5) the virtual inputs $\nu_{\dot{p}}, \nu_{\dot{q}}, \nu_{\dot{r}}$ are the time rate of change of the angular rates. At this juncture it is convenient to utilize the rotation matrix R_α that relates the body axis rates p, q, r and the stability axis rates, p_s, q, r_s. Utilizing this relationship the control algorithm can be developed in the chosen stability axis and then transformed into the required body axis commands for the inversion implemented by Equation (5.2-5). This high level architecture is presented in Figure 49 where *snsr* refers to the measured sensor values in the feedback loop. Note that *LC* in Figure 49 includes the command derivative feed-forward term.

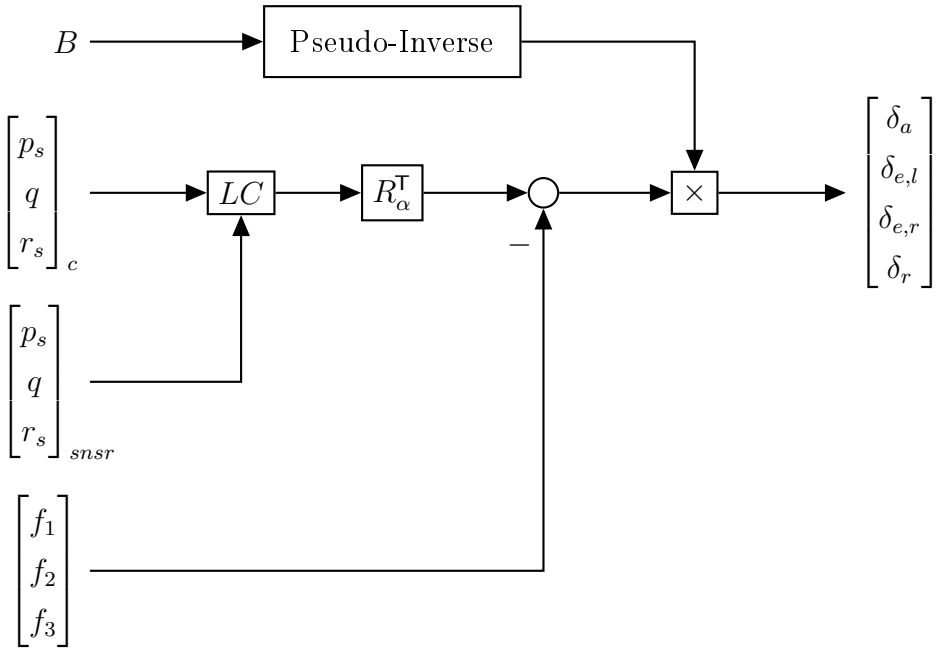

Figure 49 IRL Overview

Specifications defined by MIL-F-8785C will be used to determine a suitable ω_n for the IRL. The recommended dynamic characteristics prescribed by 8785C are first order roll, and second order for pitch and yaw. However, the yaw axis will be implemented as first order

as there will be no exposed control input for sideslip as the design goal for the yaw axis is simply to minimize deviations from zero.

5.2.1 MIL-F-8785C Requirements

The specifications defined in 8785C are provided for multiple classes of aircraft over different categories of flight. The six aircraft classes are presented in Table 6. The three flight phases are briefly introduced in Table 7. Some specifications, such as roll performance, are based on the aircraft speed range. The speed range definitions are presented in Table 8 where VL defines very low, L defines low, M for medium, and H for high. Levels 1, 2, and 3 presented in Table 8 refer to flying qualities based on the Cooper-Harper Scale, such that Level 1 is always desired.

Table 6 Air Vehicle Classes

Class	Description
I	small and light
II	medium weight, low-to-medium maneuverability
III	large, heavy, low-to-medium maneuverability
IV	high maneuverability (fighter)
V	rotorcraft
VI	V/STOL

Table 7 Flight Phases

Category	Description
A	rapid maneuvering with precise tracking
B	gradual maneuvers without precise tracking
C	gradual maneuvers with accurate flight path control

Table 8 Speed Ranges

Speed Range	Level 1	Level 2 & 3
VL	$V_{o,min} \leq V < V_{min} + 20\text{KTS}$	$V_{min} \leq V < V_{min} + 20\text{KTS}$
L	$V_{min} + 20\text{KTS} \leq V < 1.4V_{o,min}$	$V_{min} + 20\text{KTS} \leq V < 1.4V_{min}$
M	$1.4V_{o,min} \leq V < 0.7V_{max}$	$1.4V_{min} \leq V < 0.7V_{max}$
H	$0.7V_{max} \leq V \leq V_{o,max}$	$0.7V_{max} \leq V \leq V_{o,max}$

To carry out the design for the HARV aircraft a minimum speed of $V_{min} = 1.1V_{stall} = 0.18\,\text{Mach}$ is assumed where V_{stall} is defined as $\sqrt{\frac{2W}{\rho S C_{L,max}}}$. The factor of 1.1 is seemingly arbitrary and was chosen as no public source of information defining V speeds for the F-18 was found that did not introduce unnecessary complexities with further assumptions about aircraft configuration. Note that the aerodynamic model utilized does not incorporate flaps which would most likely be utilized at airspeeds this low. The maximum speed is assumed to be $V_{max} = 0.7\text{Mach}$ as this represents the flight envelope used by the HARV.[7] Under these assumptions along with Level 1 handling characteristics the speed ranges in Table 9 are utilized with a constant reference altitude of 1000 ft.

Table 9 Speed Range at 1000 ft

Speed Range	LOW (Mach)	HIGH (Mach)
VL	0.2002	0.2306
L	0.2306	0.2803
M	0.2803	0.4900
H	0.4900	0.7000

Roll Axis Requirements

The requirements provided by 8785C for the first order roll response are the time constant and the time to bank. The maximum roll mode time constants are presented in Table 10. Table 11 presents the time to bank requirements for different phases of flight and speed ranges. In Table 11 category A flight has requirements for $30, 50, 90$ degree changes while categories B and C have single requirements for 90 and 30 degrees, respectively. Utilizing Tables 10 and 11 required accelerations that can be determined which will aid in the design process.

Table 10 Maximum Roll Mode Time Constant (seconds)

Flight Phase	Class	Level 1	Level 2	Level 3
A	I, IV	1.0	1.4	10
A	II, III	1.4	3.0	10
B	all	1.4	3.0	10
C	I, II, IV	1.0	1.4	10
C	III	1.4	3.0	10

Table 11 Time To Bank Requirements (seconds)

Level	Speed Range	Category A			Category B	Category C
		30	50	90	90	30
1	VL	1.1			2.0	1.1
	L	1.1			1.7	1.1
	M	1.1		1.3	1.7	1.1
	H	1.1	1.1		1.7	1.1
2	VL	1.6			2.8	1.3
	L	1.5			2.5	1.3
	M			1.7	2.5	1.3
	H		1.3		2.5	1.3
3	VL	2.6			3.7	2.0
	L	2.0			3.4	2.0
	M			2.6	3.4	2.0
	H		2.6		3.4	2.0

Pitch Axis Requirements

Longitudinally 8785C gives various different requirements in order to cover a multitude of different aircraft types, operational missions, and flight regimes. In this research the second order equivalent system is used as prescribed by Equation (5.2-6).

$$\frac{q}{\delta} = \frac{K_q(s + 1/T_q)}{s^2 + 2\zeta\omega s + \omega^2} \tag{5.2-6}$$

The short period requirements considered are $\omega \geq 1\,\text{rad/s}$ and $0.35 \geq \zeta \geq 1.3$; thus, the choice of $\zeta = \frac{\sqrt{2}}{2}$ is sufficient. Furthermore, the bandwidth (ω) of the longitudinal axis will be made to match the roll/yaw axes. This approach will simplify the design process by only considering the more demanding and coupled roll maneuvers.

Yaw Axis Requirements

Though 8785C provides requirements for the yaw axis, these are not considered. Instead the yaw axis is matched with the roll axis. The rationale for this simplistic design is that during spin recovery sideslip is regulated to zero; thus, desirable response dynamics to pilot inputs can be neglected.

5.2.2 Required Accelerations

In this section the required accelerations to perform maneuvers in accordance with 8785C are determined. Consider a coordinated roll maneuver about the velocity vector with zero sideslip and constant angle-of-attack and velocity. This maneuver is preferred over rolling about the aircraft body axis as doing so would induce sideslip for nonzero angle-of-attack. Additionally, this maneuver requires nonzero pitch and yaw accelerations; thus, limitations of the off axis controls will be considered. The analysis for this maneuver is presented below adapted from Reference 68.

During a velocity vector roll the wind and stability axis coincide; thus, consider the stability axis to be the reference where moments are calculated. Consider the wind-stability axis equations given by Reference 50 presented here in Equation (5.2-7).

$$\begin{aligned}
\dot{\mu} &= p_w + (q_w \sin\mu + r_w \cos\mu)\tan\gamma \\
\dot{\gamma} &= q_w \cos\mu - r_w \sin\mu \\
\dot{\chi} &= (q_w \sin\mu + r_w \cos\mu)\sec\gamma \\
m\dot{V} &= T_{x,w} - D - mg\sin\gamma
\end{aligned} \tag{5.2-7a}$$

$$
\begin{aligned}
mVr_w &= T_{y,w} - C + mg\cos\gamma\sin\mu \qquad (5.2\text{-}7b)\\
-mVq_w &= T_{z,w} - L + mg\cos\gamma\cos\mu\\
L_w &= I_{xx}\dot{p}_w - I_{xz}(\dot{r}_w + p_w q_w) - (I_{yy} - I_{zz})q_w r_w\\
M_w &= I_{yy}\dot{q}_w - I_{xz}(r_w^2 - p_w^2) - (I_{zz} - I_{xx})r_w p_w \qquad (5.2\text{-}7c)\\
N_w &= I_{zz}\dot{r}_w - I_{xz}(\dot{p}_w - q_w r_w) - (I_{xx} - I_{yy})p_w q_w
\end{aligned}
$$

In Equation (5.2-7) the inertia parameters $I_{xx}, I_{yy}, I_{zz}, I_{xz}$ refer to elements of the stability axis inertia tensor, I_s and are derived from the body axis inertias using the body to stability rotation matrix defined in Equation (5.2-8).

$$I_s = R_\alpha I_b R_\alpha^{\mathsf{T}} \qquad (5.2\text{-}8)$$

In Equation (5.2-7) the thrust components are given as a function of the body axis thrust using the body to wind transformation relationship, $T_w = R_{w,b}T$.

$$
\begin{aligned}
T_{x,w} &= T\cos\alpha\cos\beta\\
T_{y,w} &= -T\cos\alpha\sin\beta \qquad (5.2\text{-}9)\\
T_{z,w} &= -T\sin\alpha
\end{aligned}
$$

Furthermore, to clarify the wind axis aerodynamic contributions used, D, C, L, as a function of the stability axis aerodynamic data provided, are given by Equation (5.2-10).

$$\begin{bmatrix} D \\ C \\ L \end{bmatrix} = R_{w,s} \begin{bmatrix} D \\ Y \\ L \end{bmatrix} \qquad (5.2\text{-}10)$$

The requirement for the roll axis is given as a first order roll response with time constant τ_r provided a step rolling moment input δ_R with magnitude p_c. This requirement is presented in the Laplace domain in Equation (5.2-11).

$$p_w(s) = \frac{1}{\tau_r s + 1}\frac{p_c}{s} \qquad (5.2\text{-}11)$$

Taking the inverse Laplace transformation the time response is obtained assuming an initial condition of zero.

$$p_w(t) = p_c(1 - e^{-t/\tau_r}) \qquad (5.2\text{-}12)$$

Differentiating Equation (5.2-12) yields the roll acceleration defined in Equation (5.2-13).

$$\dot{p}_w = -\frac{p_w(t)}{\tau_r} + p_c\frac{\delta_R}{\tau_r} \qquad (5.2\text{-}13)$$

Assume the maneuver is carried out with α, V constant and $\beta = 0$. Additionally, assume the combined aerodynamic and thrust force Z_w along the z_w direction is constant such that $Z_w = T_{z,w} - L = -n_{z,w} \times \text{weight}$. Provided $\beta = 0$ the sideforce is zero, $C = T_{y,w} = 0$. Utilizing the Y_w, Z_w force equations q_w, r_w can be solved such that combined forces $Y_w = 0$ and $Z_w = \text{constant}$.

$$q_w(t) = -\frac{Z_w + mg\cos\gamma(t)\cos\mu(t)}{mV} \tag{5.2-14}$$

$$r_w(t) = \frac{mg\cos\gamma(t)\sin\mu(t)}{mV} \tag{5.2-15}$$

Differentiating Equations (5.2-14) to (5.2-15) the accelerations are obtained.

$$\dot{q}_w = \frac{g\left(\cos\gamma(t)\sin\mu(t)\dot{\mu} + \sin\gamma(t)\cos\mu(t)\dot{\gamma}\right)}{V} \tag{5.2-16}$$

$$\dot{r}_w = \frac{g\left(\cos\gamma(t)\cos\mu(t)\dot{\mu} - \sin\gamma(t)\sin\mu(t)\dot{\gamma}\right)}{V} \tag{5.2-17}$$

Thus the total angular acceleration in wind axis is known and from it the required aerodynamic moments can be determined. However, in order to evolve q_w, r_w the wind axis Euler angles μ, γ also need to be considered. Substituting Equation (5.2-15) into Equation (5.2-7a) yields the angular rate formulations necessary to propagate μ, γ with time.

$$\dot{\mu} = p_w(t) - \frac{Z_w\sin\mu(t)\tan\gamma(t)}{mV} \tag{5.2-18}$$

$$\dot{\gamma} = -\frac{Z_w\cos\mu(t) + mg\cos\gamma(t)}{mV} \tag{5.2-19}$$

Lastly, derive a relationship between the time to bank requirements and the roll mode time constant in order to calculate the required roll rate step command. Assume the bank angle of interest is a single integration of the roll rate such that a change in the bank angle can be represented by Equation (5.2-20).

$$\begin{aligned}\Delta\mu = \mu(T) - \mu(0) &= \int_0^T p_w\, dt \\ &= p_{w,c}T + p_{w,c}\tau_r e^{-T/\tau_r} + C\end{aligned} \tag{5.2-20}$$

Taking $\mu(0) = 0$ the integration constant is determined as $C = -\tau_r p_{w,c}$.

$$\Delta\mu = p_{w,c}T - p_{w,c}\tau_r(1 - e^{-T/\tau_r}) \tag{5.2-21}$$

Solving for the step command magnitude results in Equation (5.2-22).

$$p_{w,c} = \frac{\Delta\mu}{T - \tau_r(1 - e^{-T/\tau_r})} \tag{5.2-22}$$

The set of five nonlinear relationships, Equations (5.2-13) and (5.2-16) to (5.2-19), can be integrated subject to the roll rate step command defined by Equation (5.2-22).

5.2.3 Roll Axis Design

Utilizing the set of equations developed in Section 5.2.2 the required accelerations were evaluated for all speed ranges and flight categories. To simplify the analysis the maximum roll mode time constant for category B was also taken to be $\tau_r = 1.0\,\text{s}$. The design speed for each speed range was the lower value. Table 12 presents the required accelerations as a percent of the maximum available acceleration in the required direction. A value of one in Table 12 would suggest that the required acceleration is on the surfaces of the AMS, values greater than one highlighted in red exceed the physical limitations of the aircraft.

For each flight level, category C had the most acceleration demand. These three conditions are presented in Figures 50 to 52. In the VL and L speed ranges the demands exceed the aircraft capabilities. However, this nuance is attributed to the following items. First, the aerodynamic model available did not include tables for the leading/trailing edge flaps thereby increasing the trim angle-of-attack at these lower speeds. Secondly, this analysis has been done for the ideal velocity vector roll (VVR), whereas the roll requirement specified in 8785C generally refers to a change in bank. That is to say the aircraft does not need to maintain zero sideslip throughout the maneuver. While the VVR is an ideal roll maneuver, at higher α more yaw control is required due to the transformation between the body and wind axes. As can be seen in Figures 50 to 52, the yaw axis control power is the only axis exceeding the physical limits.

Table 12 Required Roll Accelerations as Percent of Available Acceleration, τ_r = 1.0 s

Level	Speed Range	Category A			Category B	Category C
		30	50	90	90	30
1	VL	3.34			3.82	3.34
	L	1.18			1.74	1.18
	M	0.51		1.15	0.75	0.51
	H	0.09	0.15		0.14	0.09
2	VL	1.80			2.33	2.53
	L	0.71			0.97	0.89
	M			0.75	0.42	0.38
	H		0.12		0.08	0.07
3	VL	0.86			0.63	0.45
	L	0.45			0.33	0.11
	M			0.39	0.27	0.19
	H		0.04		0.05	0.04

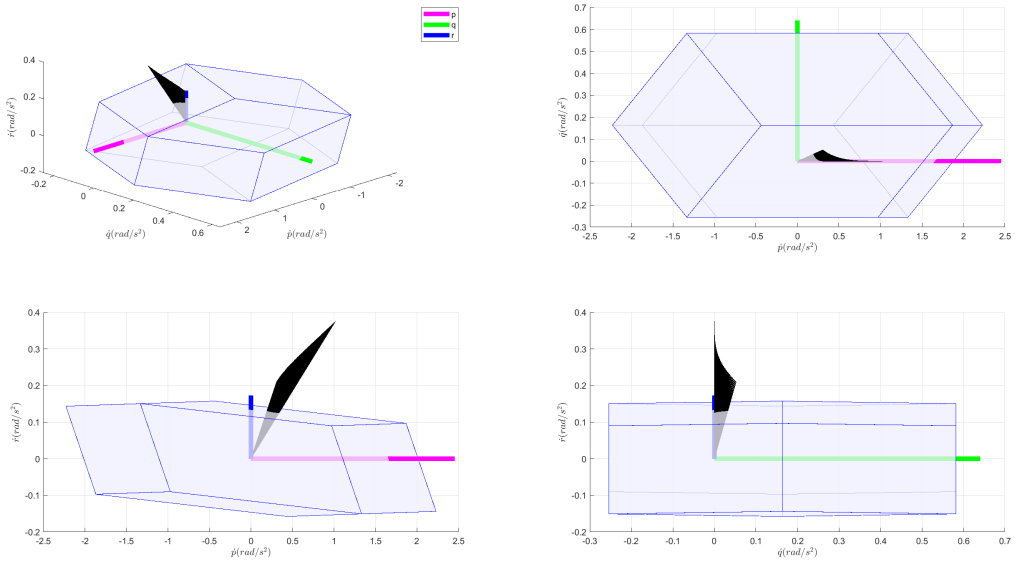

Figure 50 VVR AMS, Level 1, Category C, Speed Range VL

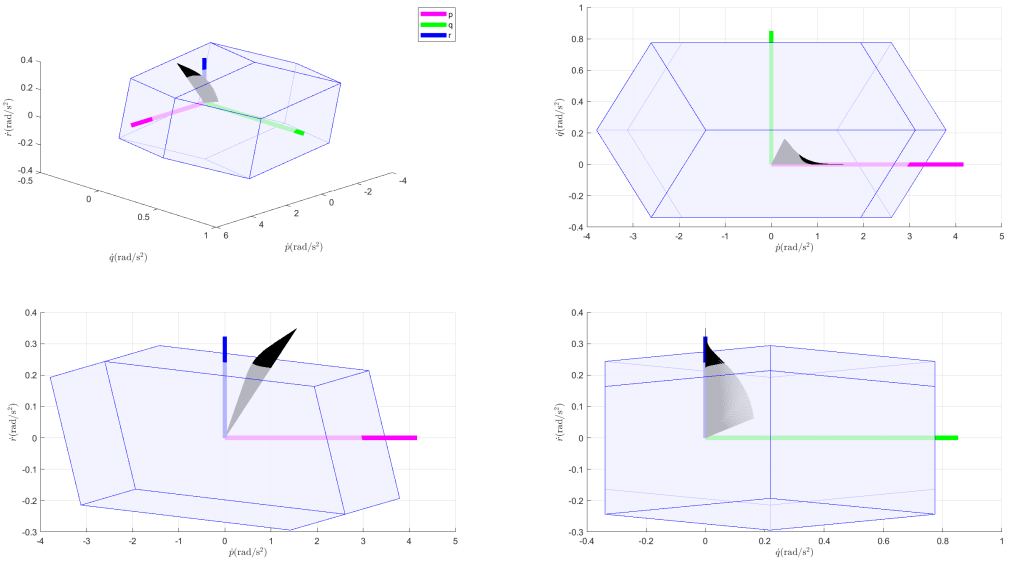

Figure 51 VVR AMS, Level 1, Category B, Speed Range L

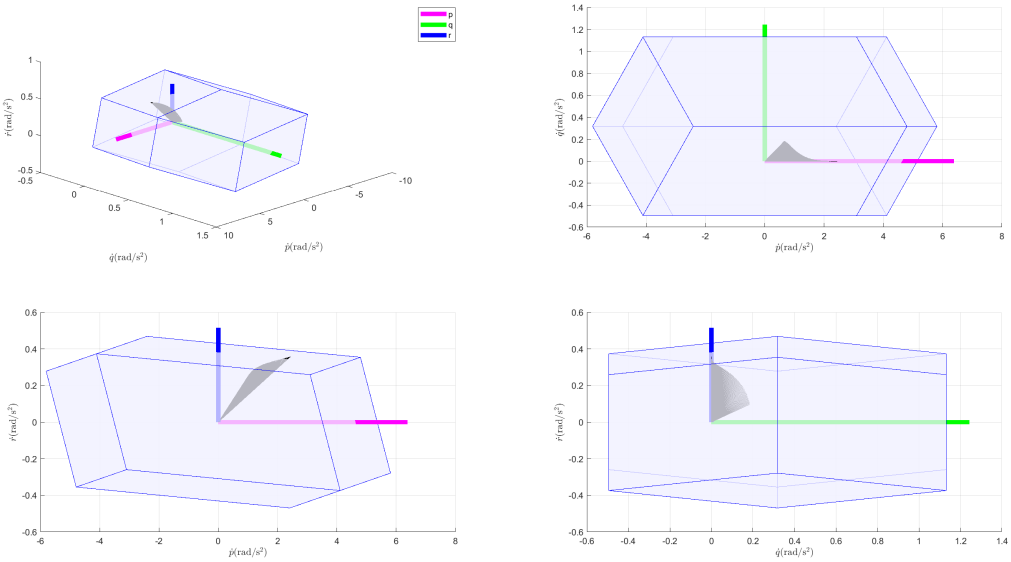

Figure 52 VVR AMS, Level 1, Category A, Speed Range M

The knowledge gained from performing the VVR analysis can now be leveraged to finalize the design of the IRL. Specifically, the goal is to design the IRL such that the actuators do not become rate/position limited as doing so will induce limit cycling and the controller may

Table 13 VL $p_{w,c}$ Step Limits

Mach	$p_{w,c}$ Step (deg/s)	$T_{\Delta\mu,90}$ (sec)
0.2000	20.75	5.333
0.2306	58.66	2.4479
0.2601	102.04	1.6992
0.2803	136.09	1.4195
0.4900	745.56	0.5351
0.3766	81.84	1.2994
0.4900	149.14	0.7998
0.7000	382.71	0.4093

become unstable. Furthermore, outer attitude control loops will be designed which require the IRL to have near perfect tracking. Thus, the aim is to determine the IRL bandwidth as a schedule of dynamic pressure.

Instead of determining a slower bandwidth for the VL IRL, a limit on the maximum roll rate step size was initially investigated. Utilizing a bisection search method the maximum roll rate step command was determined for the lower and upper speeds and is presented along with the corresponding time-to-bank 90° in Table 13. In a similar fashion, determine the Mach numbers at which the aircraft is able to achieve the 8785C requirements without alterations. This process was carried out for the three Level 1 T_{90} requirements with two different time constants. The first is the maximum time constant defined in 8785C; the second is the recommended time constant for fighter aircraft presented in Reference 42 . The results are presented in Table 14. These results present a large disparity between the initial design speed ranges and what is physically required for the ideal roll performance.

Referring back to Table 9 note that the minimum Mach to achieve the VL T_{90} falls into the M speed range. Thus limits on τ_r should be imposed for Mach < 0.2601 to ensure degraded responses aren't obtained. Additionally, as a higher bandwidth is desirable, τ_r will be transitioned to 0.2 once Mach ≥ 0.3766. This value is chosen as transitioning at a lower Mach would result in failure to achieve Level 1 handling. To summarize Table 15 presents the proposed scheduling to be implemented.

Testing of command limiting did not prove adequate, especially when outer loops were

Table 14 Minimum Mach and Step Magnitude for T_{90} Requirements

τ_r (sec)	Speed Range	T_{90} (sec)	Minimum Mach	Step Cmd (deg/s)
1.0	VL	2.0	0.2471	79.2717
	L	1.7	0.2601	101.9618
	M	1.3	0.2910	157.1965
0.2	VL	2.0	0.3287	49.9997
	L	1.7	0.3454	59.9984
	M	1.3	0.3766	81.7958

Table 15 IRL τ_r and Limit Schedule

$\overline{q}$ (lb/ft^2)	τ_r (sec)	Max $\dot{p}_{w,c}$ (deg/s^2)
57.1439	1.0	20.75
75.9677	1.0	58.66
96.6475	1.0	102.04
112.2422	1.0	136.09
202.6146	0.2	81.84
343.0064	0.2	149.14
700.0131	0.2	382.71

incorporated. As a result, the command limiting implementation was discarded. In part this deficiency is justified by the simplified aerodynamic model that did not provide flap surfaces that would be available at low speeds. Subsequently all performance based testing was done at a minimum of Mach 0.25.

5.2.4 Turn Compensation

Utilizing an innermost rate based control loop allows for turn compensation to be directly integrated.[42] This component ensures sideslip is minimized during rolling maneuvers and assists in maintaining wing loading by adding pitch and yaw rate commands. Though the MAL will include a control path that ensures zero steady state sideslip, the compensation at the innermost rate loop will begin to respond as soon as a rolling maneuver is initiated resulting in better flight characteristics.

Equation (5.2-24) defines the turn compensation component for the pitch axis and consists of two parts. The first component consists of the direction cosine between the gravity vector and the body z-axis. This contribution accounts for the change in pitch rate necessary to avoid a change in the normal acceleration subject to a nominal 1g flight condition and is defined by Equation (5.2-23a). The second component accounts for the change in pitch rate necessary to avoid a change in normal acceleration due to sideslip and is defined by Equation (5.2-23b).

$$\frac{g}{u}\cos\theta(1-\cos\varphi) \tag{5.2-23a}$$

$$p\frac{v}{u} \tag{5.2-23b}$$

$$q_{turn} = \frac{g}{u}\cos\theta(1-\cos\varphi) + p\frac{v}{u} \tag{5.2-24}$$

Equation (5.2-26) defines the turn compensation for the yaw axis and consists of three components given by Equations (5.2-25a) to (5.2-25c) that account for deviations in sideslip, the gravity direction cosine, and an integrator on nonzero lateral accelerations, respectively.

$$\beta K_\beta \tag{5.2-25a}$$

$$\frac{g}{V}\cos\theta\sin\varphi \tag{5.2-25b}$$

$$a_y K_{ay}\frac{g}{V}\frac{1}{s} \tag{5.2-25c}$$

$$r_{turn} = \beta K_\beta + \frac{g}{V}\left(\cos\theta\sin\varphi - \frac{a_y K_{ay}}{s}\right) \tag{5.2-26}$$

5.2.5 Implementation Summary

A block diagram overview of the implementation is presented in Figure 53. All three axes use the same bandwidth schedule that transitions from slow to fast dynamics as a function of dynamic pressure. In order to ensure smooth operation a low pass filter is used on ω_{IRL} as it transitions from the low speed to high speed value. In Figure 53 $PINV$ refers to the pseudo-inverse introduced in Equation (4.3-18). The input commands, $p_{s,c}, q_c, r_{s,c}$ are the commands that have included turn compensation. Namely,

$$p_{s,c} = p_{s,cmd} \tag{5.2-27a}$$

$$q_c = q_{cmd} + q_{turn} \tag{5.2-27b}$$

$$r_{s,c} = r_{s,cmd} + r_{turn} \tag{5.2-27c}$$

where the *cmd* values source from the middle attitude loop. Step and doublet command simulations were executed for the roll and pitch axes at the low speed Mach condition. The results are presented in Appendix B.1. The imperfect tracking is a result of including the actuator dynamics and nonlinearities in simulation. Figures 129 and 131 demonstrate that with ideal actuators the nonlinear inversion provides perfect tracking.

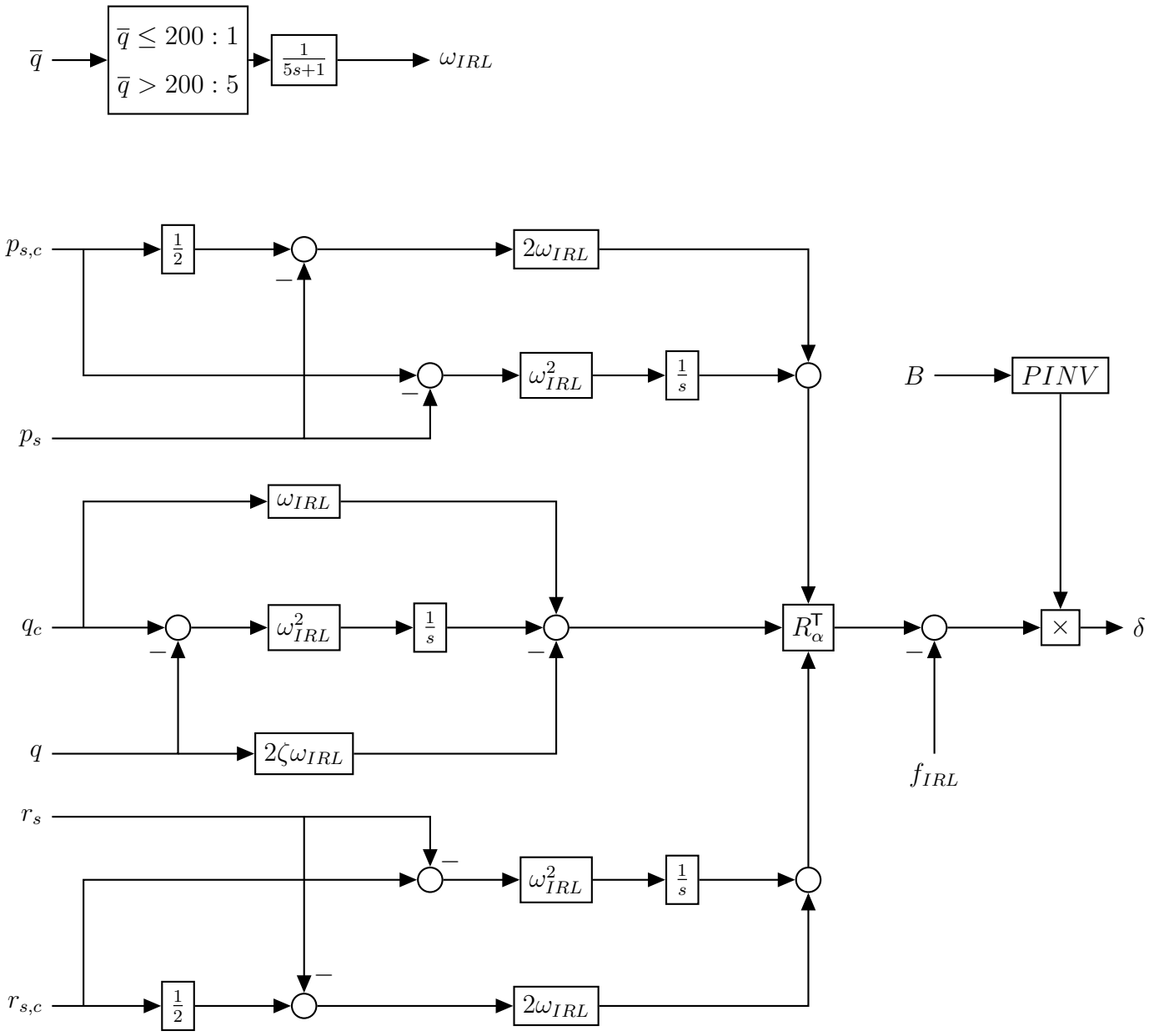

Figure 53 IRL Implementation

5.3 Middle Attitude Loop

The middle attitude control loop will generate the angular rate commands required by the IRL. The chosen CV are $\begin{bmatrix}\mu & \alpha & \beta\end{bmatrix}$. These CVs will enable another control loop to provide control over γ and maintain level coordinated flight.

In order to derive the control equations for the MAL first introduce the equation for stability axis roll rate.[50]

$$\dot{\mu} = p_w + (q_w \sin\mu + r_w \cos\mu)\tan\gamma \tag{5.3-1}$$

Considering Equations (2.2-5b), (2.2-5c) and (5.3-1) it is clear the following decomposition can be made.

$$\begin{bmatrix}\dot{\beta}\\ \dot{\alpha}\\ \dot{\mu}\end{bmatrix} = \begin{bmatrix}f_\beta\\ f_\alpha\\ f_\mu\end{bmatrix} + G\begin{bmatrix}p_s\\ q\\ r_s\end{bmatrix} \tag{5.3-2}$$

Utilizing Equation (5.3-2) it will be possible to perform an inversion that produces the necessary commands for the IRL.

In order to make this process more clear components from the governing equations can be substituted.

$$\begin{aligned}\begin{bmatrix}\dot{\beta}\\ \dot{\alpha}\\ \dot{\mu}\end{bmatrix} &= \begin{bmatrix}r_w - r_s\\ q - p_s\tan\beta - q_w\sec\beta\\ p_s\cos\beta + (q-\dot{\alpha})\sin\beta + (q_w\sin\mu + r_w\cos\mu)\tan\gamma\end{bmatrix}\\ &= \begin{bmatrix}r_w\\ -q_w\sec\beta\\ -\dot{\alpha}\sin\beta + (q_w\sin\mu + r_w\cos\mu)\tan\gamma\end{bmatrix} + \begin{bmatrix}0 & 0 & -1\\ -\tan\beta & 1 & 0\\ \cos\beta & \sin\beta & 0\end{bmatrix}\begin{bmatrix}p_s\\ q\\ r_s\end{bmatrix}\\ &= \begin{bmatrix}f_\beta\\ f_\alpha\\ f_\mu\end{bmatrix} + G\begin{bmatrix}p_s\\ q\\ r_s\end{bmatrix}\end{aligned} \tag{5.3-3}$$

Equation (5.3-3) can now be inverted with the introduction of the virtual control inputs thereby providing tracking control as follows.

$$\begin{bmatrix}p_s\\ q\\ r_s\end{bmatrix} = \begin{bmatrix}0 & 0 & -1\\ -\tan\beta & 1 & 0\\ \cos\beta & \sin\beta & 0\end{bmatrix}^{-1}\left\{\begin{bmatrix}\nu_{\dot{\beta}}\\ \nu_{\dot{\alpha}}\\ \nu_{\dot{\mu}}\end{bmatrix} + \begin{bmatrix}\dot{\beta}_d\\ \dot{\alpha}_d\\ \dot{\mu}_d\end{bmatrix} - \begin{bmatrix}f_\beta\\ f_\alpha\\ f_\mu\end{bmatrix}\right\} \tag{5.3-4}$$

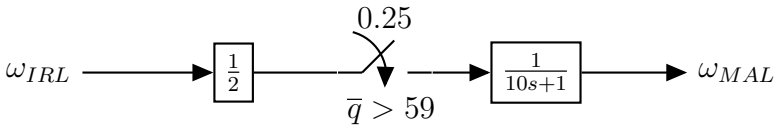

Figure 54 MAL Bandwidth Implementation

In the same manner as the IRL, the virtual control inputs are an output of the desired reference dynamics. As the MAL is placed in sequence with the IRL, the bandwidth must be slower than the IRL. Doing so will ensure the IRL can track the commands with sufficient accuracy. This sequencing is accomplished by a time scale separation as depicted in Figure 54. An additional lag was also placed on ω_{MAL} with a time constant double that of the IRL lag in order to ensure the MAL dynamics do not change too rapidly. Lastly, an empirically determined minimum value of $\omega_{MAL} = 0.25\,\text{rad/s}$ was imposed for all, $\overline{q} \leq 59\,\text{lbf/ft}^2$. This condition was empirically determined and was shown to ensure quality tracking at lower velocities.

The reference dynamics for the MAL are all first order. Though 8785C does not specify a first order α response, the smaller rise time will aid the yet to be closed γ control loop. The first order model on β was chosen so that the efforts between the roll/yaw axis are matched.

Step and doublet commands were simulated for α, μ at the low speed Mach condition. The results of these simulations are presented in Appendix B.2. The imperfect tracking is a result of two items. First the IRL does not provide perfect tracking due to nonlinearities in the actuator dynamics. Second, at the low speed condition, the time scale separation between the MAL and IRL is minimal such that there is a significant disparity between the MAL command to the IRL and the reference dynamics of the IRL (irl_pc and irl_p_rc respectively in Figure 135. Perfect tracking is demonstrated in Figure 136 by using ideal actuators and canceling the IRL reference dynamics; however, the required control surface deflections are not physically realizable as seen in Figure 137.

5.4 Outer Path Loop

The outer path loop is the outermost control loop which provides tracking of airspeed and flight path angle. The flight path angle is controlled via α and the MAL whereas airspeed is controlled directly through thrust (δ_t). The development of the OPL is based on

the split kinematic / aerodynamic approach presented in Reference 61 . The derivation that follows is done so without the influence of external winds, such that the kinematic frame coincides with the wind axis.

In this frame the ground speed velocity vector is defined by Equation (5.4-1).

$$V_k = \begin{bmatrix} V_g \\ 0 \\ 0 \end{bmatrix} \tag{5.4-1}$$

As shown in Reference 61 the ground speed velocity vector can be differentiated and set equal to the aerodynamic forces as follows.

$$\frac{dV_k}{dt} = \frac{\partial V_k}{\partial t} + \Omega_{ke}^k \times V = \begin{bmatrix} \dot{V}_g \\ 0 \\ 0 \end{bmatrix} + \Omega_{ke}^k \times \begin{bmatrix} V_g \\ 0 \\ 0 \end{bmatrix} \tag{5.4-2a}$$

$$= \frac{1}{m} \begin{bmatrix} 1 & 0 & 0 \\ 0 & \cos\mu & -\sin\mu \\ 0 & \sin\mu & \cos\mu \end{bmatrix} F_{aero} + R_{k,e} \begin{bmatrix} 0 \\ 0 \\ g \end{bmatrix} \tag{5.4-2b}$$

To reiterate the aerodynamic forces presented in Equation (5.4-2) are the wind axis forces. The μ rotation matrix translates the wind axis forces to the kinematic frame. Similarly, $R_{k,e}$ is the transformation matrix between the Earth-fixed to the kinematic frame and is defined as follows.

$$R_{k,e} = \begin{bmatrix} \cos\gamma & 0 & -\sin\gamma \\ 0 & 1 & 0 \\ \sin\gamma & 0 & \cos\gamma \end{bmatrix} \begin{bmatrix} \cos\chi & \sin\chi & 0 \\ -\sin\chi & \cos\chi & 0 \\ 0 & 0 & 1 \end{bmatrix} \tag{5.4-3}$$

The term, Ω_{ke}^e represents the angular rotation of the kinematic reference frame with respect to the Earth frame and is defined by Equation (5.4-4).

$$\Omega_{ke}^k = \begin{bmatrix} -\dot{\chi}\sin\gamma \\ \dot{\gamma} \\ \dot{\chi}\cos\gamma \end{bmatrix} \tag{5.4-4}$$

Utilizing Equations (5.4-3) and (5.4-4) the ground speed velocity vector relationship can be rewritten as follows where the k subscript has been dropped and F_A refers to the

aerodynamic forces.

$$\frac{dV_k}{dt} = \begin{bmatrix} \dot{V}_g \\ \dot{\chi} V_g \cos\gamma \\ -\dot{\gamma} V_g \end{bmatrix} = \frac{1}{m} \begin{bmatrix} 1 & 0 & 0 \\ 0 & \cos\mu & -\sin\mu \\ 0 & \sin\mu & \cos\mu \end{bmatrix} \begin{bmatrix} F_{A,x} \\ F_{A,y} \\ F_{A,z} \end{bmatrix} + \begin{bmatrix} -g\sin\gamma \\ 0 \\ g\cos\gamma \end{bmatrix} \tag{5.4-5}$$

Isolating the derivatives as shown in Equation (5.4-6).

$$\dot{V}_g = \frac{1}{m} F_{A,x} - g\sin\gamma \tag{5.4-6a}$$

$$\dot{\chi} = \frac{1}{mV_g\cos\gamma} \left(F_{A,y}\cos\mu - F_{A,z}\sin\mu\right) \tag{5.4-6b}$$

$$\dot{\gamma} = \frac{-1}{mV_g} \left(F_{A,y}\sin\mu + F_{A,z}\cos\mu\right) - \frac{g\cos\gamma}{V_g} \tag{5.4-6c}$$

Rewriting Equations (5.4-6b) and (5.4-6c) in terms of the horizontal and vertical forces.

$$\begin{aligned} F_{horizontal} &= mV_g\dot{\chi}\cos\gamma \\ F_{vertical} &= mV_g(\dot{\gamma} + \frac{g}{V_g}\cos\gamma) \end{aligned} \tag{5.4-7}$$

The total force required has the magnitude of Equation (5.4-8).

$$|F_{required}| = \sqrt{F_{horizontal}^2 + F_{vertical}^2} \tag{5.4-8}$$

At this juncture it is necessary to use the required forces to solve for the axial and vertical aerodynamic forces as this will facilitate the required thrust and lift to be determined. With this information the throttle position δ_t and angle-of-attack α will be known. From Equation (5.4-6a) it is clear the axial force command is governed by Equation (5.4-9).

$$F_{Ax,c} = m(\dot{V}_g + g\sin\gamma) \tag{5.4-9}$$

To consider the vertical aerodynamic command consider the case with zero sideforce as the IRL/MAL controllers will ensure sideslip is nearly zero at all times. Under this assumption $F_{A,z}$ will be the negative of $|F_{required}|$ (negative to ensure proper sign convention), the vertical aerodynamic command is given by Equation (5.4-10).

$$F_{Az,c} = -m\cos\gamma\sqrt{(V_g\dot{\chi})^2 + \left(g + \frac{V_g\dot{\gamma}}{\cos\gamma}\right)^2} \tag{5.4-10}$$

Aside from being sufficiently accurate for this application, neglecting the sideforce ensures the value to be square-rooted is always positive. Equations (5.4-9) and (5.4-10) provide the

required forces in the wind axis system, and now it is required to implement a controller that will generate the corresponding δ_t, α to attain these values. Unlike the inner control loops, analytical inversion of the control variables is not possible due to α being a lookup table parameter. In order to overcome this obstacle a Newton solver can be used to find the optimum control set as presented in Figure 55.

While the required forces (commands) are defined by Equations (5.4-9) and (5.4-10), the feedback forces are given by Equation (5.4-11); these account for the current iteration of α, δ_t. The Jacobian required by the Newton solver is numerically calculated using central differencing of Equation (5.4-11) with respect to α, δ_t.

$$\begin{bmatrix} F_{Ax} \\ F_{Ay} \\ F_{Az} \end{bmatrix} = R_{w,s} \left(S\overline{q} \begin{bmatrix} C_D(\alpha) \\ C_Y(\alpha) \\ C_L(\alpha) \end{bmatrix} \circ \begin{bmatrix} -1 \\ 1 \\ -1 \end{bmatrix} \right) + R_{w,b} \begin{bmatrix} \delta_t T_m \\ 0 \\ 0 \end{bmatrix} \tag{5.4-11}$$

Lastly, the reference dynamics need to be prescribed which will provide the required commands, $\nu_{\dot{V}}$, $\nu_{\dot{\gamma}}$. The speed control path employs the simple first order dynamics used throughout the system with the addition of integrator anti-windup protection. The anti-windup protection was only implemented in the speed path as recovery scenarios were encountered where the descent velocity exceeded the target velocity with the throttle fully retarded (subsequently the integrator would wind up). However, note that in practice anti-windup protection should be provided for all paths to ensure flight safety. The implementation of the anti-windup protection is presented in Figure 56. The anti-windup gain, K_{aw} was simply set to one.

The reference dynamics for flight path consist of an over damped second order system. This specification ensures a smooth initial flight path rate command while maintaining a capture with zero overshoot. Step and doublet γ commands with a constant airspeed were simulated to test the OPL. These results are presented in Appendix B.3.

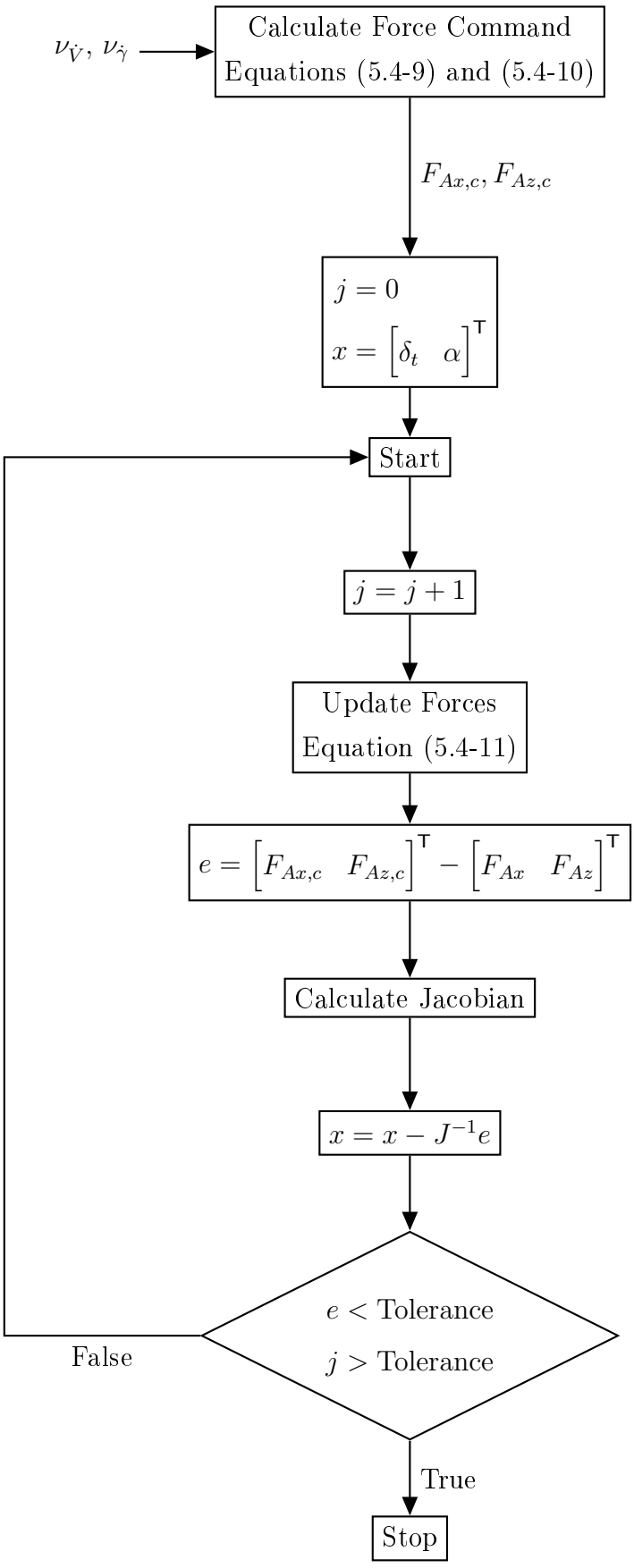

Figure 55 OPL Newton Solver

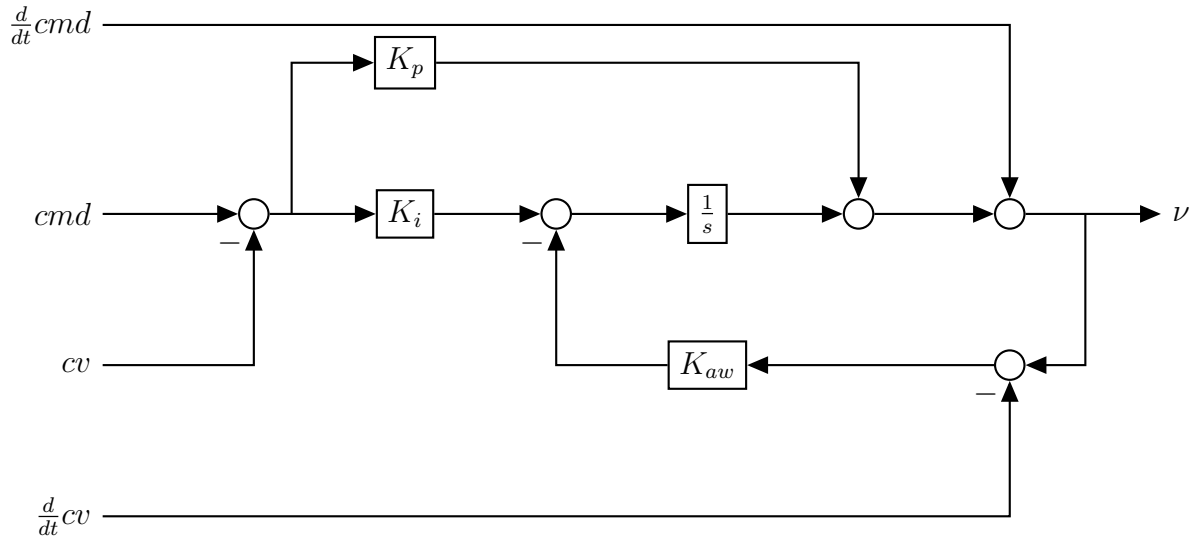

Figure 56 First Order with Anti-Windup

5.5 Stability Margin Testing

In order to ensure safe operation it is imperative to ensure the aircraft stability margins are acceptable. MIL-F-9490D, superseded by MIL-DTL-9490E provides specifications for theses margins pertaining to manned aircraft. In the standard operating envelope this amounts to a gain margin of $GM = \pm 6.0\,\text{db}$ and a phase margin of $PM = \pm 45°$.[69] The determination and extraction of the gain-phase margins from the simulation model follow the guidelines presented by Tischler detailed in the following subsections.[70]

5.5.1 Automated Sweep Inputs

The determination of frequency response data requires an input with frequency content. As an example, a pilot may induce fore and aft control inputs increasing in frequency about a trim point. As an alternative, a computer-generated sweep may also be utilized. In order to spend more time at low frequencies than at high frequencies the frequency sweep defined by Tischler was implemented and is presented here as Equation (5.5-1).

$$\delta_s = A \sin \theta(t) \tag{5.5-1a}$$

$$\theta(t) = \int_0^T \omega(t) dt \tag{5.5-1b}$$

$$\omega = \omega_{min} + K(\omega_{max} - \omega_{min}) \tag{5.5-1c}$$

$$K = C_2 \left(e^{\frac{C_1 t}{T}} - 1 \right) \tag{5.5-1d}$$

$$C_1 = 4.0 \qquad C_2 = 0.0187 \tag{5.5-1e}$$

Amplitude A is typically 10% of the maximum limits. The sweep generator includes user defined trim times before and after the sweep where δ_s remains zero. Additionally, the generator ensures a constant frequency ω_{min} for one full period. An example sweep input made by the sweep generator is presented in Figure 57.

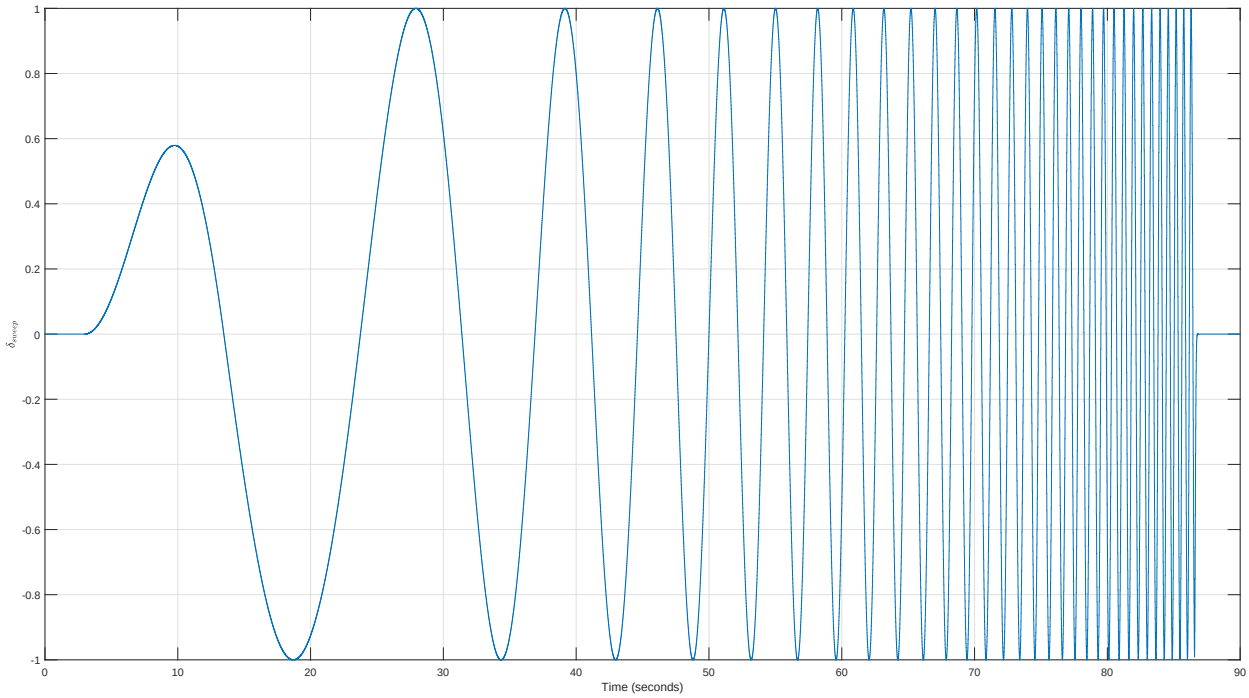

Figure 57 Sweep Input: $\omega_{min} = 0.3\,(\text{rad/s}), \quad \omega_{max} = 12\,(\text{rad/s})$

In Reference 70 recommendations pertaining to the recording time are made and are presented here in Equation (5.5-2). Equation (5.5-2a) provides the recommended recording time as a function of the minimum frequency used in the input sweep signal.

$$T_{rec} \geq (4-5)T_{max} \tag{5.5-2a}$$

$$f_{min} = \frac{\omega_{min}}{2\pi} \tag{5.5-2b}$$

$$T_{max} = \frac{2\pi}{\omega_{min}} \tag{5.5-2c}$$

$$T_{min} = \frac{1}{f_{max}} \tag{5.5-2d}$$

For the duration of the sweep input the aircraft motion needs to be bounded and should be relatively symmetric. In piloted tests this behavior is accomplished by minor corrective inputs from the pilot.

5.5.2 Frequency Response Basics

A very simplified explanation of the frequency response is as follows. Consider a periodic sine wave input $x(t)$ with amplitude A and frequency f.

$$x(t) = A\sin(2\pi f t) \tag{5.5-3}$$

After initial transients, the system output $y(t)$ will also be a sine wave of the same frequency, but with a different amplitude B and phase shift ϕ.

$$y(t) = B\sin(2\pi f t + \phi) \tag{5.5-4}$$

The complex valued frequency response function $H(f)$ has a corresponding magnification factor and phase shift given by Equations (5.5-5) and (5.5-6) respectively.

$$|H(f)| = \frac{B(f)}{A(f)} \tag{5.5-5}$$

$$\angle H(f) = \phi(f) \tag{5.5-6}$$

The frequency response $H(f)$ fully characterizes the system in a non-parametric manner; thus, zero assumptions are made about the system. If a Fourier Transform is used on time-based measured input/output signals an equivalent set of frequency-based signals are attained and are commonly referred to as the Fourier coefficients.

$$X(f) = FFT(x(t)) \tag{5.5-7a}$$

$$Y(f) = FFT(y(t)) \tag{5.5-7b}$$

In Equation (5.5-7) the Fast Fourier Transform (FFT) has been presented. However, for a finite set of data the Discrete Fourier Transform (DFT) is utilized. Given time history data with sample time Δt and N data points, the resulting Fourier transformed data will have equally spaced frequency content ranging from $f_{min} = \frac{1}{N\Delta t}$ to $f_{max} = f_s/2 = \frac{1}{2\Delta t}$.

Consider flight data collected at 50 Hz, (a typical minimum rate one can expect flight data at) with 1024 sample points. The resultant frequency data will range from 0.0488 Hz to 25 Hz evenly spaced with a frequency step of 0.0488 Hz. However, for aircraft applications one is typically only concerned with frequencies up to 13 rad/ sec ($\approx$ 2 Hz); thus, much of the content is wasted.[70]

As an alternative, the Chirp-Z Transform (CZT) can be utilized which distributes the data along an arbitrary arc of the unit circle. The CZT will return the same overall number of samples; however, the frequency range can be restricted to the frequencies of interest thereby increasing the resolution.

The Fourier coefficients are related to the frequency response function as a ratio of input to output in a similar manner as when the Laplace Transform is used (aside from being complex-valued). This relationship is presented in Equation (5.5-8) where subscript R and I denote the real and imaginary components respectively.

$$H(f) = \frac{Y(f)}{X(f)} = H_R(F) + iH_I(f) \tag{5.5-8}$$

The magnification factor and phase shift can be calculated as follows.

$$|H(f)| = \sqrt{H_R^2 + H_I^2} \tag{5.5-9a}$$

$$\angle H(f) = \tan^{-1}\left(\frac{H_I}{H_R}\right) \tag{5.5-9b}$$

Spectral Functions

The following spectral functions are utilized in frequency response analysis. The input autospectrum is

$$G_{xx} = \frac{2}{T}|X(f)|^2 \tag{5.5-10}$$

which represents the input power as a function of frequency. The output autospectrum, representing the output response power is given by Equation (5.5-11).

$$G_{yy} = \frac{2}{T}|Y(f)|^2 \tag{5.5-11}$$

The cross spectrum, which conveys the input-output phase and power information, is below.

$$G_{xy} = \frac{2}{T}(X^*(f)Y(f)) \tag{5.5-12}$$

The frequency response can be estimated from the spectral functions as shown in Equation (5.5-13).

$$H(f) = \frac{G_{xy}}{G_{xx}} \tag{5.5-13}$$

A benefit of utilizing Equation (5.5-13) is that it provides an optimum model when output noise is present. In Equations (5.5-10) to (5.5-12), T refers to the data record length. Finally, the coherence function

$$\gamma_{xy}^2 = \frac{|G_{xy}|^2}{|G_{xx}||G_{yy}|} \tag{5.5-14}$$

relates the output spectrum G_{yy} to the input spectrum G_{xx}. Under ideal circumstances the coherence will have a value of 1.

5.5.3 Gain-Phase Margin Determination

The gain and phase margins are calculated from the broken servo-loop frequency response. Utilizing an automated sweep input, δ_s, the direct estimate of the broken loop response can be determined with Equation (5.5-15).

$$GH(s) = \frac{f}{e}(s) \tag{5.5-15}$$

Using spectral functions the frequency response can determined by Equation (5.5-16).

$$GH(f) = \frac{G_{ef}}{G_{ee}} \tag{5.5-16}$$

In Equations (5.5-15) and (5.5-16), e is the error signal and f is the feedback signal. This process must be carried out for all loops that connect a sensor to a force/moment producer.[69] A generic block diagram of the relevant signals is presented in Figure 58. Results from the analysis of the IRL and MAL control loops are presented in the following two sections. No analysis was done for the OPL loop.

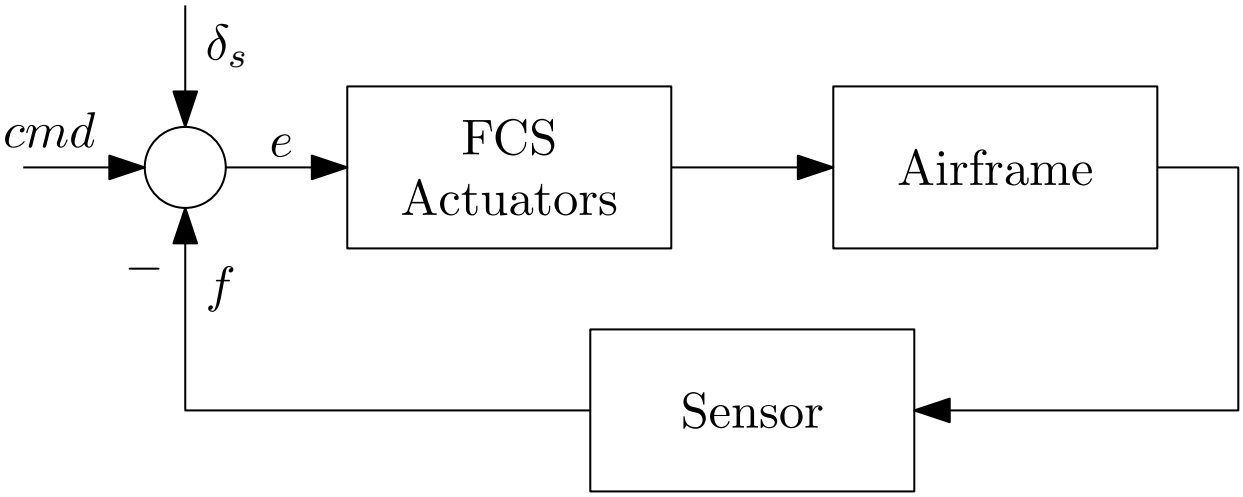

Figure 58 Broken Servo-Loop Identification

IRL Margins

Figures 59 to 61 and Tables 16 to 18 present the broken loop response data for the IRL at both low and high speed conditions. Unlike the roll and yaw axes the pitch axis data was questionable as it contained excessive noise that should not be present in the simulation environment. The reason for this contamination was not determined and the behavior was not reflected in the closed-loop response. The desirable values of 6 dB, 45° are met in all cases except the phase margin of the roll/yaw axis at low Mach. However, the levels below the threshold are not significant enough to necessitate design changes.

Table 16 IRL Roll Broken Loop Margins

	$M = 0.25$	$M = 0.60$
GM(dB)	-16.97 10.09	-69.51
ω_{GM}(rad/s)	0.2054 1.979	0.06442
PM(deg)	39.76	64.55 64.26 64.89
ω_{PM}(rad/s)	0.8747	6.17 6.195 6.223

Table 17 IRL Pitch Broken Loop Margins

	$M = 0.25$	$M = 0.60$
GM(dB)	-	-
ω_{GM}(rad/s)	-	-
PM(deg)	87.96 67.99 85.8	64.27 62.79 64.95
ω_{PM}(rad/s)	1.259 1.371 1.502	7.222 7.282 7.364

Table 18 IRL Yaw Broken Loop Margins

	$M = 0.25$	$M = 0.60$
GM(dB)	-	-31.45 -16.04
ω_{GM}(rad/s)	-	2.367 3.549
PM(deg)	41.32	58.13 57.98 58.31
ω_{PM}(rad/s)	2.517	10.36 10.37 10.39

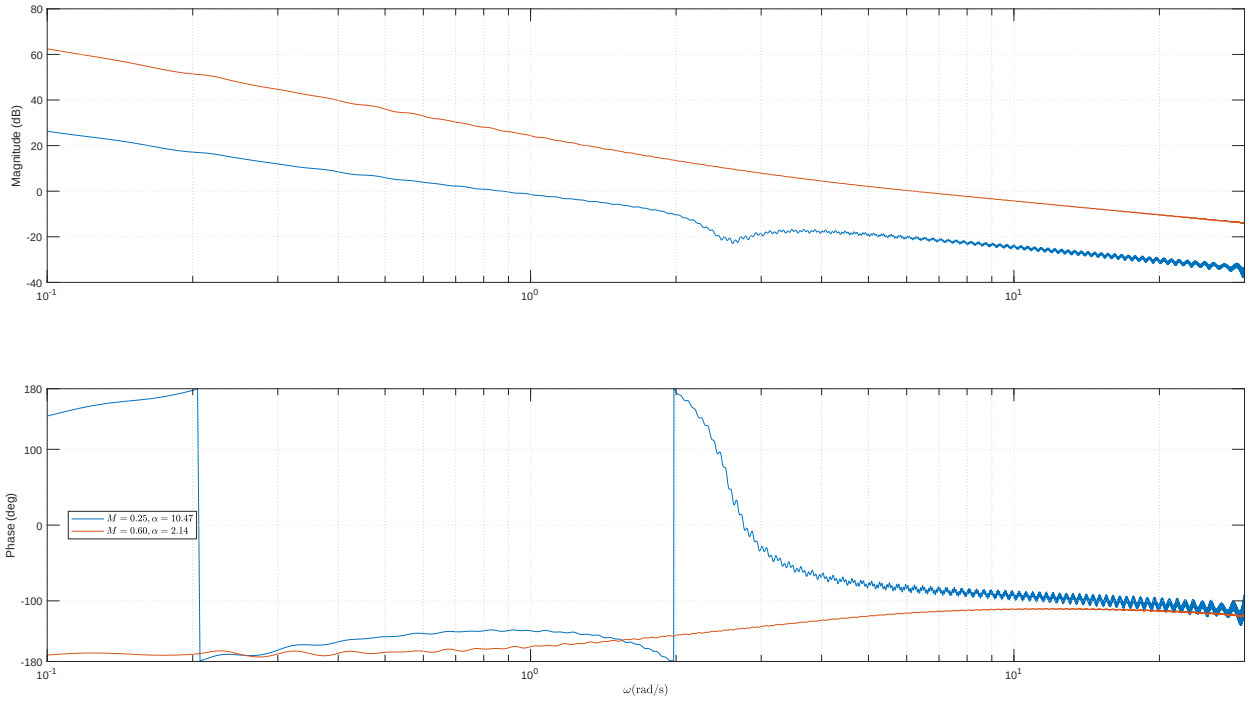

Figure 59 IRL Roll Broken Loop

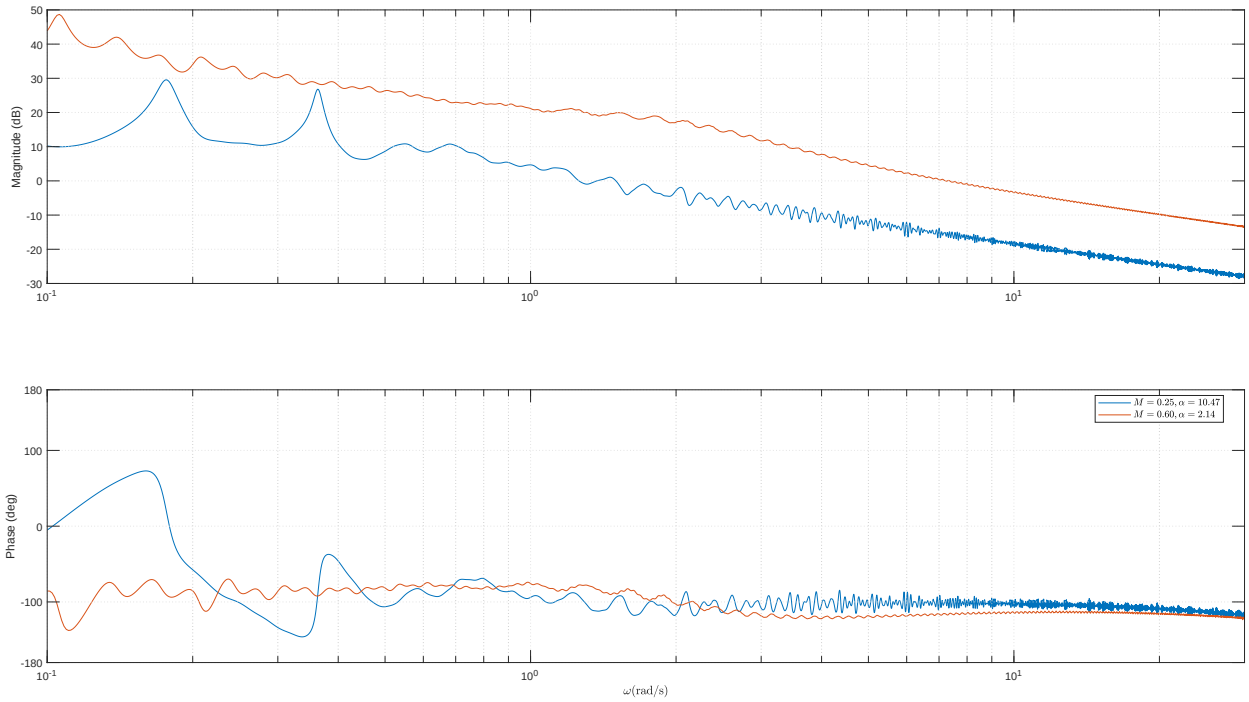

Figure 60 IRL Pitch Broken Loop

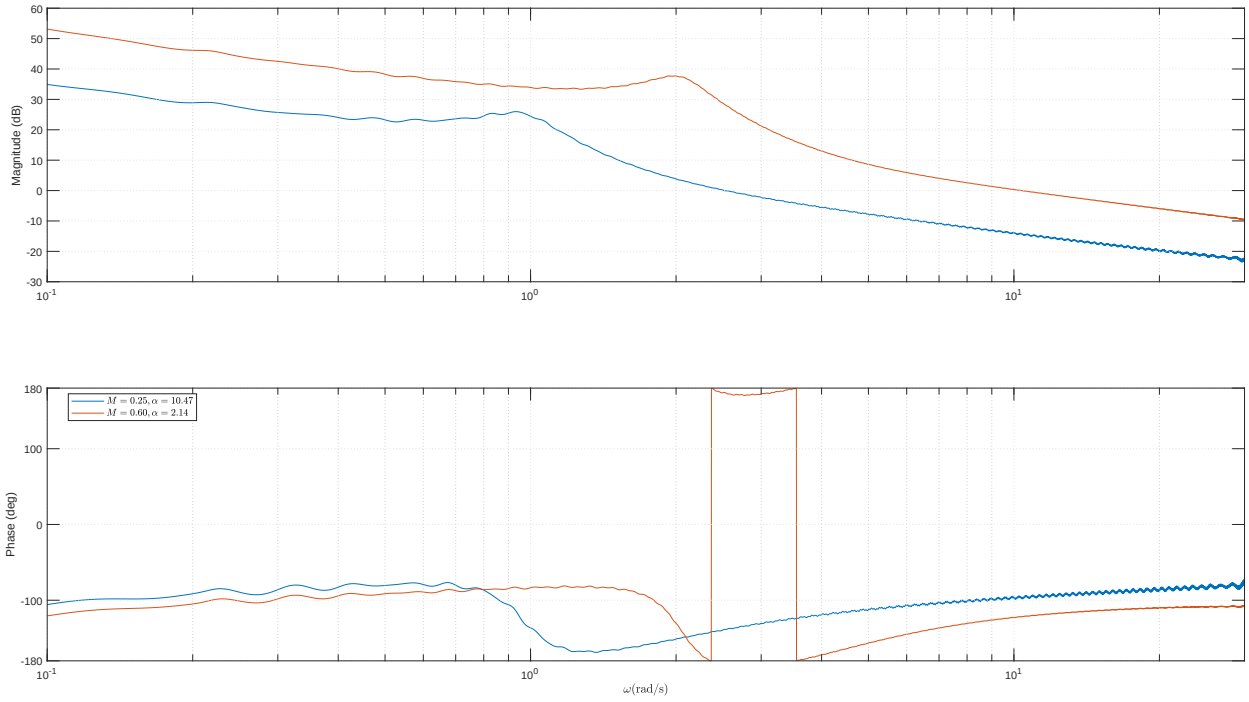

Figure 61 IRL Yaw Broken Loop

MAL Margins

The margins for the pitch axis have been omitted given the suspect quality of collected data as can be seen in Figure 63. A reason explaining why the frequency response for the pitch axis did not produce reliable data is not known. Figures 62 and 64 and Tables 19 and 20 present the broken loop response and summarizing margins for the roll and yaw axes respectively.

Table 19 MAL Roll Broken Loop Margins

	$M = 0.25$	$M = 0.60$
GM(dB)	-63.73 -9.705 9.172	-133 -11.09
ω_{GM}(rad/s)	0.1915 0.5091 2.116	0.005181 2.82
PM(deg)	27.81	43.14
ω_{PM}(rad/s)	1.051	6.296

Table 20 MAL Yaw Broken Loop Margins

	$M = 0.25$	$M = 0.60$
GM(dB)	-	-80.39 -39.22 -10.3
ω_{GM}(rad/s)	-	0.06459 2.122 4.735
PM(deg)	38.19	50.63
ω_{PM}(rad/s)	2.608	10.41

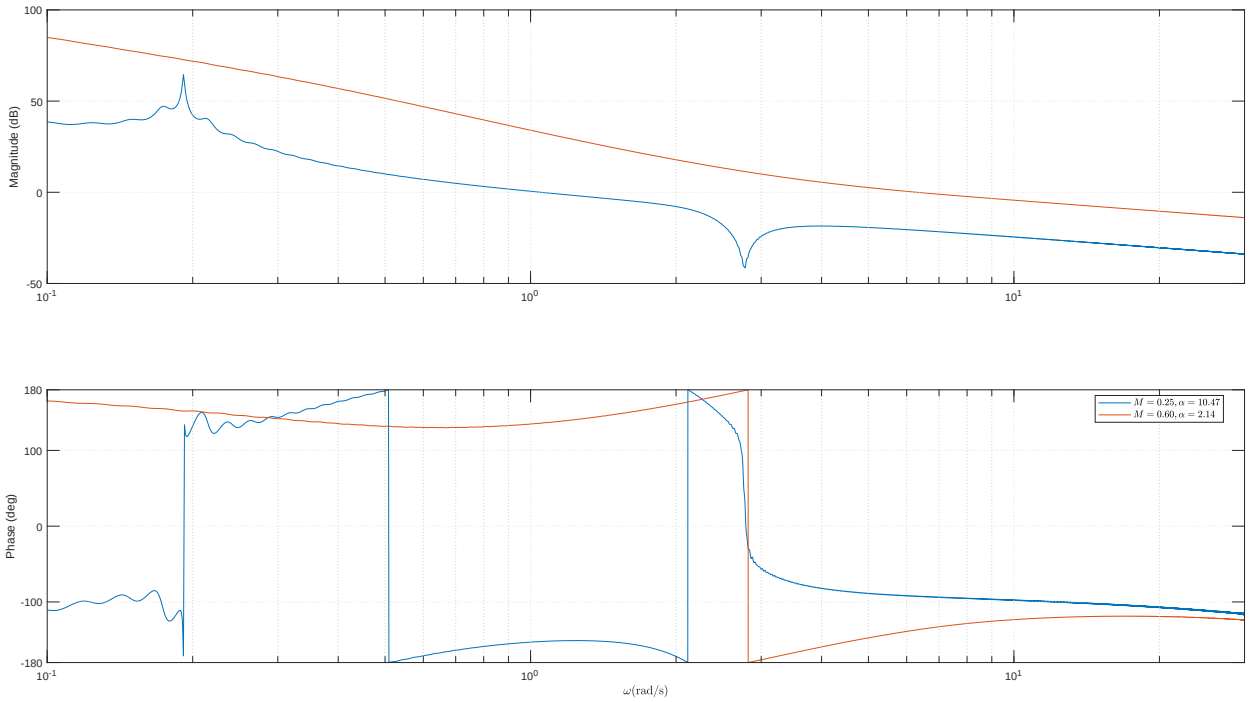

Figure 62 MAL Roll Broken Loop

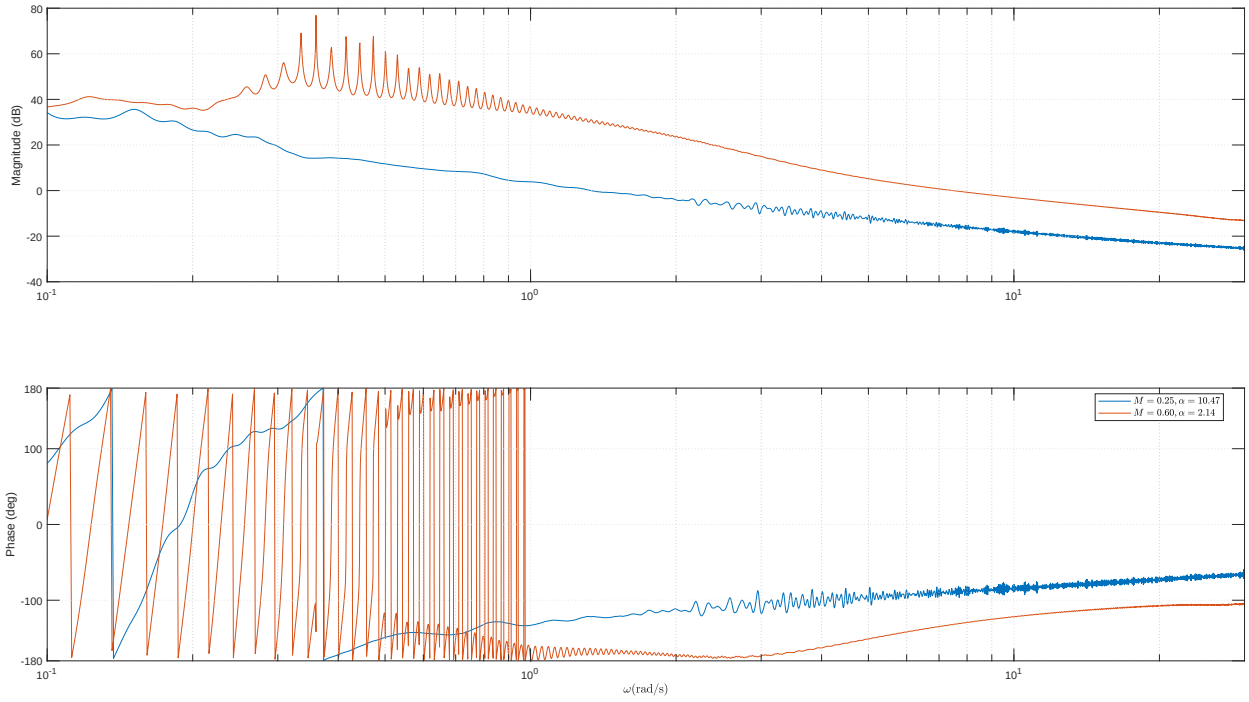

Figure 63 MAL Pitch Broken Loop

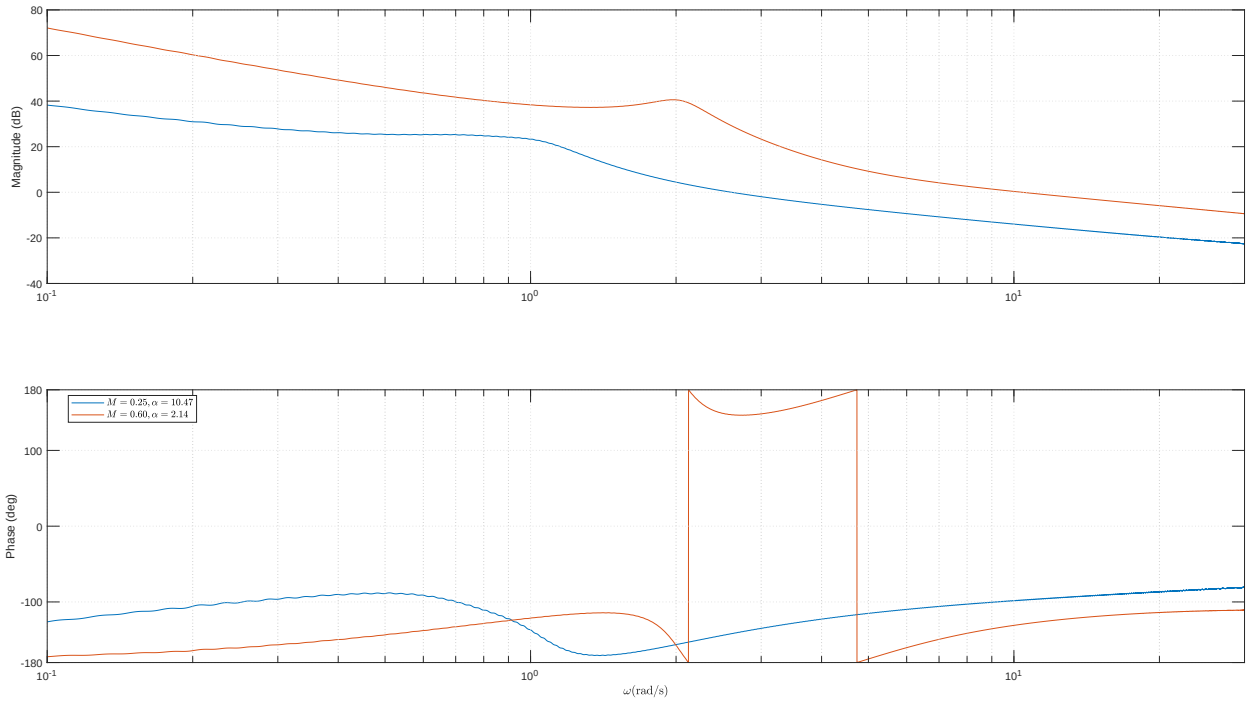

Figure 64 MAL Yaw Broken Loop

5.5.4 Model Tracking Performance

Frequency response methods can also be used to ensure the system tracks the desired model system. This task is accomplished in a similar manner as the broken servo-loop with a slightly different selection of signals as depicted in Figure 65. The closed-loop response is then given as $\frac{f}{cmd+\delta_s}$ where δ_s is the automated sweep and f is the sensor feedback signal.

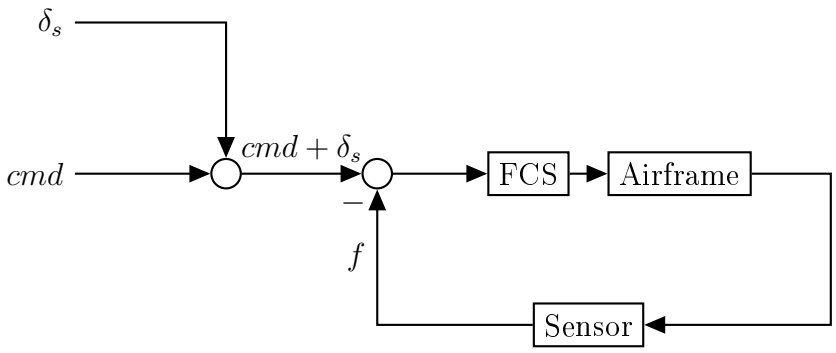

Figure 65 Closed-Loop Frequency Response Signals

In application the system is not expected to behave exactly like the linear reference model due to nonlinear dynamics, discontinuities, external disturbances, etc. As such Maximum

Unnoticeable Added Dynamics (MUAD) envelopes have been previously developed and are presented in Reference 65. These envelopes are defined by Equation (5.5-17) and are used to generate a shaded region of acceptable closed-loop response enabling a visual verification that the system is sufficiently close to the design model.

The MUAD models were utilized to validate the reference model tracking performance for both the IRL and MAL.

$$\text{Upper Gain Envelope} : \frac{3.16s^2 + 31.61s + 22.79}{s^2 + 27.14s + 1.84} \tag{5.5-17a}$$

$$\text{Lower Gain Evelope} : \frac{0.095s^2 + 9.92s + 2.15}{s^2 + 11.6 + 4.95} \tag{5.5-17b}$$

$$\text{Upper Phase Envelope} : \frac{68.80s^2 + 1100.12s - 275.22}{s^2 + 39.93s + 9.99} e^{0.006s} \tag{5.5-17c}$$

$$\text{Lower Phase Envelope} : \frac{475.32s^2 + 184100s + 29460}{s^2 + 11.66s + 0.039} e^{-0.0072s} \tag{5.5-17d}$$

IRL

The closed-loop responses with MUAD thresholds is presented in Figures 66 to 71 for both low and high Mach numbers. Unlike the broken loop response, the data collected for the pitch channel behaved as expected with a close fit to the reference dynamics documented in Figures 68 and 69. The roll and yaw channels also exhibited a response that closely fit the reference dynamics. In all cases the models are within the thresholds up to a reasonably high value of ω indicating that the system should behave as designed.

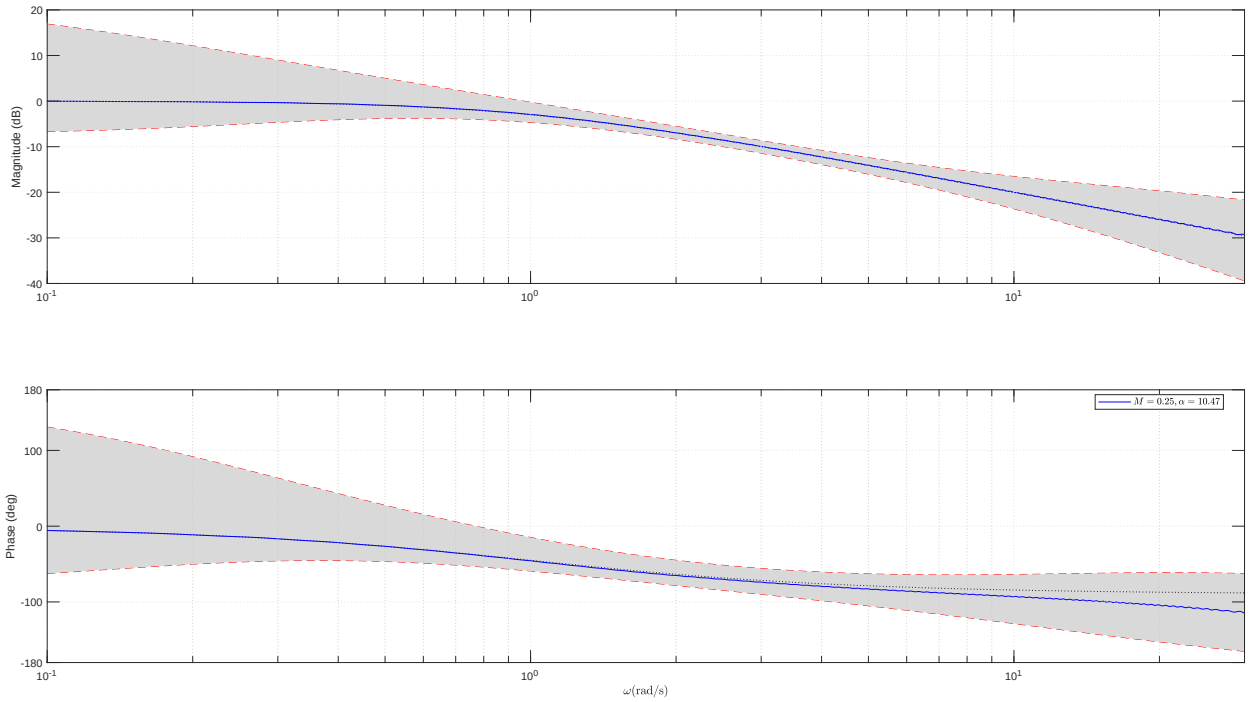

Figure 66 IRL Roll Closed-Loop Response, Mach=0.25

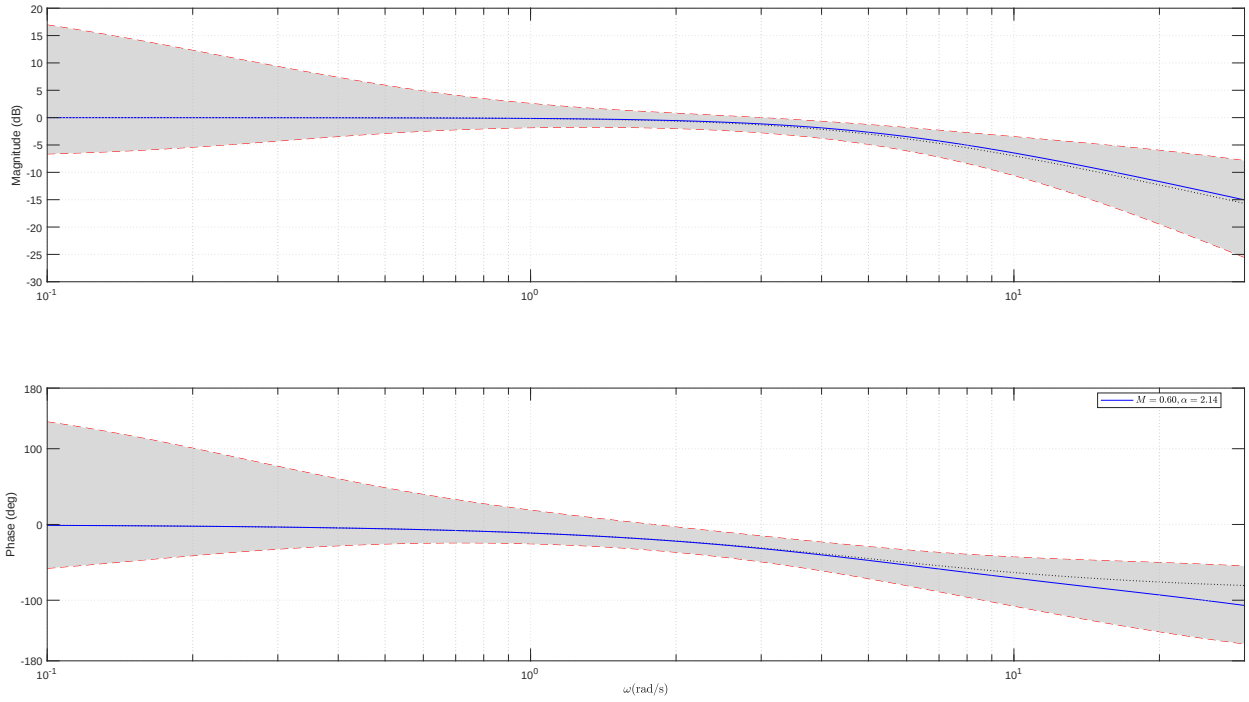

Figure 67 IRL Roll Closed-Loop Response, Mach=0.60

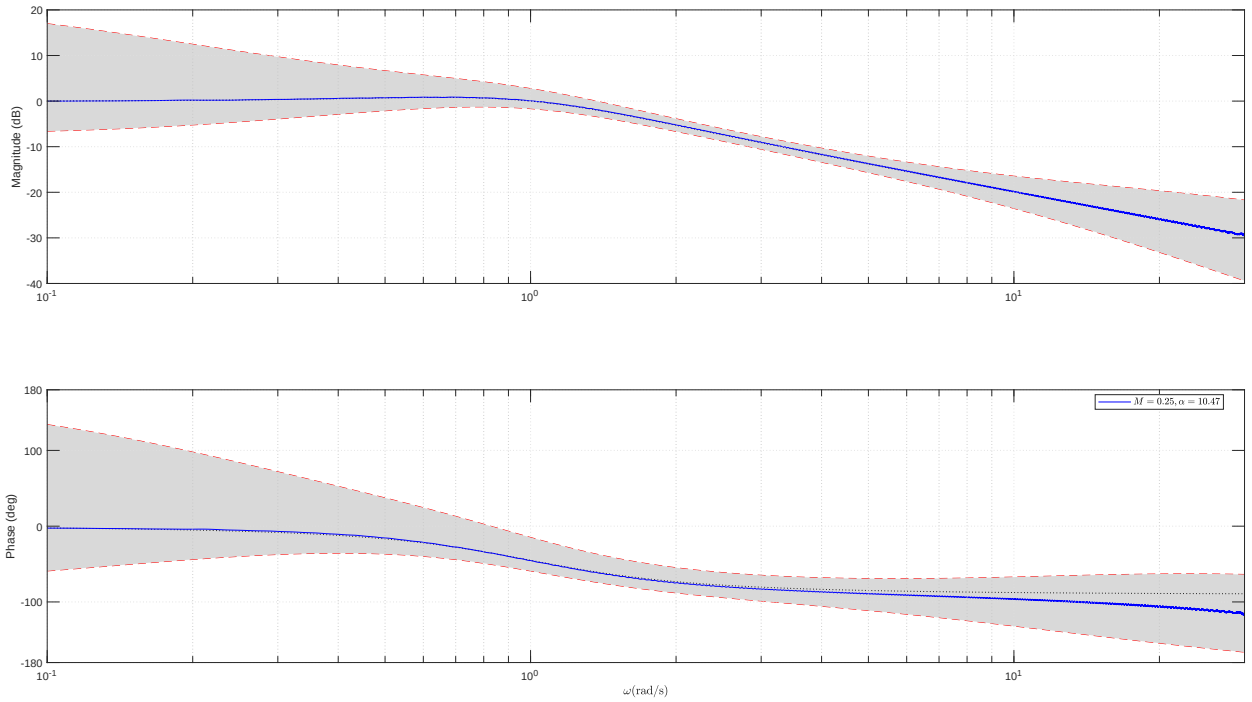

Figure 68 IRL Pitch Closed-Loop Response, Mach=0.25

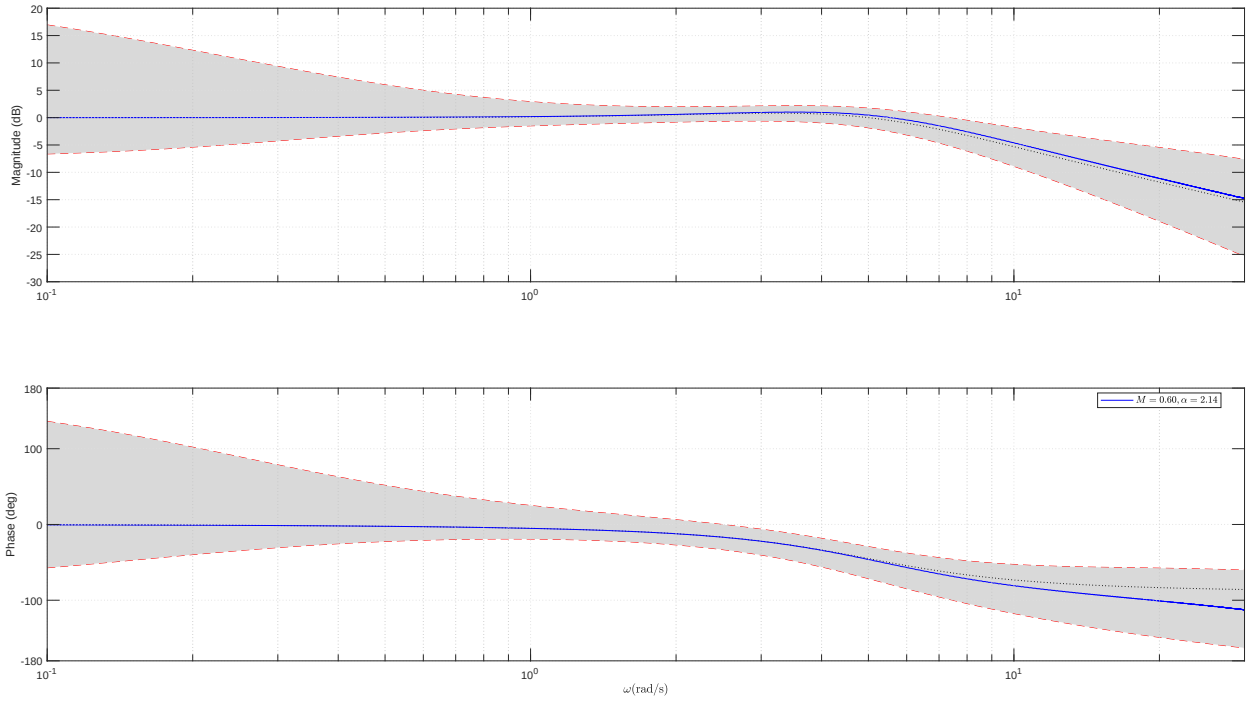

Figure 69 IRL Pitch Closed-Loop Response, Mach=0.60

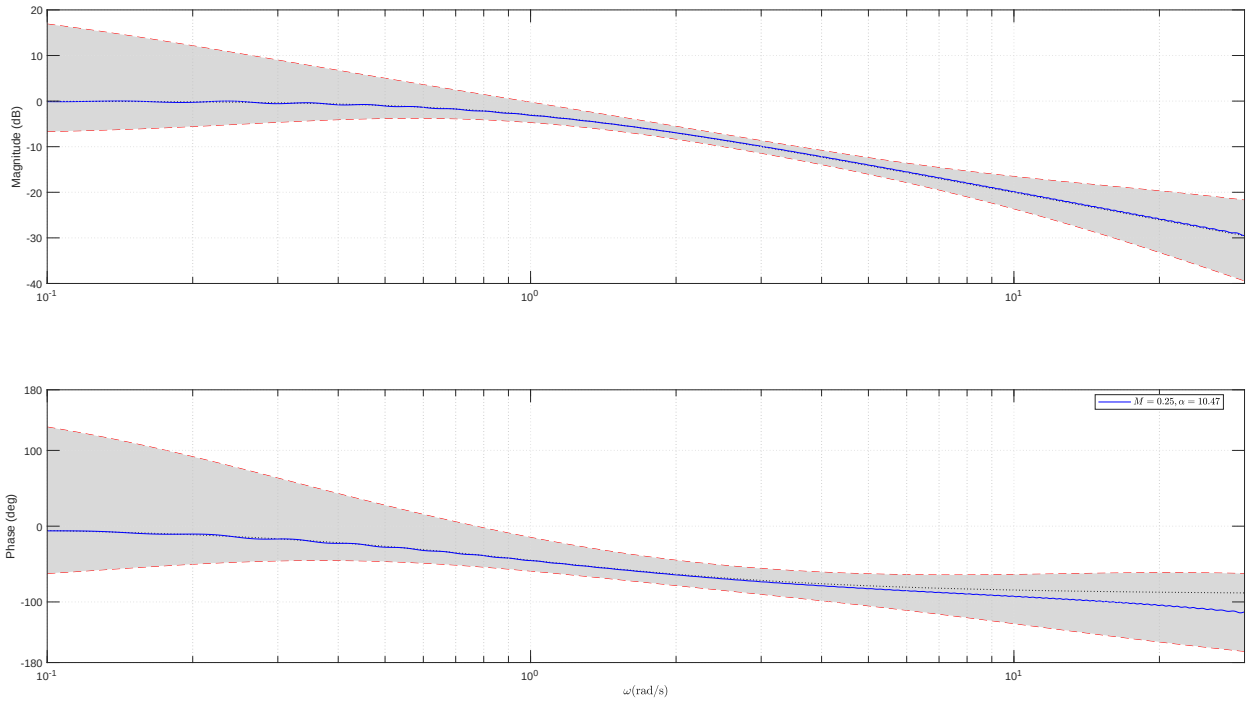

Figure 70 IRL Yaw Closed-Loop Response, Mach=0.25

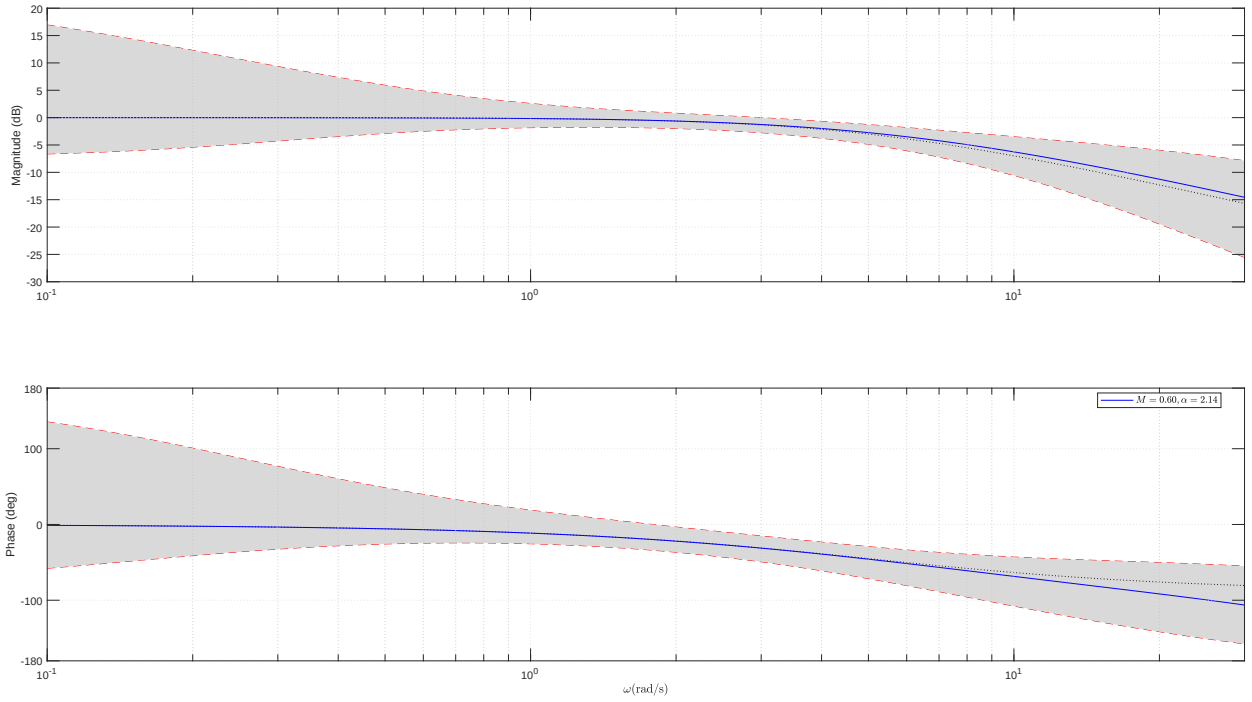

Figure 71 IRL Yaw Closed-Loop Response, Mach=0.60

MAL

The MAL closed-loop response data indicated the control loops were more susceptible to higher frequency inputs as the tracking of the reference models breaks down with higher values of ω. This degraded performance is presented in Figures 72 to 77 and depicts deviations exceeding the MUAD boundaries. The noise in the high frequency data content is exaggerated in Figures 72, 74 and 76 due to the wrapping of the phase signal to be within $\pm 180°$. Furthermore, the degraded tracking at higher ω is dominant in the low speed condition which agrees with the analysis of Section 4.3.2 that indicated insufficient control authority exists at low speeds. The larger deviations from the reference dynamics is in some part attributed to the reference models used for comparisons not entirely accounting for the exact cascaded implementation of the system. Nonetheless these plots are useful as they provide the overall response of the closed-loop system.

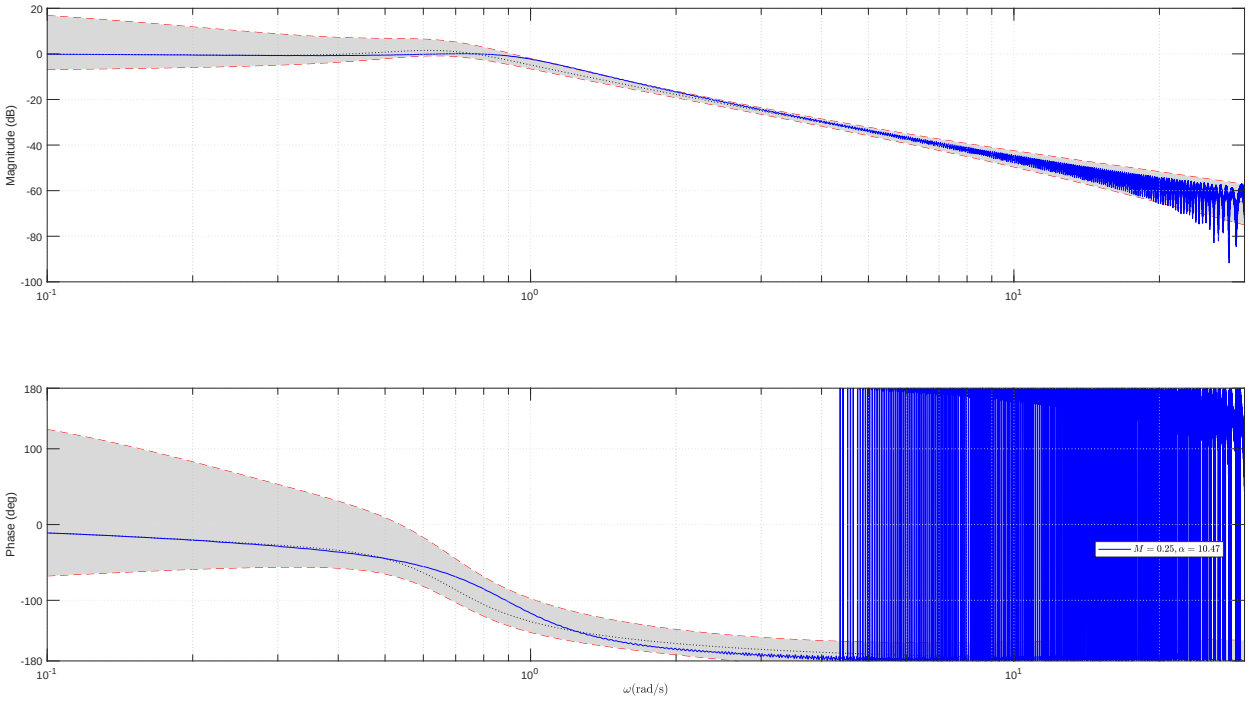

Figure 72 MAL Roll Closed-Loop Response, Mach=0.25

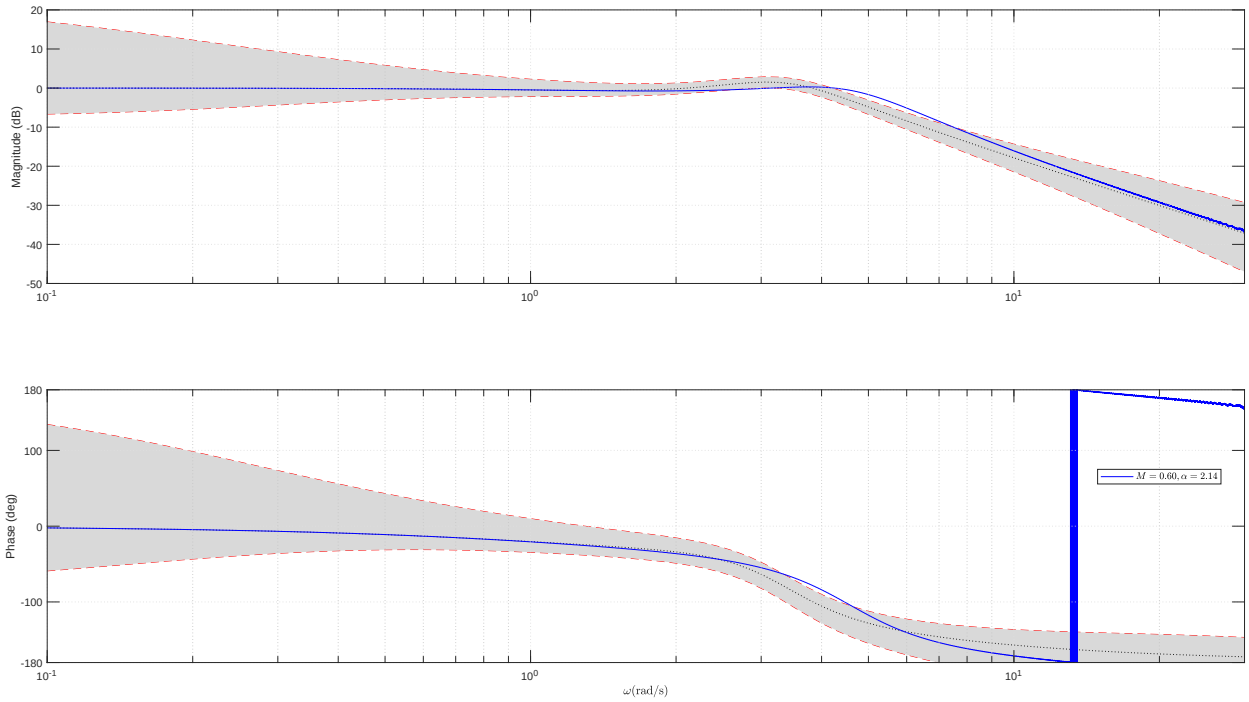

Figure 73 MAL Roll Closed-Loop Response, Mach=0.60

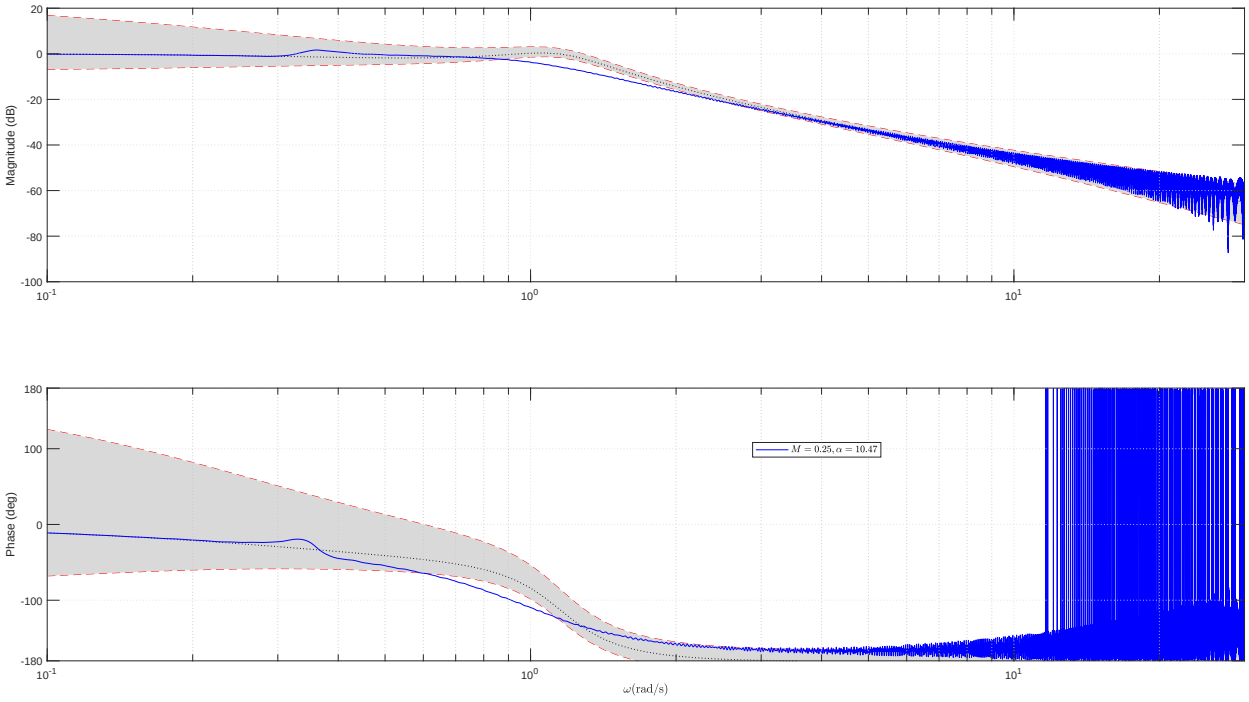

Figure 74 MAL Pitch Closed-Loop Response, Mach=0.25

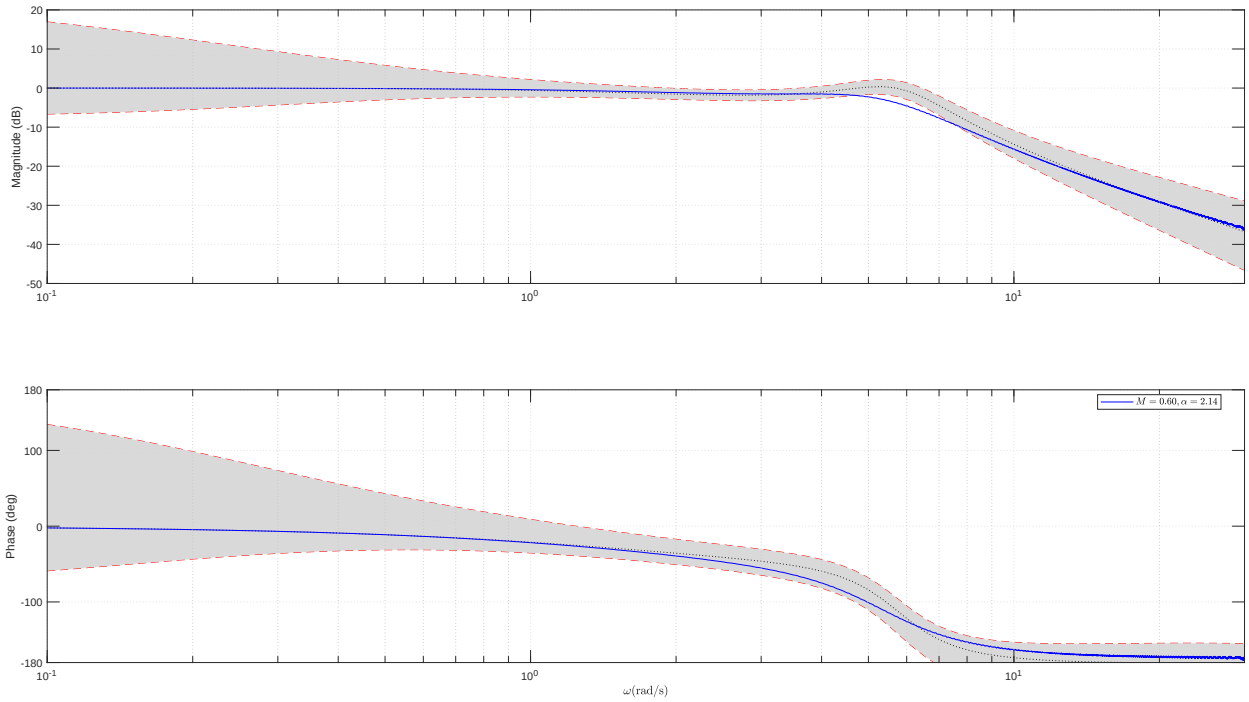

Figure 75 MAL Pitch Closed-Loop Response, Mach=0.60

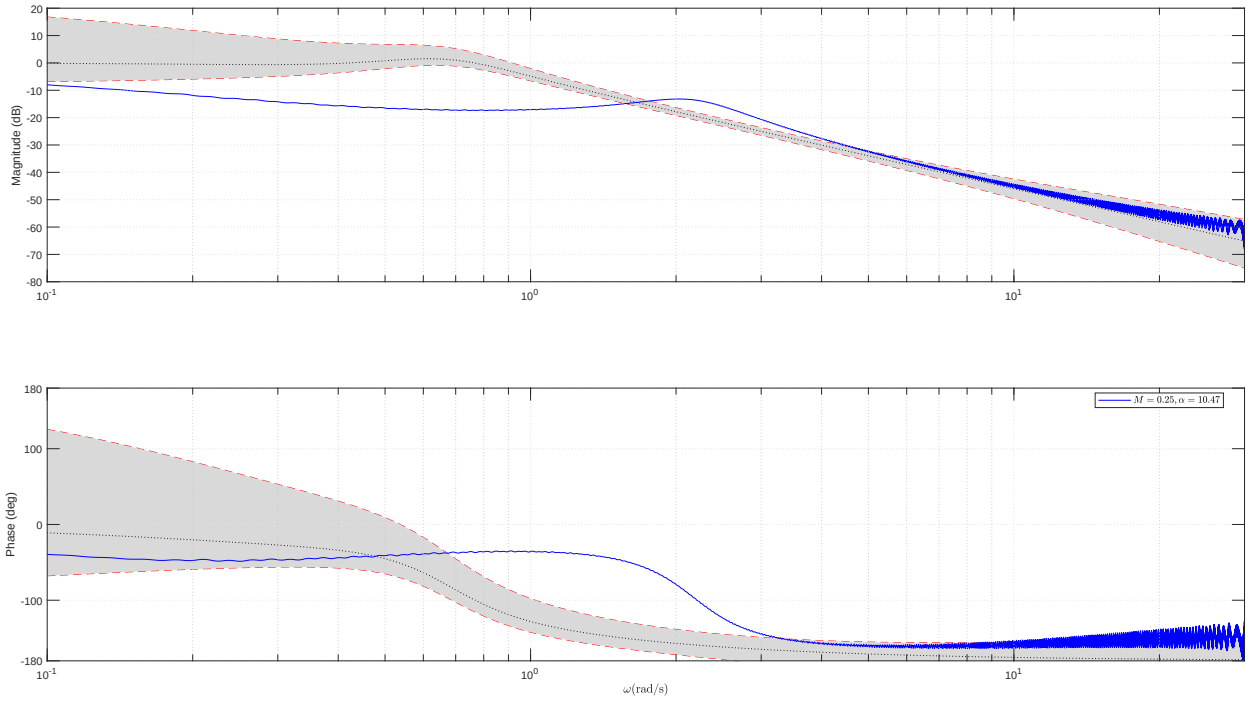

Figure 76 MAL Yaw Closed-Loop Response, Mach=0.25

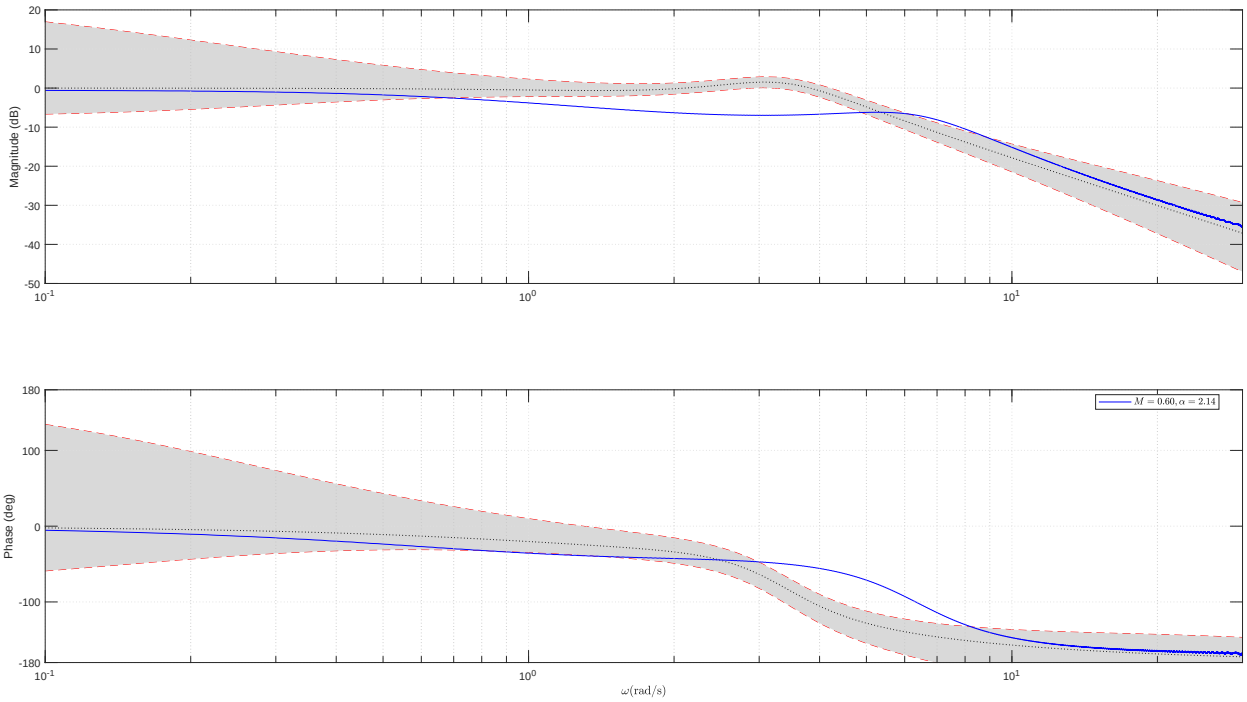

Figure 77 MAL Yaw Closed-Loop Response, Mach=0.60

5.6 Spin Recovery

The spin recovery aspect of the NDI controller consists of additional logic conditions and sequencing that unifies the IRL, MAL, and OPL together into a cohesive system as depicted in Figure 80. There are numerous strategies pertaining to spin recovery such as a lift coefficient based control as presented in Reference 71, multi-mode neutral control surface strategy as presented in Reference 72, or a more theoretical trim state targeting controller as in Reference 47. The approach taken in this thesis is a blending of a multi-mode recovery that targets maximum C_L by using a pre-determined constant recovery α. This method is not meant to be an optimized solution but, instead, a practical approach.

First and foremost the spin motion must be arrested. In some cases, it may be possible to simply neutralize the control surfaces and wait for the natural damping of the aircraft to minimize the spin motion. However, this method does not actively aid in reducing loss of altitude. Instead, full rudder deflection is commanded to counteract the large body yaw rate affiliated with spin motion. During this time the ailerons and stabilators are commanded to zero. Lastly, full thrust is commanded in order to increase dynamic pressure thereby increasing control authority. The effect of this combination results in a reduction in the spin motion as depicted in the time between *FCC ON* and *IRL ON* in Figure 78. FCC

denotes flight control computer.

Once the body yaw rate falls within the prescribed dead zone the IRL is allowed to engage. The dead zone on body yaw rate is necessary due to the limited yaw axis control authority. With the yaw rate threshold met the IRL engages and commands p_s, q, r_s to zero. During initial engagement a check for *positive control* is continually evaluated. This condition consists of all three angular channels having errors with magnitudes less than one degree per second for a minimum continuous duration of 0.25 seconds. This check ensures outer loops are not enabled prior to the IRL ability to track commands. Figure 79 presents an example of the signals of interest where the black lines represent the tolerance around the command signal required for positive control. The data in this figure represents the time from initial IRL engagement to the positive control condition being satisfied.

Once the IRL has confirmed *positive control* the MAL activates. Upon activation, the MAL commands μ and β to zero while α is commanded to attain the maximum C_L in an effort to minimize altitude loss. Commanded α begins to decay to zero once a positive rate of climb is attained in order to stop the climb in preparation for OPL engagement. The OPL engages once the α command is less than one degree and the positive climb rate is less than 100 ft/sec. This condition ensures the α required to command γ to zero is not an abrupt change. At this point the OPL takes command and maintains level flight.

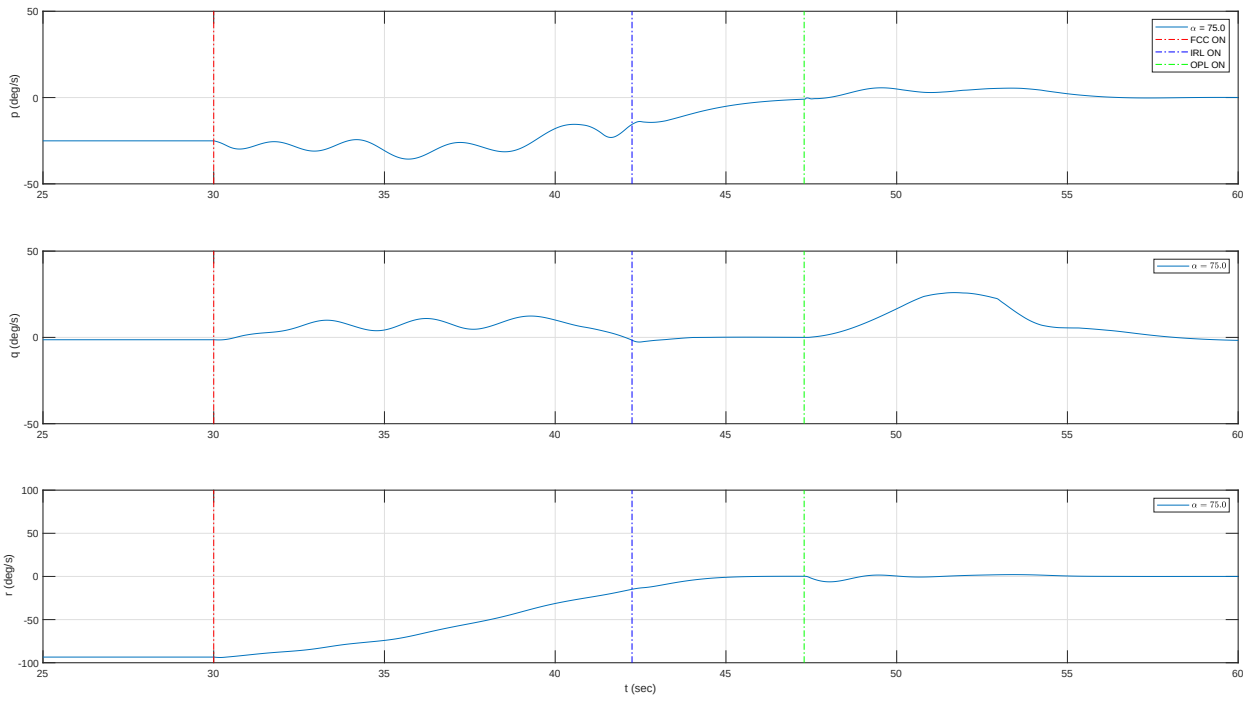

Figure 78 Body Angular Rates During Spin Recovery, $\alpha = 75.0°$

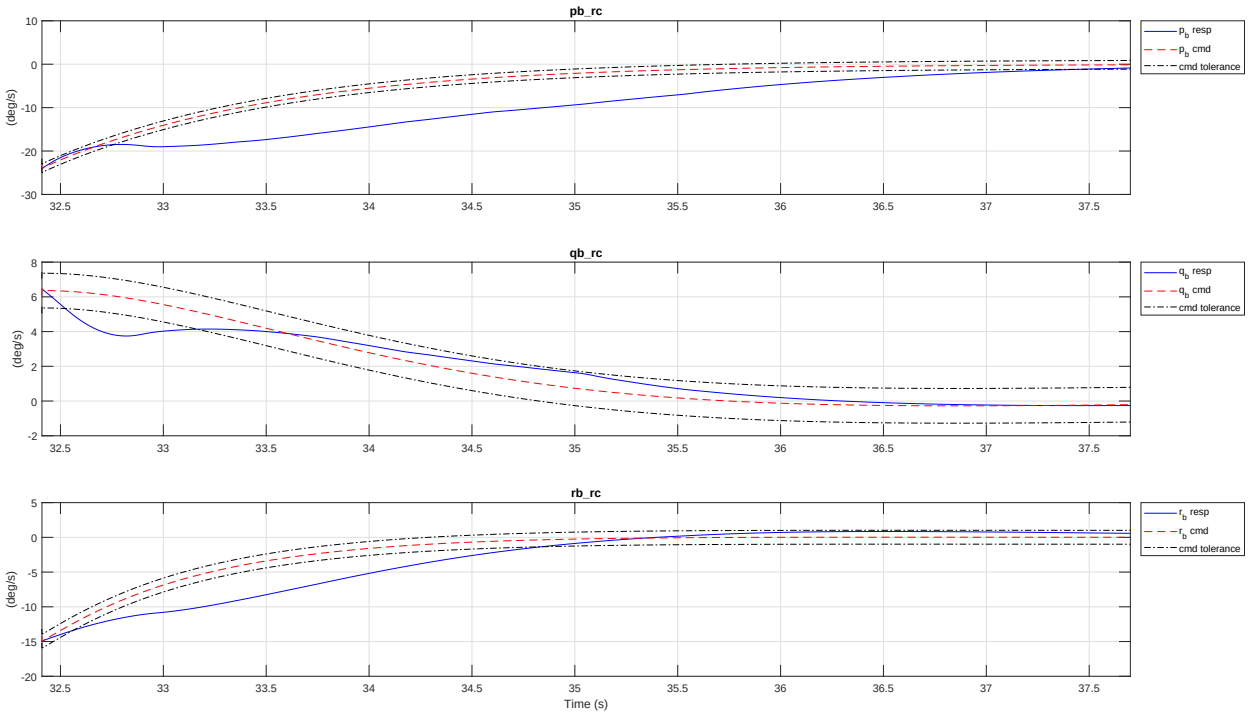

Figure 79 Positive Control Criteria Visualized

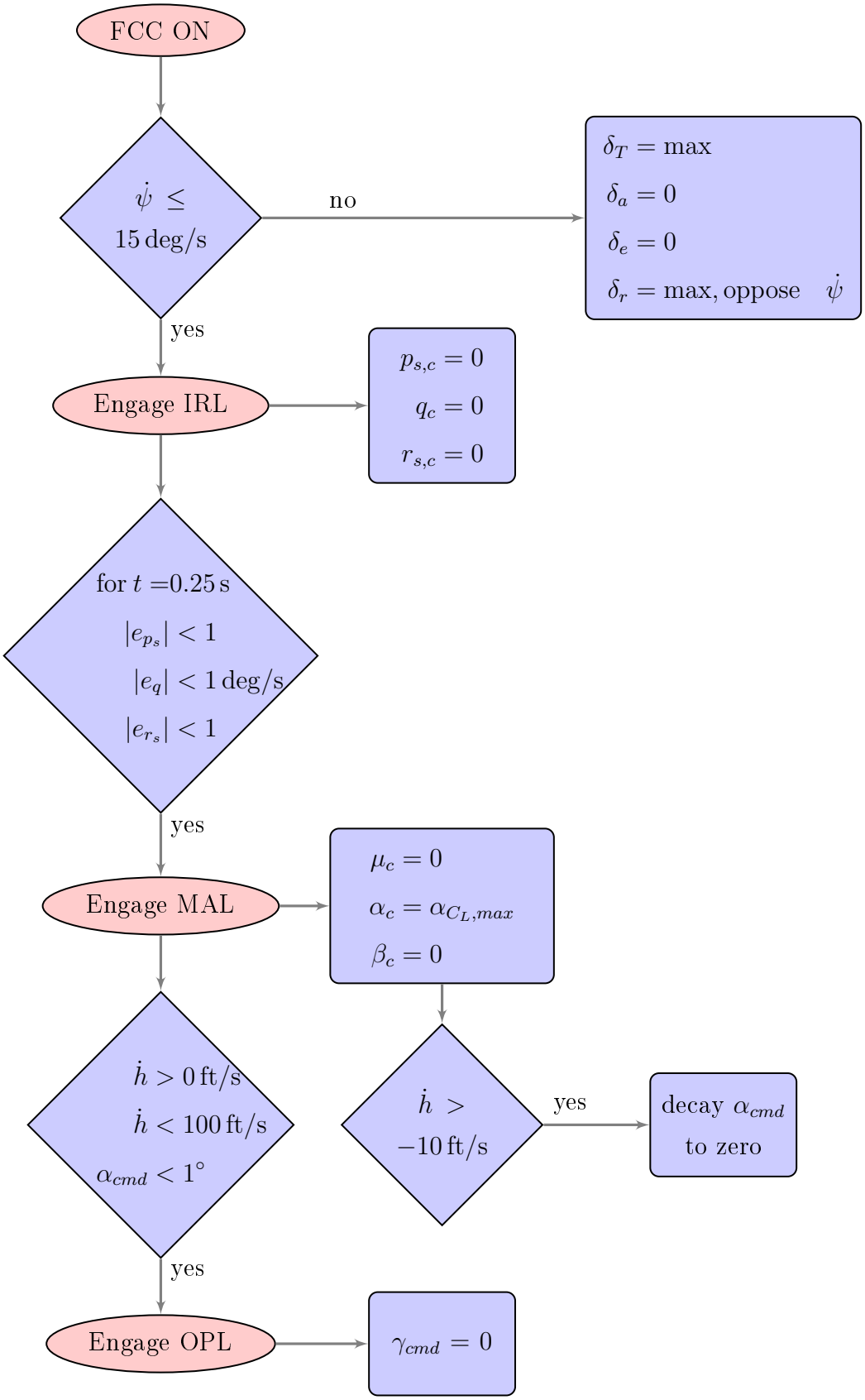

Figure 80 Spin Recovery Control

CHAPTER 6
SPIN RECOVERY SIMULATIONS

The spin recovery controller was evaluated by running 500 trimmed spin scenarios evenly spaced between $\alpha = 31°$ and 85°. The lower boundary of 31° was chosen to avoid the conditions that did not have adequate trim accuracy. The simulation was initialized from a trimmed steady state spin condition. The FCS was engaged at thirty seconds into the simulation for all but thirty-four cases in order to account for initial transients. The simulation was terminated at a fixed time of ninety seconds.

Figure 81 presents an example of the unmitigated spin at $\alpha = 71.6°$ which corresponds to the maximum NI. Note the position track taken by the aircraft mass center during the spin exhibits the classic helix shape with a rather tight radius of approximately 5 ft and a descent of approximately 17,000 ft over 90 seconds. Figure 82 presents the same condition with the FCC engaged at thirty seconds. In this figure the dashed black line projected on the vertical axes denotes the altitude at which the FCC was engaged; for clarity this altitude has been shifted to zero. The black square projected in both the vertical and horizontal axes corresponds to when the IRL became operational. The altitude loss that occurred between engagement of the FCC and the IRL becoming active corresponds to the period of time during which control surfaces were held constant to arrest the spin motion. The arresting input is very effective in quickly suppressing the helix motion. The aircraft descent has also been altered, where the altitude loss is approximately 3,500 ft over 30 seconds. After IRL engagement, the aircraft descent was completely halted after approximately 2,000 ft. The NDI controller is effective in suppressing the spin motion and restoring stabilized level flight over a short duration of time.

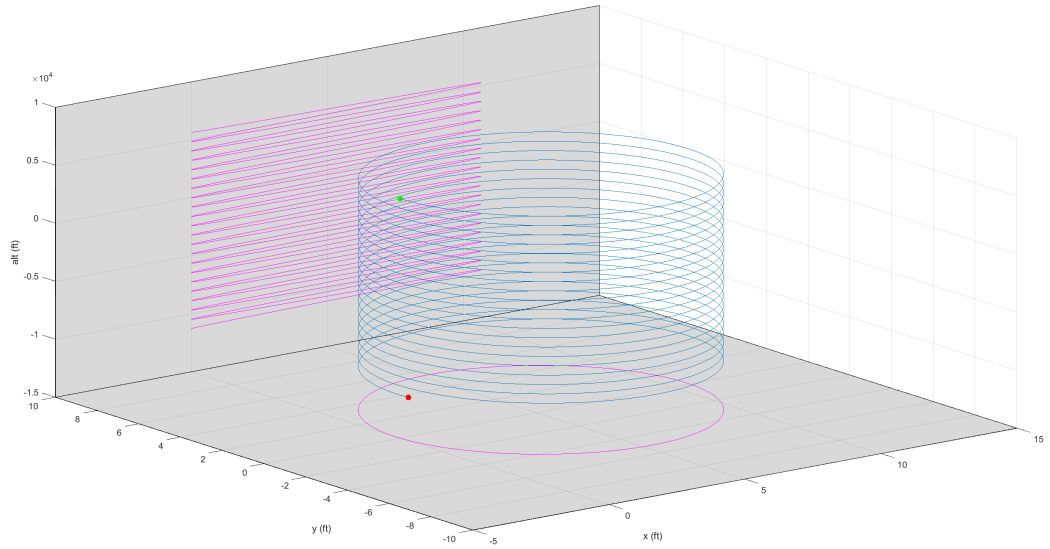

Figure 81 Unmitigated Spin Simulation, $\alpha = 71.6°, T = 90\,\text{sec}$

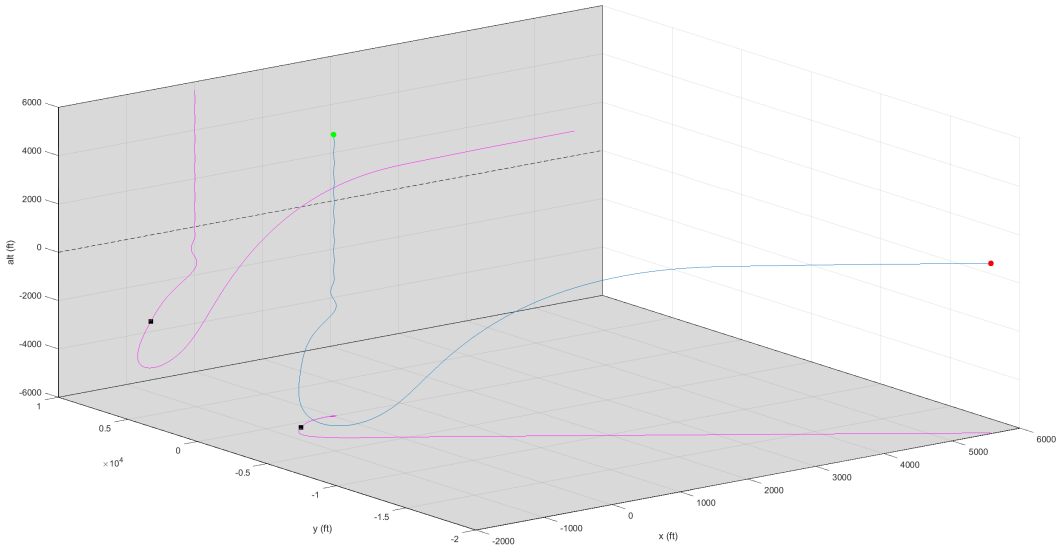

Figure 82 Recovered Spin Simulation, $\alpha = 71.6°, T = 90\,\text{sec}$

Figure 83 compares the unmitigated to the recovered spin. The data depicted in this plot represents five seconds prior to FCC engagement through the minimum altitude attained during recovery. The blue and red dashed lines in the vertical plane depict the difference in

altitude loss between the unmitigated and recovered spin, respectively. This data shows that the aircraft has an increase in altitude loss when the FCC is engaged and is attributed to the initial decrease in α intended to restore forward velocity. During this period, the aircraft follows a track with a much larger horizontal component consisting of several thousand feet.

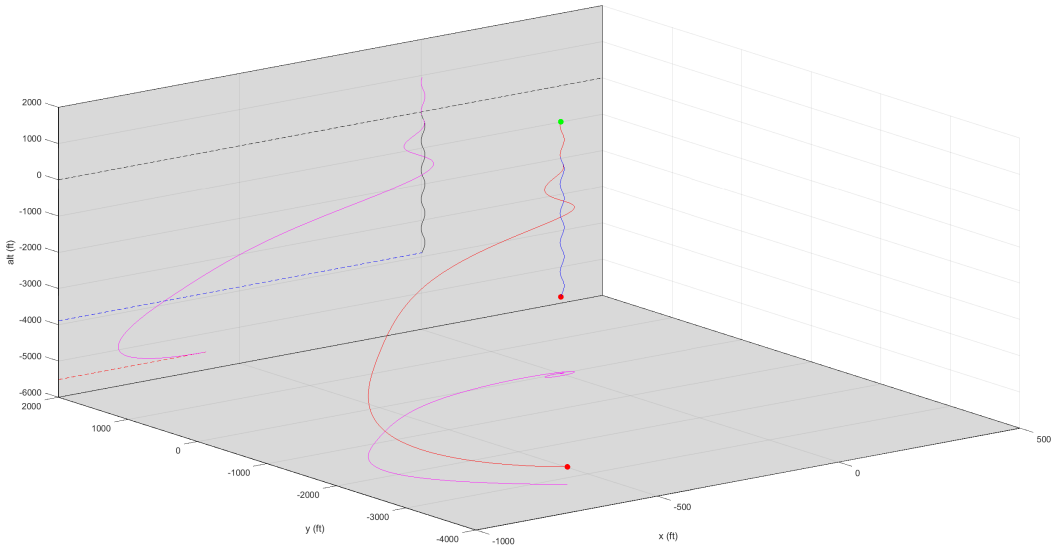

Figure 83 Unmitigated vs. Recovered Spin, $\alpha = 71.6°$

Figure 84 presents an overview of the altitude loss during recovery, time to recover, and vertical descent rate (at controller engagement) for all 500 simulations. The data points marked in red correspond to the thirty-four cases that the FCC did not engage at thirty seconds. In these cases the FCC was engaged at fifteen seconds. This change was done as the initial results for these simulations resulted in erroneously large altitude losses due to the aircraft being unstable *prior* to the engagement of the FCC. The time to recover and altitude loss was measured from the time the FCS was enabled through the time corresponding to the minimum altitude attained by the aircraft. The controller recovered from the spin in 10-25 seconds for almost every scenario.

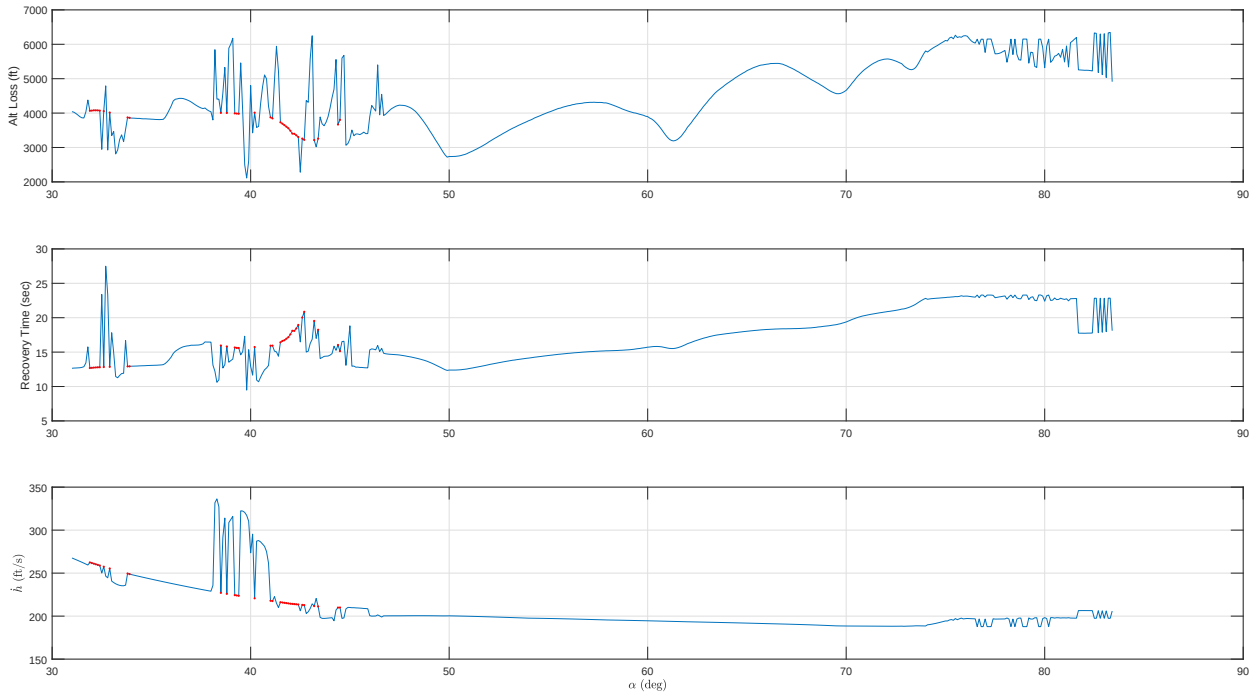

Figure 84 Spin Recovery Overview

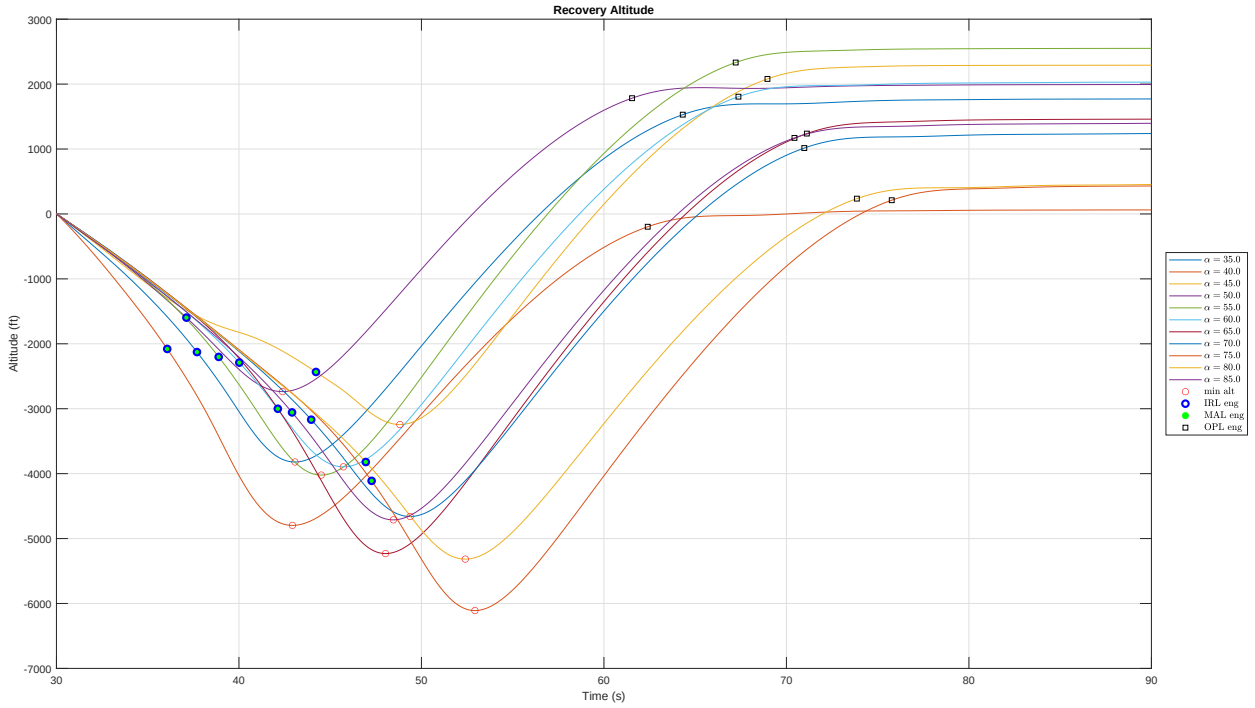

Figure 85 Spin Recovery Altitude Performance

Table 21 Recovery Results, $\alpha = 35 - 85$ deg

Alpha (deg)	Recovery Time (s)	Alt Loss (ft)
35	13.07	3823
40	12.93	4800
45	18.82	3246
50	12.39	2738
55	14.51	4024
60	15.72	3897
65	18.03	5233
70	19.38	4662
75	22.93	6111
80	22.4	5318
85	18.46	4714

Figure 85 presents the altitude performance from the time the control system is turned on until the end of simulation for $\alpha = 35 : 5 : 85$ deg. This data is tabulated in Table 21 which clearly indicates that the higher α spins require more time and, subsequently altitude, to recover. Markers have been placed that indicate when the IRL, MAL, OPL have positively engaged. The MAL engages within a few execution cycles after IRL engagement and is observed by the coincident markers in the figure. This demonstrates the ability of the IRL to rapidly gain positive control of the aircraft. In Figure 85, note how the IRL is consistently engaged in the initial descent after the spin motion is halted, and after OPL engagement the aircraft quickly levels off after the recovery ascent. Following the initial MAL engagement α quickly approaches α_c thereby increasing lift and arresting the descent. The period between the minimum altitude and the engagement of the OPL corresponds to the MAL decaying α_c which is characterized by the gradual decrease in ascent rate.

The next obvious question that needs to be addressed is how does this performance compare to the actual aircraft? Though not a direct comparison, the altitude loss for recovery from the F-18 falling leaf mode is presented in Reference 8. In this work two charts are presented, one for the altitude loss pertaining to an improved control software release and the other for pilot dive recovery inputs. The improved software had most occurrences in the range of 4000 to 6000 feet whereas the pilot dive recovery predominantly occurred in the

range of 5000 to 7000 feet. Another comparison is that of the work presented in Reference 73 which utilizes the F/A-18 FCC version 10.7. Data tabulated in this work indicates that the altitude loss with the pilot alerting spin arrows present is in the range of 2200 to 4400 feet. However, this altitude only reflects the loss while arresting the spin, and not the recovery from descent as presented in this thesis. Provided these two reference points the altitude loss demonstrated in this thesis is reasonable.

CHAPTER 7
CONCLUSION

7.1 Conclusion

This thesis provided further evidence supporting the validity of nonlinearity index theory. This validity was accomplished by utilizing the unconstrained rotational and translational six degree of freedom spin motion framework. The application of nonlinearity index theory provided a systematic process to scrutinize an otherwise complex and large aerodynamic database and dynamic model. The results supported the ability of nonlinearity index theory to identify highly nonlinear areas of the aerodynamic database, thereby reducing the need to scrutinize every table manually.

Extending the previous work of Tapolcai the spin condition was first expanded beyond the three rotational degrees of freedom to also include translational motion. This extension involved utilizing the complete rotational and translational six degree of freedom framework commonly used in aircraft simulation. Further, this required a more thorough system model of the F-18 HARV to include actuator nonlinearities, dynamics, and a simplified propulsion model.

The criteria defining a steady state spin condition was then provided using a rotation sequence adopted from Reference 32. This definition was then applied to create a trim database over the envelope of the aerodynamic model. The accuracy of the trim database was scrutinized to ensure subsequent analysis using the database would be accurate and not misleading. This analysis uncovered regions with insufficient trim accuracy that were removed from the remaining analysis. Further, observations regarding the instability of the spin conditions were noted.

Methods for model linearization were introduced with a primary focus on perturbation theory. Numerical perturbation methods were implemented and tested on both the MATLAB System and Simulink models. Rigorous testing was conducted comparing the output of the custom linearization code with the built-in tools provided with the Simulink Control Design Toolbox. This process of testing uncovered minor coding mistakes and ultimately lead to high confidence in the linearized models. The linearized and nonlinear models were simulated in parallel with perturbations applied to all states and inputs independently; the results solidified the confidence in the models.

Nonlinearity index theory was then formally introduced as a systematic process to evaluate system nonlinearities. This method of analysis provided a straightforward methodology to analyze the dynamics of the aircraft model. Utilizing the trim database NIT was applied across the aerodynamic envelope and uncovered regions with high nonlinearities. The aerodynamic database was then inspected in this region uncovering the highly nonlinear behavior of $C_{n,p}$. Nonlinear simulations with perturbations were then carried out for both high and low NI. Due to the known instabilities in the trim models the specific values of α for comparison were carefully chosen to ensure the unstable poles between the models were similar. In order to provide a quantitative measurement a normalized mean square error between the linear and nonlinear models was calculated. Comparing the duration that the fit was at least 95% between the low and high NI simulations supported the underlying theory of the NI; that is, the high NI diverged faster than the low NI.

Nonlinear dynamic inversion theory was then introduced, first with linear dynamic inversion as a simpler presentation of the underlying theory and concepts along with a trivial example. The linear theory was subsequently expanded to the nonlinear case. Further, the concept of control allocation was introduced along with the graphical representation of the attainable moment subset. The AMS was utilized as an easy to understand method of comparing control allocation strategies.

Utilizing the formally introduced concepts a nonlinear dynamic inversion controller was designed for the F-18 HARV. The design took into consideration requirements and recommendations from military standards such as MIL-STD-1797B and MIL-F-8785C. The velocity vector roll maneuver was introduced along with the governing equations that define the required accelerations. This acceleration information was then used in conjunction with the AMS in order to prescribe inner rate loop reference dynamics that closely adhered to the military specifications while not exceeding aircraft capabilities. Outer loops were then designed utilizing time scale separation principles. Basic frequency response concepts were introduced and were subsequently applied to the system to ensure compliance with gain and phase margins prescribed in MIL-DTL-9490E.

A multi-mode control logic for spin recovery was then implemented unifying the IRL, MAL, and OPL controllers. This recovery strategy leveraged common spin recovery strategies, specifically, full counter-spin rudder deflection to arrest the initial spin motion while neutralizing ailerons and stabilators. In order to provide a complete recovery system the controller targeted angle-of-attack to maximize the lift coefficient once the spin motion was

arrested thereby minimizing altitude loss. Once a positive rate of climb was attained the system gradually enabled the OPL in order to recover to straight and level flight. All together, the system was designed to fully recover from spin without any manual pilot inputs.

Lastly, numerous nonlinear simulations were conducted to validate the system. In total, 500 simulations were executed over the range of thirty-one to eighty-five degrees angle-of-attack. This data set provided sufficient evidence to demonstrate that the system is capable of successfully recovering from a wide range of spin conditions and not just a few test cases.

7.2 Recommendations

Future work expanding on this thesis may include determining the cause of the longitudinal frequency response's inaccurate representation of the broken loop system response. Another potential interesting topic of research may be utilizing the nonlinearity index theory as a means to quantify how well a control system linearizes an aircraft plant. Further, the spin recovery strategy could be optimized. Possible means to optimize recovery could include active feedback of lift coefficient estimates or by simultaneously arresting the spin while targeting a positive climb rate. Lastly, the F-18 HARV has vectored thrust capabilities which were not considered and could be leveraged.

REFERENCES

1. Abzug, M. J., and Larrabee, E. E., *Airplane Stability And Control: A History Of The Technologies That Made Aviation Possible*, second edition ed., Cambridge University Press, New York, 2002.

2. Joyce, D. A., and Joyce, D. A., *Flying Beyond The Stall The X-31 and The Advent Of Supermaneuverability*, National Aeronautics and Space Administration, Washington, DC, 2014.

3. Jamarillo, P., and Ralston, J., "Simulation of the F/A-18D 'Falling Leaf'," 21st Atmospheric Flight Mechanics Conference, AIAA, 1996. doi:10.2514/6.1996-3371.

4. Droste, C. S., and Walker, J., *The General Dynamics Case Study on the F-16 Fly-by-Wire Flight Control System*, AIAA, New York, 1985. doi:10.2514/4.867873.

5. Barfield, A., and Dazzo, J., "Multivariable Control Laws for the AFTI/F-16," 22nd Aerospace Sciences Meeting, AIAA, 1984. doi:10.2514/6.1984-237.

6. McMonagle, D., "AFTI/F-16, Task Tailoring of the Flight Control System," 2nd Flight Testing Conference, AIAA, 1983. doi:10.2514/6.1983-2748.

7. Pahle, J. W., Powers, B., Regenie, V., Chacon, V., Degroote, S., and Murnyak, S., "Research Flight-Control System Development for the F-18 High Alpha Research Vehicle," NASA-TM-104232, NASA Dryden Flight Research Facility, Edwards, California, 1991.

8. Heller, M., David, R., and Holmberg, J., "Falling Leaf Motion Suppression in the F/A-18 Hornet with Revised Flight Control Software," 42nd Aerospace Sciences Meeting and Exhibit, AIAA, 2004. doi:10.2514/6.2004-542.

9. Harris, J., and Black, G., "F-22 Control Law Development and Flying Qualities," 21st Atmospheric Flight Mechanics Conference, AIAA, 1996. doi:10.2514/6.1996-3379.

10. Harris, J. J., "F-35 Flight Control Law Design, Development and Verification," 2018 Aviation Technology, Integration, and Operations Conference, AIAA, 2018. doi:10.2514/5.9781624105678.0287.0312.

11. Walker, G., and Allen, D., "X-35B STOVL Flight Control Law Design and Flying

Qualities," 2002 Biennial International Powered Lift Conference and Exhibit, AIAA, 2002. doi:10.2514/6.2002-6018.

12. Bordignon, K., and Bessolo, J., "Control Allocation for the X-35B," 2002 Biennial International Powered Lift Conference and Exhibit, AIAA, 2018. doi:10.2514/6.2002-6020.

13. Newman, B., and Kassem, A., "Analytical Relationships for Linear Quadratic Aeroelastic Flight Control Eigenvalues," *Journal of Guidance, Control, and Dynamics*, Vol. 20, No. 6, 1997, pp. 1149–1156. doi:10.2514/2.4170.

14. Jahnke, C., and Culick, F. E. C., "Application of Bifurcation Theory to the High-Angle-of-Attack Dynamics of the F-14," *Journal of Aircraft*, Vol. 31, No. 1, 1994, pp. 26–34. doi:10.2514/3.46451.

15. Vora, A. S., and Sinha, N. K., "Direct Methodology for Constrained System Analysis with Applications to Aircraft Dynamics," *Journal of Aircraft*, Vol. 54, No. 6, 2017, pp. 2378–2385. doi:10.2514/1.C034264.

16. Mehra, R. K., Washburn, R. B., Sajan, S., and Carroll, J. V., "A Study of the Application of Singular Perturbation Theory," NASA-CR-3167, NASA Langley Research Center, Hampton, Virginia, 1979.

17. Omran, A. K., and Newman, B., "Piecewise Global Volterra Nonlinear Modeling and Characterization for Aircraft Dynamics," *Journal of Guidance, Control, and Dynamics*, Vol. 32, No. 3, 2009, pp. 749–759. doi:10.2514/1.40655.

18. Omran, A., and Newman, B., "Full Envelope Nonlinear Parameter-Varying Model Approach for Atmospheric Flight Dynamics," *Journal of Guidance, Control, and Dynamics*, Vol. 35, No. 1, 2012, pp. 270–283. doi:10.2514/1.51577.

19. Omran, A., and Newman, B., "Nonlinearity Index Theory for Aircraft Dynamic Assessment," *Journal of Guidance, Control, and Dynamics*, Vol. 36, No. 1, 2013, pp. 293–303. doi:10.2514/1.53906.

20. Abdallah, A. M., Newman, B. A., and Omran, A. M., "Measuring Aircraft Nonlinearity Across Aerodynamic Attitude Flight Envelope," Atmospheric Flight Mechanics (AFM) Conference, AIAA, 2013. doi:10.2514/6.2013-4985.

21. Tran, T. T., and Newman, B. A., "Integrator-Backstepping Control Design for Nonlinear Flight System Dynamics," Guidance, Navigation, and Control Conference, AIAA SciTech Forum, 2015. doi:10.2514/6.2015-1321.

22. Namba, T., and Uchiyama, K., "Fault-Tolerant Adaptive Flight Control System Using Feedback Linearization," Guidance, Navigation, and Control Conference, AIAA, 2011. doi:10.2514/6.2011-6717.

23. Enns, D., Bugajski, D., Hendrick, R., and Stein, G., "Dynamic Inversion: An Evolving Methodology for Flight Control Design," *International Journal of Control*, Vol. 59, 1994, pp. 71–91. doi:10.1080/00207179408923070.

24. Steinberg, M., and Page, A., "Nonlinear Adaptive Flight Control With A Backstepping Design Approach," Guidance, Navigation, and Control Conference and Exhibit, AIAA, 1998. doi:10.2514/6.1998-4230.

25. Tapolcai, D., Omran, A., and Newman, B., "Aircraft Spin Phenomenon Analysis Using Nonlinearity Index Theory," Guidance, Navigation, and Control and Co-located Conferences, AIAA, 2012. doi:10.2514/6.2012-4401.

26. Tapolcai, D., Omran, A., and Newman, B., "Aircraft Stall Phenomenon Analysis Using Nonlinearity Index Theory," Guidance, Navigation, and Control and Co-located Conferences, AIAA, 2012. doi:10.2514/6.2012-4403.

27. Tapolcai, D. P., "Nonlinearity Index Analysis of Periodic-Chaotic Stall-Spin Aircraft Motion," Master's thesis, Old Dominion University, 2013.

28. Tapolcai, D. P., Omran, A., and Newman, B., "Aircraft Stall Phenomenon Analysis Using Nonlinearity Index Theory," *Aerospace Science and Technology*, Vol. 68, 2017, pp. 288 – 298. doi:10.1016/j.ast.2017.04.008.

29. Bryant, L. W., and Gates, S. B., "The Spinning of Aeroplanes," Vol. 31, No. 199, 1927, pp. 619–688. doi:10.1017/S0368393100135448.

30. Yangos, P. J., and Yangos, J. P., "Spin: Angles And Inertial Moments," Vol. 85, No. 846, 1981, pp. 270–276. doi:10.1017/S0001924000029912.

31. Bihrle, W., and Barnhart, B., "Spin Prediction Techniques," *Journal of Aircraft*, Vol. 20, No. 2, 1983, pp. 97–101. doi:10.2514/3.44837.

32. Phillips, W. F., and Anderson, E. A., "Analytical Approximation for the Mechanics of Airplane Spin," *Journal of Aircraft*, Vol. 39, No. 6, 2002, pp. 1084–1088. doi:10.2514/2.3041.

33. Tischler, M. B., and Barlow, J. B., "Determination of the Spin and Recovery Characteristics of a General Aviation Design," *Journal of Aircraft*, Vol. 18, No. 4, 1981, pp. 238–244. doi:10.2514/3.57487.

34. Tischler, M., and Barlow, J., "Application Of The Equilibrium Spin Technique To A Typical Low-wing General Aviation Design," Guidance, Navigation, and Control and Co-located Conferences, AIAA, 1979. doi:10.2514/6.1979-1625.

35. Tischler, M. B., and Barlow, J. B., "Dynamic Analysis of the Flat Spin Mode of a General Aviation Aircraft," *Journal of Aircraft*, Vol. 19, No. 3, 1982, pp. 198–205. doi:10.2514/3.57376.

36. Engelbrecht, J., Pauck, S., and Peddle, I., "Bifurcation Analysis and Simulation of Stall and Spin Recovery for Large Transport Aircraft," Guidance, Navigation, and Control and Co-located Conferences, AIAA, 2012. doi:10.2514/6.2012-4801.

37. Junkins, J., "Adventures On The Interface Of Dynamics And Control," Aerospace Sciences Meetings, AIAA, 1997. doi:10.2514/6.1997-2.

38. Junkins, J., and Singla, P., "How Nonlinear Is It? A Tutorial on Nonlinearity of Orbit and Attitude Dynamics," *Journal of the Astronautical Sciences*, Vol. 52, No. 1-2, 2004, pp. 7–60.

39. Omran, A., and Newman, B., "Nonlinearity Index Theory for Flight Mechanics Applications," Guidance, Navigation, and Control and Co-located Conferences, AIAA, 2010. doi:10.2514/6.2010-7624.

40. Omran, A., and Newman, B., "Nonlinearity Index Theory for Aircraft Dynamic Assessment," *Journal of Guidance, Control, and Dynamics*, Vol. 36, No. 1, 2012, pp. 293–303. doi:10.2514/1.53906.

41. Mu, R., and Cheng, C., "Controller Design of Complex System Based on Nonlinear Strength," Mathematical Problems in Engineering, Hindawi, 2015. doi:10.1155/2015/523197.

42. Honeywell Technology Center, Lockheed Martin Skunk Works, and Lockheed Martin Tactical Aircraft Systems, *Application of Multivariable Control Theory to Aircraft Control Laws*, Flight Dynamics Directorate Wright Laboratory, Hanover, MD, 1996.

43. Miller, C., "Nonlinear Dynamic Inversion Baseline Control Law: Architecture and Performance Predictions," Guidance, Navigation, and Control and Co-located Conferences, AIAA, 2011. doi:10.2514/6.2011-6467.

44. Snell, S. A., Enns, D. F., and Garrad, W. L., "Nonlinear Inversion Flight Control for a Supermaneuverable Aircraft," *Journal of Guidance, Control, and Dynamics*, Vol. 15, No. 4, 1992, pp. 976–984. doi:10.2514/3.20932.

45. Reiner, J., Balas, G. J., and Garrard, W. L., "Flight Control Design Using Robust Dynamic Inversion and Time-scale Separation," *Automatica*, Vol. 32, No. 11, 1996, pp. 1493–1504. doi:10.1016/S0005-1098(96)00101-X.

46. Lane, S. H., and Stengel, R. F., "Flight Control Design Using Non-linear Inverse Dynamics," *Automatica*, Vol. 24, No. 4, 1988, pp. 471–483. doi:10.1016/0005-1098(88)90092-1.

47. Raghavendra, P., Sahai, T., Kumar, P. A., Chauhan, M., and Ananthkrishnan, N., "Aircraft Spin Recovery, With and Without Thrust Vectoring, Using Nonlinear Dynamic Inversion," *Journal of Aircraft*, Vol. 42, No. 6, 2005, pp. 1492–1503. doi:10.2514/1.12252.

48. Moorhouse, D. J., and Woodock, R. J., *Background Information and User Guide for MIL-F-8785C, Military Specification - Flying Qualities of Piloted Airplanes*, Control Dynamics Branch Flight Control Division, Department of Defense, 1982.

49. Stevens, B. L., *Aircraft Control And Simulation*, Wiley, Hoboken, New Jersey, 2003.

50. Etkin, B., *Dynamics of atmospheric flight*, Mineola, N.Y. : Dover Publications, Mineola, New York, 2005.

51. Marco, A. D., "Flight Mechanics For Pilots," `https://agodemar.github.io/FlightMechanics4Pilots/mypages/anatomy-flight/`, February 2019.

52. Sinha, N. K., *Elementary Flight Dynamics with an Introduction to Bifurcation and Continuation Methods*, CRC Press, New York, 2014. doi:10.1201/b15956.

53. Marco, A. D., Duke, E., and Berndt, J., "A General Solution to the Aircraft Trim

Problem," Modeling and Simulation Technologies Conference and Exhibit, AIAA, 2007. doi:10.2514/6.2007-6703.

54. Curry, M., and Dunbar, B., "Documentation for Dynamic Inversion Control Law for RFCS," Dryden Flight Research Center, Edwards, California. `https://www.nasa.gov/centers/dryden/history/pastprojects/HARV/Work/NASA2/nasa2.html`, March 2008.

55. Johnson, S. A., "A Simple Dynamic Engine Model for Use in a Real-Time Aircraft Simulation with Thrust Vectoring," NASA-TM-4240, Dryden Flight Research Facility, Edwards, California, 1990.

56. Strickland, M. E., Bundick, W. T., and Messina, M. D., "Simulation Model of the FA-18 High Angle-of-Attack Research Vehicle Utilized for the Design of Advanced Control Laws," NASA-TM-110216, Langley Research Center, Hampton, Virginia, 1996.

57. Buttrill, C. S., and Arbuckle, P. D., "Simulation Model of a Twin-Tail, High Performance Airplane," NASA-TM-107601, Langley Research Center, Hampton, Virginia, 1992.

58. Rauscher, M., *Introduction to Aeronautical Dynamics*, Wiley, New York, 1953.

59. McCormick, B. W., "Equilibrium Spinning of a Typical Single-Engine Low-Wing Light Aircraft," *Journal of Aircraft*, Vol. 18, No. 3, 1981, pp. 192–199.

60. MATLAB, *version 9.3 (R2017b)*, The MathWorks Inc., Natick, Massachusetts, 2017.

61. Lombaerts, T., and Looye, G., "Design And Flight Testing Of Nonlinear Autoflight Control Laws," Guidance, Navigation, and Control and Co-located Conferences, AIAA, 2012. doi:10.2514/6.2012-4982.

62. Bordignon, K. A., Beck, R., and Durham, W., *Aircraft Control Allocation*, Wiley, Chichester, West Sussex, England, 2016. doi:10.1002/9781118827789.

63. *172S Skyhawk Information Manual*, Cessna, 2004.

64. Yang, W. Y., Cao, W., Chung, T.-S., and Morris, J., *Applied Numerical Methods Using MATLAB*, Wiley-Interscience, Hoboken, New Jersey, 2005. doi:10.1002/0471705195.

65. Department of Defense, *Flying Qualities of Piloted Aircraft*, 1997.

66. Smit, M., and Craig, I., "Robust Flight Controller Design Using H-Infinity Loop-shaping And Dynamic Inversion Techniques," Guidance, Navigation, and Control Conference and Exhibit, AIAA, 1998. doi:10.2514/6.1998-4132.

67. Adams, R. J., and Banda, S. S., "Robust Flight Control Design Using Dynamic Inversion and Structured Singular Value Synthesis," *Transactions on Control Systems Technology*, Vol. 1, No. 2, 1993, pp. 80–92. doi:10.1109/87.238401.

68. Durham, W. C., Lutze, F. H., and Mason, W., "Kinematics and Aerodynamics of Velocity-vector Roll," *Journal of Guidance, Control, and Dynamics*, Vol. 17, No. 6, 1994, pp. 1228–1233. doi:10.2514/3.21337.

69. Department of Defense, "Flight Control Systems - Design, Installation, and Test of Piloted Aircraft, General Specification for," U.S. Air Force, MIL-F-9490E, 2008.

70. Tischler, M. B., and Remple, R. K., *Aircraft and Rotorcraft System Identification, Second Edition*, AIAA Education Series, Blacksburg, Virginia, 2012. doi:10.2514/4.868207.

71. Bunge, R., and Kroo, I., "Automatic Spin Recovery with Minimal Altitude Loss," SciTech Forum, AIAA, 2018. doi:10.2514/6.2018-1866.

72. Engelbrecht, J. A., Pauck, S. J., and Peddle, I. K., "A Multi-Mode Upset Recovery Flight Control System for Large Transport Aircraft," Guidance, Navigation, and Control and Co-located Conferences, AIAA, 2013. doi:10.2514/6.2013-5172.

73. Park, D. J., "Development of the F/A-18 Spin Departure Demonstration Procedure with Departure Resistant Flight Control Computer Version 10.7," Master's thesis, University of Tennessee, 2004.

APPENDIX A
F-18 HARV SIMULATION

A.1 Axes Definitions

A.1.1 Rotation Matrices

In the following rotation matrices the subscript convention is given as $R_{xb,xa}$ resulting in $\vec{x}_b = R_{xb,xa}\vec{x}_a$. Thus $R_{xb,xa}$ transforms from axis a to axis b. Since a transformation matrix is orthogonal, the inverse transformation is given by the transpose, $R_{xa,xb} = R_{xb,xa}^{\mathsf{T}}$.

Body to Earth-fixed NED

The transformation from the body axes b to the inertial NED frame

$$R_{E_{NED},b} = \begin{bmatrix} \cos\theta\cos\psi & -\cos\varphi\sin\psi + \sin\varphi\sin\theta\cos\psi & \sin\varphi\sin\psi + \cos\varphi\sin\theta\cos\psi \\ \cos\theta\sin\psi & \cos\varphi\cos\psi + \sin\varphi\sin\theta\sin\psi & -\sin\varphi\cos\psi + \cos\varphi\sin\theta\sin\psi \\ -\sin\theta & \sin\varphi\cos\theta & \cos\varphi\cos\theta \end{bmatrix} \tag{A.1-1}$$

Body to Stability

The transformation from the body axis b to the stability axis s

$$R_{s,b} = \begin{bmatrix} \cos\alpha & 0 & \sin\alpha \\ 0 & 1 & 0 \\ -\sin\alpha & 0 & \cos\alpha \end{bmatrix} \tag{A.1-2}$$

Stability to Wind

The transformation from the stability axis s to the wind axis w

$$R_{w,s} = \begin{bmatrix} \cos\beta & \sin\beta & 0 \\ -\sin\beta & \cos\beta & 0 \\ 0 & 0 & 1 \end{bmatrix} \tag{A.1-3}$$

Body to Wind

The transformation from the body axis b to the wind axis w

$$R_{w,b} = R_{w,s}R_{s,b} = \begin{bmatrix} \cos\alpha\cos\beta & \sin\beta & \sin\alpha\cos\beta \\ -\cos\alpha\sin\beta & \cos\beta & -\sin\alpha\sin\beta \\ -\sin\alpha & 0 & \cos\alpha \end{bmatrix} \tag{A.1-4}$$

Individual Rotation Matrices

The 3-2-1 Euler rotations for body axis,

$$R_\psi = \begin{bmatrix} \cos\psi & -\sin\psi & 0 \\ \sin\psi & \cos\psi & 0 \\ 0 & 0 & 1 \end{bmatrix} \tag{A.1-5}$$

$$R_\theta = \begin{bmatrix} \cos\theta & 0 & \sin\theta \\ 0 & 1 & 0 \\ -\sin\theta & 0 & \cos\theta \end{bmatrix} \tag{A.1-6}$$

$$R_\varphi = \begin{bmatrix} 1 & 0 & 0 \\ 0 & \cos\varphi & -\sin\varphi \\ 0 & \sin\varphi & \cos\varphi \end{bmatrix} \tag{A.1-7}$$

The 3-2-1 wind axis rotations,

$$R_\chi = \begin{bmatrix} \cos\chi & -\sin\chi & 0 \\ \sin\chi & \cos\chi & 0 \\ 0 & 0 & 1 \end{bmatrix} \tag{A.1-8}$$

$$R_\gamma = \begin{bmatrix} \cos\gamma & 0 & \sin\gamma \\ 0 & 1 & 0 \\ -\sin\gamma & 0 & \cos\gamma \end{bmatrix} \tag{A.1-9}$$

$$R_\mu = \begin{bmatrix} 1 & 0 & 0 \\ 0 & \cos\mu & -\sin\mu \\ 0 & \sin\mu & \cos\mu \end{bmatrix} \tag{A.1-10}$$

Rotations required from wind to body,

$$R_\alpha^\mathsf{T} = \begin{bmatrix} \cos\alpha & 0 & -\sin\alpha \\ 0 & 1 & 0 \\ \sin\alpha & 0 & \cos\alpha \end{bmatrix} \tag{A.1-11}$$

$$R_{-\beta}^\mathsf{T} = \begin{bmatrix} \cos\beta & -\sin\beta & 0 \\ \sin\beta & \cos\beta & 0 \\ 0 & 0 & 1 \end{bmatrix} \tag{A.1-12}$$

A.2 Block Diagram Conventions

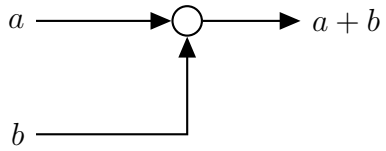

Figure 86 Block Diagram Summing Junction

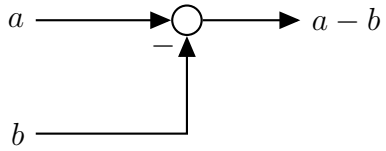

Figure 87 Block Diagram Summing Junction, Negative Input

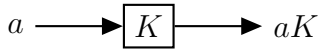

Figure 88 Block Diagram Gain

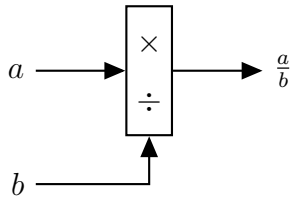

Figure 89 Block Diagram Division

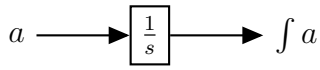

Figure 90 Block Diagram Integrator

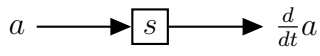

Figure 91 Block Diagram Differentiation

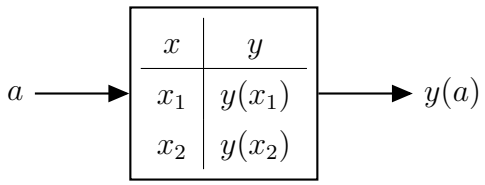

Figure 92 Block Diagram Table

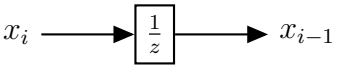

Figure 93 Block Diagram Unit Delay

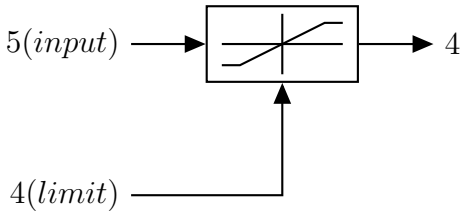

Figure 94 Block Diagram Saturation

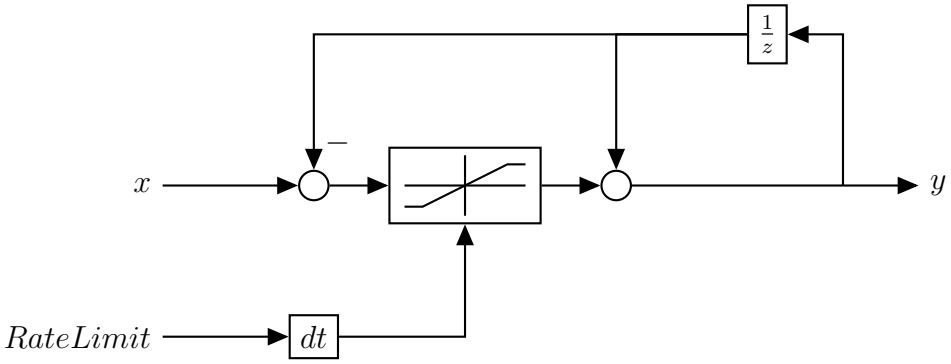

Figure 95 Block Diagram Rate Limit

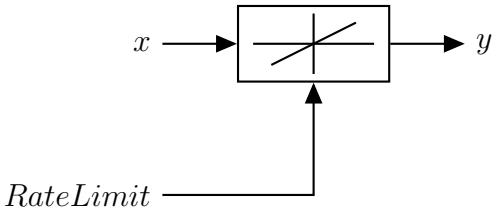

Figure 96 Rate Limit Block Diagram Mask

Table 22 Trim Solver Constraints

Parameter	min	max
V	100 (ft/s)	Mach 0.8
R (ft)	1e-3	500
σ	$-90°$	$90°$
φ	$-90°$	$90°$
θ	$-90°$	$0°$
δ_a	$-25°$	$42°$
δ_e	$-24°$	$10.5°$
δ_r	$-30°$	$30°$

A.3 Trim Solution Database

The trim solution database was generated numerically using the built in routine *lsqnonlin*. This solver is tailored for solving nonlinear systems and enables constraints to be placed on the free variables. The constraints proved necessary in order to generate physically attainable results. The constraints utilized are presented in Table 22

The trim solutions used to generate the nonlinearity index were inspected for validity by inspecting the state derivative values and agreement of the solved and specified α. The desired state derivative error (from zero) is $|\text{error}| < 1e-6$ where the angular units are measured in degrees. A summary of the solutions is presented in Table 23 and Figure 98 and demonstrates that the majority of the solutions are reasonably close to steady state. The trim states are presented in Figure 99 as a function of the desired spin α. Similarly, Figure 100 depicts the state derivatives affiliated with the desired spin α where the ideal value for all parameters is zero. The calculated spin radius is presented in Figure 102 and shows that solutions for $\alpha < 55$ yielded a spin radius greater than the wingspan.

From Figure 100 it is observed that the worse trim errors are encountered at high α spin conditions. This is seen more clearly in the general case presented in Figure 97.

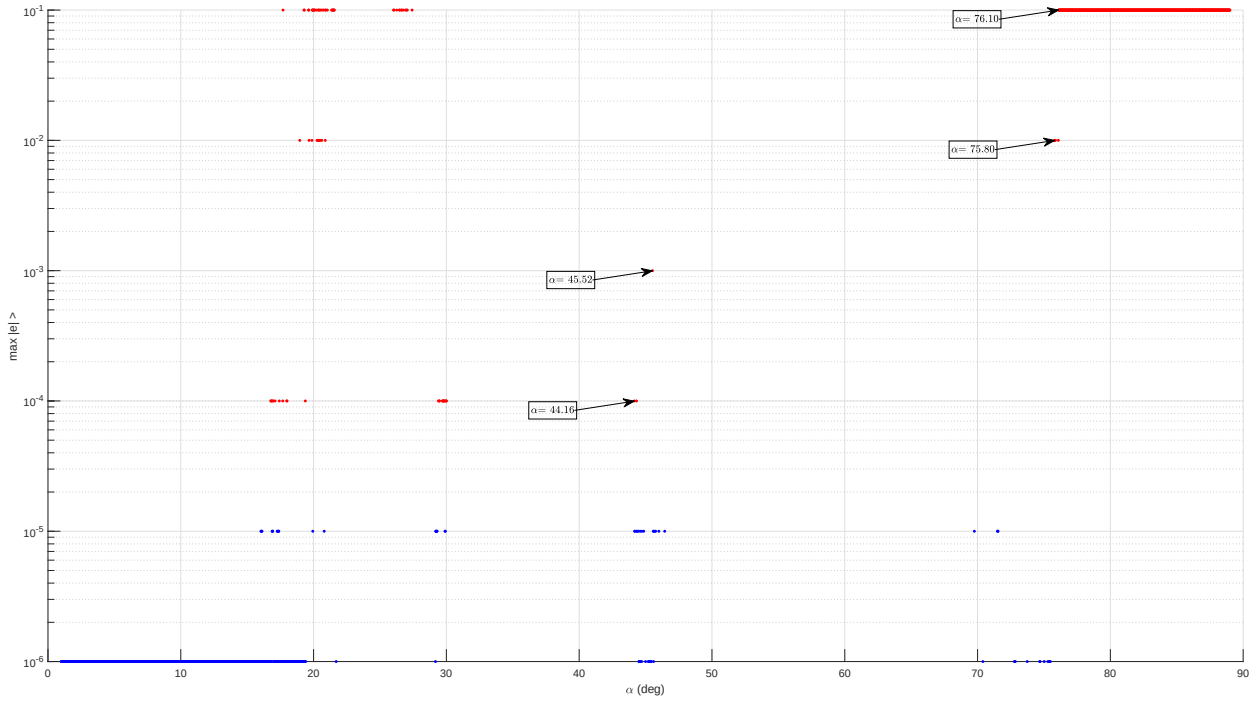

Figure 97 Maximum Trim Error vs. Alpha

Table 23 Nonlinearity Index Trim Solutions (4401 solutions)

	min	avg	max	> 37.42 (ft) (%)	left (%)	right (%)
R (ft)	1.484	30.79	78.22	42.7		
Ω (rpm)	-19.11	-8.65	22.42		88.1	11.9

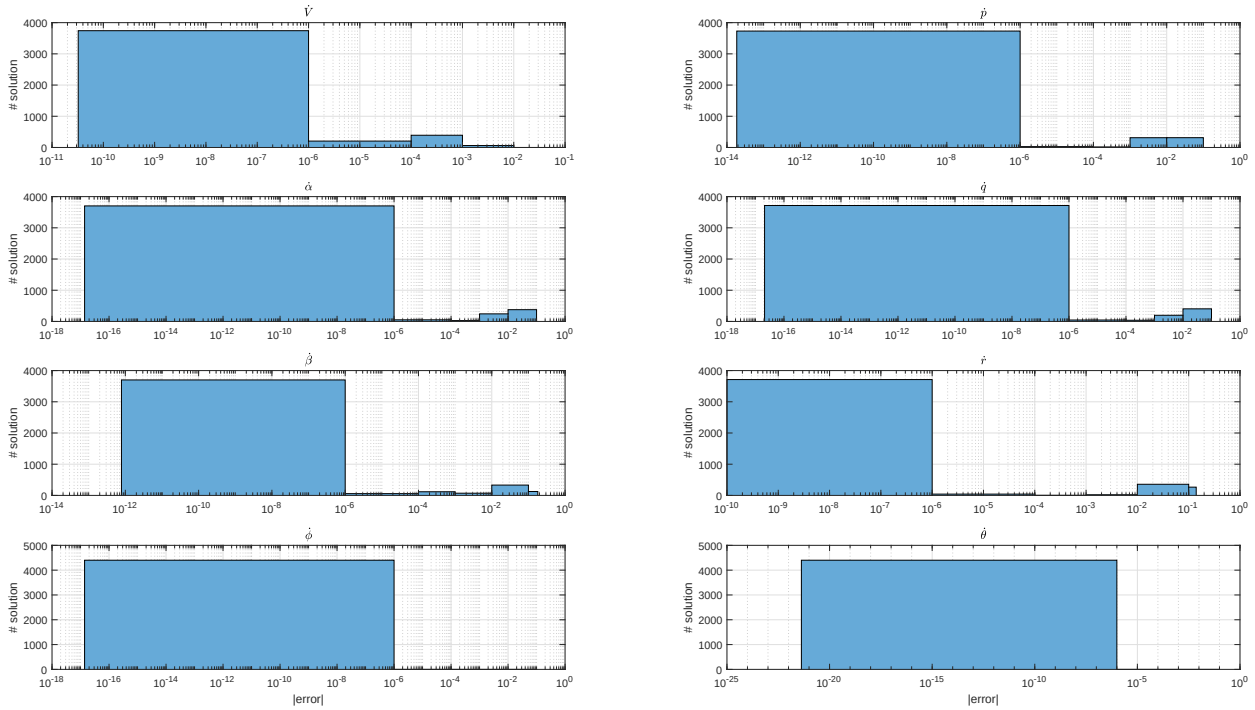

Figure 98 Trim Solution Error Histogram

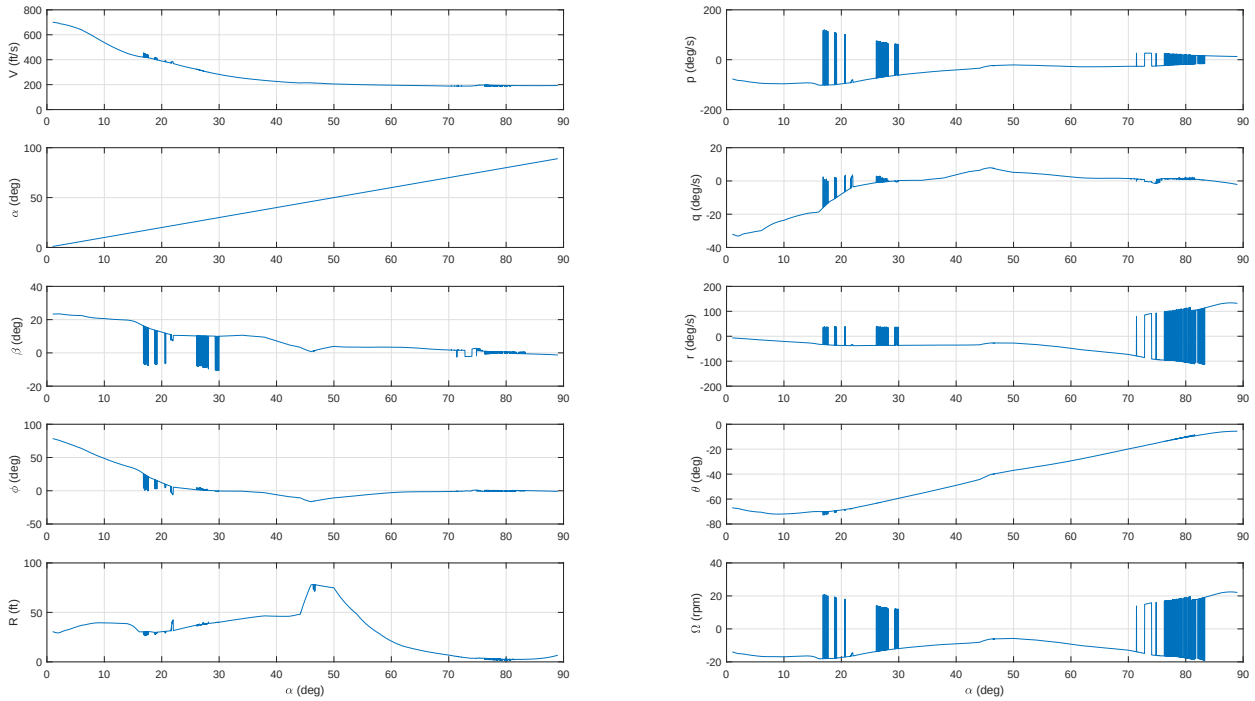

Figure 99 Spin Trim States

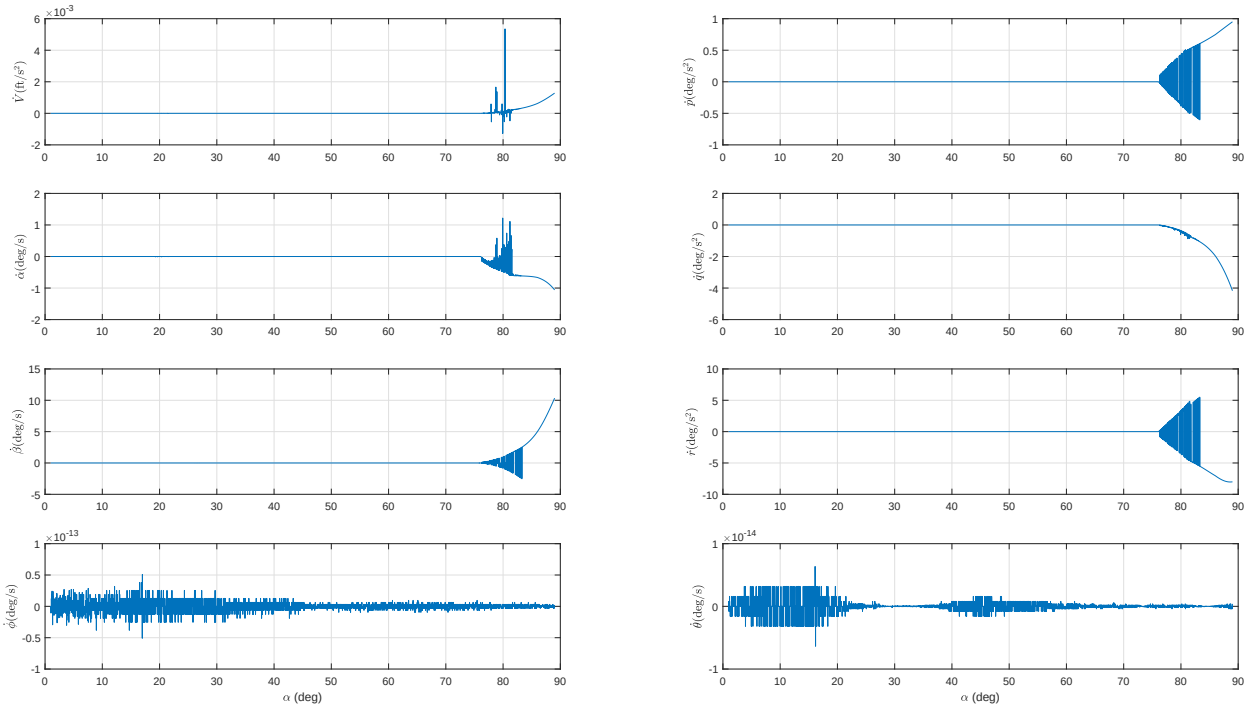

Figure 100 Spin Trim State Derivatives

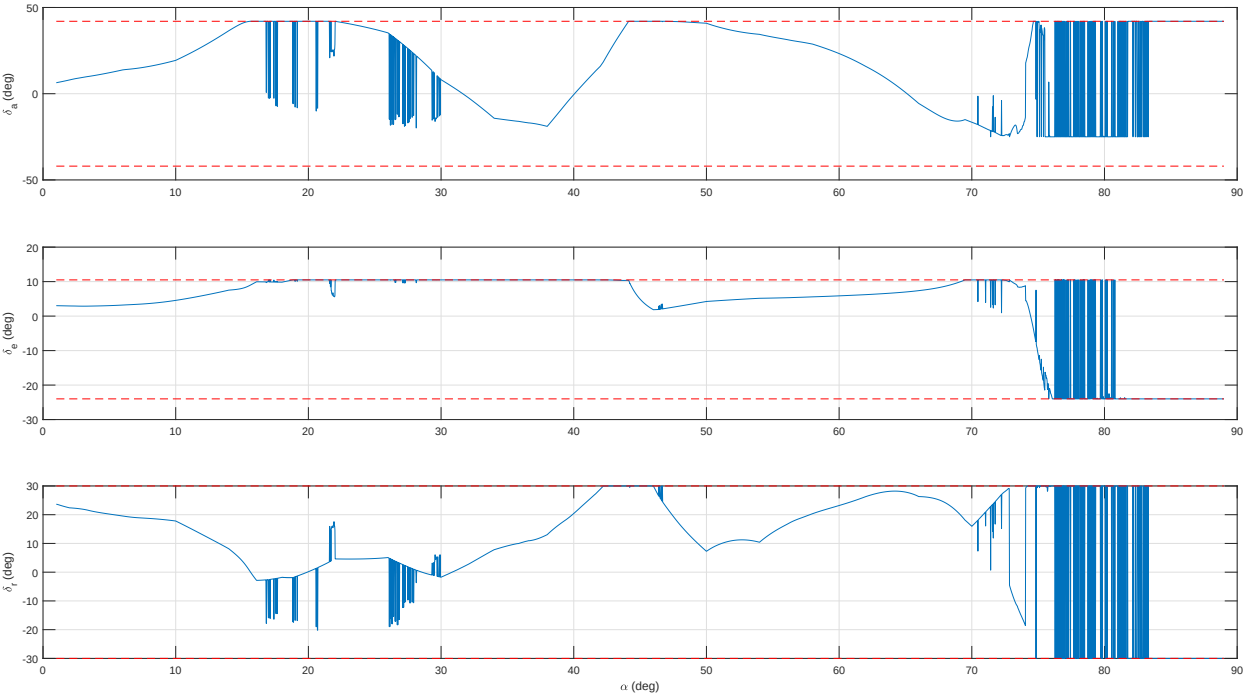

Figure 101 Spin Trim Controls

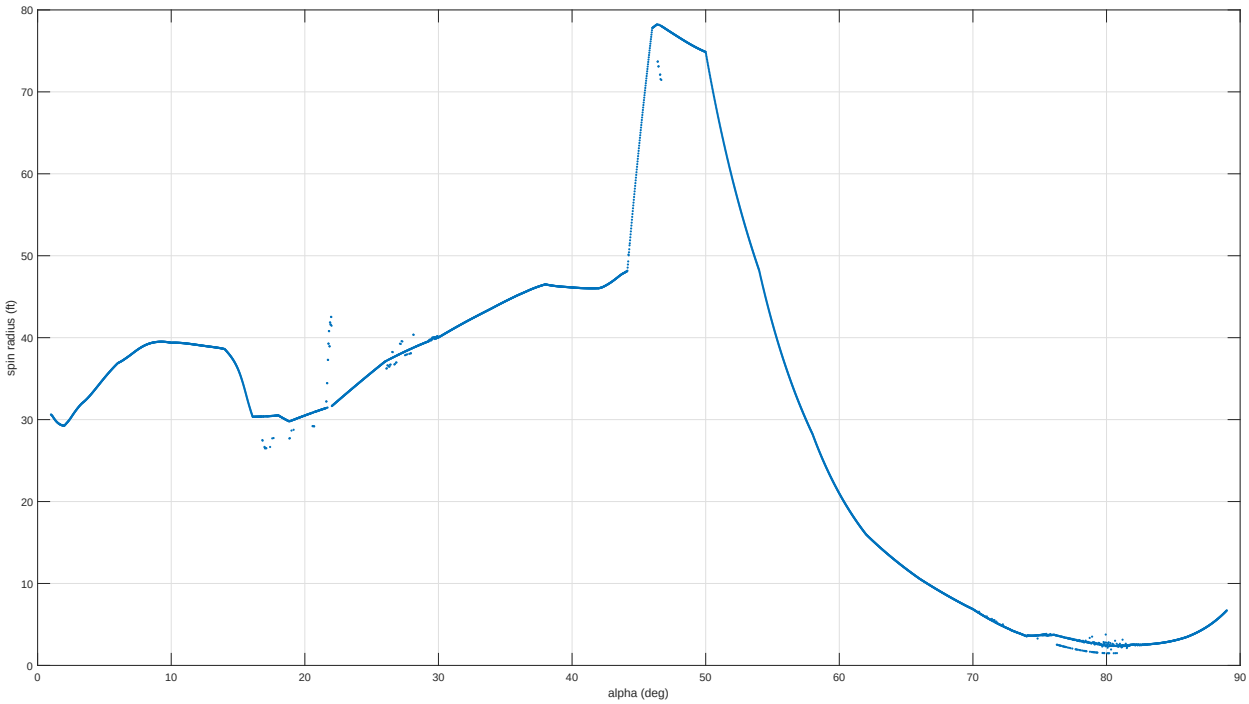

Figure 102 Spin Radius vs. Alpha

Trim Solution Stability

Through nonlinear simulations it was discovered that the model was unstable over most of the range of α. The instability resulted in divergence from steady state even for an accurate trim solution. Initially it was thought that the divergence may be a result of numerical error in the trim solution; however, this was disproved by simulation.

To prove that the instability is the source of divergence, let us compare the stable model at $\alpha = 56.36°$, $\max \text{real(ev)} = -6.2179\text{e}{-5}$ to the unstable model at $\alpha = 56.38°$, $\max \text{real(ev)} = 2.1155\text{e}{-4}$. Figure 104 shows that after 25e3 seconds the unstable model diverges. Noting Figure 103 and Table 24 the difference between the trim points is negligible while the behavior when simulated is not.

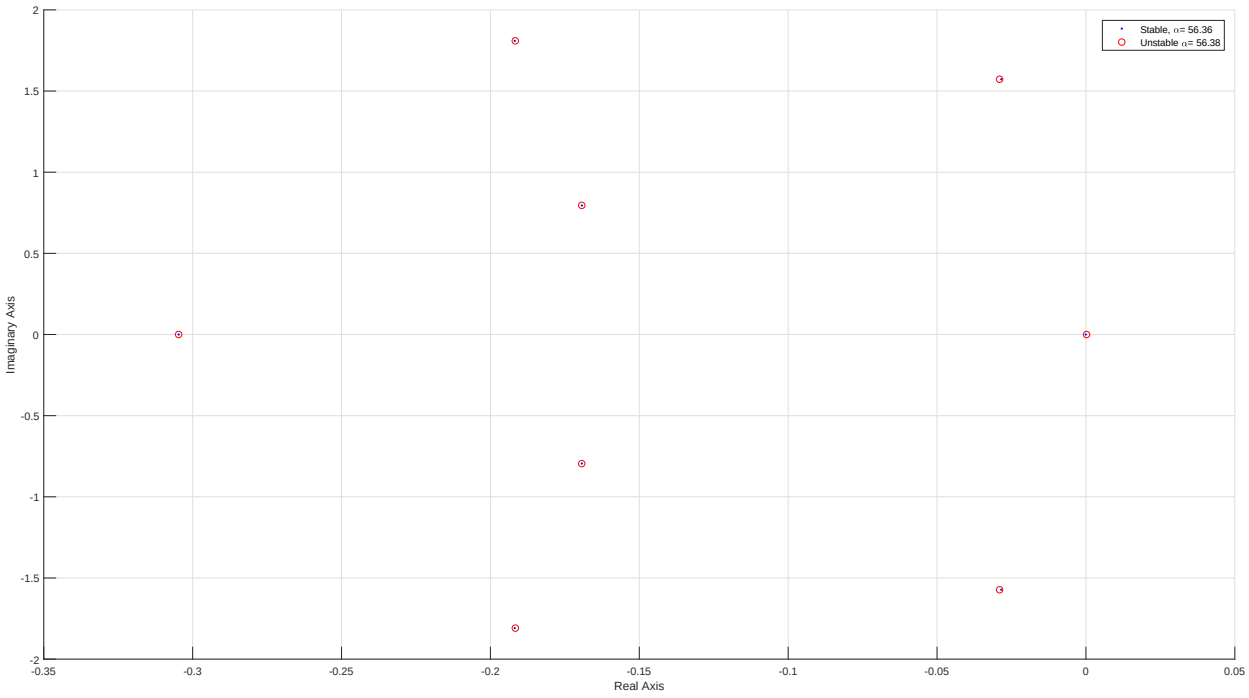

Figure 103 Eigen Values, $\alpha = 56.36, 56.38$ deg

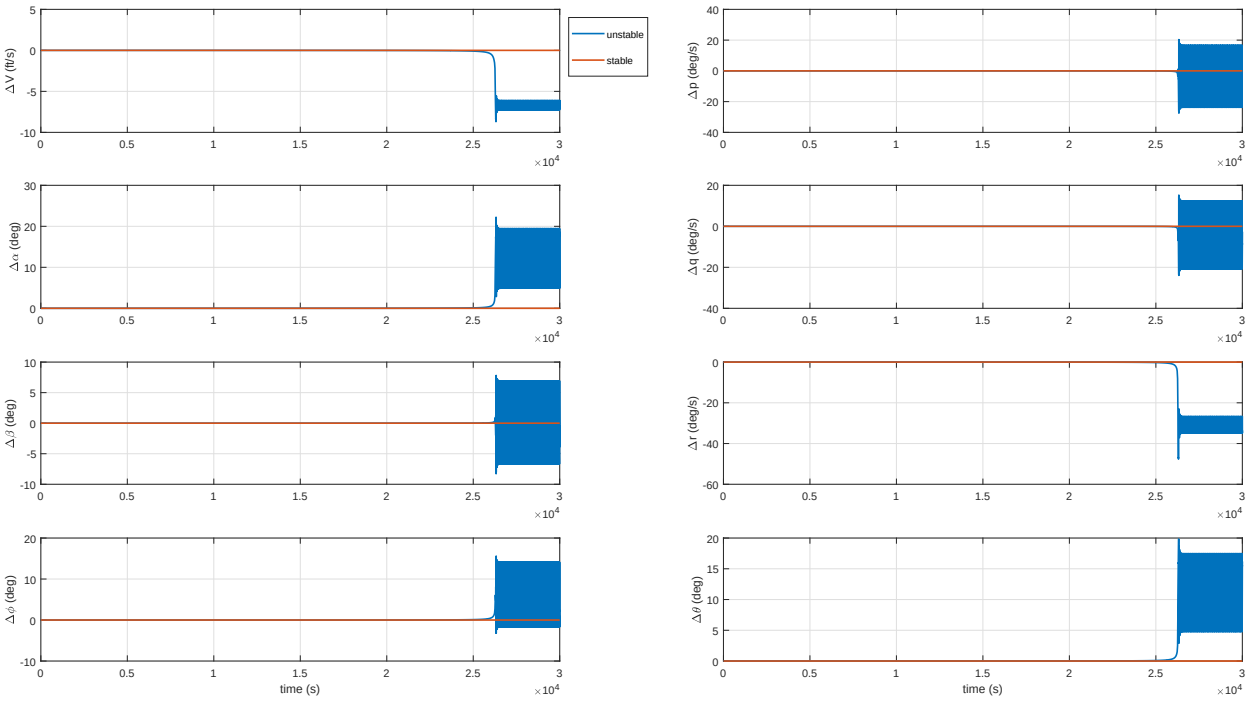

Figure 104 Stable $\alpha = 56.36°$ vs. Unstable $\alpha = 56.38°$

Table 24 Trim Summary, Stable vs. Unstable

α(deg)	56.36	56.38
funcVal	1.1e-28	6.4e-29
exitFlag	3	1
V_d(ft/s)	196.6	196.6
R(ft)	34.72	34.63
Ω(rpm)	-7.688	-7.696
σ(ft)	11.33	11.31
$\dot{V}$(ft/s^2)	9.4e-10	9.4e-10
$\dot{\alpha}$(deg/s)	-8.3e-14	-6.0e-14
$\dot{\beta}$(deg/s)	4.6e-09	4.6e-09
$\dot{p}$(deg/s^2)	-6.4e-08	-6.3e-08
$\dot{q}$(deg/s^2)	-2.9e-14	7.2e-15
$\dot{r}$(deg/s^2)	-6.7e-08	-6.7e-08
$\dot{\varphi}$(deg/s)	0.0e+00	3.2e-15
$\dot{\theta}$(deg/s)	8.0e-16	0.0e+00
V(ft/s)	198.5	198.5
α(deg)	56.36	56.38
β(deg)	3.399	3.399
p(deg/s)	-24.68	-24.69
q(deg/s)	3.707	3.7
r(deg/s)	-38.8	-38.84
φ(deg)	-5.457	-5.441
θ(deg)	-32.34	-32.33
δ_a(deg)	30.95	30.92
δ_e(deg)	5.36	5.364
δ_r(deg)	17.38	17.43

As the trim points become more unstable the sensitivity to trim accuracy increases. To visualize this batches of no greater than 350 runs across increasing instability were simulated and the time at which any state diverged by 1 was noted. All conditions simulated had a trim error of $|e| < 1e-6$ at a maximum to ensure the comparison was focused on the stability alone. In Figure 105 the black circles denote the minimum divergence time of any

state in a particular simulation whereas the colored dots denote all state divergence times across the block of simulations.

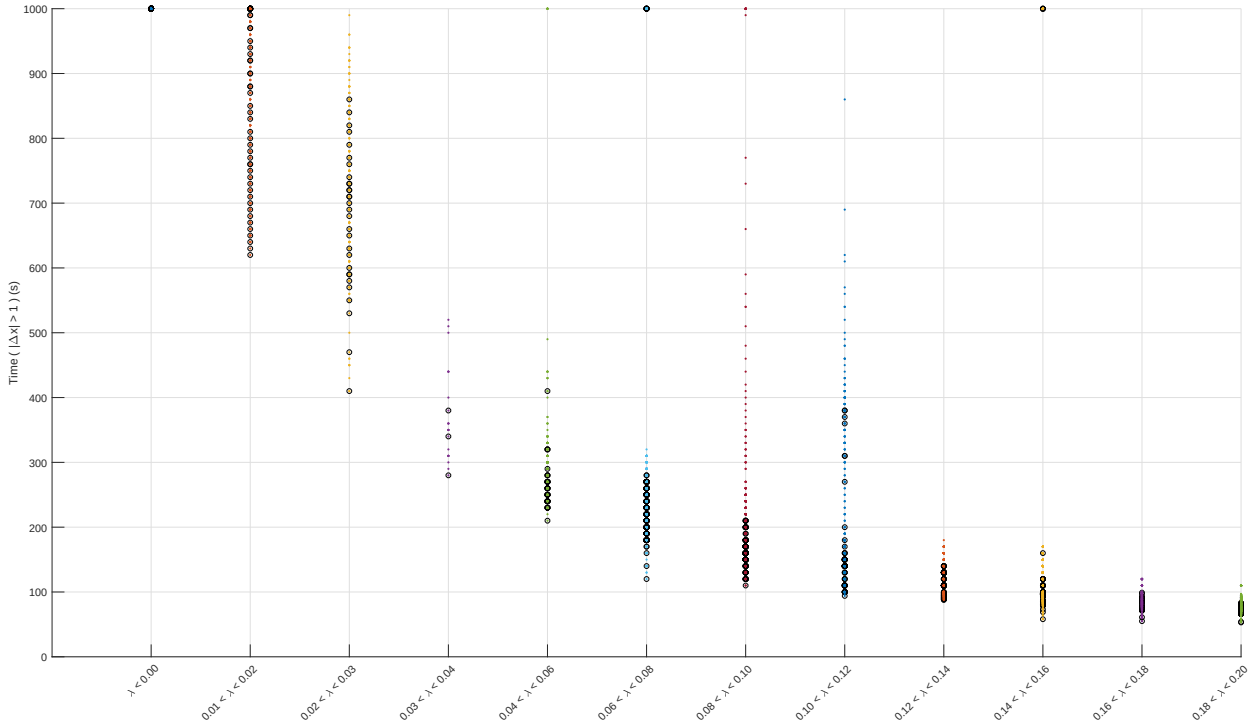

Figure 105 Unstable Eigen Values vs. Divergence Time

A.4 Linear Body EOM Entries

$$a_{11} = k_1 u \left(\theta_1 \sin\alpha - \theta_2 \cos\alpha\right)$$

$$a_{12} = r + k_1 v \left(\theta_1 \sin\alpha - \theta_2 \cos\alpha\right)$$

$$a_{13} = -q + k_1 w \left(\theta_1 \sin\alpha - \theta_2 \cos\alpha\right)$$

$$a_{15} = -w - k_3 \frac{V}{m} \left(C_{D,q} \cos\alpha - C_{L,q} \sin\alpha\right)$$

$$a_{16} = v$$

$$a_{18} = -g \cos\theta$$

$$a_{21} = -r + k_1 u \theta_3 - k_2 \frac{u}{mV} \theta_4$$

$$a_{22} = k_1 v \theta_3 - k_2 \frac{v}{mV} \theta_4$$

$$a_{23} = p + k_1 w \theta_3 - k_2 \frac{w}{mV} \theta_4$$

$$a_{24} = w + k_2 \frac{V}{m} C_{y,p}$$

$$a_{26} = k_2 \frac{V}{m} C_{y,r} - u$$

$$a_{27} = g \cos\varphi \cos\theta$$

$$a_{28} = -g \sin\varphi \sin\theta$$

$$a_{31} = q - u k_1 \left(\theta_1 \cos\alpha + \theta_2 \sin\alpha\right)$$

$$a_{32} = -p - v k_1 \left(\theta_1 \cos\alpha + \theta_2 \sin\alpha\right)$$

$$a_{33} = -w k_1 \left(\theta_1 \cos\alpha + \theta_2 \sin\alpha\right)$$

$$a_{34} = -v$$

$$a_{35} = u - k_3 \frac{V}{m} \left(C_{L,q} \cos\alpha + C_{D,q} \sin\alpha\right)$$

$$a_{37} = -g \cos\theta \sin\varphi$$

$$a_{38} = -g \cos\varphi \sin\theta$$

$$a_{41} = \frac{I_{zz}}{{I_{xz}}^2 - I_{xx} I_{zz}} Sb\rho u \left[\frac{b}{4v}\theta_6 - \theta_5\right] + \frac{I_{xz}}{{I_{xz}}^2 - I_{xx} I_{zz}} Sb\rho u \left[\frac{b}{4V}\theta_9 - \theta_8\right]$$

$$a_{42} = \frac{I_{zz}}{{I_{xz}}^2 - I_{xx} I_{zz}} \left[\frac{Sb^2\rho v}{4V}\theta_6 - Sb\rho v\theta_5\right] + \frac{I_{xz}}{{I_{xz}}^2 - I_{xx} I_{zz}} \left[\frac{Sb^2\rho v}{4V}\theta_9 - Sb\rho v\theta_8\right]$$

$$a_{43} = \frac{I_{zz}}{{I_{xz}}^2 - I_{xx} I_{zz}} \left[\frac{Sb^2\rho w}{4V}\theta_6 - Sb\rho w\theta_5\right] + \frac{I_{xz}}{{I_{xz}}^2 - I_{xx} I_{zz}} \left[\frac{Sb^2\rho w}{4V}\theta_9 - Sb\rho w\theta_8\right]$$

$$a_{44} = k_2 \frac{Vb}{I_x} C_{l,p}$$

$$a_{45} = \frac{r}{I_x} \left(I_y - I_z\right)$$

$$a_{46} = \frac{1}{I_x} \left(q \left(I_y - I_z\right) + k_2 V b C_{l,r}\right)$$

$$a_{51} = Sc\rho \frac{u}{I_y} \theta_7$$

$$a_{52} = Sc\rho\frac{v}{I_y}\theta_7$$

$$a_{53} = Sc\rho\frac{w}{I_y}\theta_7$$

$$a_{54} = \frac{-r}{I_y}\left(I_x - I_z\right)$$

$$a_{55} = k_3\frac{Vc}{I_y}C_{m,q}$$

$$a_{56} = \frac{-p}{I_y}\left(I_x - I_z\right)$$

$$a_{61} = \frac{I_{\mathrm{xz}}}{{I_{\mathrm{xz}}}^2 - I_{\mathrm{xx}}I_{\mathrm{zz}}}\left[\frac{Sb^2\rho u}{4V}\theta_6 - Sb\rho u\theta_5\right] + \frac{I_{\mathrm{xx}}}{{I_{\mathrm{xz}}}^2 - I_{\mathrm{xx}}I_{\mathrm{zz}}}\left[\frac{Sb^2\rho u}{4V}\theta_9 - Sb\rho u\theta_8\right]$$

$$a_{62} = \frac{I_{\mathrm{xz}}}{{I_{\mathrm{xz}}}^2 - I_{\mathrm{xx}}I_{\mathrm{zz}}}\left[\frac{Sb^2\rho v}{4V}\theta_6 - Sb\rho v\theta_5\right] + \frac{I_{\mathrm{xx}}}{{I_{\mathrm{xz}}}^2 - I_{\mathrm{xx}}I_{\mathrm{zz}}}\left[\frac{Sb^2\rho v}{4V}\theta_9 - Sb\rho v\theta_8\right]$$

$$a_{63} = \frac{I_{\mathrm{xz}}}{{I_{\mathrm{xz}}}^2 - I_{\mathrm{xx}}I_{\mathrm{zz}}}\left[\frac{Sb^2\rho w}{4V}\theta_6 - Sb\rho w\theta_5\right] + \frac{I_{\mathrm{xx}}}{{I_{\mathrm{xz}}}^2 - I_{\mathrm{xx}}I_{\mathrm{zz}}}\left[\frac{Sb^2\rho w}{4V}\theta_9 - Sb\rho w\theta_8\right]$$

$$a_{64} = \frac{1}{I_z}\left(q\left(I_x - I_y\right) + k_2VbC_{n,p}\right)$$

$$a_{65} = \frac{p}{I_z}\left(I_x - I_y\right)$$

$$a_{66} = k_2\frac{Vb}{I_z}C_{n,r}$$

$$a_{74} = 1$$

$$a_{75} = \sin\varphi\tan\theta$$

$$a_{76} = \cos\varphi\tan\theta$$

$$a_{77} = \frac{\sin\theta\left(q\cos\varphi - r\sin\varphi\right)}{\cos\theta}$$

$$a_{78} = \frac{r\cos\varphi + q\sin\varphi}{\cos\theta^2}$$

$$a_{85} = \cos\varphi$$

$$a_{86} = -\sin\varphi$$

$$a_{87} = -r\cos\varphi - q\sin\varphi$$

$$b_{12} = -\frac{S\overline{q}}{m}\left(\cos\alpha\left(C_{D,\delta_{el}} + C_{D,\delta_{er}}\right) - \sin\alpha\left(C_{L,\delta_{el}} + C_{L,\delta_{er}}\right)\right)$$

$$b_{21} = \frac{S\overline{q}}{m}C_{y,\delta_a}$$

$$b_{22} = \frac{S\overline{q}}{m}\left(C_{y,\delta_{el}} + C_{y,\delta_{er}}\right)$$

$$b_{23} = \frac{S\overline{q}}{m}C_{y,\delta_r}$$

$$b_{32} = -\frac{S\overline{q}}{m}\left(\cos\alpha\left(C_{L,\delta_{el}} + C_{L,\delta_{er}}\right) + \sin\alpha\left(C_{D,\delta_{el}} + C_{D,\delta_{er}}\right)\right)$$

$$b_{41} = \frac{S\overline{q}b}{I_x}C_{l,\delta_a}$$

$$b_{42} = \frac{S\overline{q}b}{I_x}\left(C_{l,\delta_{el}} + C_{l,\delta_{er}}\right)$$

$$b_{43} = \frac{S\overline{q}b}{I_x}C_{l,\delta_r}$$

$$b_{52} = \frac{S\overline{q}c}{I_y}\left(C_{m,\delta_{el}} + C_{m,\delta_{er}}\right)$$

$$b_{61} = \frac{S\overline{q}b}{I_z}C_{n,\delta_a}$$

$$b_{62} = \frac{S\overline{q}b}{I_z}\left(C_{n,\delta_{el}} + C_{n,\delta_{er}}\right)$$

$$b_{63} = \frac{S\overline{q}b}{I_z}C_{n,\delta_r}$$

$$\theta_1 = \left(C_{L,0} + \left(C_{L,\delta_{el}} + C_{L,\delta_{er}}\right)\delta_e + \frac{cq}{4V}C_{L,q}\right)$$

$$\theta_2 = \left(C_{D,0} + \left(C_{D,\delta_{el}} + C_{D,\delta_{er}}\right)\delta_e + \frac{cq}{4V}C_{D,q}\right)$$

$$\theta_3 = \left(C_{y,\beta}\beta + C_{y,\delta_a}\delta_a + \left(C_{y,\delta_{el}} + C_{y,\delta_{er}}\right)\delta_e + C_{y,\delta_r}\delta_r + \frac{bp}{2V}C_{y,p} + \frac{br}{2V}C_{y,r}\right)$$

$$\theta_4 = \left(C_{y,p}p + C_{y,r}r\right)$$

$$\theta_5 = \left(C_{l,\beta}\beta + C_{l,\delta_a}\delta_a + \left(C_{l,\delta_{el}} + C_{l,\delta_{er}}\right)\delta_e + C_{l,\delta_r}\delta_r + \frac{bp}{2V}C_{l,p} + \frac{br}{2V}C_{l,r}\right)$$

$$\theta_6 = \left(C_{l,p}p + C_{l,r}r\right)$$

$$\theta_7 = \left(C_{m,0} + \left(C_{m,\delta_{el}} + C_{m,\delta_{er}}\right)\delta_e + \frac{cq}{4V}C_{m,q}\right)$$

$$\theta_8 = \left(C_{n,\beta}\beta + C_{n,\delta_a}\delta_a + \left(C_{n,\delta_{el}} + C_{n,\delta_{er}}\right)\delta_e + C_{n,\delta_r}\delta_r + \frac{bp}{2V}C_{n,p} + \frac{br}{2V}C_{n,r}\right)$$

$$
\begin{aligned}
\theta_9 &= (C_{n,p}p + C_{n,r}r) \\
k_1 &= \frac{S\rho}{m} \\
k_2 &= \frac{Sb\rho}{4} \\
k_3 &= \frac{Sc\rho}{4} \\
k_4 &= Sb\rho
\end{aligned} \tag{A.4-1}
$$

A.5 Linear Hybrid Wind EOM Entries

$$
\begin{aligned}
a_{11} &= \frac{1}{m}\left(SV\rho\left(\sin\beta\theta_6 - \cos\beta\theta_5\right) + k_1\sin\beta\theta_1 - k_2 q\cos\beta C_{D,q}\right) \\
a_{12} &= \frac{S\overline{q}}{m}\left(\sin\beta\theta_2' - \cos\beta\theta_3'\right) + g\cos\beta\left(\sin\alpha\sin\theta + \cos\alpha\cos\varphi\cos\theta\right) \\
a_{13} &= g\left(\cos\beta\cos\theta\sin\varphi + \cos\alpha\sin\beta\sin\theta - \cos\varphi\sin\alpha\sin\beta\cos\theta\right) \\
&\quad + \frac{S\overline{q}}{m}\left(\theta_2\cos\beta + \sin\beta\left(\theta_3 + C_{y,\beta}\right)\right) \\
a_{14} &= \frac{1}{m}k_1 V\sin\beta C_{y,p} \\
a_{15} &= -\frac{1}{m}k_2 V\cos\beta C_{D,q} \\
a_{16} &= \frac{1}{m}k_1 V\sin\beta C_{y,r} \\
a_{17} &= g\cos\theta\left(\cos\varphi\sin\beta - \cos\beta\sin\alpha\sin\varphi\right) \\
a_{18} &= -g\left(\sin\beta\sin\varphi\sin\theta + \cos\alpha\cos\beta\cos\theta + \cos\beta\cos\varphi\sin\alpha\sin\theta\right) \\
a_{21} &= \frac{k_5}{V\cos\beta}\left(\sin\alpha\sin\theta + \cos\alpha\cos\varphi\cos\theta\right) - \frac{k_3}{\cos\beta}\theta_4 \\
a_{22} &= \frac{k_5}{\cos\beta}\left(\cos\alpha\sin\theta - \cos\varphi\sin\alpha\cos\theta\right) - \tan\beta\left(r\cos\alpha - p\sin\alpha\right) \\
&\quad - \frac{k_4}{\cos\beta}\left(\theta_4' + \frac{c}{2V}qC_{L,q}'\right) \\
a_{23} &= -p\cos\alpha - r\sin\alpha \\
&\quad - \frac{\sin\beta}{\cos\beta^2}\Bigg(\sin\beta\left(p\cos\alpha + r\sin\alpha\right) + k_5\left(\sin\alpha\sin\theta - \cos\alpha\cos\varphi\cos\theta\right) \\
&\quad + k_4\left(\theta_4 + \frac{c}{2V}qC_{L,q}\right)\Bigg)
\end{aligned}
$$

$$
\begin{aligned}
a_{24} &= -\frac{\cos\alpha \sin\beta}{\cos\beta} \\
a_{25} &= 1 - \frac{k_2}{m\cos\beta} C_{L,q} \\
a_{26} &= -\frac{\sin\alpha \sin\beta}{\cos\beta} \\
a_{27} &= -\frac{k_5}{\cos\beta} \cos\alpha \cos\theta \sin\varphi \\
a_{28} &= \frac{k_5}{\cos\beta} \left(\sin\alpha\cos\theta - \cos\alpha\cos\varphi\sin\theta\right) \\
a_{31} &= k_3 \left(\sin\beta\theta_5 + \cos\beta\theta_6\right) \\
&\quad - \frac{k_5}{V} \left(\cos\varphi\sin\alpha\sin\beta\cos\theta - \cos\alpha\sin\beta\sin\theta - \cos\beta\cos\theta\sin\varphi\right) \\
a_{32} &= k_4 \left(\theta_2' \cos\beta + \theta_3' \sin\beta\right) \\
&\quad + p\cos\alpha + r\sin\alpha - k_5 \left(\sin\alpha\sin\beta\sin\theta + \cos\alpha\cos\varphi\sin\beta\cos\theta\right) \\
a_{33} &= k_5 \left(\cos\alpha\cos\beta\sin\theta - \sin\beta\cos\theta\sin\varphi - \cos\beta\cos\varphi\sin\alpha\cos\theta\right) \\
&\quad + k_4 \left(\theta_3\cos\beta - \theta_2\sin\beta + C_{y,\beta}\cos\beta\right) \\
a_{34} &= \sin\alpha + \frac{k_1}{m} C_{y,p} \cos\beta \\
a_{35} &= \frac{k_2}{m} C_{D,q} \sin\beta \\
a_{36} &= \frac{k_1}{m} C_{y,r} \cos\beta - \cos\alpha \\
a_{37} &= k_5 \left(\cos\alpha\sin\beta\cos\theta - \cos\beta\sin\varphi\sin\theta + \cos\varphi\sin\alpha\sin\beta\sin\theta\right) \\
a_{38} &= k_5 \left(\cos\alpha\sin\beta\cos\theta - \cos\beta\sin\varphi\sin\theta + \cos\varphi\sin\alpha\sin\beta\sin\theta\right) \\
a_{41} &= -\frac{k_1}{k_i} \left(4V(I_{xz}\theta_{11} + I_z\theta_8) + b(I_{xz}\theta_{10} + I_z\theta_7)\right) \\
a_{42} &= -\frac{S\overline{q}b}{k_i} \left((I_{xz}\theta_{11}' + I_z\theta_8') + \frac{b}{2V}(I_{xz}\theta_{10}' + I_z\theta_7')\right) \\
a_{43} &= -\frac{S\overline{q}b}{k_i}(I_{xz}C_{n,\beta} + I_z C_{l,\beta}) \\
a_{44} &= -\frac{1}{k_i}(I_{xz}(I_x - I_y + I_z)q + k_1 V b(I_{xz}C_{n,p} + I_z C_{l,p})) \\
a_{45} &= \frac{1}{k_i}\left((I_{xz}^2 + I_z^2 - I_y I_z)r - I_{xz}(I_x - I_y + I_z)p\right) \\
a_{46} &= \frac{1}{k_i}\left((I_{xz}^2 + I_z^2 - I_y I_z)q - k_1 V b(I_{xz}C_{n,r} + I_z C_{l,r})\right) \\
a_{51} &= \frac{k_2}{I_y} \left(4V\theta_9 + cqC_{m,q}\right)
\end{aligned}
$$

$$a_{52} = \frac{S\overline{q}c}{I_y}\left(\theta'_9 + \frac{c}{2V}qC'_{m,q}\right)$$

$$a_{54} = -(\frac{2I_{xz}}{I_y}p + k_6 r)$$

$$a_{55} = \frac{k_2 V c}{I_y}C_{m,q}$$

$$a_{56} = \frac{2I_{xz}}{I_y}r - k_6 p$$

$$a_{61} = -\frac{k_1}{k_i}\left(4V(I_{xz}\theta_8 + I_x\theta_{11}) + b(I_{xz}\theta_7 + I_x\theta_{10})\right)$$

$$a_{62} = -\frac{S\overline{q}b}{k_i}\left(I_{xz}\theta'_8 + I_x\theta'_{11} + \frac{b}{2V}(I_{xz}\theta'_7 + I_x\theta'_{10})\right)$$

$$a_{63} = -\frac{S\overline{q}b}{k_i}(I_{xz}C_{l,\beta} + I_x C_{n,\beta})$$

$$a_{64} = -\frac{1}{k_i}(k_1 V b(I_{xz}C_{l,p} + I_x C_{n,p}) + (I_x^2 - I_y I_x + I_{xz}^2)q)$$

$$a_{65} = \frac{1}{k_i}\left(I_{xz}(I_x - I_y + I_z)r - (I_x^2 - I_y I_x + I_{xz}^2)p\right)$$

$$a_{66} = \frac{1}{k_i}\left(I_{xz}(I_x - I_y + I_z)q - k_1 V b(I_{xz}C_{l,r} + I_x C_{n,r})\right)$$

$$a_{74} = 1$$

$$a_{75} = \sin\varphi\tan\theta$$

$$a_{76} = \cos\varphi\tan\theta$$

$$a_{77} = \tan\theta\left(q\cos\varphi - r\sin\varphi\right)$$

$$a_{78} = \frac{r\cos\varphi + q\sin\varphi}{\cos\theta^2}$$

$$a_{85} = \cos\varphi$$

$$a_{86} = -\sin\varphi$$

$$a_{87} = -r\cos\varphi - q\sin\varphi$$

$$b_{11} = \frac{S\overline{q}}{m}\sin\beta C_{y,\delta_a}$$

$$b_{12} = \frac{S\overline{q}}{m}\left(\sin\beta\left(C_{y,\delta_{el}} + C_{y,\delta_{er}}\right) - \cos\beta\left(C_{D,\delta_{el}} + C_{D,\delta_{er}}\right)\right)$$

$$b_{13} = \frac{S\overline{q}}{m}\sin\beta C_{y,\delta_r}$$

$$b_{22} = -\frac{k_3 V}{\cos\beta}\left(C_{L,\delta_{el}} + C_{L,\delta_{er}}\right)$$

$$b_{31} = k_3 V\cos\beta C_{y,\delta_a}$$

$$b_{32} = k_4\Big(\cos\beta \left(C_{y,\delta_{el}} + C_{y,\delta_{er}}\right) + \sin\beta \left(C_{D,\delta_{el}} + C_{D,\delta_{er}}\right) \Big)$$

$$b_{33} = k_3 V \cos\beta C_{y,\delta_r}$$

$$b_{41} = -\frac{S\overline{q}b}{k_i}(I_z C_{l,\delta_a} + I_{xz} C_{n,\delta_a})$$

$$b_{42} = -\frac{S\overline{q}b}{k_i}\left(I_z \left(C_{l,\delta_{el}} + C_{l,\delta_{er}}\right) + I_{xz}\left(C_{n,\delta_{el}} + C_{n,\delta_{er}}\right)\right)$$

$$b_{43} = -\frac{S\overline{q}b}{k_i}\left(I_z C_{l,\delta_r} + I_{xz} C_{n,\delta_r}\right)$$

$$b_{52} = \frac{S\overline{q}c}{I_y}\left(C_{m,\delta_{el}} + C_{m,\delta_{er}}\right)$$

$$b_{61} = -\frac{S\overline{q}b}{k_i}\left(I_x C_{n,\delta_a} + I_{xz} C_{l,\delta_a}\right)$$

$$b_{62} = -\frac{S\overline{q}b}{k_i}\left(I_x \left(C_{n,\delta_{el}} + C_{n,\delta_{er}}\right) + I_{xz}\left(C_{l,\delta_{el}} + C_{l,\delta_{er}}\right)\right)$$

$$b_{63} = -\frac{S\overline{q}b}{k_i}\left(I_x C_{n,\delta_r} + I_{xz} C_{l,\delta_r}\right)$$

$$\theta_1 = C_{y,p}p + C_{y,r}r$$

$$\theta_2 = \theta_6 + \frac{b}{2V}\theta_1$$

$$\theta_3 = \theta_5 + \frac{c}{2V} q C_{D,q}$$

$$\theta_4 = C_{L,0} + \left(C_{L,\delta_{el}} + C_{L,\delta_{er}}\right)\delta_e$$

$$\theta_5 = C_{D,0} + \left(C_{D,\delta_{el}} + C_{D,\delta_{er}}\right)\delta_e$$

$$\theta_6 = C_{y,\beta}\beta + C_{y,\delta_a}\delta_a + \left(C_{y,\delta_{el}} + C_{y,\delta_{er}}\right)\delta_e + C_{y,\delta_r}\delta_r$$

$$\theta_7 = C_{l,p}p + C_{l,r}r$$

$$\theta_8 = C_{l,\beta}\beta + C_{l,\delta_a}\delta_a + \left(C_{l,\delta_{el}} + C_{l,\delta_{er}}\right)\delta_e + C_{l,\delta_r}\delta_r$$

$$\theta_9 = C_{m,0} + \left(C_{m,\delta_{el}} + C_{m,\delta_{er}}\right)\delta_e$$

$$\theta_{10} = C_{n,p}p + C_{n,r}r$$

$$\theta_{11} = C_{n,\beta}\beta + C_{n,\delta_a}\delta_a + \left(C_{n,\delta_{el}} + C_{n,\delta_{er}}\right)\delta_e + C_{n,\delta_r}\delta_r$$

$$k_1 = \frac{Sb\rho}{4}$$

$$k_2 = \frac{Sc\rho}{4}$$

$$k_3 = \frac{S\rho}{2m}$$

$$k_4 = \frac{S\overline{q}}{mV}$$

$$
\begin{aligned}
k_5 &= \frac{g}{V} \\
k_6 &= \frac{(I_x - I_z)}{I_y} \\
k_i &= I_{xz}^2 - I_x I_z
\end{aligned}
\tag{A.5-1}
$$

A.6 Linear Wind Model Validation

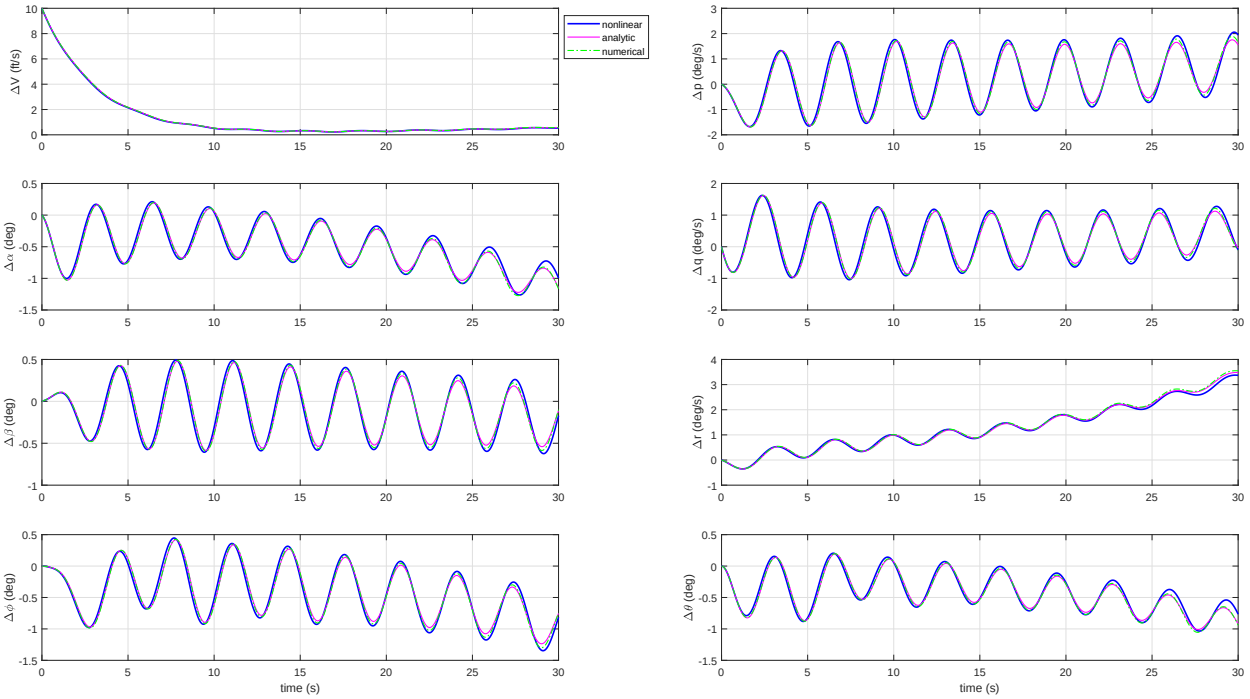

Figure 106 Linearized Wind, Perturbation: $\Delta V = 10.00$(ft/s)

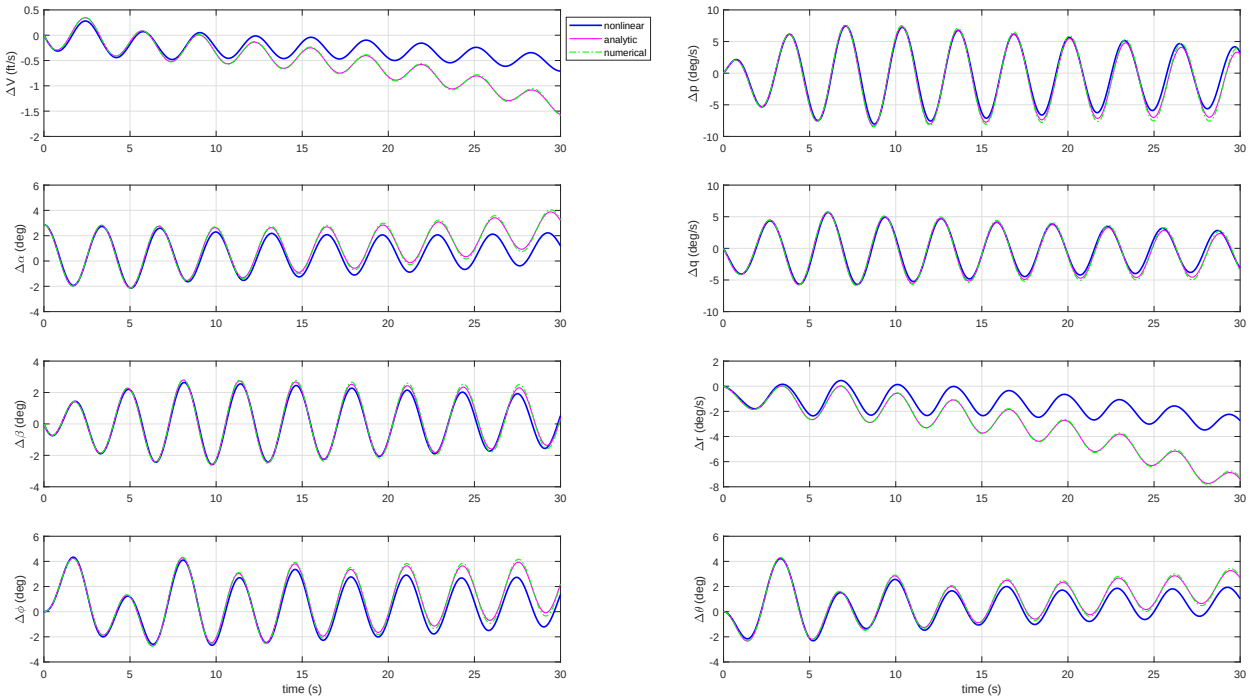

Figure 107 Linearized Wind, Perturbation: $\Delta\alpha = 0.05$(rad)

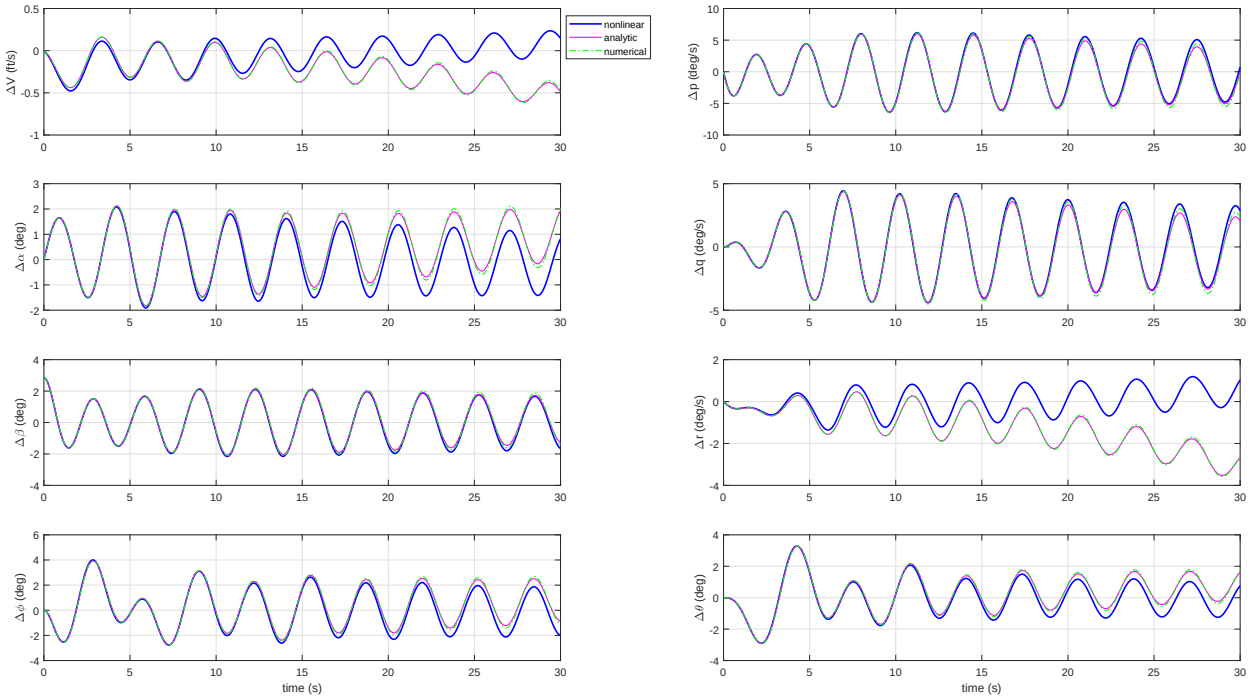

Figure 108 Linearized Wind, Perturbation: $\Delta\beta = 0.05$(rad)

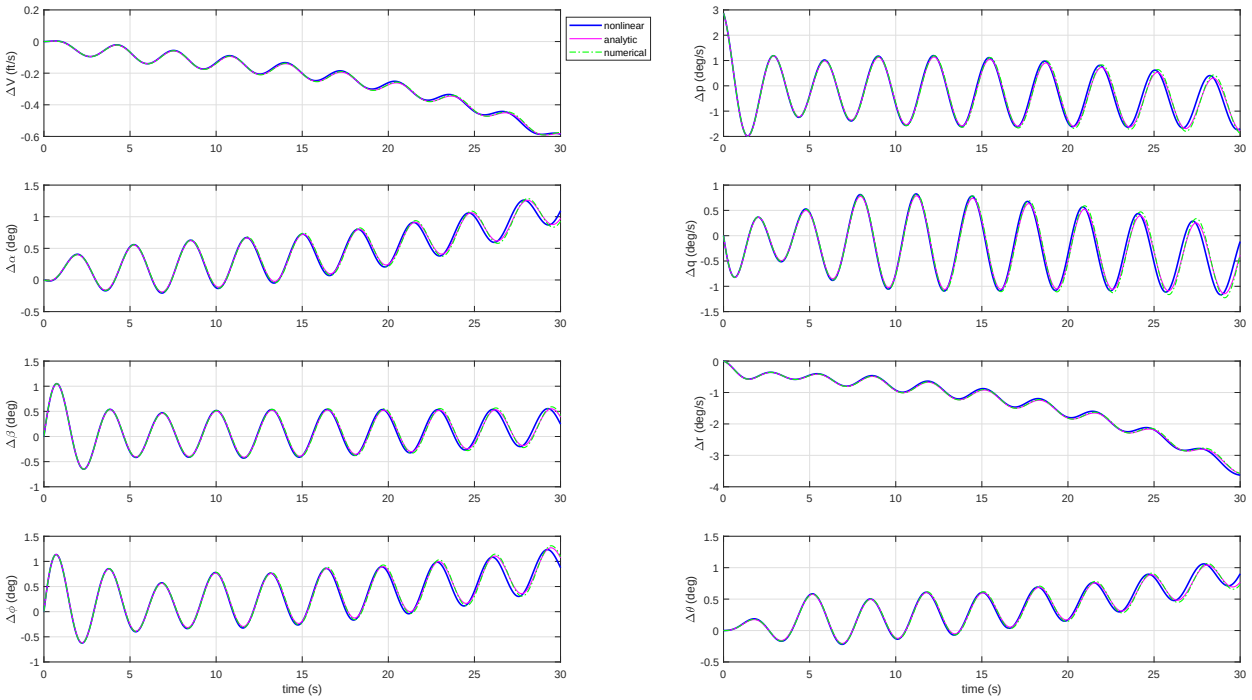

Figure 109 Linearized Wind, Perturbation: $\Delta p = 0.05(\text{rad/s})$

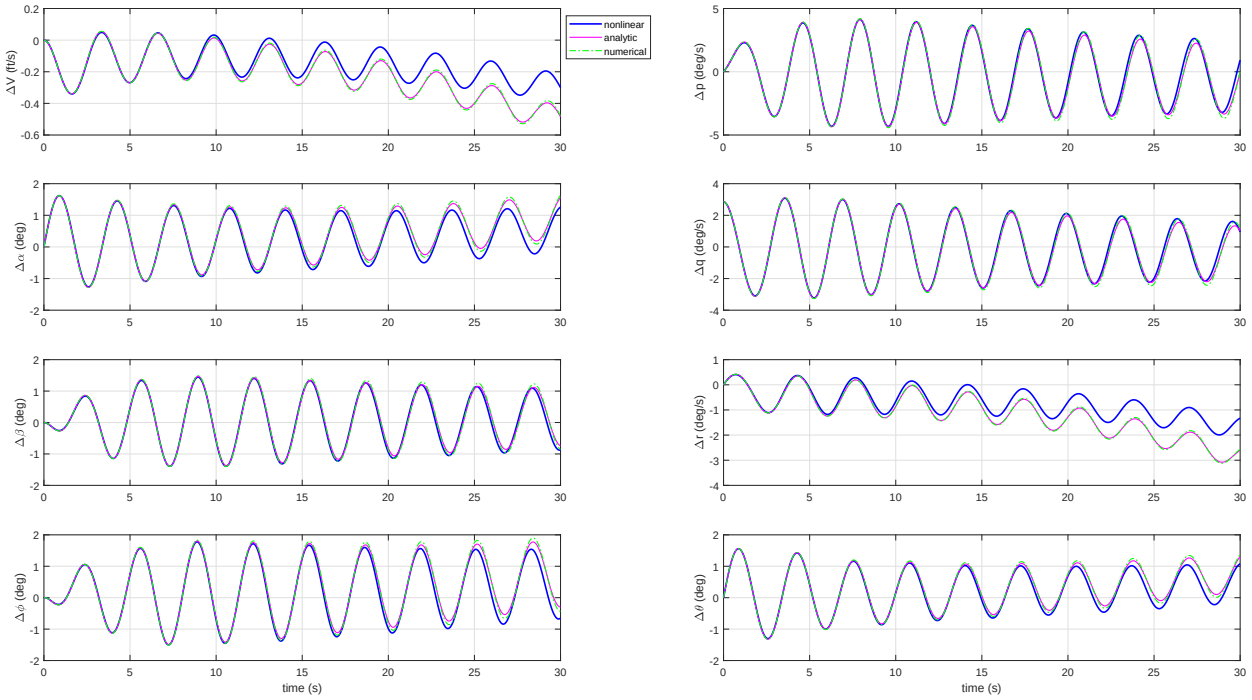

Figure 110 Linearized Wind, Perturbation: $\Delta q = 0.05(\text{rad/s})$

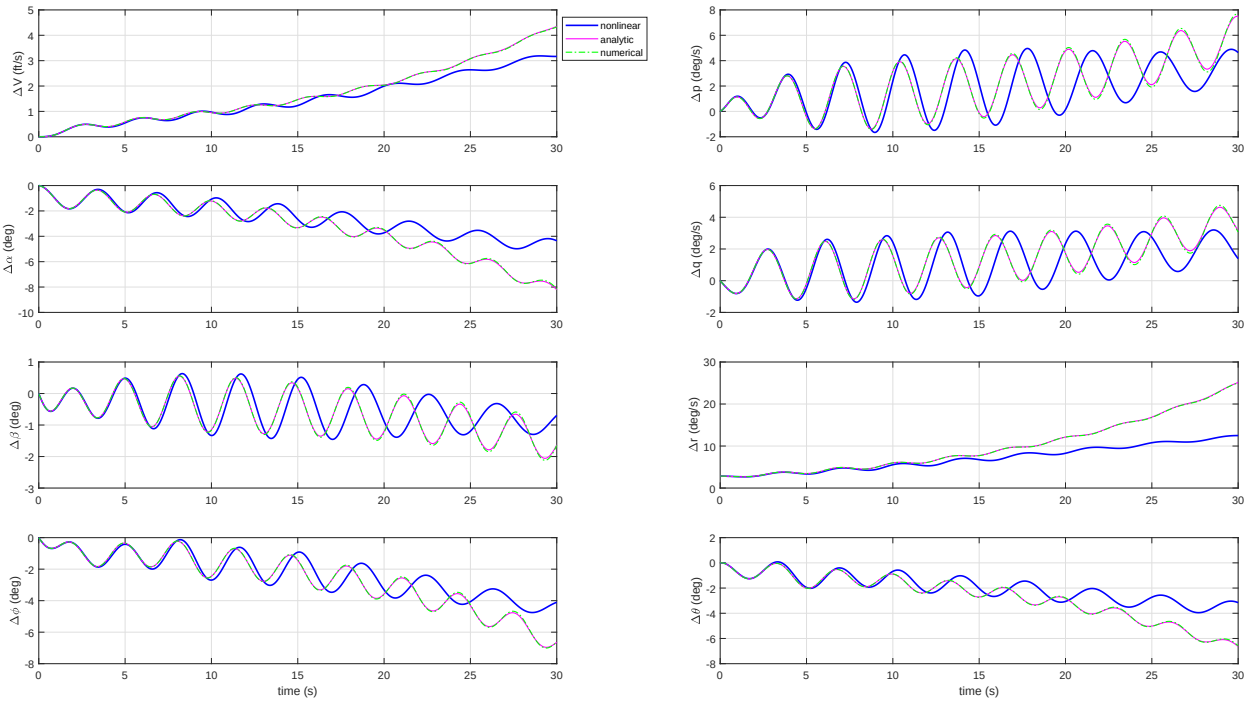

Figure 111 Linearized Wind, Perturbation: $\Delta r = 0.05(\text{rad/s})$

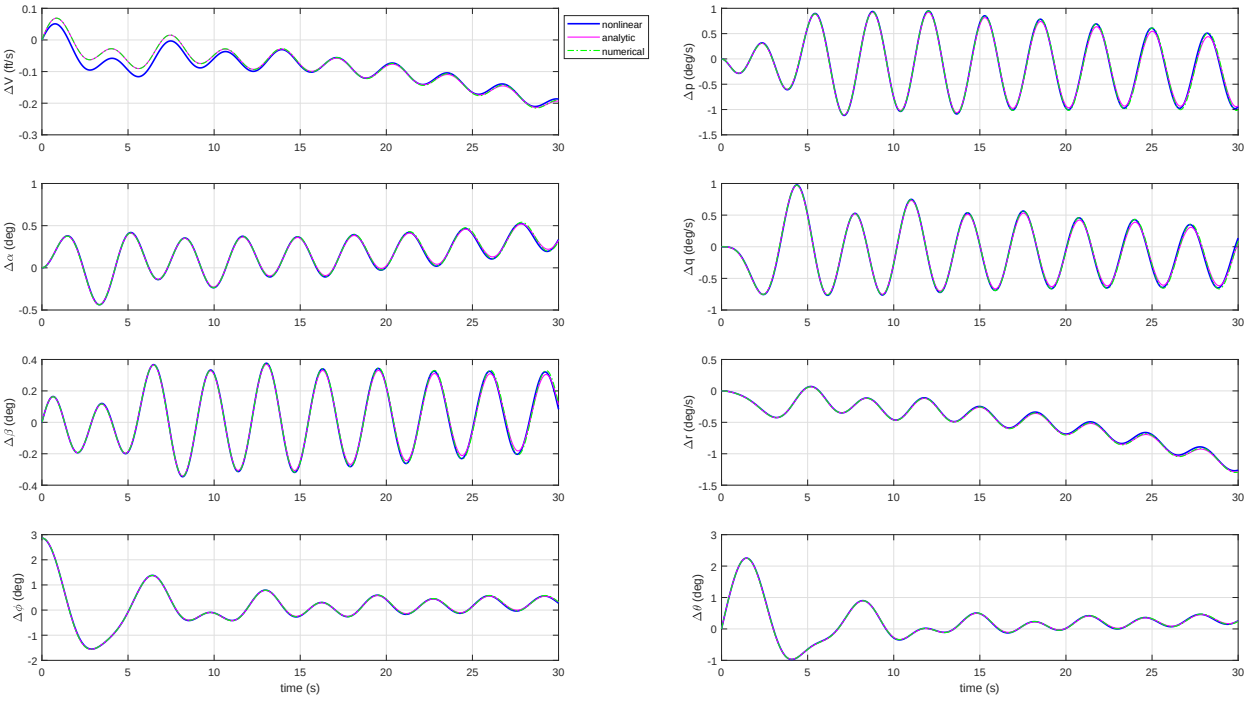

Figure 112 Linearized Wind, Perturbation: $\Delta\varphi = 0.05(\text{rad})$

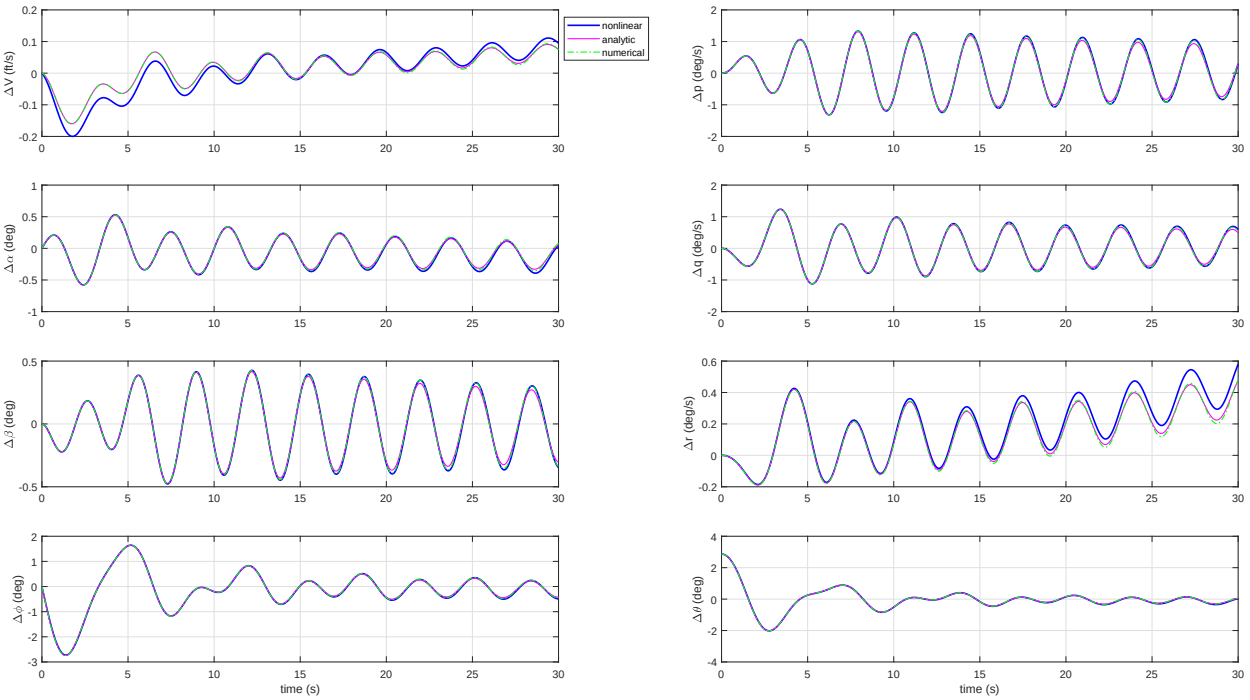

Figure 113 Linearized Wind, Perturbation: $\Delta\theta = 0.05(\text{rad})$

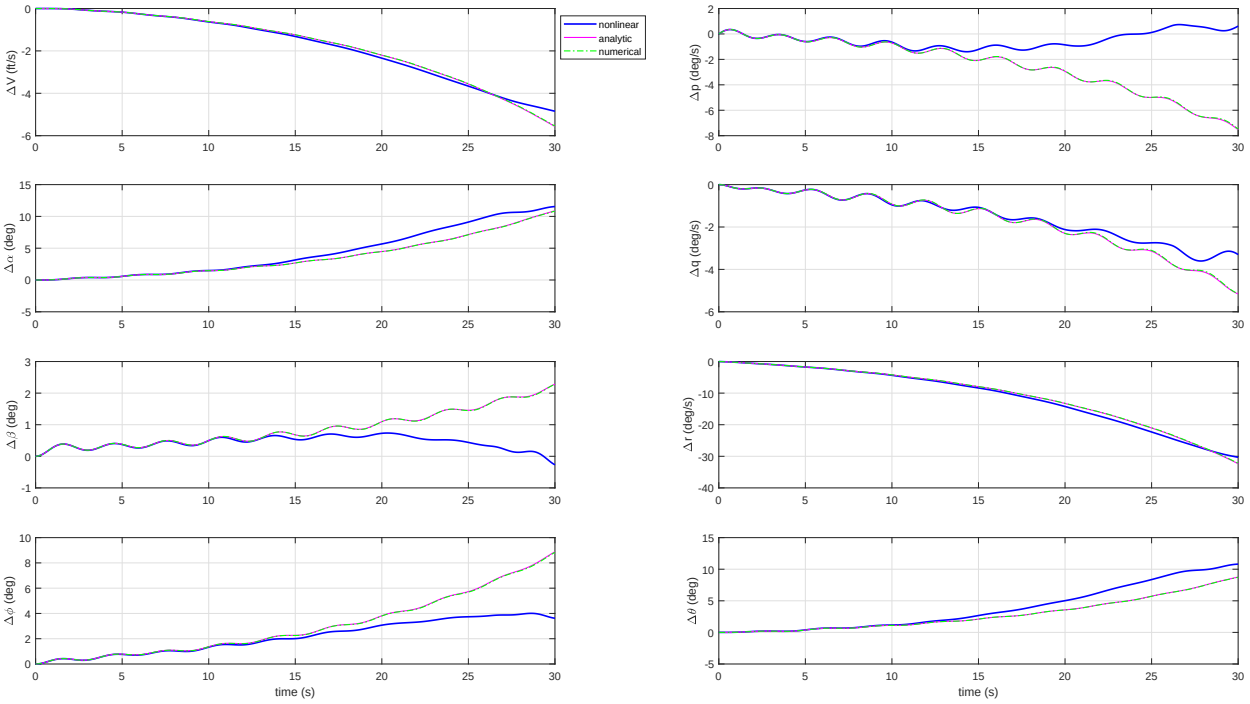

Figure 114 Linearized Wind, Perturbation: $\Delta\delta_a = 0.05(\text{rad})$

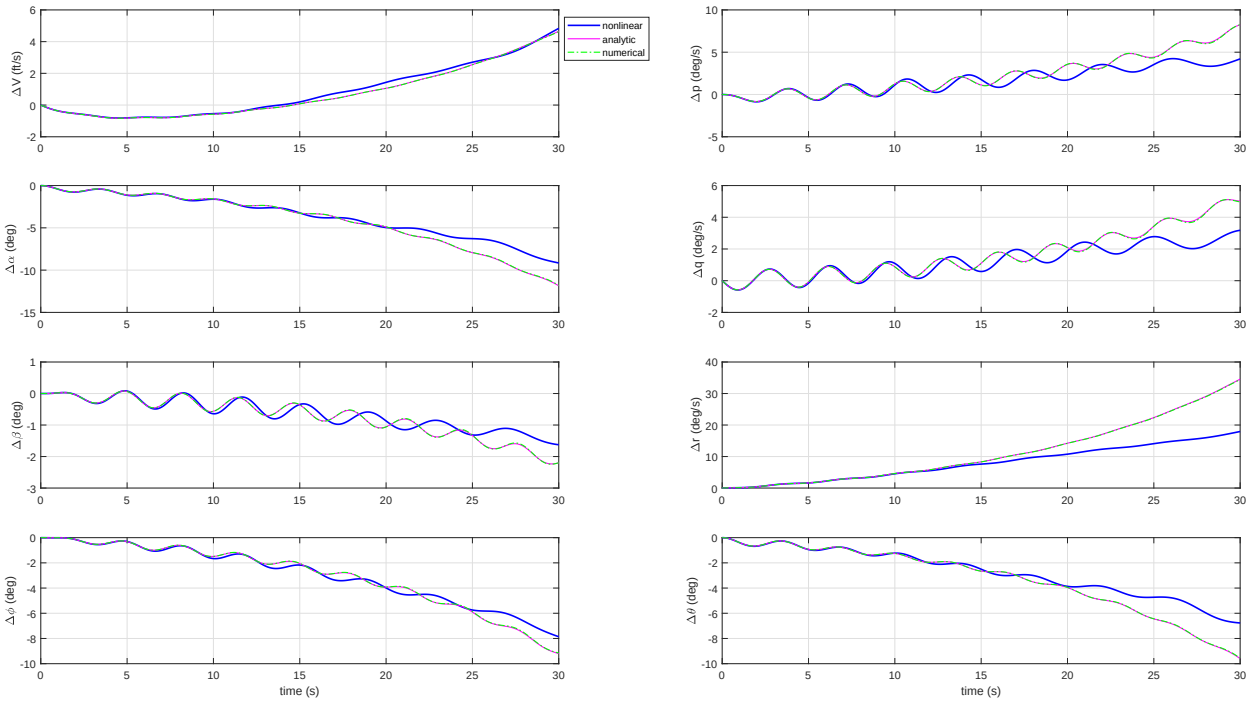

Figure 115 Linearized Wind, Perturbation: $\Delta\delta_e = 0.05(\text{rad})$

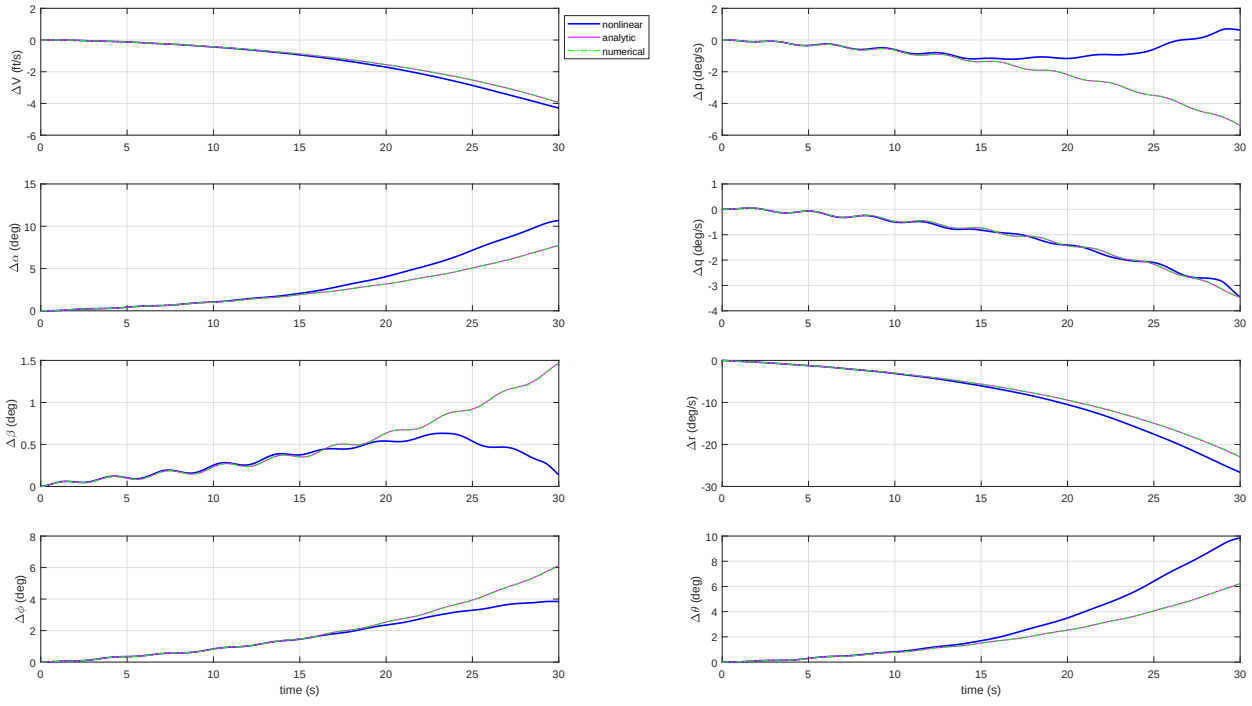

Figure 116 Linearized Wind, Perturbation: $\Delta\delta_r = 0.05(\text{rad})$

A.7 Linear Body Model Validation

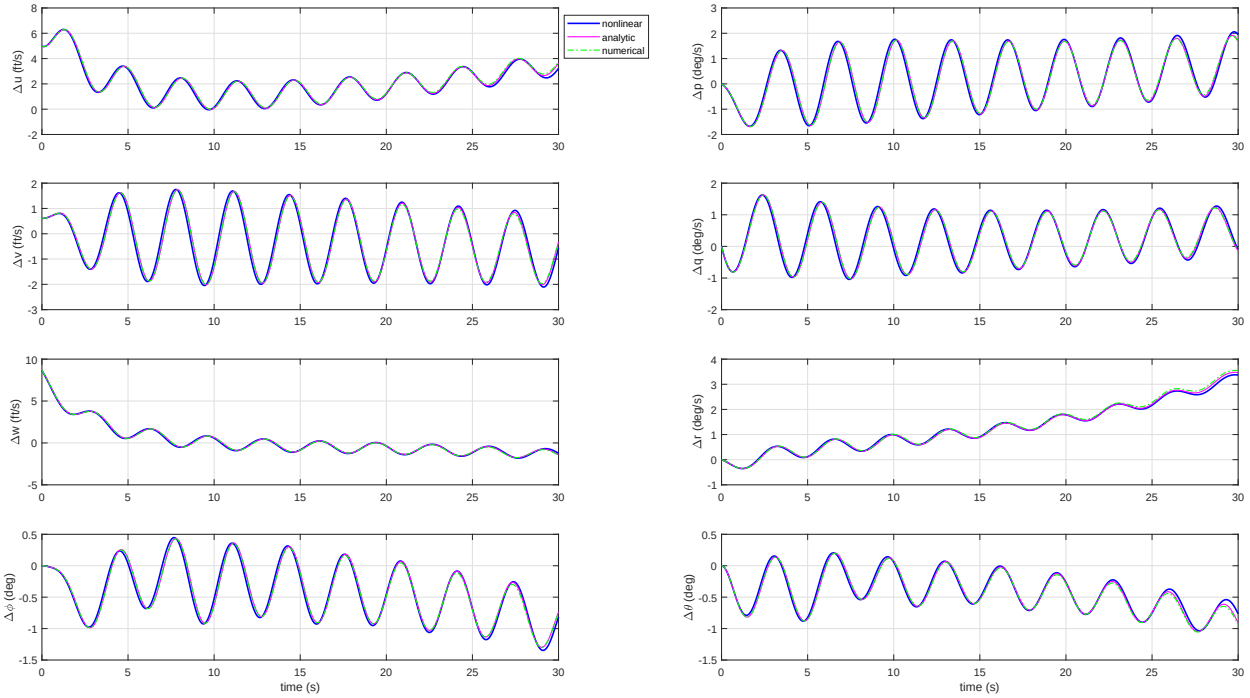

Figure 117 Linearized Body, Perturbation: $\Delta V = 10.00(\text{ft/s})$

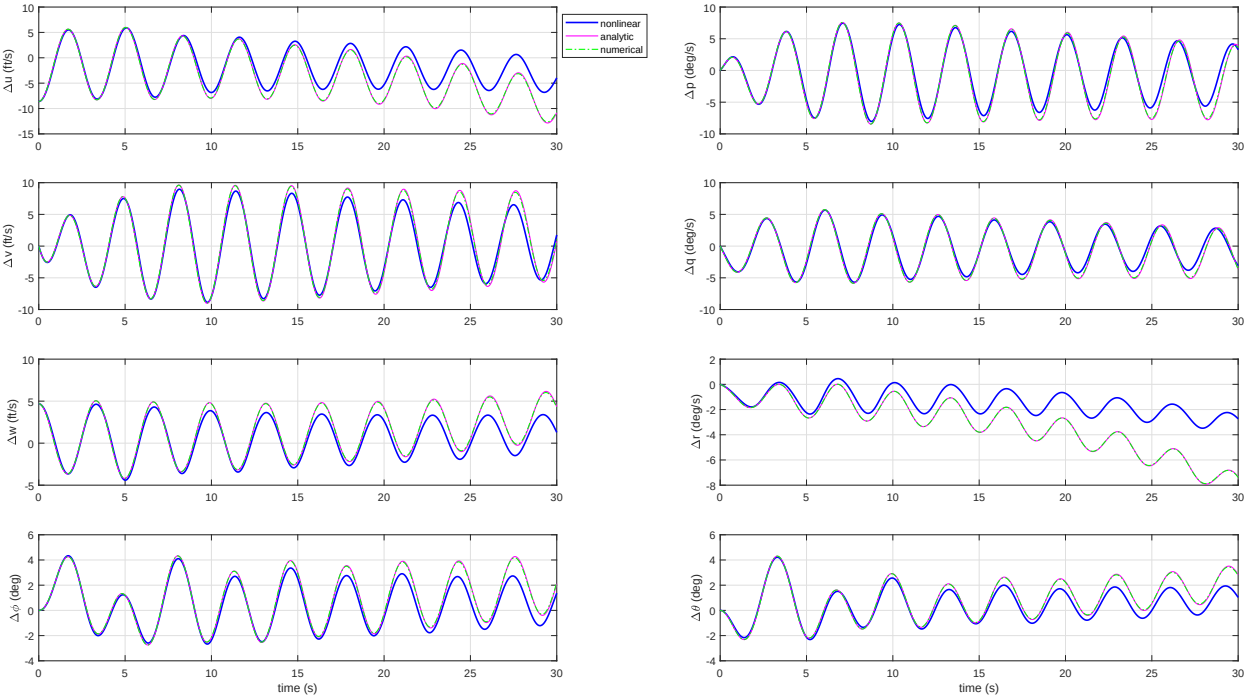

Figure 118 Linearized Body, Perturbation: $\Delta\alpha = 0.05(\text{rad})$

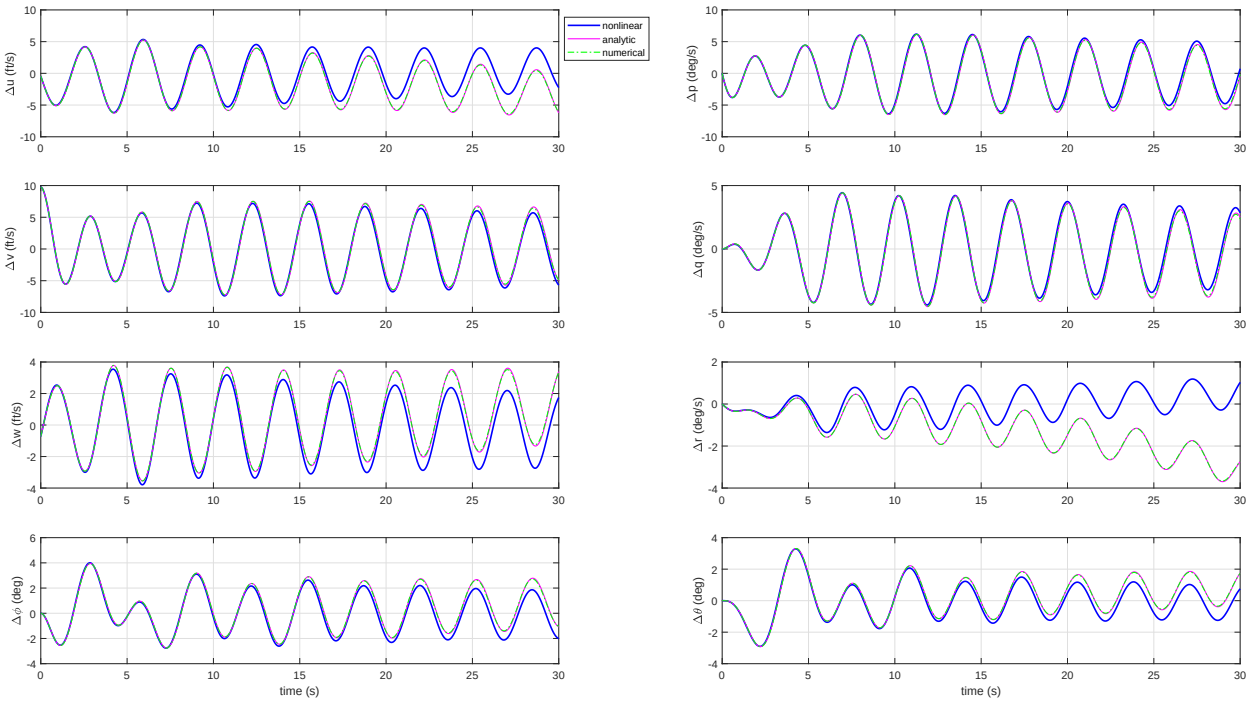

Figure 119 Linearized Body, Perturbation: $\Delta\beta = 0.05(\text{rad})$

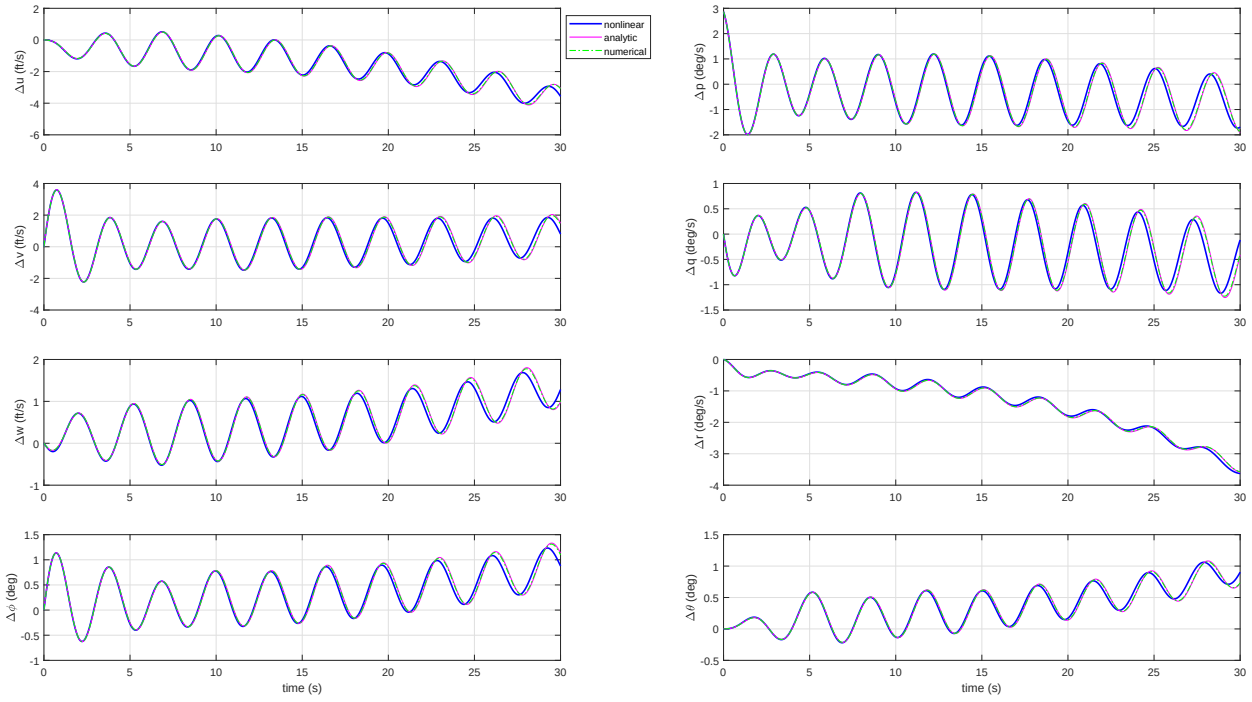

Figure 120 Linearized Body, Perturbation: $\Delta p = 0.05(\text{rad/s})$

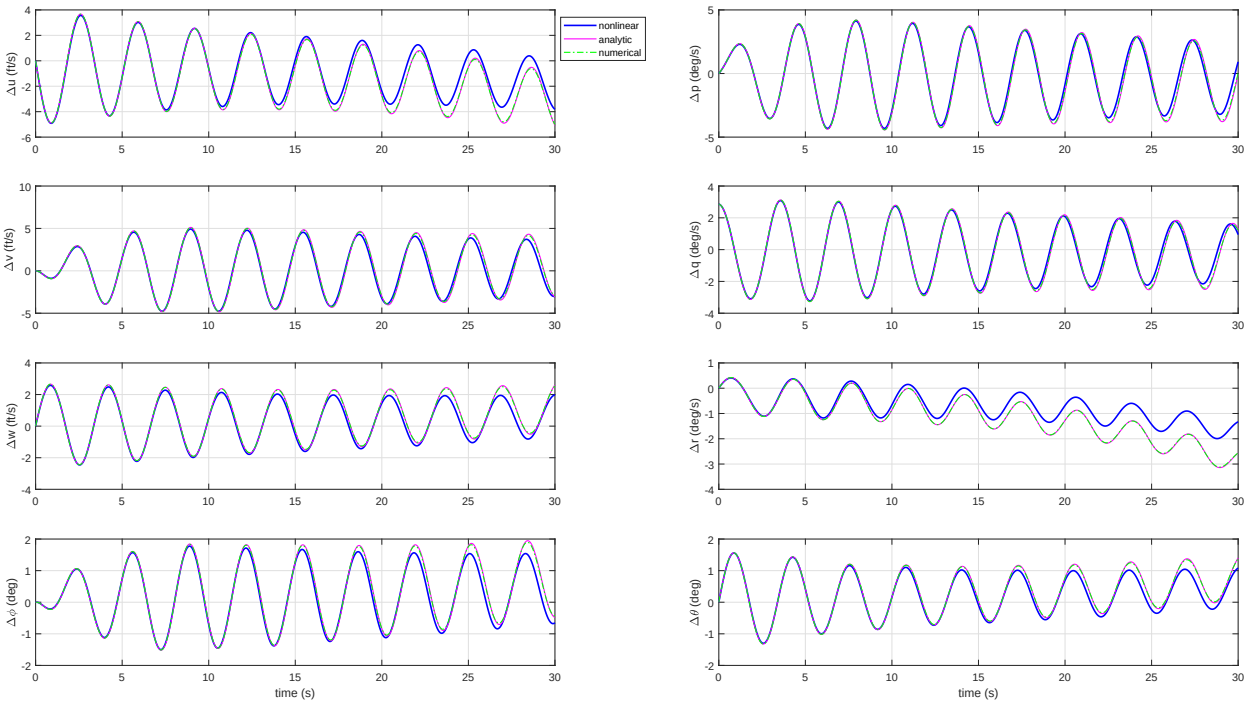

Figure 121 Linearized Body, Perturbation: $\Delta q = 0.05(\text{rad/s})$

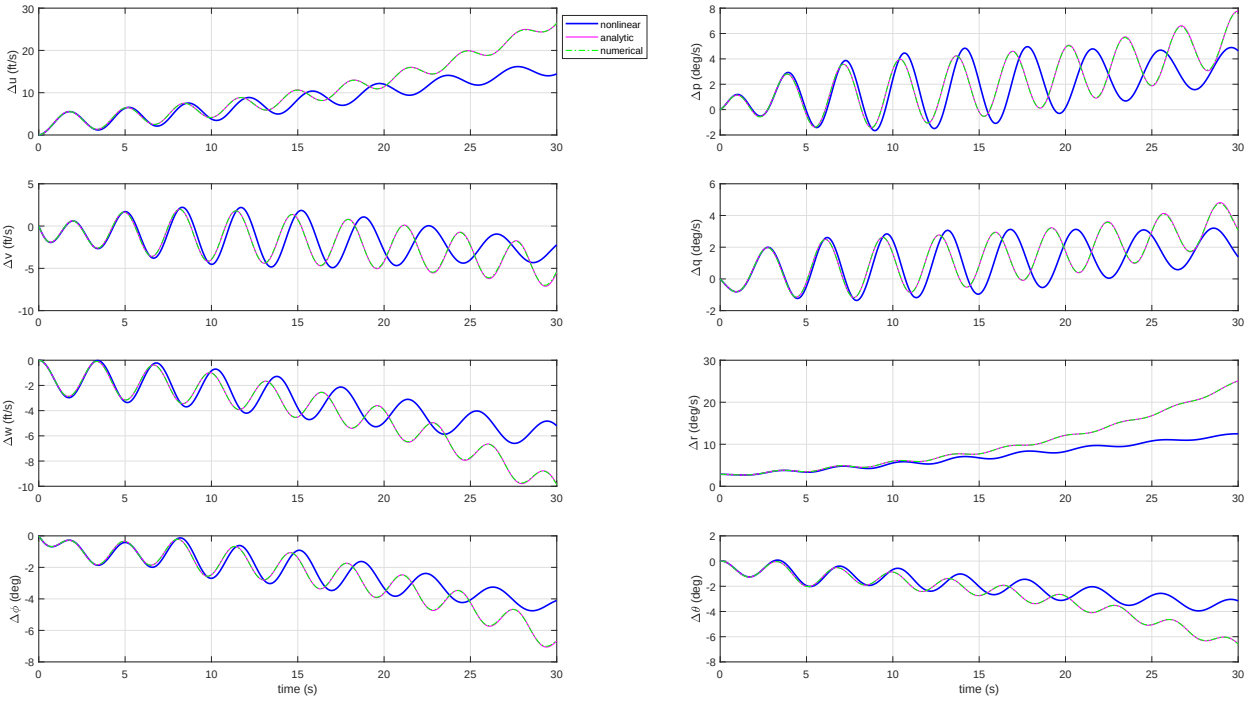

Figure 122 Linearized Body, Perturbation: $\Delta r = 0.05(\text{rad/s})$

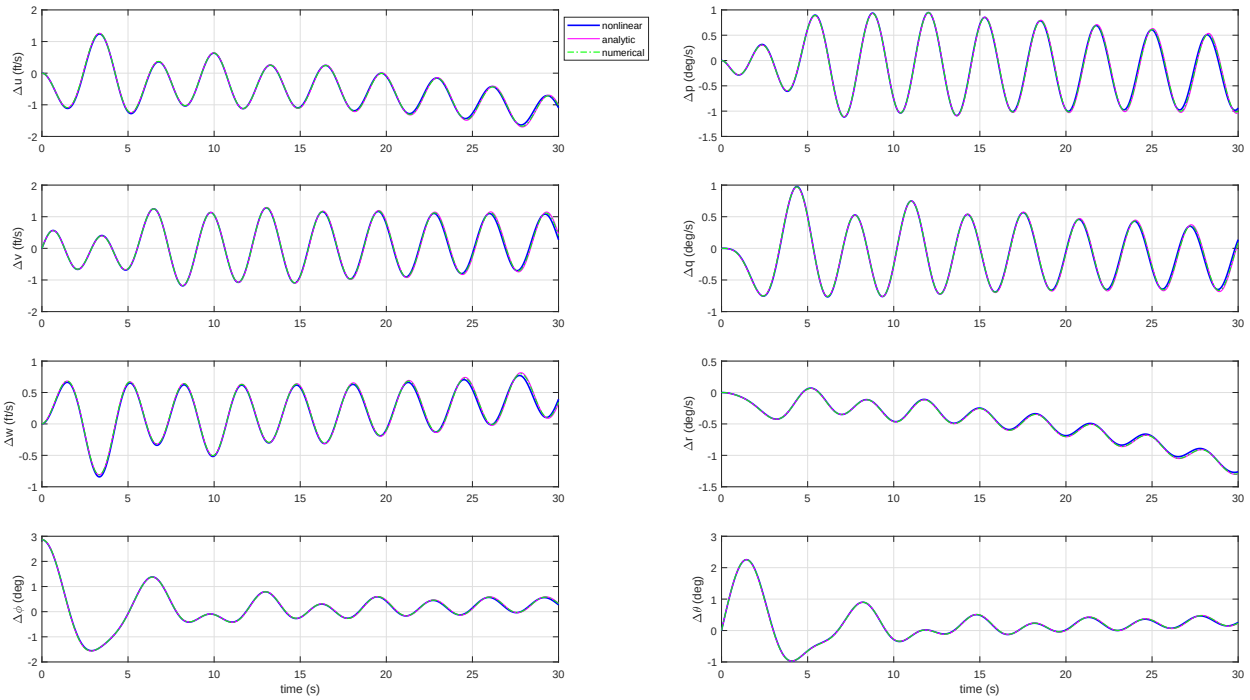

Figure 123 Linearized Body, Perturbation: $\Delta\varphi = 0.05(\text{rad})$

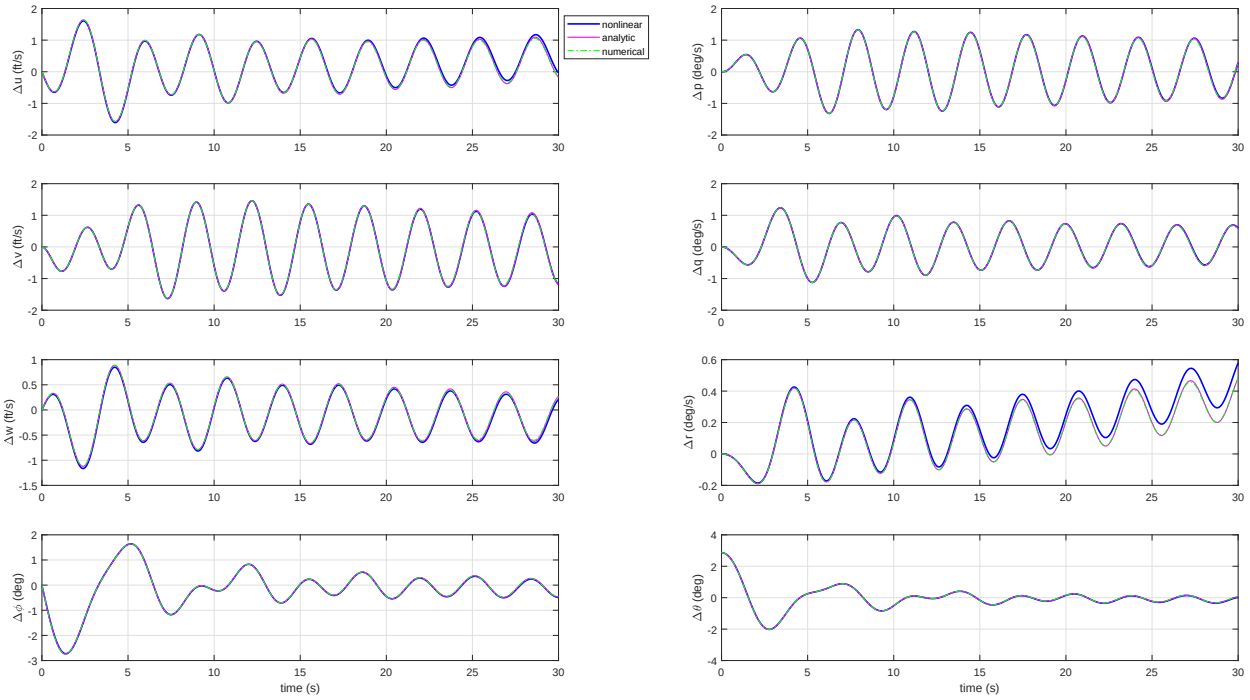

Figure 124 Linearized Body, Perturbation: $\Delta\theta = 0.05(\text{rad})$

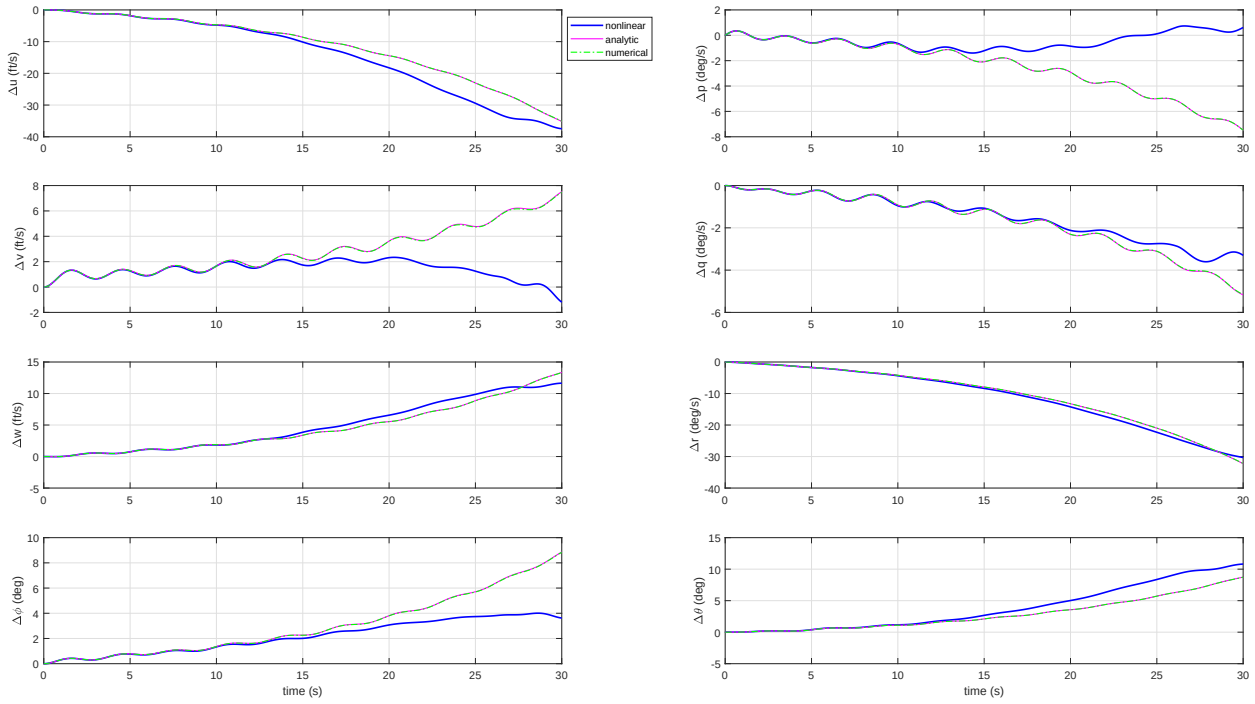

Figure 125 Linearized Body, Perturbation: $\Delta\delta_a = 0.05(\text{rad})$

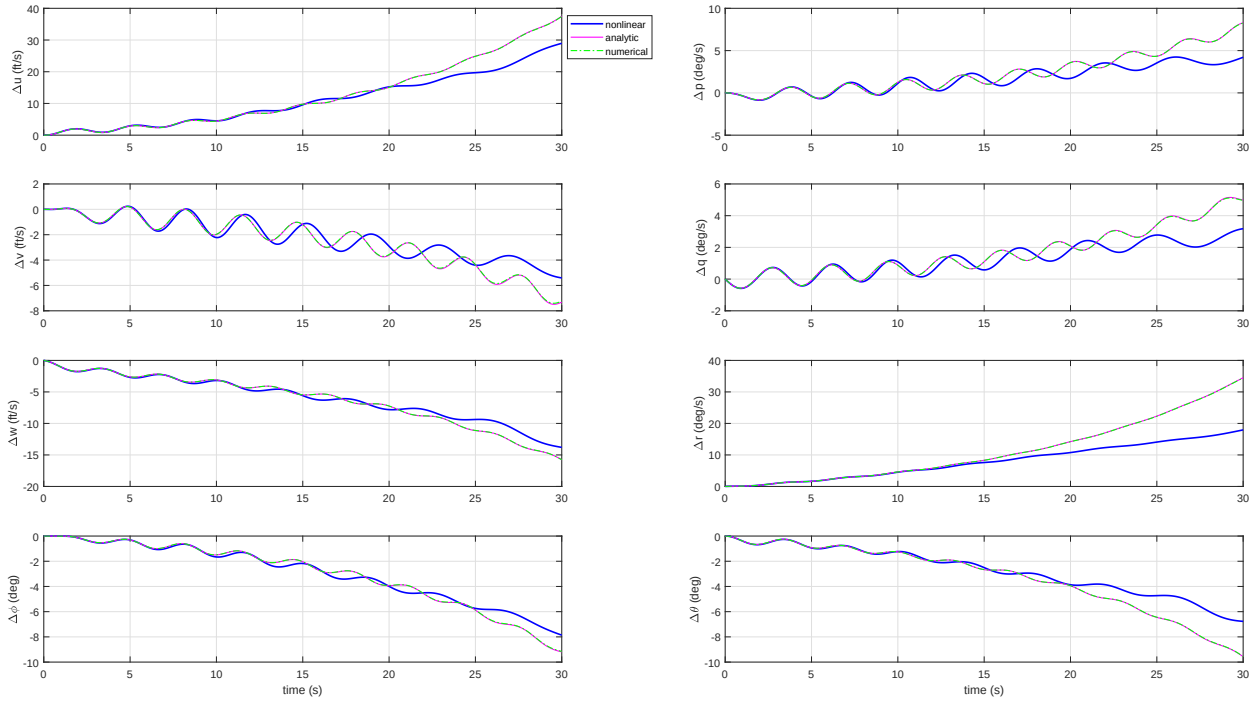

Figure 126 Linearized Body, Perturbation: $\Delta\delta_e = 0.05(\text{rad})$

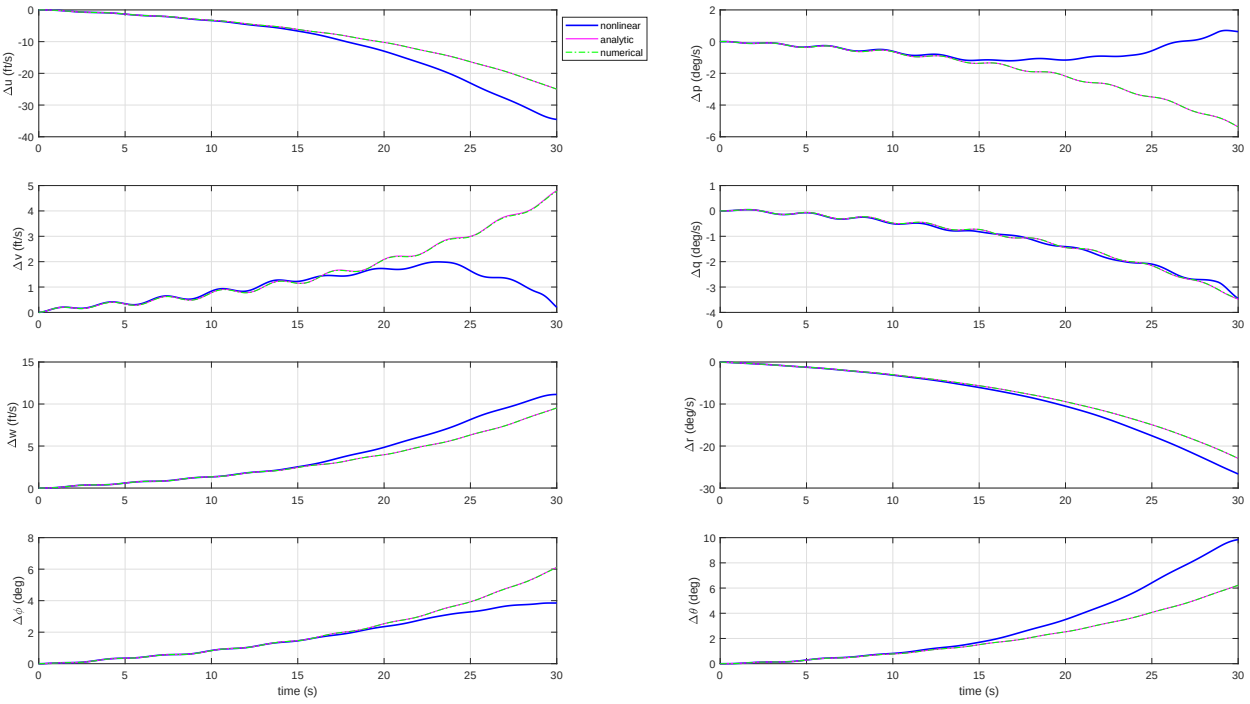

Figure 127 Linearized Body, Perturbation: $\Delta\delta_r = 0.05(\text{rad})$

APPENDIX B
NDI CONTROL

B.1 IRL Time Responses

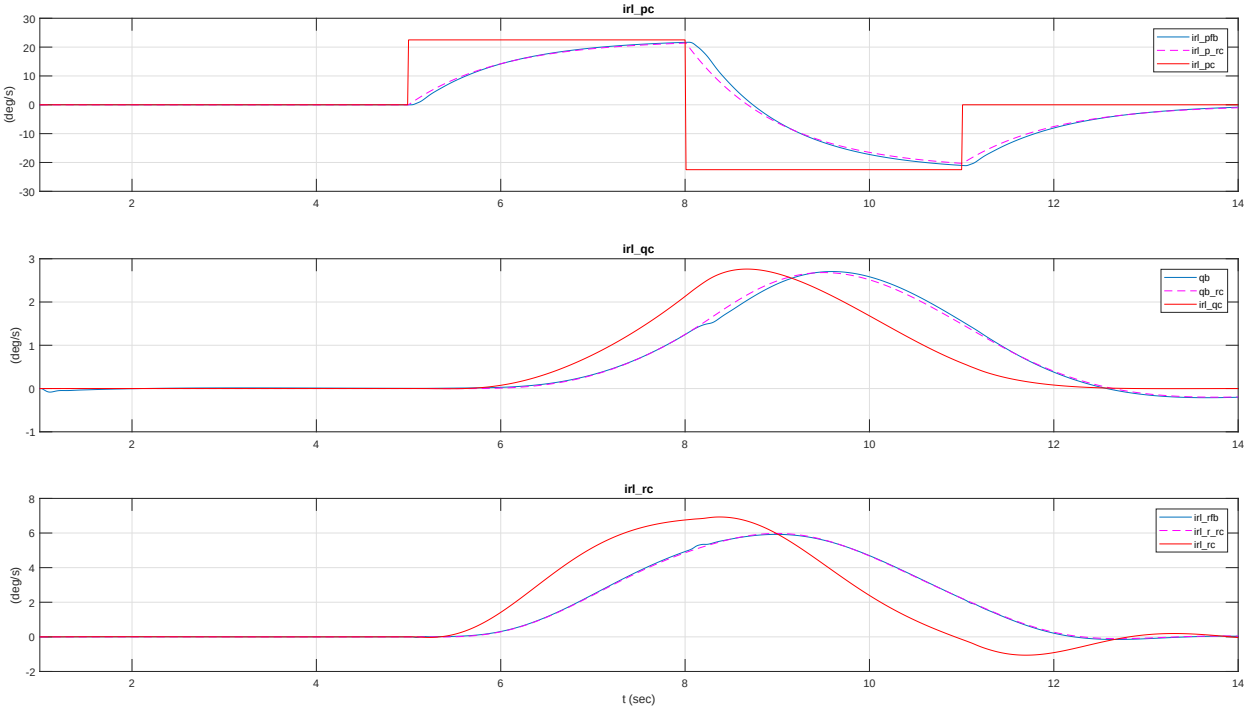

Figure 128 IRL p Doublet

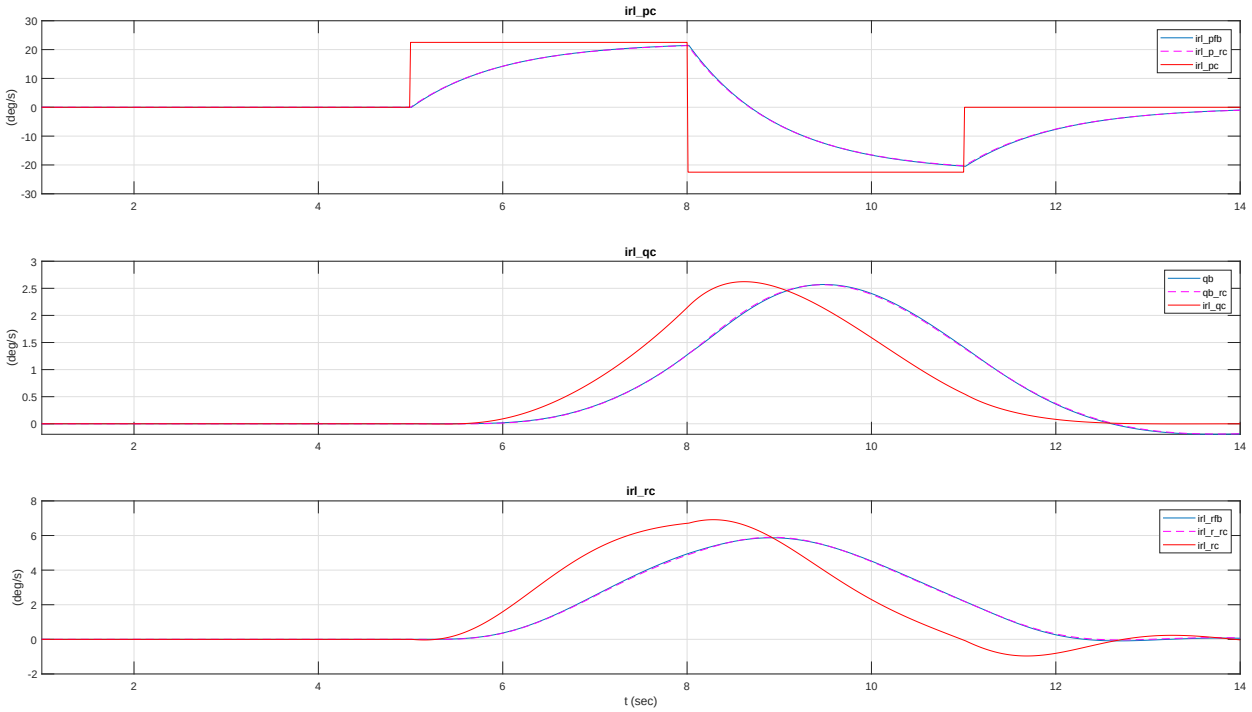

Figure 129 IRL p Doublet, Without Actuator Dynamics/Nonlinearities

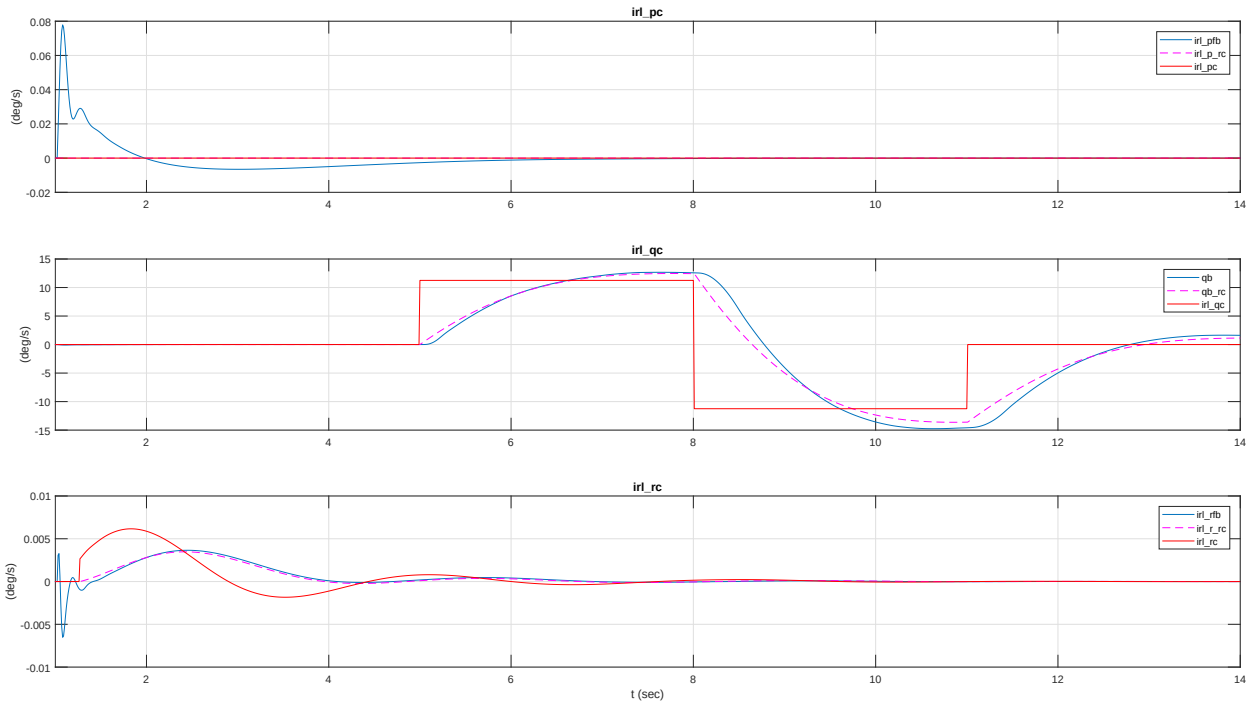

Figure 130 IRL q Doublet

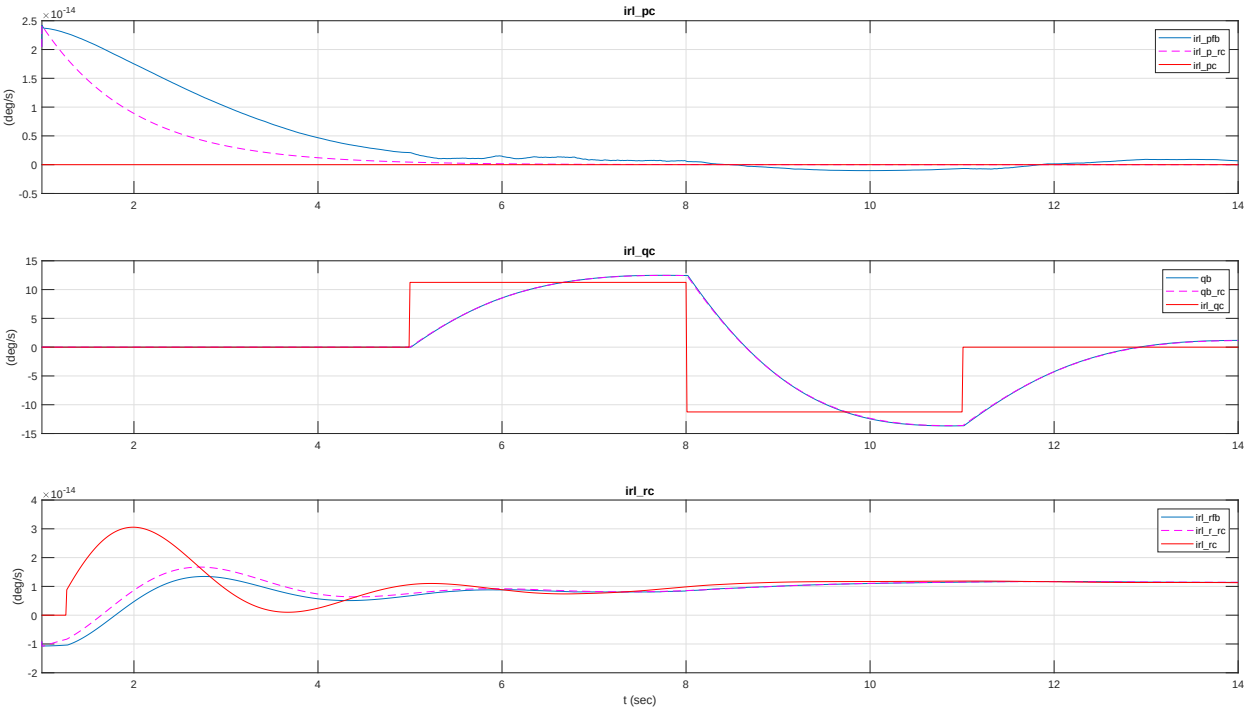

Figure 131 IRL q Doublet, Without Actuator Dynamics/Nonlinearities

B.2 MAL Time Responses

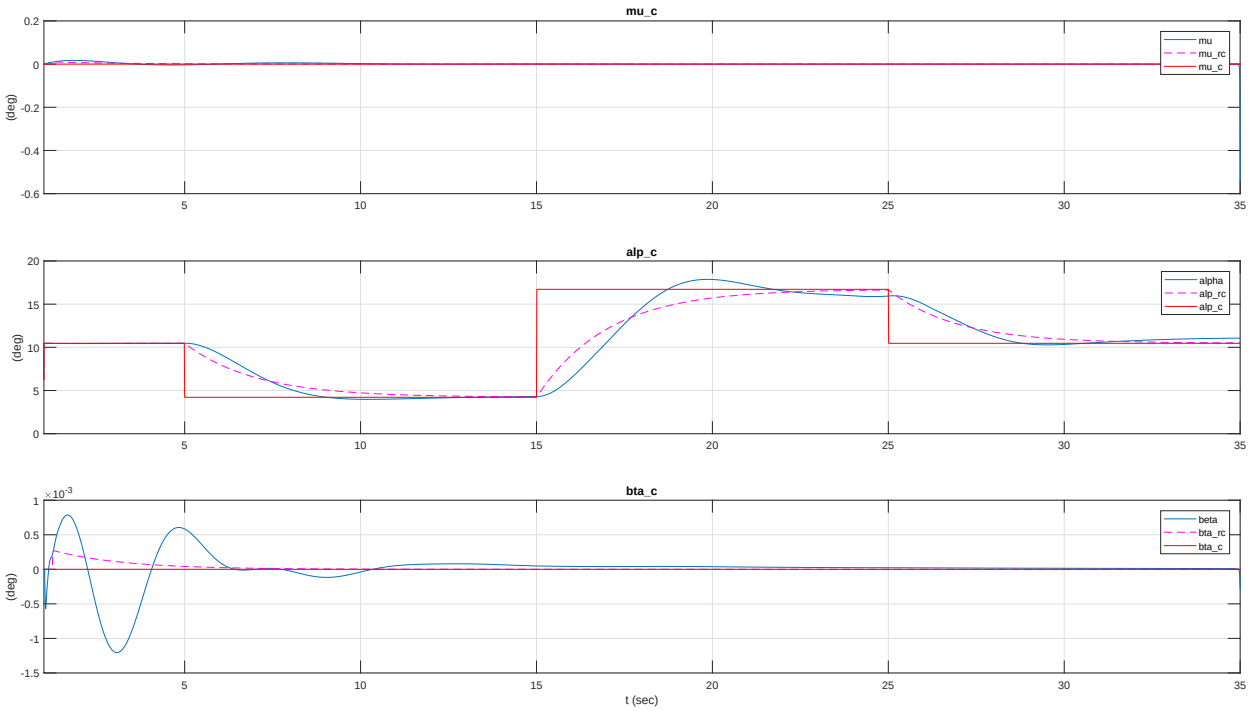

Figure 132 MAL α Doublet

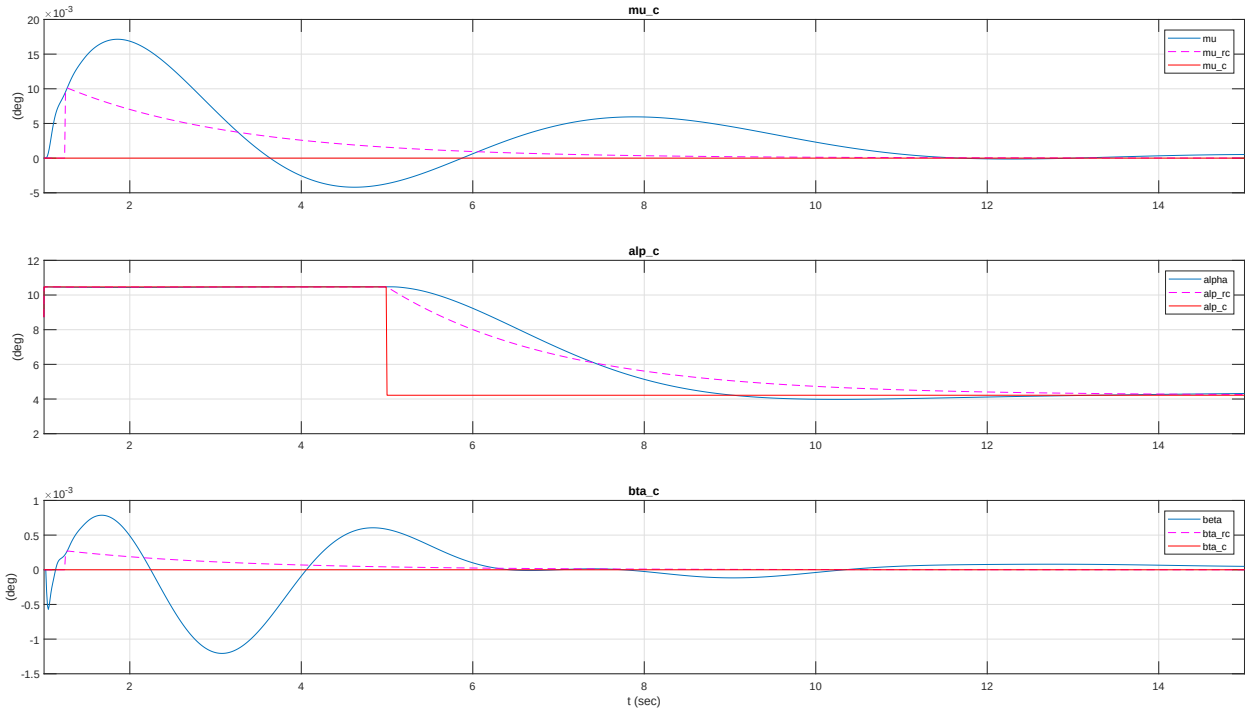

Figure 133 MAL α Step

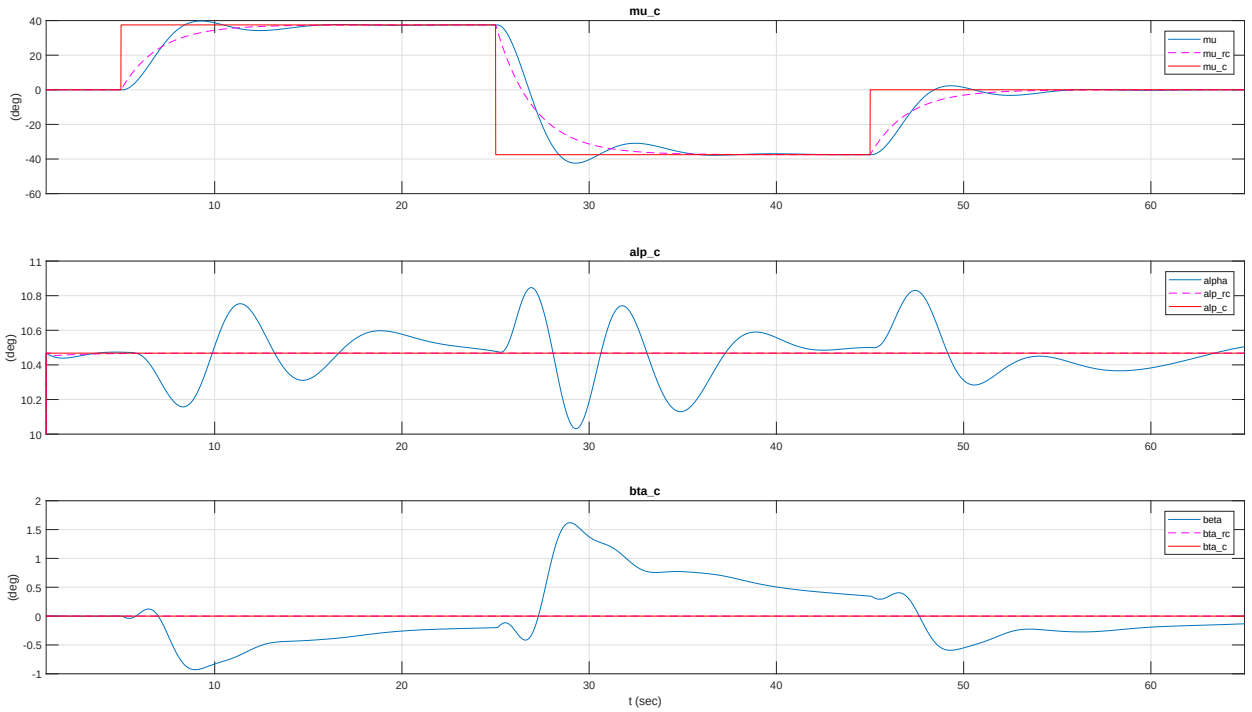

Figure 134 MAL μ Doublet

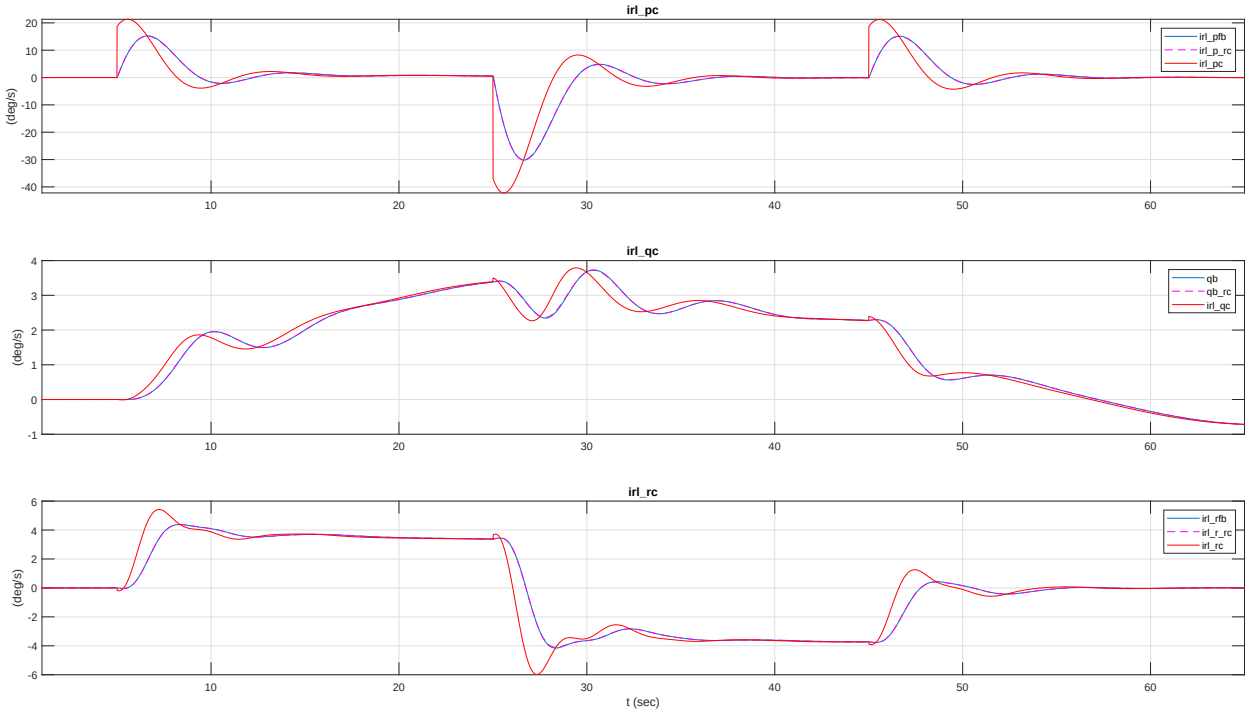

Figure 135 IRL μ Doublet

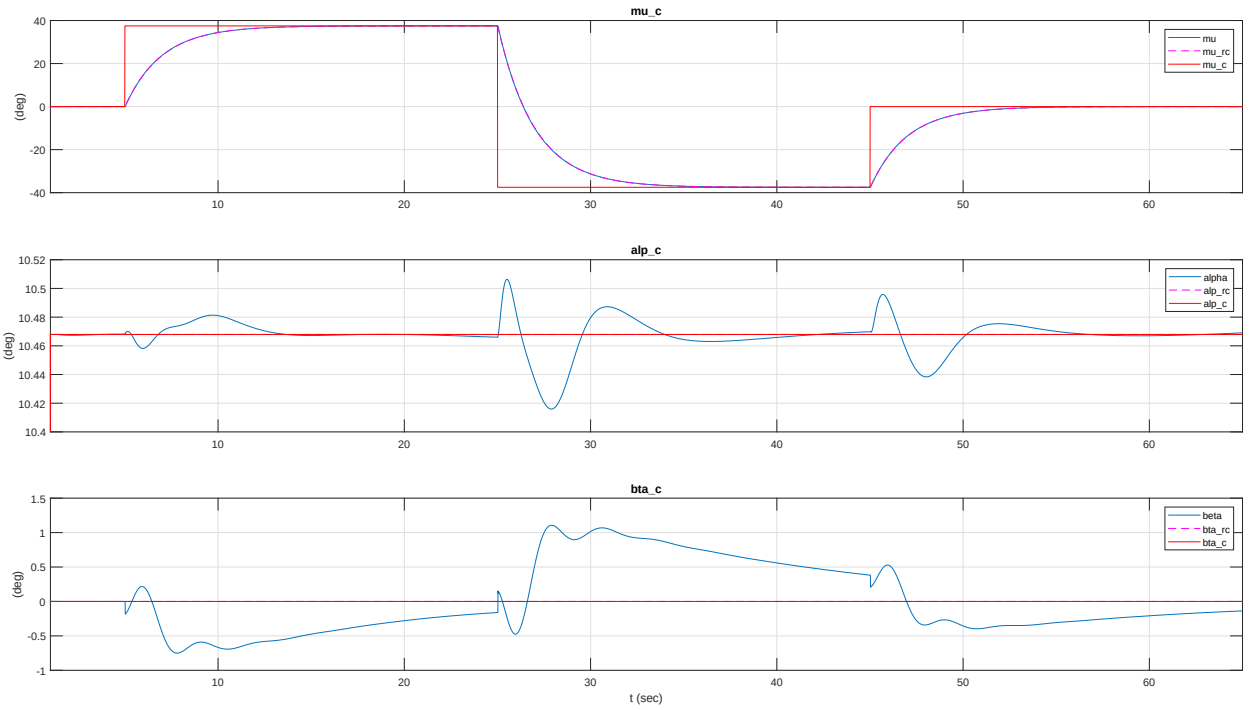

Figure 136 MAL μ Doublet, Without Actuator Dynamics/Nonlinearities

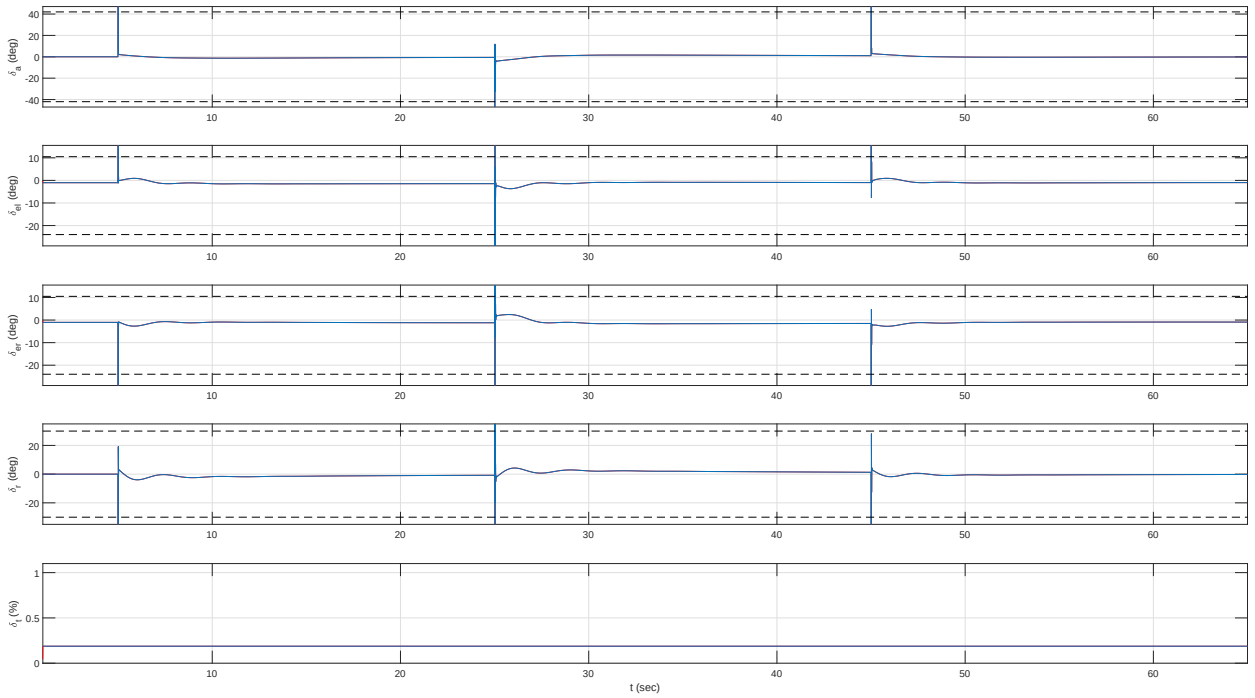

Figure 137 MAL μ Doublet, Control Requirements for Perfect Tracking

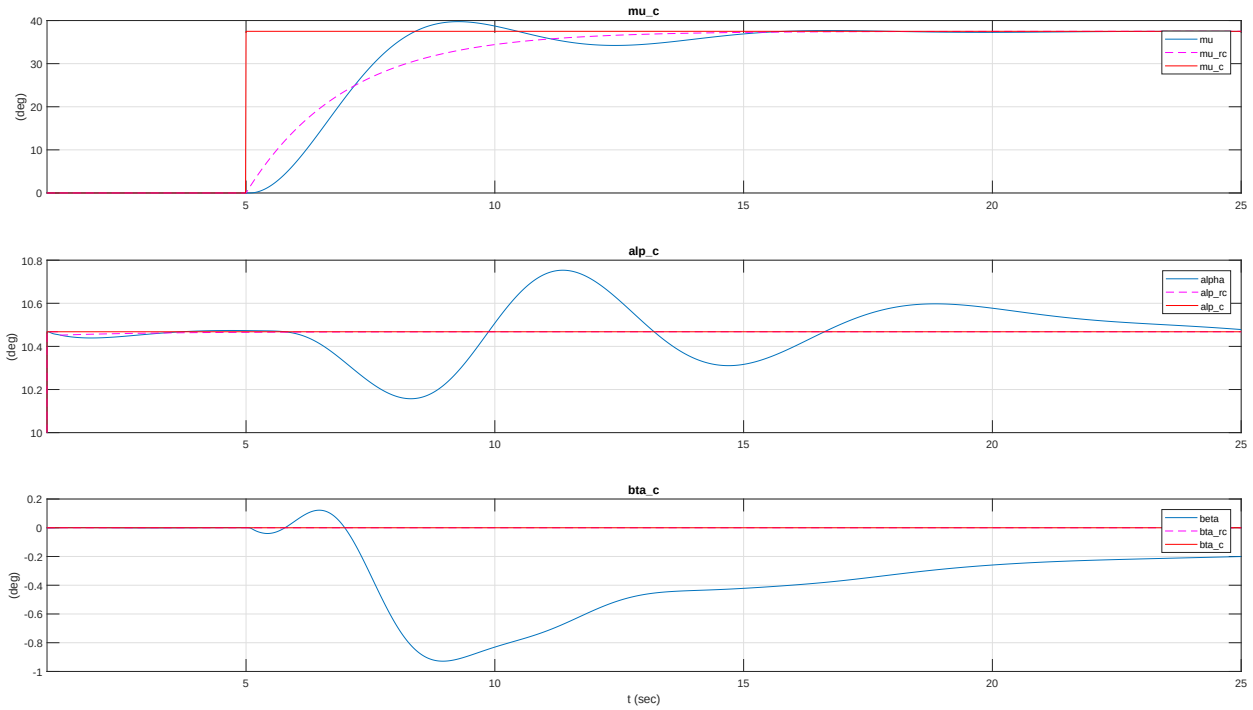

Figure 138 MAL μ Step

B.3 OPL Time Responses

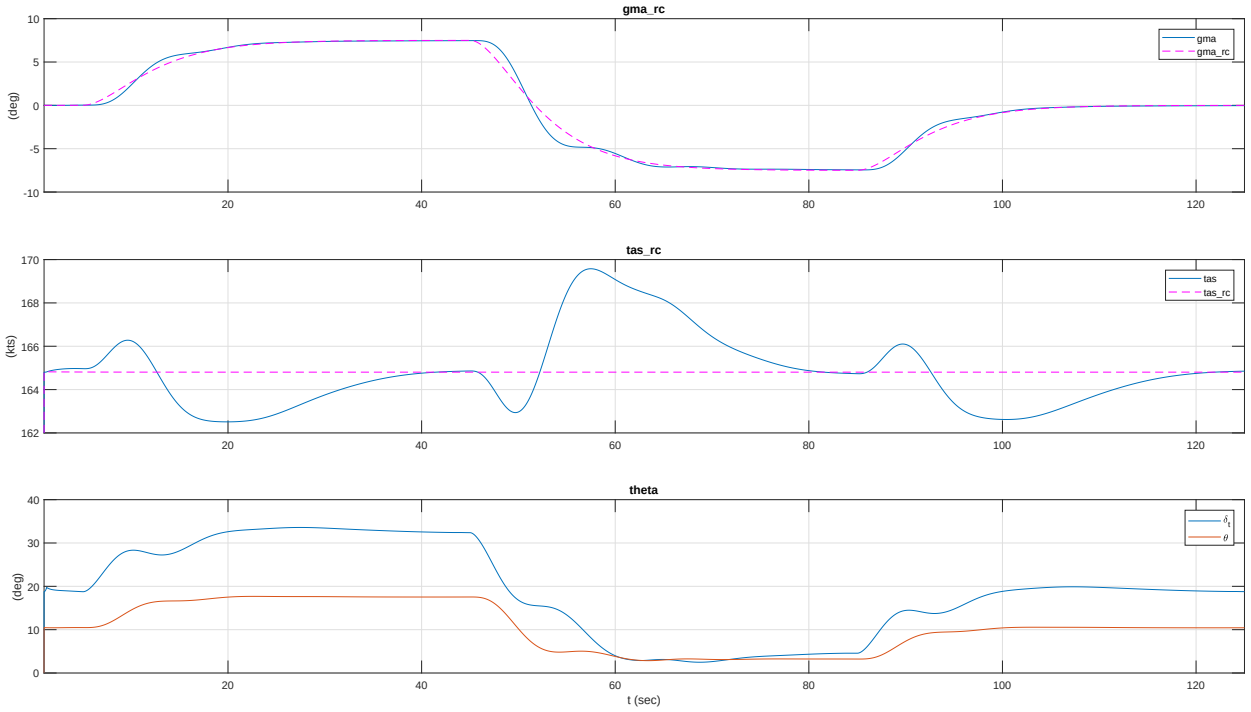

Figure 139 OPL γ Doublet

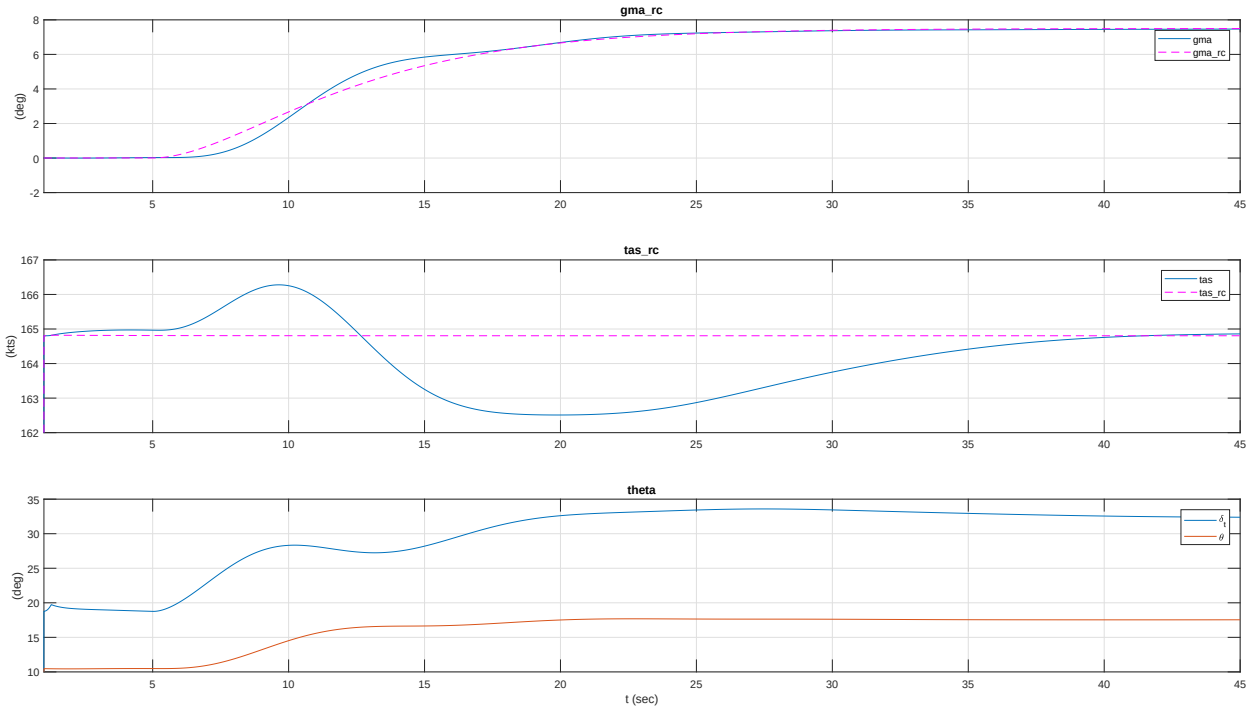

Figure 140 OPL γ Step

VITA

Jeffry Walker
Department of Aerospace Engineering
Old Dominion University
Norfolk, VA 23529

Jeffry Walker earned a B.S. in Mechanical Engineering from Old Dominion University in December of 2012. During his undergraduate studies Mr. Walker funded and lead a five degree of freedom anthropomorphic manipulator design project where he served as the lead electronics integration and control design engineer. Mr. Walker started his graduate studies under the accelerated BS/MS program in his final year of undergraduate studies enabling him to pursue his interest in aerospace engineering. In 2012 he joined Bihrle Applied Research as an Aerospace Engineer. While at Bihrle Applied Research Mr. Walker served as the primary engineer for simulation of the Boeing 777 autopilot and flight control system for use in full flight training simulators. Mr. Walker also served as a support engineer for the simulation of the Boeing 767 autopilot system. In 2015 he left Bihrle Applied Research to pursue his passion for the outdoors enabling him to work as a mountain guide for Mountain Madness during the 2016 season. Resuming engineering, he served as a Flight Control and Simulation Engineer at General Atomics Aeronautical Systems Inc. where he worked on the MQ-25 development team. In 2018, Mr. Walker left General Atomics in order to resume his graduate studies and ultimately resumed work at Bihrle Applied Research supporting multiple programs funded by the Air Force Research Laboratory. Mr. Walker intends to pursue future research and development in the field of flight control and autonomy with specific application to rotorcraft.

Typeset using LaTeX.